Institute of Engineering Surveying
and Space Geodesy

GPS and PSI Integration for Monitoring Urban Land Motion

By
Jonathan M Leighton MSc

Thesis submitted to the University of Nottingham for
the degree of Doctor of Philosophy
March 2010

Abstract

Urban ground motion due to natural or man-made geological processes is an issue of major importance for local authorities, property developers, planners and buyers. Increased knowledge of this phenomena would benefit all involved but the measurement techniques in common use have either spatial or temporal inadequacies. A technique known as Persistent Scatterer Interferometry (PSI) has been developed which can map ground motion to high precision over large areas with a temporal scale measured in years. PSI takes advantage of the high number of Synthetic Aperture Radar (SAR) images available to mitigate the atmospheric effects that inhibit standard Interferometric SAR (InSAR) techniques. This however involves assumptions about the nature of atmospheric variability, such as its randomness over time, or its spatial extent. In addition, little is known about the Persistent Scatterers (PS) themselves and PSI is only able to provide results relative to a reference PS. The reference PS point is often arbitrarily chosen and may itself be in an area undergoing ground motion, thus adding a degree of ambiguity to any relatively derived motion. The purpose of this work is to investigate possible solutions to these shortfalls and quantify any improvements made.

A corner reflector network is established in the Nottingham area of the UK. A data archive is collated over three years containing Global Positioning System (GPS) data at the corner reflector sites, data from surrounding Continuous GPS (CGPS) sites and levelling data. Due to conflicts with the European Space Agency (ESA) Environmental Satellite (ENVISAT), there were insufficient SAR images to compute a fully integrated corner reflector PSI study. Instead, the project focussed on atmospheric correction of PSI results using absolute ZWD estimates. Zenith Wet Delay (ZWD) estimates are derived from a Precise Point Positioning (PPP) GPS processing method which does not rely on a network of ground stations and therefore produces absolute ZWD estimates which are less prone to biases and noise. These are interpolated across a PSI study area and used to mitigate the long wavelength effects of atmopheric water vapour in the PSI differential interferograms. The corrected PSI results are then compared to uncorrected results, GPS derived motion and levelling

data.

Results between the ZWD corrected PSI study and the uncorrected study show statistical improvements in some areas and reductions in others. Correlation factors between double-differenced levelling observations and double-differenced PSI results improve from 0.67 to 0.81. PSI deformation rates also show improvement when compared to GPS deformation rates, although some results do not satisfy statistical tests.

Acknowledgements

This PhD project has been undertaken at the Institute of Engineering Surveying and Space Geodesy, University of Nottingham in conjunction with the British Geological Survey (BGS). Funding for the project was supplied partly by the Natural Environment Research Council and partly by the Engineering and Physical Sciences Research Council.

A very special thankyou to my principal supervisor, Andrew Sowter, who has mentored me and lifted my spirits in moments of doubt. I am also grateful for the continued support from my other two supervisors; Richard Bingley and Norman Teferle for their guidance throughout the project.

I would also like to thank the staff at BGS for supporting my work and providing access to facilities which have profoundly affected the outcome. In particular, my main point of contact Doug Tragheim has provided help and assistance on many levels, and Stuart Marsh, who has supervised my progress for the BGS University Funding Initiative and been able to wave problems away whenever they have arisen. Thanks also to Martin Culshaw and Luke Bateson for their input during the first half of the project.

Further thanks go to Charles Werner and Urs Wegmüller at Gamma Remote Sensing for their help with Gamma software, Colin Fane at Ordnance Survey for the loan of the pillar spider, Mark Warren for helping me understand PSI and Mark Haynes, formerly of Nigel Press Associates.

A special thanks must go to those who helped me on ENVISAT pass days; Andrew Sowter, Ahmed Taha, Stephen Blake, Huib de Ligt, Sean Ince, Sam Waugh, Ligia Adamska, Jenny Williams, Doug Tragheim, Luke Bateson and the various other students who were somehow convinced to give up their Saturdays for me.

Finally, a very special thanks to my girlfriend Jenny Williams for her unshaking belief in me and for her superior grasp of the English language.

Contents

Acronyms and Abbreviations **xvi**

1 Introduction **1**

1.1 Background 1

1.2 Urban Planning History 1

1.3 Urban Ground Motion 3

1.4 Detection and Measurement of Subsidence 3

1.5 Integration 4

1.6 Aims and Objectives 5

1.7 Research Methodology 5

1.8 Thesis Overview 6

1.9 Summary 7

2 Background **8**

2.1 Radar Overview 8

2.1.1 Early Radar 9

2.1.2 Side Looking Airborne Radar (SLAR) 9

2.1.3 SAR 10

2.2 SAR Operation 10

2.2.1 Coherent Imaging 11

2.2.2 SAR Geometry 11

2.2.3 Range Resolution 12

2.2.4 Azimuth Resolution 13

2.2.5 Geometric Distortion 14

2.2.6 Properties of SAR Images . . . 15
2.3 InSAR . . . 17
2.3.1 Interferometric Phase . . . 18
2.3.2 Phase Contributions . . . 18
2.3.3 InSAR Geometry . . . 19
2.3.4 The InSAR Model . . . 20
2.3.5 Interferogram Processing Flow . . . 21
2.3.5.1 Coregistration . . . 22
2.3.5.2 Resampling and Interpolation . . . 22
2.3.5.3 Interferogram Generation . . . 22
2.3.5.4 Coherence Estimation . . . 24
2.3.5.5 Filtering . . . 24
2.3.5.6 Multilooking . . . 25
2.4 Differential Interferometry . . . 25
2.4.1 Two-pass DInSAR . . . 26
2.4.2 DInSAR Errors and Limitations . . . 27
2.4.3 Phase Unwrapping . . . 27
2.4.4 Stacking . . . 29
2.5 Atmospheric Effects in InSAR . . . 30
2.6 Persistent Scatterer Interferometry . . . 31
2.6.1 Identification of Candidate PS Points . . . 32
2.6.2 Differential Phase . . . 33
2.6.3 Estimating Linear Deformation . . . 34
2.6.3.1 Applying the Phase Model . . . 34
2.6.3.2 Phase Unwrapping . . . 36
2.6.3.3 Atmospheric Phase . . . 37
2.7 GPS . . . 38
2.7.1 History and Concept . . . 38
2.7.2 System Overview . . . 39
2.7.2.1 The Space Segment . . . 39
2.7.2.2 The Control Segment . . . 39

2.7.2.3 The User Segment . . . 40
2.7.3 Observables and Signal Structure . . . 40
2.7.3.1 The Pseudo-Range Observable . . . 41
2.7.3.2 The Carrier Phase Observable . . . 43
2.8 PPP . . . 45
2.8.1 The PPP Observation Model . . . 46
2.8.2 PPP Errors and Models . . . 47
2.8.2.1 Multipath . . . 48
2.8.2.2 Absolute Antenna Phase Centre Corrections . . . 48
2.8.2.3 Ocean Tide Loading . . . 50
2.8.2.4 Earth Body Tides . . . 50
2.8.2.5 Tectonic Plate Motion . . . 50
2.8.2.6 Tropospheric Delay . . . 51
2.9 Summary . . . 53

3 InSAR Integration Review **54**
3.1 Introduction . . . 54
3.2 InSAR Integration Research . . . 55
3.2.1 Atmospheric Delay Background . . . 55
3.2.2 InSAR Atmospheric Calibration . . . 56
3.2.3 Corner Reflectors in InSAR . . . 57
3.3 Research Motivations . . . 59
3.3.1 Corner Reflectors for PSI . . . 59
3.3.2 Atmospheric Phase Assumptions . . . 60
3.3.3 GPS in PSI . . . 61
3.3.4 PSI Validation . . . 62
3.4 Summary of Limitations . . . 62
3.5 Summary . . . 63

4 The Nottinghamshire Site **64**
4.1 Introduction . . . 64
4.2 Orientation . . . 65

4.3 Geography . . . 65
4.4 Geological Setting . . . 65
4.5 Potential Geohazards . . . 67
4.5.1 Coal Mining . . . 67
4.5.2 Boreholes . . . 68
4.5.3 Caves . . . 68
4.5.4 Alluvial Deposits . . . 68
4.5.5 Made Ground . . . 68
4.6 Climate and Meteorology . . . 69
4.7 Logistics and Resources . . . 69
4.8 Data Sources . . . 70
4.8.1 SAR Data . . . 70
4.8.2 Continuous GPS Stations . . . 70
4.9 Summary . . . 71

5 Data Acquisition 72
5.1 Introduction . . . 72
5.2 The Nottinghamshire Corner Reflector Array (NCRA) . . . 73
5.2.1 Size Constraints . . . 73
5.2.2 Site Selection Criteria . . . 73
5.2.2.1 Stability . . . 74
5.2.2.2 GPS Considerations . . . 75
5.2.2.3 Site Clutter . . . 75
5.2.3 NCRA Sites . . . 75
5.2.4 Reflector Modifications . . . 75
5.2.5 Alignment . . . 76
5.2.6 Permanent Sites . . . 79
5.3 SAR Data . . . 80
5.3.1 Cat-1 Project . . . 80
5.3.2 ENVISAT Pass Geometries . . . 81
5.3.3 Selecting the AOI . . . 82

5.4 Field Observation Planning 82
5.4.1 GPS Observation Planning 83
5.4.2 Processing Aims 83
5.4.3 Session Length 84
5.4.4 Session Timing 85
5.4.5 Session Test Analysis 87
5.5 The NCRA Dataset 88
5.5.1 Dataset Analysis 88
5.5.2 Site Visibility 91
5.6 Existing PSI Results and Levelling 92
5.7 Implications of the Reduced Dataset 94
5.8 Summary 95

6 Methodology and Results **96**
6.1 GPS Data Processing 96
6.1.1 Overview 96
6.1.2 Pre-Processing Checks 97
6.1.3 A Priori Position Estimates 100
6.1.4 PPP Processing 100
6.1.4.1 Orbits and Clocks 101
6.1.4.2 Absolute Antenna Phase Centre Corrections 102
6.1.4.3 Solid Earth Tides 102
6.1.4.4 Polar Tides 102
6.1.4.5 Ocean Tides 102
6.1.4.6 Hydrostatic Troposphere Mapping 103
6.1.5 Post-Processing Checks 103
6.1.6 Tropospheric Zenith Delay Estimates 103
6.2 SAR Data Processing 104
6.2.1 Overview 105
6.2.2 PSI Preparation 105
6.2.2.1 Calibration 105

6.2.2.2 Orbits . . . 106
6.2.2.3 Baselines . . . 106
6.2.2.4 DEM Preparation . . . 106
6.2.2.5 Slave Scene Coregistration . . . 107
6.2.2.6 Stacking . . . 108
6.2.3 PSI Processing . . . 110
6.2.3.1 Candidate PS Selection . . . 111
6.2.3.2 Quality Control . . . 112
6.2.3.3 Regression Analyses . . . 113
6.2.3.4 First Regression . . . 113
6.2.3.5 Baseline Improvement . . . 114
6.2.3.6 Second Regression . . . 114
6.2.3.7 Third Regression . . . 115
6.2.3.8 Fourth Regression . . . 115
6.2.3.9 Fifth Regression . . . 115
6.3 Precise Levelling . . . 115
6.3.1 Levelling Methodology . . . 116
6.3.2 Levelling Results . . . 116
6.4 GPS Results and Analysis . . . 117
6.4.1 GPS Time series . . . 117
6.5 PSI Results and Analysis . . . 123
6.5.1 Nottingham City Centre . . . 123
6.5.1.1 Uplift in the Wollaton Area (A1) . . . 123
6.5.1.2 Uplift in the Hucknall Area (A2) . . . 126
6.5.1.3 Subsidence in the Lenton Industrial Area (A3) . . . 128
6.5.1.4 Subsidence in the Gedling Area (A4) . . . 128
6.5.2 PSI Statistics . . . 129
6.5.2.1 Geocoding Accuracy . . . 129
6.5.2.2 PSI Consistency . . . 129
6.6 PSI and GPS Comparison . . . 131
6.7 Summary . . . 133

7 ZWD Correction for PSI **135**

7.1 APS Correction using ZWD 135

7.1.1 ZWD Estimates 136

7.1.2 Observation Geometry 136

7.1.2.1 Elevation Mask 137

7.1.2.2 ZWD and APS Comparison Model 137

7.1.3 ZWD and APS Correlation 138

7.1.3.1 Undifferenced Comparison 139

7.1.3.2 Results 139

7.1.4 ZWD Screens 141

7.1.4.1 Interpolation Testing 142

7.1.4.2 AOI ZWD Values 143

7.1.5 ZWD Integration 144

7.2 Results and Analysis 144

7.2.1 PSI Result Comparison 146

7.2.1.1 PSI Rejection 146

7.2.1.2 Deformation Rates 146

7.2.1.3 Residual Phase 149

7.2.1.4 Deformation Uncertainties 150

7.2.1.5 Height Corrections 152

7.2.2 Levelling Comparison 152

7.2.3 GPS Comparison 154

7.2.3.1 NOTT and IESG 155

7.2.3.2 BGS1 and KEYW 156

7.2.3.3 WNCO 156

7.2.4 Atmospheric Effects on PSI Time Series 157

7.3 Discussion 158

7.4 Summary 159

8 Conclusions and Recommendations **160**

8.1 Review of Aims and Objectives 160

8.2 Integration Research 161
8.3 Corner Reflectors in PSI 161
8.4 Observation Model 162
8.4.1 ENVISAT Data 162
8.4.2 Reflector Visibility 162
8.4.3 Field Observations 163
8.4.4 Discussion 163
8.5 GPS and PSI Integration 166
8.5.1 Data Quality 166
8.5.2 PPP Processing Model 166
8.5.3 PSI Processing Model 166
8.5.4 Geometry and Interpolation 167
8.5.5 ZWD Correction 167
8.5.6 Discussion 167
8.6 Recommendations for Further Work 168
8.7 Summary 168

Appendices **A-1**

A Corner Reflector Theory **A-1**

A.1 Man-made Passive Corner Reflectors A-1

List of Figures

1.1 Underground void collapse 2

2.1 SAR geometry 12
2.2 Foreshortening in radar images 14
2.3 Layover in radar images 15
2.4 Shadow in radar images 15
2.5 Argand diagram of an SLC pixel 16
2.6 Constructive and destructive interference 17
2.7 Earth and ellipsoidal InSAR geometry 20
2.8 Interferogram of Nottinghamshire 23
2.9 Coherence image of Nottinghamshire 24
2.10 Wrapped and unwrapped interferometric phase 28
2.11 The PSI phase regression process 36
2.12 The GPS signal structure 41
2.13 Code timestamp offset 42
2.14 TEQC analysis 49
2.15 ZTD mapping 52

4.1 The Nottingham site AOI 66
4.2 CGPS stations in and around the AOI 71

5.1 NPA trihedral corner reflector 74
5.2 Reflector base modifications and OS pillar mount 77
5.3 The OS pillar mount 78
5.4 Trihedral reflector geometry 79

5.5 Central UK and the project study area 81
5.6 Project subscene area 82
5.7 ZWD profile examples 86
5.8 Kinematic position profile examples 87
5.9 SinC interpolation 92
5.10 Reflector site intensity analysis 93

6.1 NCRA GPS pre-processing 98
6.2 CGPS pre-processing 99
6.3 Perpendicular baseline chart 107
6.4 Nottinghamshire multi-looked intensity image 108
6.5 Stacking result 110
6.6 The PSI processing flow 111
6.7 Hucknall precise levelling campaign 116
6.8 NCRA GPS position time series 118
6.9 CGPS position time series 119
6.10 CGPS daily position time series 122
6.11 Nottinghamshire PSI result 124
6.12 Nottingham city PSI result 125
6.13 Nottingham city PSI result and local geology 126
6.14 Persistent Scatterers P1 to P4 127
6.15 PSI Statistics 130
6.16 GPS and PSI velocity estimates 133

7.1 GPS wet delay and APS geometry 138
7.2 ZWD and APS Correlation 140
7.3 ZWD and APS scatterplot 141
7.4 ZWD screen network stations 142
7.5 Three dimensional ZWD screen 143
7.6 ZWD screens 145
7.7 The ZWD corrected PSI result 147
7.8 Differences in deformation rates 148

7.9 Residual phase standard deviations 149
7.10 Deformation uncertainties 150
7.11 Spatial distribution of deformation uncertainties 151
7.12 Height corrections 152
7.13 Hucknall precise levelling campaign 153
7.14 Levelling results 154
7.15 GPS and PSI velocity estimates 155
7.16 GPS and PSI velocity estimates 157

A.1 Retro-reflectance in two dimensions A-2
A.2 Effective trihedral reflector area A-3

List of Tables

4.1 CGPS stations in and around the AOI 70

5.1 NCRA Site Locations 76
5.2 GPS profile analysis 89
5.3 Reflector sites and ASAR acquisition dates 90

6.1 RMS and Velocities for GPS stations 121

7.1 ZWD Corrected PSI Stack 136

Acronyms and Abbreviations

AMSL	Above Mean Sea Level
AOAD/M_T	Allen Osborne Associates Dorne Margolin Model T
AOI	Area of Interest
APOLLO	Apache Point Observatory Lunar Laser-ranging Operation
APPS	Automatic Precise Positioning Service
APS	Atmospheric Phase Screen
ARP	Antenna Reference Point
ASAR	Advanced SAR
ASKE	Askerton Triangulation Pillar
BGS	British Geological Survey
BIGF	The British Isles continuous GNSS Facility
CA	Coarse Acquisition
CATS	Create and Analyse Time Series
CDMA	Code Division Multiple Access
CGPS	Continuous GPS
DEM	Digital Elevation Model
DORIS	Doppler Orbitography and Radiopositioning Integrated by Satellite
DSM	Digital Surface Model
EBT	Earth Body Tides
ECMWF	European Centre for Medium-Range Weather Forecasts
EDINA	University of Edinburgh national academic data centre
EGPS	Episodic GPS
ENVISAT	Environmental Satellite
ERP	Earth Rotation Parameters

ERS	European Remote Sensing Satellite
ESA	European Space Agency
EUMETNET	European National Meteorological Services Network
FLINN	Fiducial Laboratories for an International Natural sciences Network
FM	Frequency Modulated
Gamma	Remote sensing consultation company based in Bern, Switzerland
GCP	Ground Control Point
GDOP	Geometric Dilution of Precision
GEONET	GPS Earth Observation Network in Japan
GIPSY-OASIS II	GPS Inferred Positioning System and Orbit Analysis Simulation Software II
GMF	Global Mapping Function
GNSS	Global Navigation Satellite System
GOA-II	GPS Inferred Positioning System and Orbit Analysis Simulation Software II
HOOB	Hoober OS GNSS Station
HRSC	High Resolution Stereo Scanner
IESG	IESSG GNSS Station
IESSG	Institute of Engineering Surveying and Space Geodesy
IGS	International GNSS Service
IPAF	Italian Processing and Archiving Facility
IPTA	Interferometric Point Target Analysis
ITRF	International Terrestrial Reference Frame
JERS	Japanese Earth Resources Satellite
JPL	Jet Propulsion Laboratory
KEYW	Keyworth OS GNSS Station
L1/L2	GPS L1 and L2 signals
LEEK	Leek OS GNSS Station
LICF	Lichfield OS GNSS Station
LINO	Lincoln OS GNSS Station
LOS	Line of Site

MCF	Minimum Cost Flow
MCS	Master Control Station
MILF	Milford OS Triangulation Pillar
MLE	Maximum Likelihood Estimator
MP	Multipath
MP1/2	RMS values of the de-trended estimates of the P-code multipath on L1/2
MZWD	Mapped Zenith Wet Delay
NCRA	Nottingham Corner Reflector Array
NNSS	Navy Navigation Satellite System AKA 'TRANSIT' or 'NAVSAT'
NOTT	Nottingham OS GNSS Station
NPA	Nigel Press Associates
NRT	Near RealTime
OS	Ordnance Survey
OTL	Ocean Tide Loading
PCO	Phase Centre Offsets
PCV	Phase Centre Variations
PPP	Precise Point Positioning
PR	Pseudo-range
PRF	Pulse Repetition Frequency
PRN	Pseudo-Random Noise
PS	Persistent Scatterer
PSI	Persistent Scatterer Interferometry
PSIC4	PSI Codes Cross-Comparison and Certification for Long-Term Differential Interferometry
PVW	Precipitable Water Vapour
Radar	Radio Detection And Ranging
RADARSAT	Canadian remote sensing satellites 1 and 2
RAF	Royal Air Force
RCS	Radar Cross Section
RDC	Range-Doppler Coordinates

RINEX	Receiver Independent Exchange Format
RMS	Root Mean Square
RMSE	Root Mean Square Error
SAR	Synthetic Aperture Radar
SBAS	Small Baseline Subset
SCIGN	Southern California Integrated GPS Network
SD	Standard Deviation
SEASAT	Remote sensing satellite operated by JPL
SLAR	Side Looking Airborne Radar
SLC	Single-Look Complex
SLR	Satellite Laser Ranging
SNR	Signal to Noise Ratio
SRIF	Square-Root Information Filter
SRTM	Shuttle Radar Topography Mission
STUN	Spatio-Temporal Unwrapping Network
SVD	Single Value Decomposition
TEQC	Translation, Editing, and Quality Check
TOPEX/Poseidon	Joint satellite mission between the US and the French to map ocean surface topography
TRANSIT	Navy Navigation Satellite System AKA 'NNSS' or 'NAVSAT'
TRF	Terrestrial Reference Frame
UNAVCO	University Navstar Consortium
UTC	Coordinated Universal Time
UTM	Universal Transverse Mercator
VLBI	Very Long Baseline Interferometry
VRS	Virtual Reference Station
VV	Vertical transmitted and vertical received polarisation
WNCO	West Notts College Triangulation Pillar
ZHD	Zenith Hydrostatic Delay
ZTD	Zenith Total Delay
ZWD	Zenith Wet Delay

Chapter 1

Introduction

1.1 Background

Monitoring the urban environment is extremely important. As populations rise, cities expand into areas of greater potential natural and man-made hazards. In the UK, applications for new building developments now have to be submitted with a subsidence report. This is a very costly process, and subsequently there is an ever increasing requirement for knowledge that might influence decision making. Surveying techniques are useful in this respect but they often only provide sparse but accurate results, such as those provided by Thames Valley network of GPS stations (Bingley et al., 1999). With the advent of InSAR, a remote sensing technique known as PSI (Ferretti et al., 2001) has become possible that is capable of giving good results over a much denser network of points (around 100 to 500/km^2). However, it too has limitations and concerns about its consistency have also been voiced (Racoules et al., 2006).

1.2 Urban Planning History

Many modern cities in the UK are literally built on the foundations of the less well informed past. Prior to the industrial age, building material extraction and mineral extraction for fuel was an unregulated activity and has a history that reaches into the middle ages (Charsley et al., 1990).

Throughout the industrial age the geological environment underpinned the economic development of many urban areas and the requirement for underground resources such as building materials and fossil fuels outweighed any real concern for the environment. To exacerbate this, many cities expanded so rapidly that planning decisions were often poorly made (Childe, 1950, Howard et al., 2010), and the legacy of ground motion due to mineral extraction, backfill and urban waste is widespread (Bell et al., 2009).

Consequently, the location, depth and extent of many types of shallow underground voids is completely unknown (Waltham, 1989, Howard et al., 2010) and these can sometimes lead to ground motion or even catastrophic collapse (see figure 1.1). Much of this activity occurred on the edges of population centres as they were then, many of which are now at the heart of modern cities.

Figure 1.1: An example of sudden collapse resulting from unknown underground voids (Waltham, 1989).

1.3 Urban Ground Motion

The characteristics and causes of ground motion in urban areas are wide and varied and provide a constant challenge to geologists, scientists and engineers (Galloway et al., 1999, Capes and Marsh, 2009). In this age of enhanced environmental awareness, quantifying these motions is at the forefront of risk awareness and planning strategies. Insurance companies, planners, developers and property buyers would all benefit from better knowledge of urban ground motion and its underlying causes. Damage to buildings and infrastructure costs insurance companies hundreds of millions of pounds each year (BGS, 2002), a cost which is then reflected in premiums and policy excess. Geohazards, as they are termed, can also threaten livelihoods, seriously injure and endanger life. An understanding of the factors behind urban ground motion can come from a number of different sources, including historic evidence, hydrology, geology and knowledge of the nature and precise location of the motion. These motions may lie undetected until they manifest as structural damage which ranges from slight to catastrophic. Methods that are able to alert planners and engineers before this occurs, are therefore invaluable.

1.4 Detection and Measurement of Subsidence

There are methods that can be used to measure subsidence post detection such as GPS, which can be placed optimally with the benefit of hindsight. A greater challenge is detecting subsidence in the first place. This can be done in a number of ways including methods involving airborne imagery (Eyers and Mills, 2002), photogrammetry (Faig, 1984) and High Resolution Stereo Scanners (HRSC) (Spreckels, 1999). The equipment, planning and continued financial outlay required for these methods puts them beyond the reach of many though.

PSI studies are playing an increasing role in ground motion studies (Capes and Marsh, 2009). To some extent, this has probably become self perpetuating as high profile PSI results have generated media attention (Smith, 2002, Amos, 2007) which has led to a wider awareness of geohazards and a demand for more data.

There are however, issues with the technique that hinder its wider application. These include:

- Atmospheric error can only be mitigated to a certain degree
- Only relative deformations can usually be derived
- Attempts to validate the technique have not always been successful (Racoules et al., 2006)
- It is not clear how this new approach can be optimally integrated with other data
- The temporal sampling rate is generally poor

All techniques tend to have established strengths and weaknesses and dealing with these optimally is part of the wider challenge of integrated research. Often, a solution to an issue may be to combine existing techniques in order to somehow play off their strengths and weaknesses which leads to something that is more useful than the sum of its parts.

1.5 Integration

One strategy to minimise the issues mentioned above would be to integrate PSI with sources of data that complement its weaknesses. GPS is one such source; atmospheric error can be estimated to a high degree, it can estimate absolute deformation, it is well validated and its temporal sampling rate is excellent.

There is no obvious solution as to how a link between the two techniques might be facilitated, but one method is through the use of trihedral corner reflectors. Corner reflectors provide a precise, identifiable position both in the image as a high intensity pixel, and on the ground as a pre-surveyed control point. They also provide an opportunity to create artificial point scatterers in the PSI process. These might be used to somehow control or validate the PSI process.

By-products from GPS processing, such as the atmospheric delay term could be used to mitigate the atmospheric error term in a PSI analysis. Both GPS and PSI are

affected by the atmosphere in similar ways, therefore correlation and the potential for correcting PSI studies is a theoretical possibility.

1.6 Aims and Objectives

Considering the statements above, the overarching theme in this work concerns the subject of GPS and PSI integration both through the use of corner reflectors and through the relation and potential correlation of their respective parameters. Three project aims are now stated regarding this:

- Study background areas and conduct a literature search concerning GPS and PSI integration.
- Analyse what value corner reflectors might bring to PSI.
- Consider how GPS might be integrated with PSI.

These project aims are necessarily broadly defined. They can be further broken down where necessary into a set of project objectives:

- Identify gaps in GPS and PSI integration research.
- Investigate the potential for long-term corner reflectors and their use as artificial PS points.
- Investigate the potential for reference point bias removal using corner reflectors.
- Consider how GPS might be used to improve PSI atmospheric phase screens.
- Determine how GPS might be used to validate PSI studies.

1.7 Research Methodology

Having stated explicitly what the objectives of the project are, the research methodology now gives an outline of how these objectives may be achieved:

- Detail the background topics relevant to this research, referencing definitive sources.
- Select a suitable test site for the project and establish a network of small, passive corner reflectors.
- Design an observation model involving high precision GPS concurrent with SAR overpasses and build a catalogue of SAR images with the reflectors in place.
- Build a large enough catalogue of SAR images for a PSI study with the corner reflectors as valid PS points.
- Use PPP GPS derived Zenith Wet Delay (ZWD) parameters to correct long-wavelength effects in PSI differential interferograms.
- Compare GPS and PSI derived velocities before and after ZWD correction.
- Provide recommendations for further work.

1.8 Thesis Overview

This thesis is arranged into eight chapters which are now outlined.

Following this chapter, chapter 2 explains many of the fundamental principles and techniques relevant to the thesis. These include SAR, InSAR, PSI, GPS, PPP.

This leads into chapter 3 which is a literature search involving the relevant subjects of the mitigation of atmospheric delay in InSAR and PSI through the integration of other data sources. Also, corner reflector research is reviewed and the chapter finishes by detailing research gaps in the field.

Chapter 4 discusses the choice of Nottingham as the test site for the project. This includes the geography and geology, the availability of existing SAR data and GPS data and logistical concerns.

Chapter 5 then leads on from this describing the observations that were required from the field observation stage of the project and how these were obtained. This includes a section detailing the establishment of a corner reflector array in Nottinghamshire.

The chapter finishes by summarising what data was collected during the field campaign and how the various successes and failures of this resulted in a shift in emphasis from PSI corner reflector research to atmospheric correction of PSI studies.

Chapter 6 presents the methodology used to process the GPS and SAR and levelling datasets. Results are then presented, and a discussion of their respective quality is analysed. The datasets are also compared to other sources or information wherever possible. Finally, the PSI and GPS datasets are compared with each other which naturally leads into the next chapter.

Chapter 7 uses the GPS results processed in the previous chapter to compute ZWD estimates for the ENVISAT acquisition times at stations both inside and outside the AOI. ZWD values for every pixel in the AOI are then interpolated and the estimates are integrated into a PSI analysis. The results from this are then analysed against the existing PSI analysis, the precise levelling data and the height components of the GPS station velocities.

Chapter 8 provides reflective comment on the various aspects of the project. The aims and objectives are restated, summarising how each was achieved, to what level of success and what could be done in future to improve results. This leads to a list of recommendations for future work.

1.9 Summary

The opening chapter of the thesis has provided a backdrop to the relevance of monitoring geohazards, pointing out how current monitoring strategies suffer from limitations that might be overcome through integration with other data sources. Aims and objectives followed by research methodologies were then stated. An overview of the thesis was then provided briefly describing each chapter in turn.

Chapter 2

Background

The following chapter begins with a short background to early developments in Radio Detection And Ranging (RADAR) which then progresses onto SAR. Following a discussion of relevant principles, InSAR is introduced which naturally leads onto Differential InSAR (DInSAR) and a detailed description of PSI. The basics of GPS and the associated observables are then introduced which leads to a section discussing the PPP technique.

2.1 Radar Overview

Radar is a system that uses transmitted and received electromagnetic waves to determine the presence and range of fixed or moving objects. Generally speaking, microwaves or radio waves are emitted by a transmitter, reflected by a target and then detected by a receiver, which is often co-located with the transmitter. The time taken for the pulses to be transmitted, reflected and received is directly proportional to the distance to the object that reflected them (Ulaby et al., 1982). An optimised system has advantages over conventional optical imagery in that it can operated day and night, through clouds, fog and rain, as well as at long ranges (Madisetti and Williams, 1998).

2.1.1 Early Radar

The history of radar can be traced back to 1904 when Christian Hülsmeyer patented a rudimentary device called a Telemobiloscope which could detect distant metallic objects by means of transmitting and receiving electromagnetic waves using a one metre wavelength and a tunable *Pulse Repetition Frequency* (PRF) (Thumm, 2007). The two world wars were a driving force for radar and its many military applications. Post war efforts by the Massachusetts Institute of Technology (MIT) laboratory produced the first radars capable of operating at microwave wavelengths through perfection of the cavity magnetron (MIT, 1952). Radar imaging at this time was generally radial in nature with the distance to the object as one coordinate, and the angle to the object relative to the orientation of the radar antenna as the other. An improvement to this system and the removal of most of the large distortions inherent in it came with development of the Plan Position Indicator wherein the antenna was rotated about an axis to produce an image similar to a ground map (Ulaby et al., 1982).

2.1.2 Side Looking Airborne Radar (SLAR)

The basic SLAR design involved a non-rotating antenna which was fixed parallel to an aircraft fuselage with a fixed beam perpendicular to this being moved along by the aircraft's motion. Because non-rotating antenna size was less of an issue, a much higher spatial resolution was achievable. In radar imagery, the two dimensions are *range* or *cross-track* (perpendicular to the sensor) and *azimuth* or *along-track* (parallel to the flight direction). Good range resolution is achieved using a high bandwidth pulsed waveform (Madisetti and Williams, 1998). The SLAR azimuth resolution is dependent on the ground range and the beam width, with the beam width dependent only on the wavelength and the antenna length (Messina, 1996). The upshot of this is that with an optimised (as short as possible) wavelength, higher resolution can only be achieved by either flying lower or using a smaller beam width, which is achieved by using a larger antenna.

2.1.3 SAR

Despite the advances that SLAR brought, physical limitations were inevitably reached by those exploiting the data as they made increasing demands of the system (Lillesand et al., 2004). In 1951, Carl Wiley of the Goodyear Aircraft Company (later Lockheed Martin) in Arizona began working on a *Doppler Beam Sharpening* (DBS) technique. This provided a solution to the limitations of SLAR by synthesising a much larger antenna than was actually available from the motion of the platform (Lasswell, 2002).

The basic idea of the synthesis requires a processor to store the returned signals as amplitudes and phases for a given time period T whilst moving between two points at a velocity v. The processor then reconstructs the signal as if it were obtained by a single antenna of length $v \cdot T$ which for reasons mentioned above, means a higher resolution can be achieved, especially in the azimuth direction. In fact, the consequences of this relationship are such that the along-track resolution is theoretically independent of the range. The pixel dimension in the along-track direction for SAR can be as small as

$$r_a = \frac{l}{2} \tag{2.1}$$

where l is the along-track length of the real aperture. So, whereas SLAR requires a large antenna, SAR calls for a short antenna (Ulaby et al., 1982), but this too has physical limits (§2.2.4).

Entire branches of scientific research have evolved through the success of ESA's space based SAR program (Castel, 2000). ESA's most recent SAR platform, ENVISAT, was launched in 2002 and provides the SAR data used in this project. Henceforth, unless otherwise stated, SAR is taken to mean space based SAR.

2.2 SAR Operation

Some fundamental aspects of the SAR system are now discussed.

2.2.1 Coherent Imaging

SAR is a coherent active microwave imaging system (Skolnik, 1990). In a coherent system, two or more waves may be different in amplitude and initial phase but have the same frequency so that they vibrate in unison. The main advantage of a coherent system is that it preserves the phase of the received signal for later processing; this is in contrast to optical systems which use non-coherent and hence non-phase preserving natural light from the Sun. The SAR phase observation offers users remarkable opportunities to exploit the data in ways which are therefore not available with optical imagery.

2.2.2 SAR Geometry

Figure 2.1 below shows the basic geometry of a SAR system. Received echoes are converted to range and sorted into range bins; any two echoes from the same pulse that return at the same time will have an equivalent range and will therefore be superimposed. The side looking configuration eliminates this ambiguity as echoes from the far range will take longer to return than those from the near range (Woodhouse, 2006).

The flight path of the satellite is known as the *velocity vector*. The microwave beam illuminates an area on the ground known as the *swath*; the width of this swath depends on the *elevation beamwidth*, and this is proportional to the wavelength and the length of the antenna. The portion of the swath closest to the satellite's nadir is known as the *near range*, whilst the portion furthest from nadir is the *far range*. The angle between the transmitted microwave beam and the nadir of the satellite is the *incidence angle* (θ), which will increase as the beam moves from near to far range. The range from the SAR to a given target is the *slant range* (ρ) which is clearly a function of the incidence angle amongst other things such as topography. The antenna pattern is generally aimed perpendicular to the velocity vector which is known as the look direction, nevertheless, there is always a slight *squint angle* steering the antenna away from the zero-Doppler direction.

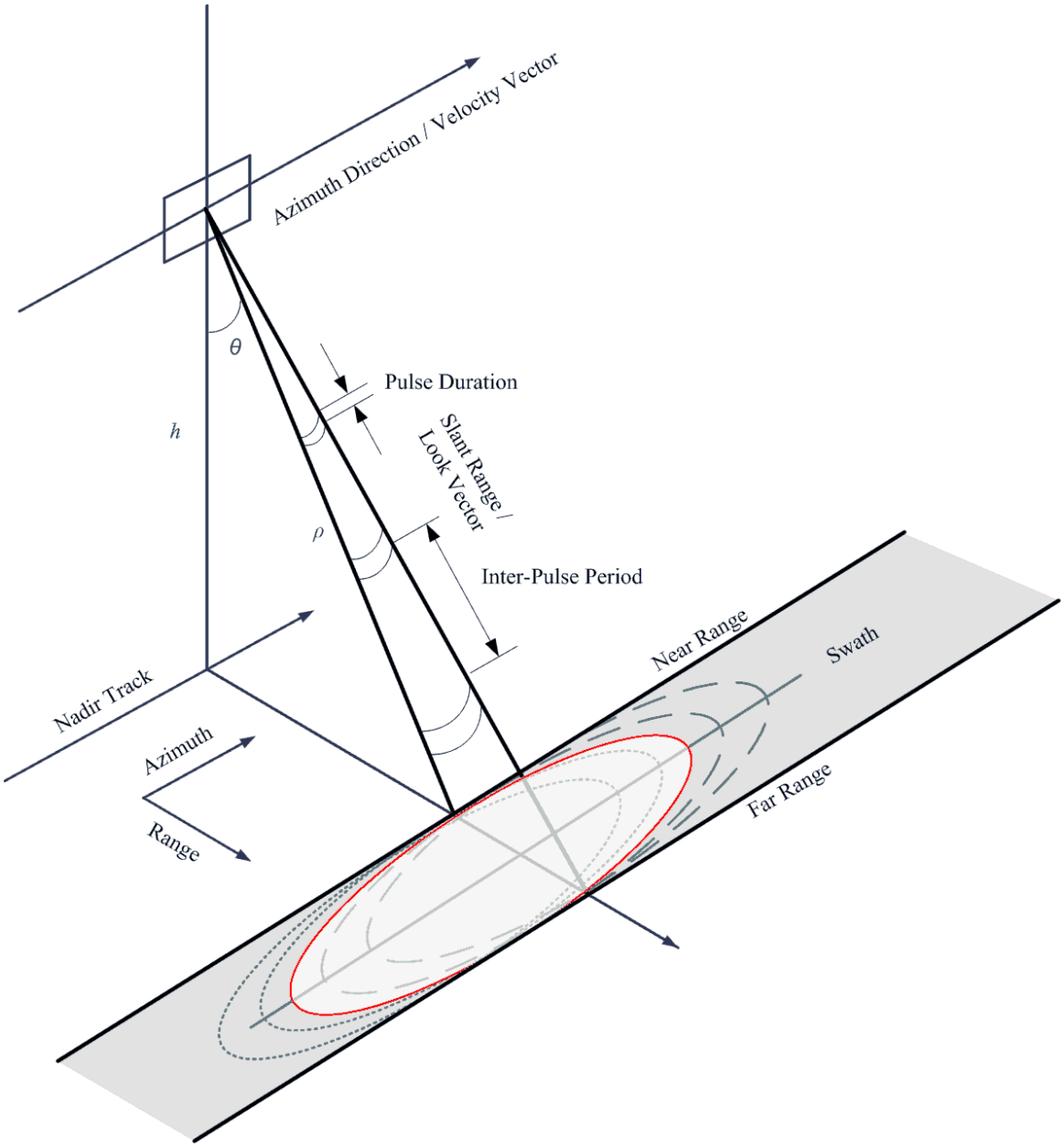

Figure 2.1: The geometry of a SAR system. Pulses are emitted at high frequency as the platform moves along the velocity vector (Skolnik, 1990). The footprint of each pulse is indicated by successive ellipses in the swath. The entire image is bound in range by the near and far range limits and in azimuth by the early and late azimuth times. The side looking nature of the instrument reduces range ambiguity in the echos.

2.2.3 Range Resolution

Spatial resolution (in either direction) is the shortest distance between two points such that they can be discerned as separate objects in the image. For range resolution, two targets must be separated by a distance (in slant range) greater than half the

physical length of the pulse (Curlander and McDonough, 1991).

Prior to transmission, a pulse is Frequency Modulated (FM); this is called *chirping*. The pulse is then transmitted and reflected from scatterers or targets on the Earth; the reflectance depends mainly on the roughness and dielectric properties of the imaged surface. The echoes from the pulse are then received by the sensor at different times which are directly proportional to their ranges (Skolnik, 1990). Chirping means that a matched filter can be applied to the received signal; here the different frequency components of the signal are individually delayed so that they all arrive at the same time. This is analogous to transmitting a short high powered pulse but requires less energy. This is important because the shorter the pulse, the closer two objects can be resolved before their echoes overlap. (Woodhouse, 2006)

2.2.4 Azimuth Resolution

For two objects to be resolved in the azimuth direction, they must be separated by a distance greater than the focused beamwidth on the ground (Levrini and Zink, 2002). Azimuth resolution is dependent on the synthetic aperture of the system. The Doppler effect due to the motion of the platform causes a frequency shift in the received signal. From the moment a target first enters the beam, multiple backscattered echoes from pulses are recorded which continues until the target leaves the beam. The beam footprint on the ground is a few kilometres in the azimuth direction for ENVISAT; this is the azimuth resolution of the *real* aperture. The synthesis involves resolving the multiple returns from a single target into a single response which effectively reduces the azimuth resolution from a few kilometres to a few metres (Hanssen, 2001).

The process of synthesising the returns is called *azimuth compression* and is analogous to the matched filtering (also known as *range compression*) that is used to improve the range resolution, albeit this time with a natural, Doppler chirp. For a more complete description of azimuth resolution, refer to Ulaby et al. (1982).

2.2.5 Geometric Distortion

A consequence of the side looking nature of SAR (and SLAR) is geometric distortion which manifests itself in several distinct ways. These are *foreshortening*, *layover* and *shadow*, which are all distortions created by topographic relief features. These distortions are all linked to fundamental operational parameters of the SAR such as the incidence angle, the PRF and the antenna design (Woodhouse, 2006).

Foreshortening occurs when features such as the sides of hills face the look direction. In figure 2.2, the base of the slope (A) and the summit (B) will return pulses which will arrive back at the sensor at similar times because of the near equivalent slant range, irrespective of the actual ground range between them.

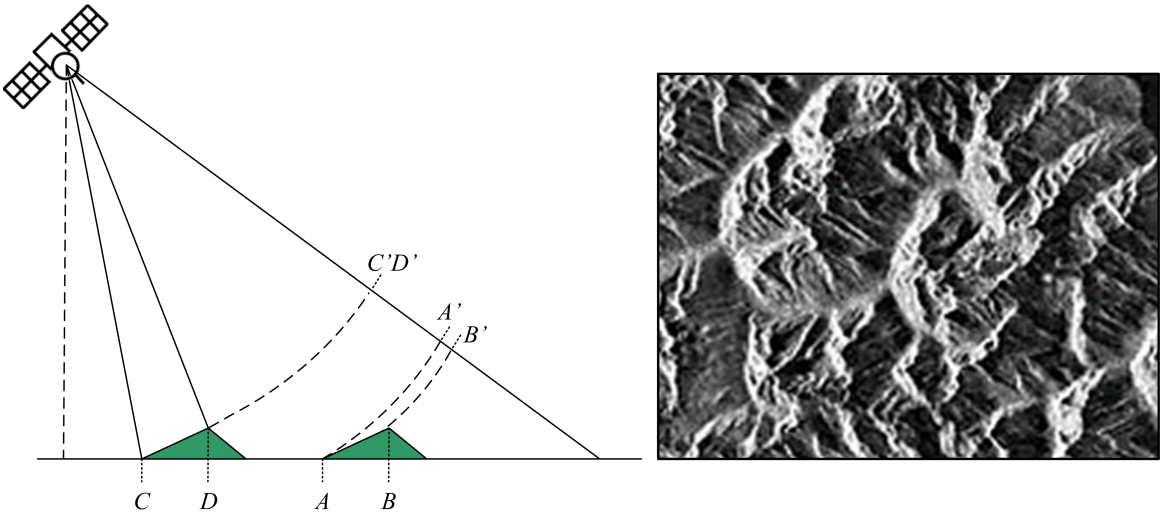

Figure 2.2: (Left) Two cases of foreshortening. Points A and B will appear much closer in the radar image than in reality because echoes from the points will arrive at the sensor at similar times because the path lengths are similar. Points C and D are indistinguishable in the radar image because their echoes arrive at the sensor at exactly the same time because the path lengths are the same. **(Right)** a radar image with foreshortening areas facing the look direction (left side of the image) of the SAR. Radar image © Natural Resources Canada.

Layover can be considered an even more extreme version of foreshortening where the slant range to the top of a feature (B in figure 2.3) is less than the slant range to the bottom (A). The return signal from B will be received before the return signal from A and therefore will be placed in the wrong range bin.

Shadow occurs when the radar beam is unable to illuminate one side of a feature. In the diagram, A is a relief feature where the slope facing away from the look direction

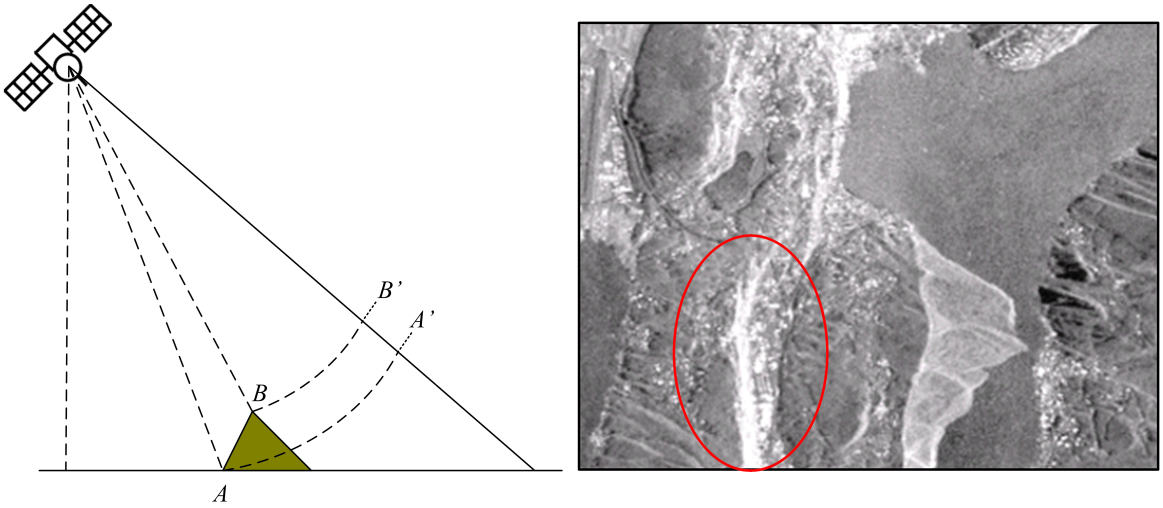

Figure 2.3: (Left) The echo from B will be received before the echo from A despite the fact that B is further in terms of ground range. Consequently B will be laid over A. **(Right)** A real example of layover in a radar image. Radar image © Natural Resources Canada.

is too steep to be illuminated by the SAR. This casts a shadow on the far range side of the feature and no information can be discerned about the area labelled B.

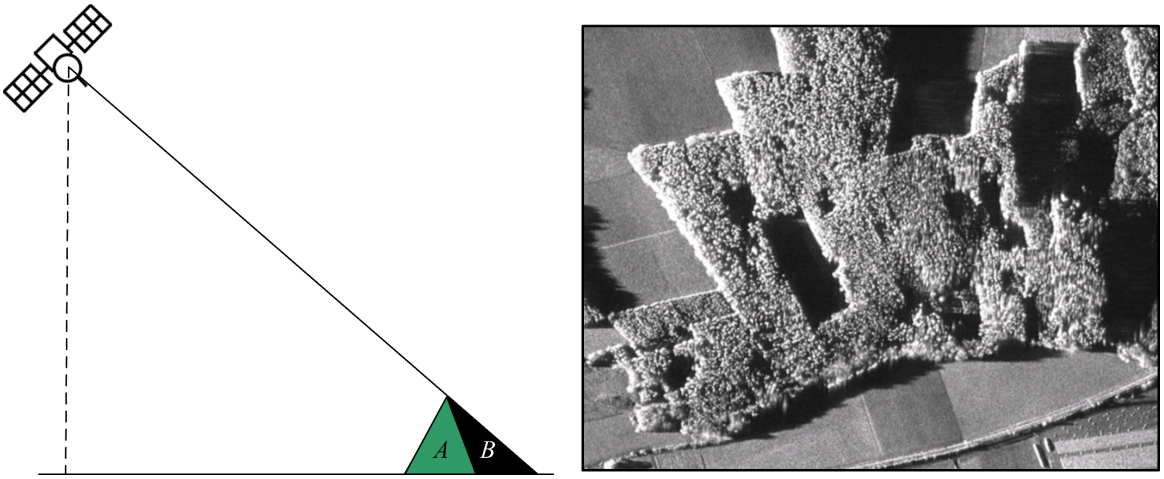

Figure 2.4: (Left) Area A casts a shadow and no information can be determined from B. This is exacerbated with low elevation angles. **(Right)** A low elevation angle airborne SAR image with heavy shadowing on the far range (right) side of the trees. Radar image © Natural Resources Canada.

2.2.6 Properties of SAR Images

SAR images used in interferometry are often focussed into slant range, *Single-Look Complex* (SLC) arrays of pixels. Each complex pixel with coordinates x and y has a

real *in-phase* component (q) and an imaginary *quadrature* (i) component. Figure 2.5 shows how these are related to the amplitude and phase values. Deriving the phase and amplitude values is equivalent to a cartesian to polar coordinate conversion, which for the quadrant shown is

$$\alpha = \sqrt{x^2 + y^2} \tag{2.2}$$

$$\varphi = tan^{-1}\left(\frac{y}{x}\right) \tag{2.3}$$

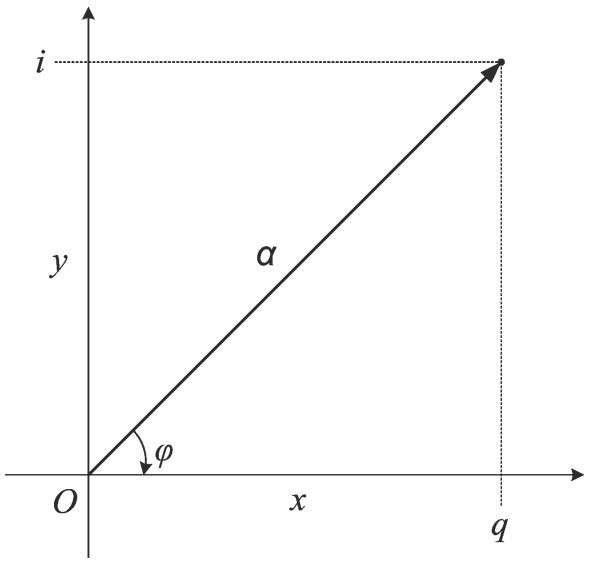

Figure 2.5: An SLC pixel with coordinates x and y represented using an Argand diagram. The real, in-phase value (q) and imaginary, quadrature value (i) are stored in complex form and relate to the phase (φ) and amplitude (α) via a cartesian to polar coordinate conversion.

The image resolution of an SLC image pixel (approximately 20m in range for ENVISAT) compared to the wavelength (5.6cm) is large and the area represented by a pixel can contain hundreds of individual targets, each of which has its own complex reflection coefficient. Any of these elements can cause delay or rotation in the phase, or put another way, each pixel's phase value is the sum of many unknown complex numbers and this resultant sum is therefore random and not a useful parameter on its own (Massonnet and Feigl, 1998).

If the elementary targets for a pixel remain stable between the acquisition of two images and the corresponding phases are differenced, the random element is

eliminated. This can isolate useful contributions to the phase or to the way the phase may have changed, and is the basis for *InSAR*.

2.3 InSAR

Interference is a consequence of the principle of the superposition of waves first noted by Thomas Young in 1801 in his two slit experiment (Born et al., 1959). Superimposed waves of electromagnetic energy interact in such a way that the resultant wave amplitude is the sum of the amplitudes of the individual waves (Towne, 1988). As the SAR frequency is fixed, the phase difference between the waves will remain constant and be preserved; systems with this property are said to be *coherent*. Figure 2.6 depicts superposition of two coherent waves (a) constructively interfering and (b) destructively interfering where a is the amplitude and λ is the wavelength.

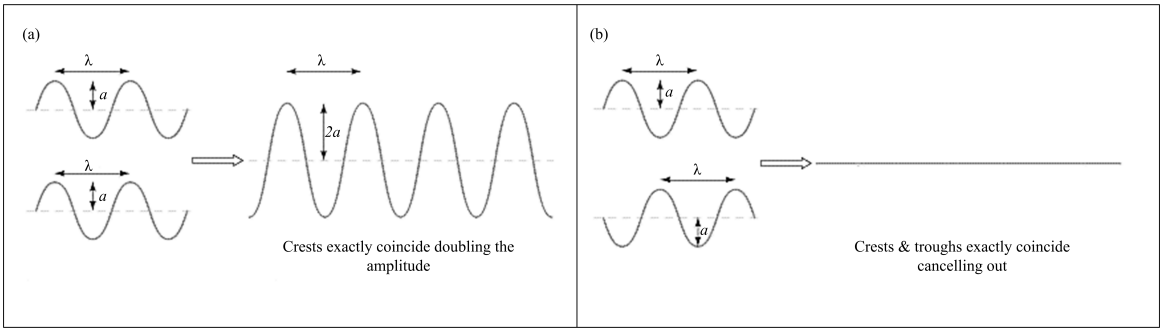

Figure 2.6: Combining coherent waves produces **(A)** constructive interference when they are in phase and **(B)** destructive interference when they are out of phase. These are the maxima and minima cases, all other cases in between are also possible.

As discussed in §2.2.2, it is not possible to distinguish between points that are horizontally displaced that have the same slant range, such as P and P_0 in figure 2.7. However, figure 2.7 also suggests that trigonometry could be used whereby two SAR acquisitions from slightly different positions are used to observe the angular difference between P_0 on an ellipsoid and P on the Earth. Because the angle from P to S_1 and S_2 is so small, the problem must be solved using distances but the required accuracy for the distances is in the mm range and the range information from the orbits is three orders of magnitude worse than this (Hanssen, 2001). The solution lies in using the phase. The SAR phase measurement for any given pixel contains a dominant

random element due to scattering, but the quantity is similar (to varying degrees) for both the acquisitions and therefore differencing removes most of it. The essence of InSAR can therefore be summed up as the use of differenced or *interferometric* phase information to derive high resolution spatial information.

2.3.1 Interferometric Phase

The interferometric phase results in interference fringes in accordance with the same principles evident in Young's experiment; fringes in an interferogram occur because the sources are coherent but come from different positions. The further apart the sensor positions are affects how many fringes appear in the image. SAR geometry implies that the fringe rate is dependent on the *perpendicular baseline* ($B_\perp$). Fringes will occur across the image because of the increasing distance from sensor to ground between near range and far range objects, this is exacerbated with Earth curvature. Knowledge of the interferometric phase requires knowledge of the positions of the sensors at the time of the acquisitions to reconstruct the SAR geometry.

Usually the two images are taken from the same orbit track, which means the minimum temporal baseline for a repeat-pass configuration is equal to the orbital cycle (thirty-five days for ERS-1, ERS-2 and ENVISAT). If targets in an area remain stable over time, then repeat-pass interferometry may be possible with a temporal baseline measured in years. In general though most targets decorrelate temporally; surface water or snow will come and go, sand will be blown, seasons and weather will affect vegetation and human intervention such as agriculture will cause significant change. In addition, geometric decorrelation occurs proportional to $B_\perp$, because as $B_\perp$ increases, so does the fringe rate, and high fringe rates are more sensitive to noise effects. A $B_\perp$ value which results in a fringe rate $> 2\pi$ per resolution cell is known as the *critical baseline* and images from baselines greater than this are not useful in standard InSAR. The critical baseline for ENVISAT is 1100m (Holzner et al., 2002).

2.3.2 Phase Contributions

The phase in a single SAR image can be thought of as the sum of three components:

- Phase due to range
- Phase due to scattering
- Phase due to noise

Although the scattering component is unpredictable, it is a deterministic quantity; if two acquisitions occurred under identical conditions, then the scattering components would be identical. In real terms, the scattering components are often similar in the images; under these circumstances, the image can be thought of as *coherent* (Hanssen, 2001). The level of correlation depends on temporal decorrelation, the baseline geometry and the determination of the Doppler-centroid frequency. The noise component is Gaussian and much of it can be filtered reasonably effectively. Thus, the phase difference ($\delta\rho$ in figure 2.7) is mainly dependent on the difference in range (Zebker et al., 1994). This takes no account of variations in phase delay due to atmospheric inhomogeneity as yet.

Due to the differencing of the scattering component, the InSAR phase is a much more useful parameter than SAR phase. The InSAR phase can also be thought of as the sum of a number of contributions:

- Phase due to the Earth curvature over the scene
- Phase due to topographic features such as hills and valleys.
- Phase due to motion that may have occurred between the two acquisition dates
- Phase due to the delaying effect of the atmosphere on electro-magnetic waves
- Phase due to noise

The InSAR phase model in equation form is:

$$\Phi = \phi_{Earth} + \phi_{topography} + \phi_{deformation} + \phi_{atmosphere} + \phi_{noise} \tag{2.4}$$

2.3.3 InSAR Geometry

The geometric configuration for repeat-pass InSAR can be seen in figure 2.7.

Two SAR acquisitions, S_1 and S_2, are separated in time and by a geometric baseline B and a perpendicular baseline ($B_\perp$). In an error free environment, the measured phases at S_1 and S_2 are mainly proportional to the round trip distances (ρ and $\rho+\delta\rho$) from the sensor to the surface and back again (Zebker et al., 1994).

2.3.4 The InSAR Model

A geometric description of the interferometric phase (ϕ) begins with:

$$\phi = \frac{4\pi}{\lambda}\delta\rho \tag{2.5}$$

where λ is the SAR wavelength and $\delta\rho$ represents the path difference between S_1 and S_2. $\delta\rho$ can be determined by

$$(\rho + \delta\rho)^2 = \rho^2 + B^2 - 2\rho B sin(\theta - \alpha) \tag{2.6}$$

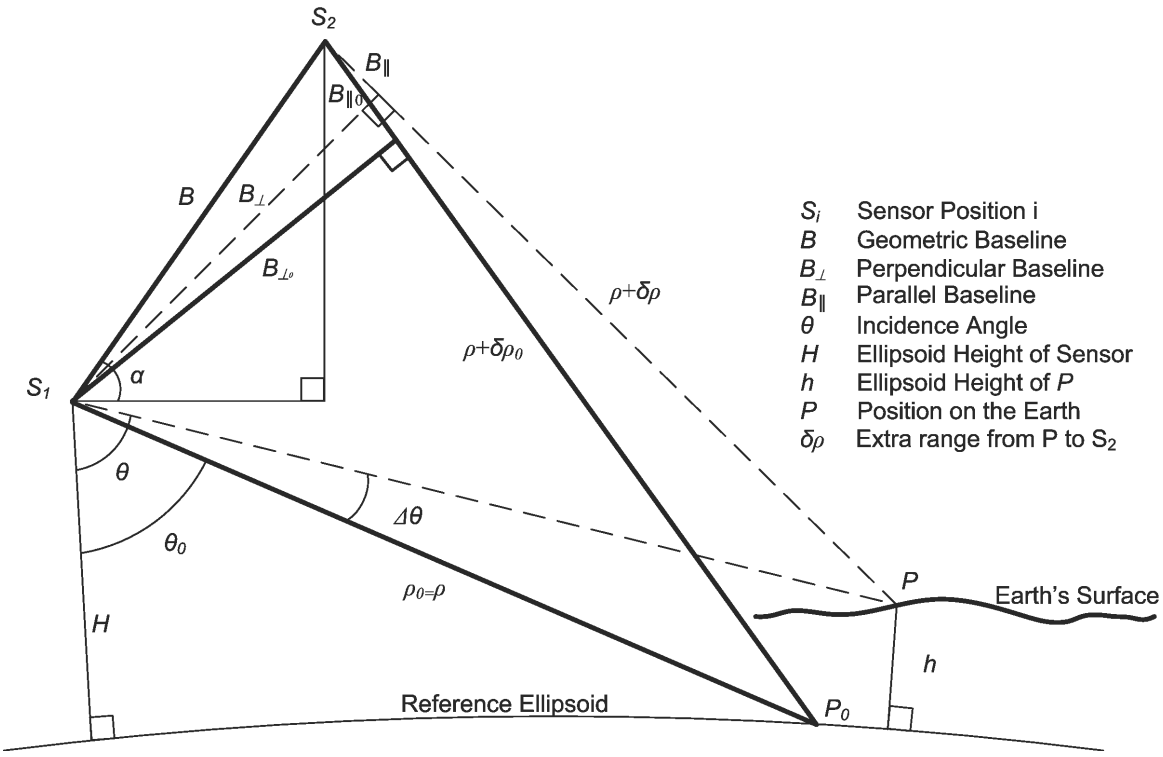

Figure 2.7: Earth and ellipsoidal InSAR Geometry. The interferometric phase is related to the extra path length ($\delta\rho$) between S_2 and P. The dashed triangle represents InSAR geometry with respect to the Earth's surface whilst the bold triangle refers to the ellipsoid. Terms labelled with a subscripted $_0$ refer to ellipsoidal geometry (Hanssen, 2001).

where θ is the look angle and α is the angle between the baseline and the horizontal at S_1. Rearranging gives

$$2\rho\delta\rho + \delta\rho^2 = B^2 - 2\rho B sin(\theta - \alpha) \tag{2.7}$$

dividing by 2ρ throughout and assuming $\frac{\delta\rho^2}{2\rho}$ to be negligible in space based SAR geometry gives

$$\delta\rho = \frac{B^2}{2\rho} - Bsin(\theta - \alpha) \tag{2.8}$$

Adopting the far-field approximation, the first term on the right hand side of equation 2.8 is considered negligible (Zebker and Goldstein, 1986) and the difference in path length becomes

$$\delta\rho = -Bsin(\theta - \alpha) \tag{2.9}$$

substituting into equation 2.5 gives

$$\phi = -\frac{4\pi}{\lambda} Bsin(\theta - \alpha) \tag{2.10}$$

In practice, determining $\delta\rho$ in equation 2.9 in this purely geometric sense is not possible due to the 2π phase ambiguity (§2.4.3) and orbit inaccuracies but the relationship between the changes in $\delta\rho$ and θ can be determined using a simple derivative and an initial value of θ with respect to the reference ellipsoid. For a full explanation see Hanssen (2001).

2.3.5 Interferogram Processing Flow

The following sections follow typical steps involved in interferogram creation. Initially, unfocused or *raw* data, must first be focussed into SLC data. The raw signal data for a point target is spread in azimuth and range and focusing collects the dispersed energy into a single pixel. The two main focusing techniques are the range-Doppler and wavenumber domain techniques (Bamler, 1992). Typically, interferograms are then formed as follows.

2.3.5.1 Coregistration

The repeat-pass configuration involves two SAR images taken from different times from orbits that are only known to a certain degree and are only repeatable to a certain degree which means the start times (the acquisition times of the first azimuth line) will vary and the corresponding look angles and therefore scattering features of the area will be different. This results in images different in area, size, rotation and backscatter. The aim of coregistration is to determine a transformation that will map the location of each slave pixel in the master image. For interferometry to succeed, the images must be co-registered to within 0.12 of a pixel which yields a negligible 4% decrease in coherence (Just and Bamler, 1994). A standard approach to this issue is to estimate coregistration offsets between a master (truth) image and a slave image. This process is usually sub-divided into two stages termed coarse and fine coregistration, interested readers should refer to Hanssen (2001).

2.3.5.2 Resampling and Interpolation

Interpolation is required to determine the values of the slave image pixels at their new locations. The choice of interpolation kernel is again a trade-off between accuracy and computational effort. An investigation into interpolation kernels was conducted by Hanssen and Bamler (1999) who concluded that the choosing the optimal interpolation kernel depends on the correlation properties of the signal. Li and Bethel (2008) also tested various resampling algorithms making the point that computing power had reached a point where many processor intensive algorithms were now viable options. They concluded that there is no single interpolation kernel that fits all SAR resampling situations.

2.3.5.3 Interferogram Generation

Post resampling, the slave and master images can be considered two identically sized complex arrays of values. Interferograms are formed by multiplying each complex pixel from the master with the complex conjugate of the corresponding pixel in the

slave image:

$$p(x, y) = s_1(x, y)s_2^*(x, y) \tag{2.11}$$

where $p(x, y)$ is the interferogram pixel value at (x, y), s_1 is the master SLC pixel value at (x, y) and $s_2^*(x, y)$ is the complex conjugate of the slave SLC pixel value at (x, y). This multiplies the amplitude values but differences the phase. The resulting array is itself complex consisting of the multiple of the two amplitudes and interferometric (InSAR) phase. Figure 2.8 is an interferogram centred on the city of Nottingham in the UK, covering an area of approximately 1500km^2. The image shows phase as a periodic colour cycle and the product of the amplitudes as brightness. Areas of low amplitude, especially in the left of the image, correspond to rural areas which have decorrelated much more than the more stable urban mass of Nottingham in the centre. Stable amplitude over time is therefore a reasonably good measure of fringe visibility.

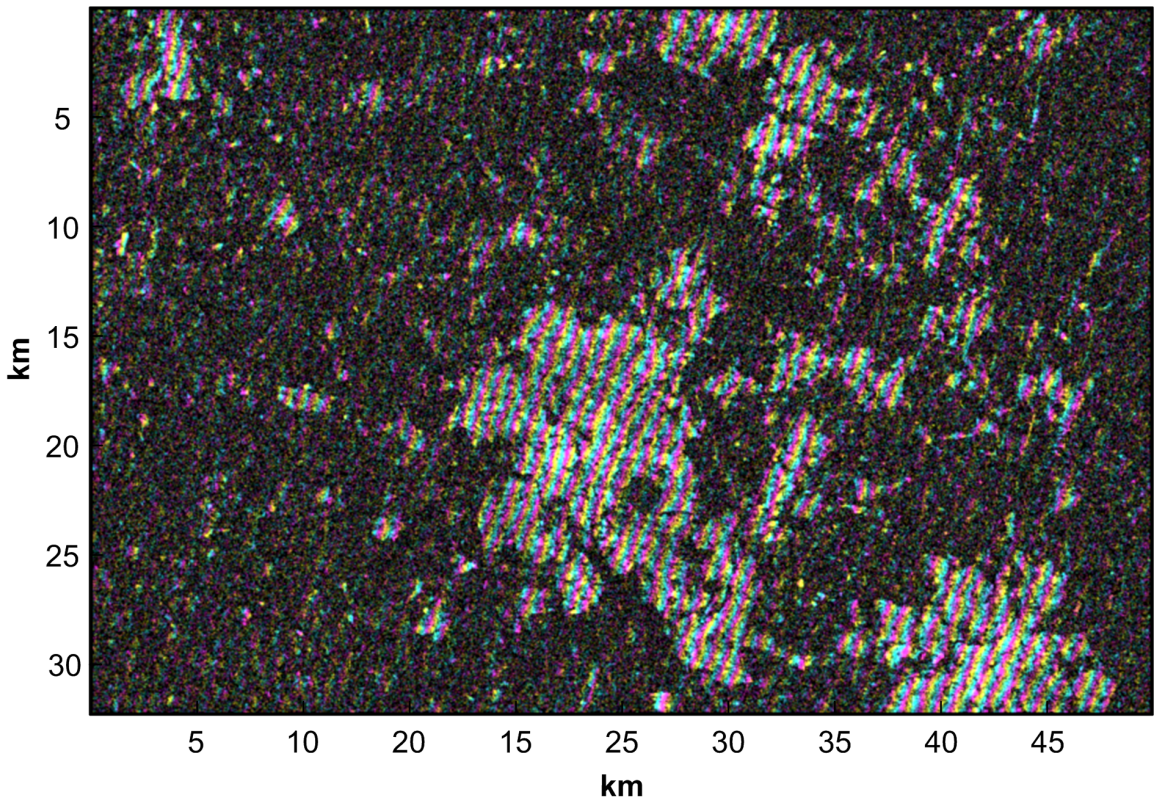

Figure 2.8: Interferogram of the Nottinghamshire area showing phase as a periodic colour cycle and magnitude as brightness. From ENVISAT data: 12 June 2004 and 17 July 2004, $B_\perp$ = 34m. One colour cycle represents 2π rad.

2.3.5.4 Coherence Estimation

Coherence in SAR interferometry is a useful by-product of the interferogram creation process and is a measure of the correlation of the phase information of two corresponding signals from a minimum of zero (no correlation) to a maximum of 1 (perfect correlation). Coherence is only useful when considered over a finite interval of time or space (Woodhouse, 2006). The coherence as a measure of phase correlation between two numbered SAR scenes ($\gamma_{S_1S_2}$) is defined as:

$$\gamma_{S_1S_2} = \left| \frac{\langle S_1 S_2 *^2 \rangle}{\sqrt{\langle |S_1|^2 \rangle \langle |S_2|^2 \rangle}} \right| \tag{2.12}$$

where S_1 and S_2 represent the complex pixel values for the two scenes and $\langle\ \rangle$ represents averaging over a neighbourhood. As urban structures tend to change less over time than vegetation, higher coherence is usually found in towns and cities in the mid latitudes, this can be seen in figure 2.9 which shows the corresponding coherence image (left) and amplitude image (right) for the interferogram shown in figure 2.8 of the Nottinghamshire area.

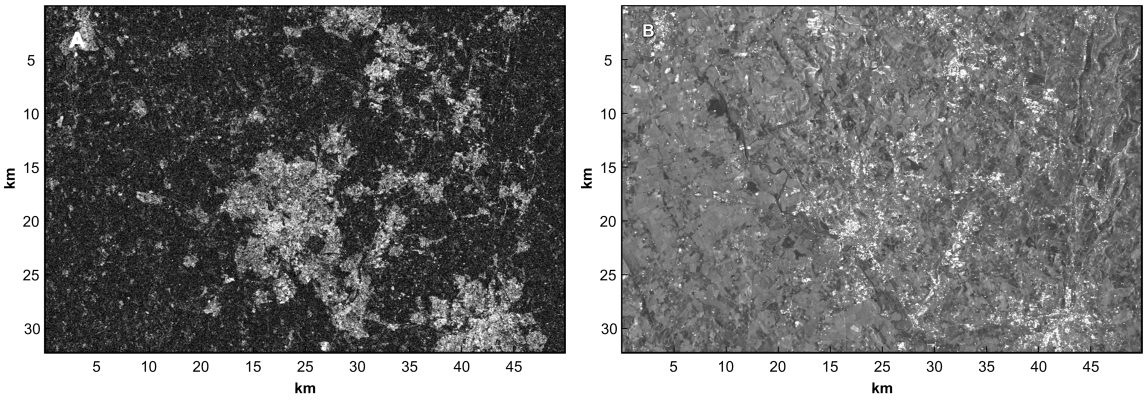

Figure 2.9: (A) Coherence Image of the Nottinghamshire area showing coherence as brightness. **(B)** The corresponding amplitude image taken from an average of thirty-four scenes. The two images show how lower (darker) coherence is correlated with rural areas. Coherence computed from ENVISAT data: 12 June 2004 and 17 July 2004, $B_\perp = 34$m.

2.3.5.5 Filtering

Generally speaking, filtering attenuates frequencies in an image outside of a given range and is commonly used to reduce Gaussian noise. Two-dimensional bandpass

filters specified in terms of normalized centre frequencies are common in SAR interferometry. Adaptive filtering methods are becoming more and more common in InSAR, these are filters with no fixed impulse response width. Instead the impulse response width is adapted based on certain data characteristics including signal-to-noise ratio, coherence, fringe rate and the terrain gradient (Goldstein and Werner, 1998). The general aim is apply a stronger filter to areas that may require it more whilst preserving areas that do not.

2.3.5.6 Multilooking

Here, complex interferogram data in a specified window is averaged to decrease noise. This is often prescribed in a multilook ratio such as 1:5 or 2:10, the latter corresponds to an averaging of twice in range and ten times in azimuth. These are common ratios for ENVISAT data as they result in almost square pixels. This of course increases the pixel size by the same amount in the respective direction, but improves phase statistics (Lee et al., 1994) because the standard deviation of the estimated phase is proportional to the number of pixels over which the average is computed. This in turn improves the reliability of phase unwrapping (Goldstein et al., 1988).

2.4 Differential Interferometry

DInSAR is an extension to InSAR involving either two SAR interferograms (three or four-pass) or one SAR interferogram and a simulated interferogram synthesized from a Digital Elevation Model (DEM) (two-pass). DInSAR differences the coherent combinations of interferograms for change detection studies and was demonstrated as a technique for mapping elevation changes in agricultural areas in California to centimetre level accuracy using SEASAT data by Gabriel et al. (1989). Since then it has been has been used in a wide array of subjects involving such as the study of the Landers earthquake (Massonnet et al., 1993). Here the author used a two-pass approach with ERS-1 data utilising a DEM to remove the topographic signal. Zebker et al. (1994) developed the three-pass method and was able to show good agreement between DInSAR results and standard survey measurements. Other applications

include glacial motion (Goldstein et al., 1993), vulcanology (Massonnet et al., 1995), landslides (Fruneau et al., 1996) and subsidence (Massonnet and Feigl, 1998).

2.4.1 Two-pass DInSAR

High resolution DEMs have become widely available in recent years (Farr et al., 2007). Synthesising the topographic interferogram from an existing DEM has several advantages over the three-pass method:

- Atmospheric phase error is eliminated for the topographic interferogram.
- Phase noise due to differencing is reduced.
- There is no chance of any unknown deformation events contaminating the topographic interferogram.
- Potential decorrelation issues will be reduced.
- There is only one interferogram requiring unwrapping.

However, in order to create the simulated interferogram, a number of issues must be overcome. The DEM will probably be georeferenced with respect to an orthogonal mapping projection and with a different spatial resolution to the SAR data. Below is a typical processing chain to create the topographic interferogram using DEM data:

- Using the SAR orbits, transform the DEM data to Range-Doppler Coordinates (RDC).
- Over or undersample DEM pixels to roughly the same resolution as the master scene, interpolating any gaps as necessary.
- Simulate the amplitude for the DEM as though the DEM were viewed from the geometry of the master SLC.
- Estimate a linear offset between the DEM and the SAR master scene.
- Estimate a polynomial (typically third order) between the DEM and the SAR master scene.

- Coregister and resample the DEM using a method described in §2.3.5.1 and 2.3.5.2.

2.4.2 DInSAR Errors and Limitations

DInSAR is in effect a double-differencing technique; SAR phase is differenced to create the interferogram and two interferograms are differenced to create the differential interferogram. Differencing techniques in general suffer because there are multiple sources of noise to contend with. Two-pass DInSAR has the advantage over three pass in that there are less sources of phase noise, but it introduces a DEM error.

Data availability is also an issue. SAR platforms are a sparse data source and conflicts between users are common. DInSAR requires that the dates spanning a deformation event such as an earthquake are ideally as uncontaminated as possible from other influences such as temporal decorrelation and unrelated motion; this may not be possible.

2.4.3 Phase Unwrapping

§2.3 postulated that spatial information may be determined from the angular differences between two SAR acquisitions. This is equivalent to measuring cumulative angular phase differences between neighbouring resolution cells in a SAR interferogram (Hanssen, 2001). The interferometric phase is only known modulo 2π, therefore an integer number of 2π cycles has to be added to this to determine the absolute phase difference. The relationship between modulo phase and absolute phase is illustrated in figure 2.10. The top diagram represents the wrapped modulo phase measurement in an interferogram with the 'sawtooth' jumps of 2π. The bottom diagram represents the smoother reconstructed phase post unwrapping. The phase here has no noise, no discontinuities and it is a one dimensional example making unwrapping a trivial computational task.

In reality, a number of issues make phase unwrapping the single most difficult computational task in InSAR. Most of these issues span from a much deeper, general issue in signal processing; real, continuous signals must be sampled and converted to

digital signals for computing purposes and a sufficient sampling rate is required if the original signal is to be represented satisfactorily (Ghiglia and Pritt, 1998). At some later stage, the ideal is to reconstruct the original continuous form of the data from the discrete samples. If the data is complete, without error and sampled at a high enough rate, then reconstruction is reduced to a computational exercise. In many real scenarios however, the signal cannot be perfectly reconstructed and unwrapping some interferograms to an acceptable degree may be impossible.

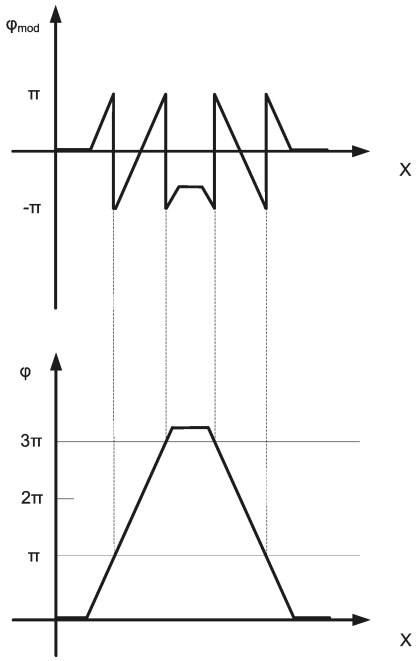

Figure 2.10: The measurable, wrapped modulo 2π interferometric phase between two points in an interferogram **(top)** and the reconstructed unambiguous phase post unwrapping **(bottom)**.

Making use of phase measurements in InSAR and DInSAR routinely involves unwrapping at some point. Incorrect phase unwrapping is a source of error and according to Zebker et al. (1994) the performance of a phase unwrapping algorithm depends on two factors: the SNR of the interferogram and the interferometric fringe spacing. The two main approaches to phase unwrapping are residue-based algorithms as proposed by Goldstein et al. (1988) and least squares algorithms proposed by Zebker and Lu (1998). In contrast to the example shown in figure 2.10, phase is often unwrapped in two orthogonal directions. Gradients between adjacent pixels are computed and integrated over a given path and therefore the resulting interfero-

gram describes phase values relative to the starting point (Ghiglia and Pritt, 1998). Atmospheric phase, poor coherence, discontinuities, temporal decorrelation and large perpendicular baselines all exacerbate the issue. A comprehensive examination of phase unwrapping is provided by Ghiglia and Pritt (1998).

2.4.4 Stacking

Stacking is a means of combining multiple interferograms of the same area. One of the issues with standard interferometry is the large number of parameters which must be estimated from a relatively small number of observations. Stacking involves averaging the stack to improve the Signal to Noise Ratio (SNR) (Sandwell and Price, 1998, Sandwell and Sichoix, 2000). Assuming that the error statistics for all the interferograms in the stack are the same, the quality of the SNR improves because unwrapped phases from interferograms add up linearly (e.g., interferograms with one and two year temporal baselines (B_T) result in an unwrapped phase effectively covering three year interval) whilst error terms only increase with the square root of the number of pairs. This means that the standard deviation of the phase rate from any single interferogram is proportional to the inverse of the cumulative time interval (Wegmüller et al., 2000):

$$\sigma(\dot{\phi}_i) = \frac{\sigma(\phi)}{\Delta T_i} \tag{2.13}$$

where $\sigma(\dot{\phi}_i)$ is the standard deviation of the phase rate of interferogram i, and ΔT is the cumulative time interval. As ΔT increases, $\sigma(\dot{\phi}_i)$ decreases. The estimate of the average $\dot{\phi}_i$ from any point in the interferogram stack is:

$$\dot{\phi}_i = \sum w_i \phi_i \tag{2.14}$$

where w_i represents the weights derived from the square of the time intervals of the individual interferograms. Stacking does not need to have a common master, so arbitrary pairs with optimum B_T and $B_\perp$ can be selected. Stacking can be used for designing filters to suppress noise (Wegmüller et al., 2000), to improve the ratio between the subsidence signal and atmospheric error (ibid) or as an priori estimate

of motion for PSI.

2.5 Atmospheric Effects in InSAR

InSAR images tend to exhibit irregular artefacts which according to Zebker et al. (1997), Delacourt et al. (1998), Hanssen (1998) and Massonnet and Feigl (1998) are due to spatial and temporal atmospheric inhomogeneity across the SAR scene. In particular, Zebker et al. (1997) states that these artefacts result mainly from signal delay as radar waves pass through areas of atmospheric water vapour; these delays are usually around 2-3m in Northern temperate Europe (Hanssen, 1998). Tropospheric variations in pressure and temperature also contribute to the distortions, but these effects are much smaller in magnitude.

The corresponding phases ϕ_1 and ϕ_2 from two SAR acquisitions for a given pixel are:

$$\phi_1 = \frac{4\pi}{\lambda} L_1, \quad \phi_2 = \frac{4\pi}{\lambda} L_2 \tag{2.15}$$

where λ is the radar wavelength and L_1 and L_2 are the slant ranges. The propagation delay of radar signals corresponding to each acquisition can be expressed as:

$$\phi_1 = \frac{4\pi}{\lambda}(L_1 + \Delta L_1), \quad \phi_2 = \frac{4\pi}{\lambda}(L_2 + \Delta L_2) \tag{2.16}$$

where ΔL_1 and ΔL_2 are the respective propagation delays. The interferometric phase (ϕ) then becomes:

$$\phi = \frac{4\pi}{\lambda}(L_1 - L_2) + \frac{4\pi}{\lambda}(\Delta L_1 - \Delta L_2) \tag{2.17}$$

The first term on the right hand side of equation 2.17 is interferometric phase induced by topography and deformation whereas the second term is induced by atmospheric phase errors. The challenge is separating the two terms accurately as one can be interpreted as the other.

For repeat-pass interferometry, localised inhomogeneity at the time of the first acquisition would result in a slower propagation velocity with respect to the reference

phase resulting in a positive phase change in the interferogram. A similar effect at the time of the second acquisition would result in a negative phase change in the interferogram. The sign of the phase change is therefore independent of perpendicular baseline considerations (ibid). Also, because of the relative nature of interferometric observations, only variations in the signal delay can be measured, and not absolute atmospheric delay. Note that in areas of significant topography, changes in atmospheric conditions due to height cannot be ignored (Delacourt et al., 1998).

Understanding the varying scales at which water vapour can manifest is a crucial factor when designing an effective mitigation strategy. Water vapour fields that are most likely to affect interferograms occur at the microscale (1km horizontally and vertically) and the mesoscale (a few to several hundred kilometres horizontally and from the surface of the Earth to 10km vertically). A full account of the atmospheric effects on InSAR is given by Hanssen (1998).

2.6 Persistent Scatterer Interferometry

PSI exploits the spatial and temporal characteristics of the differential phases of PS points in a stack of SAR images to map deformation rates over time. PS points are temporally phase stable points that by definition are the dominant scatterer within a resolution cell. PS points do not exhibit geometric decorrelation in the way that distributed targets do; this permits a more complete use of available data including interferometric pairs with baselines longer than the critical baseline. PSI requires a much larger number of scenes than standard InSAR in order to select statistically reliable PS points and also to enable more reliable estimates of atmospheric phase.

This extension to the conventional InSAR model was first proposed by Ferretti et al. (1999) which was later named and patented as the *Permanent Scatterer Technique* (Ferretti et al., 2001). The authors selected pixels within the stack with low amplitude dispersion over time; these points are thought to relate to optimally aligned features that give consistently stable amplitude reflectance such as hard urban features. The process of isolating the deformation phase from other phase contributions then follows.

Since Ferretti's original contribution, numerous variations on this theme have been

postulated and tested such as the Small Baseline Subset (SBAS) (Berardino et al., 2002), the Coherent Pixel Technique (Mora et al., 2003), the Interferometric Point Target Analysis (IPTA) (Werner et al., 2003), the Stable Point Network (Duro et al., 2004), the Stanford Method for Persistent Scatterers (Hooper et al., 2004), the Spatio-Temporal Unwrapping Network (STUN) (Kampes, 2006), and the 3-Pass Persistent Scatterer Processor (3PaPS) (Warren, 2007). The applications of PSI techniques are many and varied and such as monitoring subsidence due to mineral or gas extraction (Kemeling et al., 2004, Cuenca and Hanssen, 2008, Ketelaar, 2009), urban subsidence monitoring (Ferretti et al., 2000a, Worawattanamateekul et al., 2003) and volcanic and crustal deformation monitoring (Hooper and Pedersen, 2008, Paganelli and Hooper, 2008, Perski et al., 2008).

The main stages of PSI analysis are now discussed. This follows a typical processing chain involving a stack of coregistered SLC ENVISAT images with a resampled and coregistered DEM.

2.6.1 Identification of Candidate PS Points

Generally, a deformation model cannot be applied to every pixel in a given area because of temporal decorrelation. Therefore, individual pixels must be examined as to the quality of the differential phase over time before phase contributions can be separated. Reliably determining this at the outset is not directly achievable as error terms such as atmospheric phase dominate the process (Mora et al., 2003). Therefore, a number of strategies exist to first determine potential or *candidate* PS points as a starting point. This list can later be revised as knowledge of the contributing phase terms increases.

Several methods exist for finding candidate PS points. Original methods involved an examination of a pixel's amplitude variation over time. Ferretti et al. (2001) computed the ratio of the standard deviation of the amplitude over the mean for each pixel. This was then thresholded at a given level. Pixels dominated by a point scatterer will show less random speckle behaviour over time and they ought to show similar intensity when viewed from different angles (Werner et al., 2003).

Another method that uses amplitude examines whether pixels display low spectral

diversity (Werner et al., 2003); this is based on the theory that dominating point targets in a resolution cell have a spectral diversity different to that of distributed targets, even when viewed from different directions. Rabus et al. (2004) found that combining the backscatter and spectral diversity methods produced more robust results (for stacks with less than 40 scenes) than Ferretti's original method.

Coherence can also be used as a measure of point quality as coherent pixels are more likely to be PS points (Mora et al., 2003). This however involves a trade-off with a permanent decrease in image resolution, but unlike Ferretti et al. (2001), the technique is not dependent upon such large stacks of (30 or more) images to obtain statistically reliable points. Differential interferograms must first be formed to first estimate the coherence.

Hooper (2006) used differential interferograms to determine pixels with low noise. The noise term was separated from the interferometric phase through a patch averaging technique. The averaging technique requires that the location of other PS points are already known which is achieved through an iterative amplitude dispersion and coherence computation.

2.6.2 Differential Phase

Using either an existing DEM or a DEM generated from a subset of the available images (§2.4), the differential phase is revealed by subtracting the DEM from the interferometric pairs. The quality of the differential interferograms will vary depending on the quality of DInSAR model parameters such as the orbits and the size of the baselines (Bamler and Hartl, 1998). The quality of the DEM will have an effect on the differential interferograms, although the PS results do not depend on it (Kampes, 2006) since height corrections are estimated in the PS process.

The differential phase consists of:

$$\Phi = \phi_{atm} + \phi_{orb} + \phi_{defm} + \phi_{DEM} + \phi_n \tag{2.18}$$

where Φ is the differential phase and ϕ_{atm}, ϕ_{orb}, ϕ_{defm}, ϕ_{DEM}, ϕ_n are the respective phase terms due to atmosphere, orbit errors, deformation, DEM errors and noise.

Briefly examining these in turn:

- The atmospheric and orbit errors are both spatially correlated and random over time. This makes them difficult to separate and the so called Atmospheric Phase Screens (APSs) determined per interferogram may contain some degree of orbital error within them depending on the processing method used.

- The deformation phase is correlated temporally and spatially. Some methods divide this term into non-linear and linear deformation (Ferretti et al., 2000b, Mora et al., 2003, Werner et al., 2003), while others assume all deformation to be linear (Ferretti et al., 2001).

- The DEM error is a temporal constant through the stack and can be modelled as a function of the individual baselines (Ferretti et al., 2001).

- The noise term is random temporally and spatially and is mitigated by the fact the PS points are often selected based on the fact that they have low noise characteristics (Hooper, 2006). Filtering methods can also be employed to reduce noise (Lyons and Sandwell, 2003).

2.6.3 Estimating Linear Deformation

Strategies to determine deformation estimates from a stack of coregistered wrapped differential interferograms vary widely in detail although they usually have common processes. Offered here is a general explanation of the main steps with no focus on any particular method. Non-linear deformation is referred to from time to time although the focus is linear deformation which is more relevant to this work.

2.6.3.1 Applying the Phase Model

The original method (Ferretti et al., 2001) first involved iteratively estimating and removing linear phase ramps from the interferograms; these were assumed to be related to atmospheric and orbit error (Kampes, 2006). This limited the process to areas of 5 x 5km. Improvements on this were made (Ferretti et al., 2000b, Colesanti et al., 2003a) whereby the atmospheric phase was not assumed to be planar and

determined later in the process (see below). Assuming the latter strategy above, an algorithm (see Kampes (2006) for a description of this) is used to fit a model to the wrapped differential phases which determines the DEM error and the linear deformation velocities; this process is now described in more detail.

The PS points are first connected through a network process such as Delaunay triangulation (Delaunay, 1934). If the distance between two neighbouring points does not exceed some pre-determined limit (this ranges from between 1km (Hanssen, 1998, Mora et al., 2003) to 2-3km (Colesanti et al., 2003a, Kampes, 2006)) then an assumption is made that the atmospheric variability between them is negligible. The short distances will also hopefully mean that phase differences are smaller than π since the observed data is wrapped.

From this optimised network, phase differences between neighbouring points are determined through the stack and a two-dimensional phase regression computation takes place. This involves an examination of the linear correlation between the phase differences and the respective perpendicular baselines. Such correlations are directly related to errors in height, although at this stage only *differences* in the height errors can be determined because only phase differences are known. The phase differences between the points are also examined to see how they vary over time. Smoothly varying phases are related to the deformation estimate. Again, at this stage, only differences in the deformation estimates are determined. The two aspects of the phase regression can be computed using a periodogram (Ferretti et al., 2001, Adam et al., 2003).

Figure 2.11 shows four plots of the two-dimensional phase regression process. The left hand pair show the baseline dependence of the phase difference (top) and the time dependence of the phase difference between two neighbouring points in the triangulation network; a relatively low height correction is indicated. The right hand pair show a much higher height correction. Also revealed in the process is the standard deviation of the phase which can be used as a quality measure for rejecting erroneous PS candidates.

Phase that is not be attributable to either deformation phase or height correction phase is termed residual phase. This is usually assumed to contain atmospheric error,

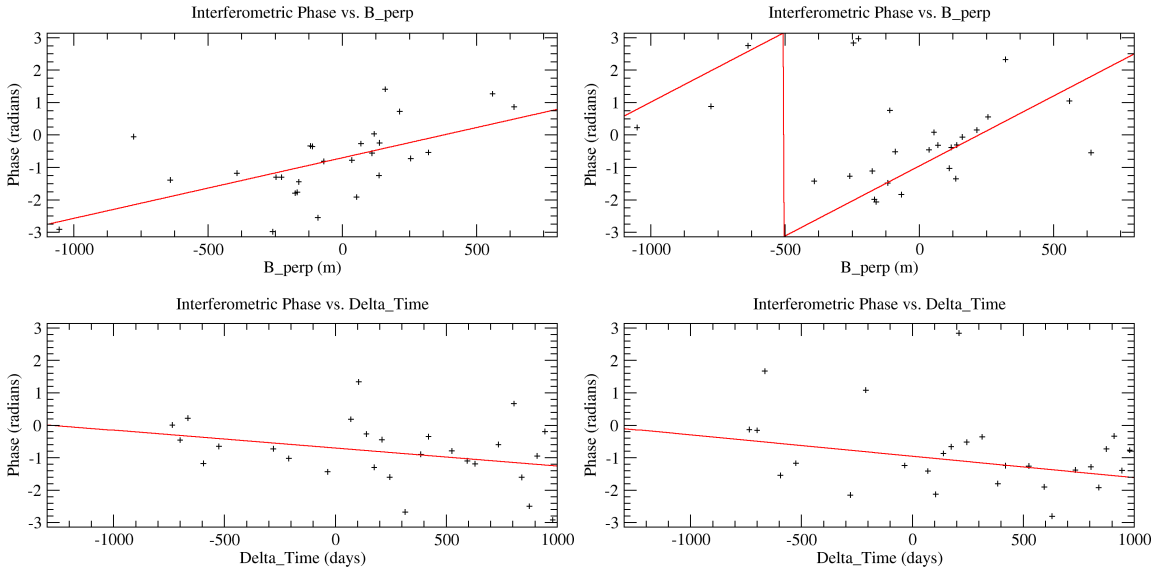

Figure 2.11: Two examples (**left** and **right**) of the PSI phase regression process are shown, each with two plots (**top** and **bottom**). The baseline dependence of the phase differences between a reference pixel and another pixel for a stack of interferograms is shown in each of the **top** images; this is related to the relative height correction between the points. The time dependence of the phase difference between the same points is shown in the **bottom** images; this is related to the relative deformation estimate. The **left** hand case indicates a small height correction whilst in the **right** hand pair it is much larger. Both the deformation estimates indicate similar (relative) subsidence.

non-linear deformation and noise; this is discussed below.

2.6.3.2 Phase Unwrapping

Since the observed phase data is only known modulo 2π, spatial phase unwrapping reveals the PS point phases from the phase differences. This can only succeed if the residual phase difference terms are $< \pi$ (Kampes, 2006) although lower estimates have been suggested as being more realistic (Colesanti et al., 2003b).

The components of the residual phase differences should be small in a well conditioned PSI analysis. For instance, the atmospheric delay phase difference between points <1km is commonly below 0.3 rad (Ferretti et al., 2000b); non-linear phase is assumed to be low if the linear model provides a good approximation and the phase noise should be low because PS points with low amplitude dispersion usually relate to a low noise standard deviation (Kampes, 2006).

The unwrapping is initiated at a sufficiently high quality reference PS point; this

point must also necessarily be connected to other points to allow unwrapping a sufficient chance to succeed. The resulting phases at each PS point are of course relative values as they are derived with respect to the initial phase value at the reference point.

2.6.3.3 Atmospheric Phase

For the linear method, atmospheric phase is now estimated from the unwrapped residual phase; the non-linear method here deviates by estimating non-linear deformation first (Ferretti et al., 2000b). The atmospheric phase is spatially correlated over short distances and assumed to be temporally random (Mora et al., 2003, Kampes, 2006), and therefore with a sufficiently large enough stack of interferograms, it can be estimated by low pass filtering in the spatial domain and high pass filtering in the temporal domain. Most methods interpolate the atmospheric phase for every pixel (Ferretti et al., 2001); this can happen concurrently with the filtering (Colesanti et al., 2003a) through Kriging (Matheron, 1963). Other methods do not interpolate and instead rely on a sufficiently dense set of PS points that permits spatial filtering of the points alone (Werner et al., 2003).

The atmospheric phase can then be subtracted from the differential interferograms. Methods deviate here, for instance Ferretti et al. (2001) conducts a fresh search for PS points using phase stability as the criteria and the parameter estimation is repeated. Werner et al. (2003) only uses the amplitude derived candidate points for the whole (iterative) process; points may be rejected and later re-introduced, but the process does not permit a search for new PS points. Methods for deriving non-linear deformation often do not iterate.

The PSI process is optimised with a uniformly distributed interferogram stack (both temporally through the stack and spatially distributed PS points in the images), an area of study small enough not to invalidate assumptions about the atmosphere and low enough rates of deformation to avoid aliasing (Ferretti et al., 2001).

2.7 GPS

GPS is one of the Global Navigation Satellite Systems (GNSS) in use today; it was developed by the United States Department of Defence for military purposes and is now operated by the United States Air Force. It is capable of providing users operating suitably equipped receivers on or close to the Earth with timing, position and velocity.

This section aims to give an overview of the system highlighting topics particularly relevant to the research presented in this thesis. More thorough descriptions of GPS can be found in Hofmann-Wellenhof et al. (2001); Leick (1994) and Parkinson and Spilker (1996).

2.7.1 History and Concept

Space based global trilateration (a means of determining position using distances) became a theoretical possibility when scientists realised they could measure Doppler shift from Sputnik, launched by the Soviet Union in 1957 (Hofmann-Wellenhof et al., 2001). This led on to the Navy Navigation Satellite System (NNSS or TRANSIT) which used the Doppler signal as a means of determining the time of closest approach of a TRANSIT satellite, which when combined with other similar measurements and a knowledge of satellite ephemerides could provide users with position.

GPS was conceived in order to replace TRANSIT after prototype testing in 1972 using balloon carried transmitters. The GPS concept was approved and ratified in 1973 and the research and developmental phase began in earnest. The first block-I satellite was launched in 1978 and the system was declared operational in 1993. By 1994 a constellation of twenty-four satellites were in orbit.

Today, over thirty satellites from different generations exist in six orbital planes and provide huge benefit to a vast array of diverse fields and disciplines such as navigation, banking and meteorology. The system is designed to provide instantaneous position and velocity in any weather conditions, twenty-four hours a day, anywhere on the Earth. Ranges from satellite to receiver are computed from the transit time of the signals, these are known as *pseudo-ranges* as they are not corrected for any errors

that may exist in the clocks. The satellite positions are measured frequently and vary smoothly, therefore with enough pseudo-ranges, a position in a suitable coordinate system is resolvable using trilateration.

2.7.2 System Overview

GPS consists of three distinct segments:

- The space segment
- The control segment
- The user segment

These are now discussed in turn.

2.7.2.1 The Space Segment

The operational satellite constellation consists of twenty-four spacecraft plus spares in six near circular orbital planes inclined at 55° from the equator at around 20,200km above the Earth. The planes are arranged 60° apart providing coverage from at least four satellites from any position on or near Earth. Although generations of GPS satellite vary, the payload generally consists of four atomic clocks and transceivers to receive input data from the control segment and transmit navigation signals. Each satellite transmits the same two L-band carrier-waves known as L1 (1575.42Mhz) and L2 (1227.60Mhz); receivers can distinguish between the satellites because the system employs spread-spectrum Code Division Multiple Access (CDMA). Here, each satellite has its own *Pseudo-Random Noise* (PRN) sequence encoded into its signal; these are know as Gold Codes (Gold and Dixon, 1998).

2.7.2.2 The Control Segment

The satellite orbits are tracked from Earth based ground control stations in Hawaii, Kwajalein, Ascension Island, Diego Garcia and Cape Canaveral with a Master Control Station (MCS) in Colorado Springs. Four of these stations also have ground antennas.

The purpose of this segment is to monitor the health of the constellation. Monitoring stations relay information to the MCS which then computes the orbital parameters and clock corrections. This information is then passed to the ground antennas and uploaded to the satellites. The satellites then transmit this *ephemeris* data in their navigation message which is modulated onto the L1 carrier-wave.

2.7.2.3 The User Segment

Since its initial conception for military purposes, GPS now has an ever increasing plethora of applications and uses throughout the scientific, commercial and leisure domains. GPS receivers are simplex, allowing an unlimited number of users and the technology has become much cheaper in recent years due to mass production. Receiver antenna pairs can be roughly classified into two main groups: 1. Low cost, which have an integrated antenna and are now common place in the mobile phone industry and 2. Geodetic, which have a separate antenna and make the best use of the observables available.

2.7.3 Observables and Signal Structure

The GPS signal is a complex combination of modulations (Spilker Jr, 1978) as illustrated in figure 2.12. Atomic clock timing produces the fundamental frequency (f_0) of 10.23MHz from which the two carrier-wave frequencies are derived. The Coarse Acquisition (CA) code is a repeating PRN code which is different for each satellite and is modulated onto L1, repeating every millisecond. The Precise (P) code is much longer and is modulated onto both L1 and L2 repeating every seven days. By default, the P Code is encrypted for non-authorised users into the Y Code, more about this below. The navigation message is a 50Hz signal modulated onto the L1 signal and contains data bits that describe orbits, clock corrections and other system parameters. The ranges determined from each part of the signal are the GPS observables and are based on measured time or phase difference between a code transmitted from a satellite and an identical code generated in the receiver.

A complete description of the GPS signal structure is given in the Interface Control

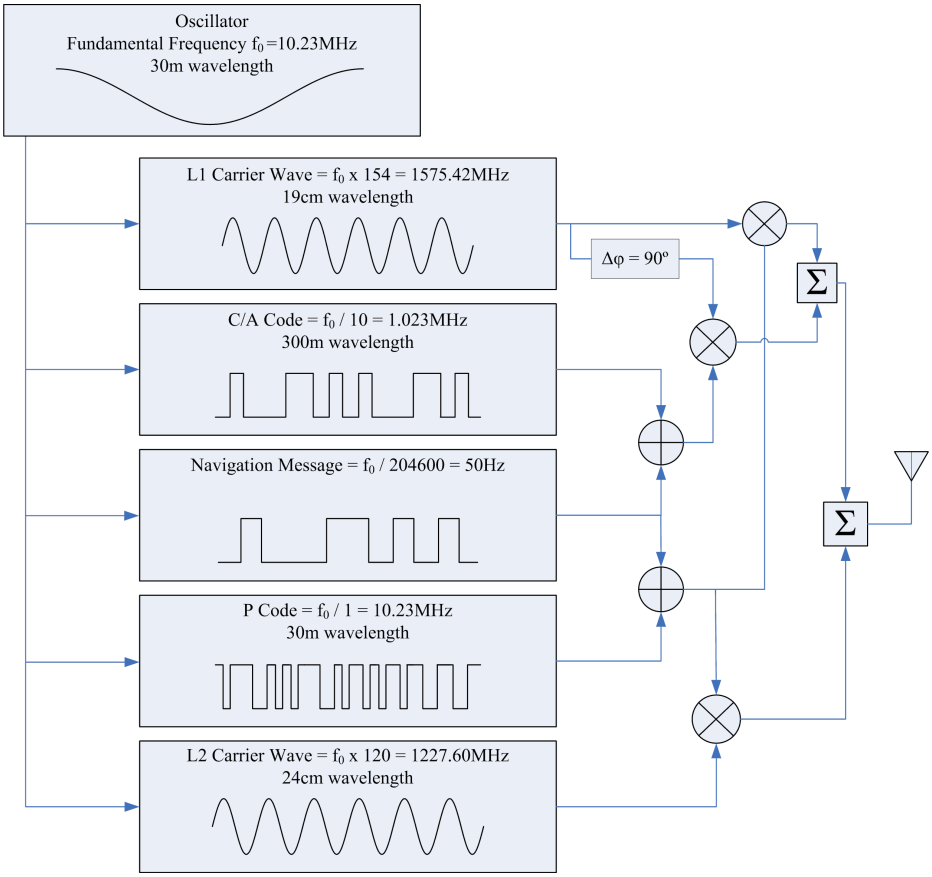

Figure 2.12: The GPS signal structure. The L1 and L2 carrier-waves are derived from the fundamental frequency of 10.23Mhz. Codes and a navigation message are modulated onto the carrier-waves (Seeber, 2003).

Document on the United States Coast Guard website (`http://www.navcen.uscg.gov/pubs/gps/icd200/`).

2.7.3.1 The Pseudo-Range Observable

The term 'pseudo-range' in this thesis refers specifically to code measurements. Pseudo-ranges are a fundamental observable used for determining a satellite-receiver distance. In principle, an identical continuous code is generated by a satellite and a receiver at the same time. The satellite's version of the code takes time to reach the receiver and the offset between the receiver's generated code and the satellite's transmitted code is directly proportional to the distance between the two antennas. This is illustrated in figure 2.13.

In practice, the receiver's clock is usually of quartz quality and therefore signifi-

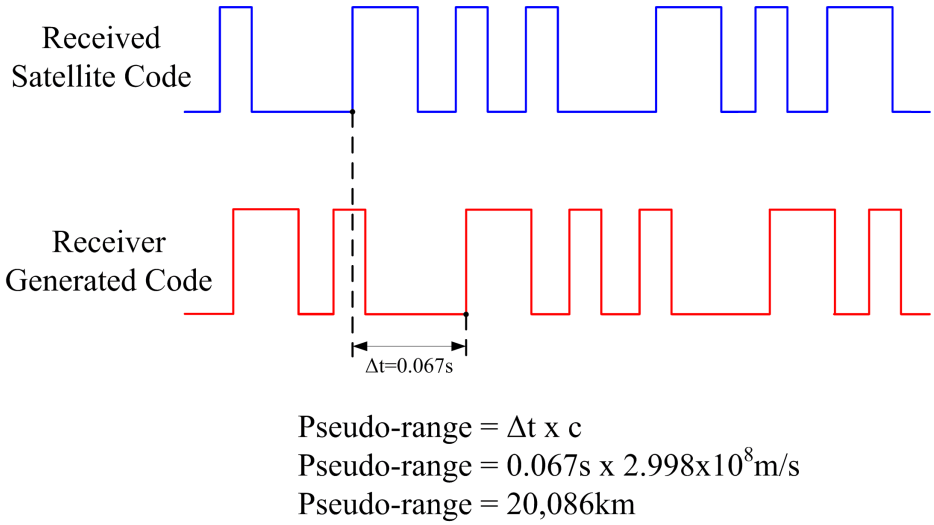

Figure 2.13: GPS receivers compare a time stamped internally generated code and a time stamped satellite transmitted code to obtain an offset which is proportional to the distance between them.

cantly less accurate than the satellite's, and the satellite's clocks will also drift with respect to GPS system time. Adopting conventions used in Bingley (2005), the explicit time frames of a receiver (τ), a satellite (t) and the GPS system time (T), the system time is related to the receiver and satellite clocks by

$$T = t + \delta t \tag{2.19}$$

$$T = \tau + \delta\tau \tag{2.20}$$

where δt and $\delta\tau$ are the satellite and receiver clock offsets respectively. A pseudo-range (PR) between receiver r and satellite s is the difference between the time of reception in the receiver time frame (τ_r) and the time of transmission in the satellite time frame (t^s) scaled by the speed of light in vacuo (c)

$$PR_r^s = c(\tau_r - t^s) \tag{2.21}$$

The true geometric range (ρ) is the difference between the time of reception in the GPS time frame (T_r) and the time of transmission in the GPS time frame (T^s) scaled by the speed of light in vacuo

$$\rho_r^s = c(T_r - T^s) \tag{2.22}$$

Substituting 2.19 and 2.20 into 2.22 gives

$$\rho_r^s = c((\tau_r + \delta\tau_r) - (t^s + \delta t^s)) \tag{2.23}$$

which can be rearranged to

$$\rho_r^s = c(\tau_r - t^s) - c(\delta\tau_r - \delta t^s) \tag{2.24}$$

and finally substituting equation 2.21 into 2.24 yields the basic pseudo-range equation

$$PR_r^s = \rho_r^s - c[\delta\tau_r - \delta t^s] \tag{2.25}$$

Some of the terms in 2.25 do not have rigorously defined time frames. Expressing time frames in brackets after each term, equation 2.25 can be re-written as

$$PR_r^s(\tau_r) = \rho_r^s(T^s, T_r) - c[\delta\tau_r(\tau_r) - \delta t^s(t^s)] \tag{2.26}$$

Adding terms to account for the errors in the satellite's ephemeris ($deph_r^s$), the signal delay biases due to the ionosphere ($dion_r^s$) and the troposphere ($dtrop_r^s$), and including an observation residual (v_r^s), a more rigorous expression for a pseudo-range is given by

$$PR_r^s(\tau_r) = \rho_r^s(T^s, T_r) - c[\delta\tau_r(\tau_r) - \delta t^s(t^s)] + deph_r^s + dion_r^s + dtrop_r^s + v_r^s \tag{2.27}$$

2.7.3.2 The Carrier Phase Observable

The pseudo-ranges discussed above are modulated onto a carrier wave using binary bi-phase modulation. It is this modulated carrier wave that is transmitted from the satellite. The phase of the carrier wave offers a much more precise observable because the resolution is in the order of decimetres, compared to the code's which are 30

to 300m long per bit. The carrier phase observable ($\phi_r^s(\tau_r)$) between satellite s and receiver r consists of the fractional part of the wavelength and the change in the integer number of cycles that have occurred since the receiver locked on to the satellite. The carrier phase observable therefore contains an integer ambiguity (N_r^s) term; this is the unknown number of integer cycles between satellite s and receiver r and cannot be determined directly.

Substituting the pseudo-range on the left hand side of equation 2.27 for the integer ambiguity and carrier phase, and changing the units from metres to cycles, gives the basic carrier phase equation when rearranged

$$\phi_r^s(\tau_r) = \frac{f}{c}\rho_r^s(T^s, T_r) - f[\delta\tau_r(\tau_r) - \delta t^s(t^s)] + N_r^s \tag{2.28}$$

Equation 2.28 shows the basic carrier phase equation. In reality the receiver will make an arbitrary guess at the value of the integer ambiguity when it first locks on to each satellite. Thus N_r^s represents the correction required to that guess in order to determine the true integer ambiguity. Adding in the error terms introduced in equation 2.27 yields the full carrier phase equation

$$\phi_r^s(\tau_r) = \frac{f}{c}\rho_r^s(T^s, T_r) - f[\delta\tau_r(\tau_r) - \delta t^s(t^s)] + N_r^s + \frac{f}{c}deph_r^s - \frac{f}{c}dion_r^s + \frac{f}{c}trop_r^s + v_r^s \tag{2.29}$$

Note that $\frac{f}{c}dion_r^s$ is negative for the carrier phase observable because the carrier wave signal is advanced by the ionosphere. The user's position is implicit within the geometric range

$$\rho_r^s(T^s, T_r) = \sqrt{(X^s - X_r)^2 + (Y^s - Y_r)^2 + (Z^s - Z_r)^2} \tag{2.30}$$

where X^s, Y^s and Z^s are the earth frame co-ordinates of the satellite and X_r, Y_r and Z_r are the earth frame co-ordinates of the receiver. The satellite positions are calculated from the ephemeris data leaving four unknowns to be solved, and requiring pseudo-range measurements from at least four satellites. Note that unlike the pseudo-range observable, it is not normally possible to determine an

instantaneous stand-alone position using the carrier phase observable because each observation has its own integer ambiguity term and in any case, the errors and biases are around two orders of magnitude larger than the size of the observable. These obstacles are usually overcome through relative positioning. For a fuller account of this and related subjects, interested readers should consult Hofmann-Wellenhof et al. (2001), Seeber (2003) and Leick (2004). Alternatively, an advanced technique known as PPP that utilises carrier phase observations is also able to overcome these issues.

2.8 PPP

PPP brings together undifferenced carrier phase and pseudo-range observations from a user's GPS receiver, and highly accurate clock and orbit data computed from globally distributed networks such as the International GNSS Service (IGS). This enables users to compute a precise position without the need to resort to concurrent data or positions from other sources for error mitigation. Station effects that result from geophysical and atmospheric phenomena are present in the solution and users can choose to apply models to remove or mitigate certain factors so that others may be preserved. Satellite specific errors and biases may also be modelled.

Although PPP type experiments preceded it (Héroux and Kouba, 1995, Henriksen et al., 1996, Lachapelle et al., 1996), PPP in its most common current form was first proposed by Zumberge et al. (1997a). The aim was to develop an efficient approach to offer the accuracy achieved at IGS stations to other users. The approach was tested by analysing daily carrier phase data from CGPS stations, achieving millimetre repeatabilities horizontally and centimetre repeatabilities vertically. In a follow up paper Zumberge et al. (1997b) computed satellite clock and orbit information using a subset of the IGS network known as the Fiducial Laboratories for an International Natural sciences Network (FLINN). Many FLINN stations are equipped with atomic clocks which provide a much more stable time reference at the receiver site. Three dimensional positional accuracies for a receiver utilising FLINN orbits were 0.004m with daily repeatabilities of 0.019m.

From a theoretical point of view, the fundamental difference between PPP and

relative positioning is the treatment of the clocks and the ambiguity modelling. Relative techniques are able to remove the clock biases and the ambiguity through single, double and triple differencing. In PPP, the clock biases and the ambiguities are considered unknowns and are estimated using a stochastic model with a sequential filter such as the Square-Root Information Filter (SRIF); this is a modified Kalman filter developed at the Jet Propulsion Laboratory (JPL) by Bierman (1977). SRIF allows parameters to have either time uncorrelated behaviour (white noise) or time dependent behaviour (random walk) or non-varying behaviour (Blewitt, 1993). These different aspects are applicable to different parameters; for instance, a white noise model is used to estimate satellite clock bias (Kouba and Héroux, 2000) whereas a random walk model is used to estimate the tropospheric delay (ibid).

2.8.1 The PPP Observation Model

Continuing the observation model in §2.7.3, equations 2.27 and 2.29 are the two fundamental GPS observables; the pseudo-range and carrier phase respectively. PPP requires both of these to succeed and is usually performed using dual frequency data for reasons explained below. For relative positioning, single differencing between two receivers and one satellite removes the satellite clock error and the satellite ephemeris error ($\delta t^s(t^s)$ and $deph_r^s$) and double differencing (between two single differences) removes the receiver clock error ($\delta t^s(t^s)$) and (indirectly) the integer ambiguity term (N_r^s) (Hofmann-Wellenhof et al., 2001).

Obviously in PPP, these terms remain, but since high precision orbit and clock products are being used, $\delta t^s(t^s)$ and $deph_r^s$ can be considered known and can be removed. The ionospheric advance can be removed using dual frequency data to form the ionospherically free observable (Leick, 1994) and irregularities in the ionosphere due to the Total Electron Content are mitigated using a model included in the orbit products (Feltens and Schaer, 1998). Furthermore, the tropospheric delay ($dtrop_r^s$) can be divided into a hydrostatic component and a wet component (§2.8.2.6). The hydrostatic component is dominant and predictable which accounts for 90% of the tropospheric delay. The remaining wet delay can be expressed as a product of the ZWD and a mapping function. The PPP observation model (Kouba, 2009a) for the

pseudo-range and the carrier phase observables is therefore

$$PR_r^s(\tau_r) = \rho_r^s(T^s, T_r) - c[\delta\tau_r(\tau_r)] + MZWD_r^s + v_r^s \tag{2.31}$$

$$\phi_r^s(\tau_r) = \frac{f}{c}\rho_r^s(T^s, T_r) - f[\delta\tau_r(\tau_r)] + N_r^s + \frac{f}{c}MZWD + v_r^s \tag{2.32}$$

where MZWD is the weighted average of the mapped slant delays. Because the equations above now only contain station specific terms, there is no point attempting relative processing as it would result in uncorrelated station solutions that are equivalent to independent PPP solutions (Kouba, 2009a). In reality, precise solutions must also consider the temporally varying nature of the hydrostatic delay, this is discussed below in 2.8.2.6.

The receiver clock ($\delta\tau_r(\tau_r)$) is a large error source within PPP. The timing of operations within a GPS receiver is usually governed by a quartz clock, which is significantly less stable than the atomic clocks used on board the satellites. The drift in typical quartz clocks of 0.1ns/sec in receivers generates errors in the order of several centimetres per second (Kouba, 2009a). The receiver clock can either be modelled as a white noise process (Zumberge et al., 1997b) or as a random walk process (Witchayangkoon, 2000).

The carrier phase ambiguities (N_r^s) can not normally be fixed to integer values due to code biases in the receiver and satellites; these normally difference in relative solutions. Various cutting-edge strategies exist (Blewitt, 2008, Kouba, 2009a) to resolve this, but they are not applicable to episodic campaigns (Blewitt, 2008).

2.8.2 PPP Errors and Models

To provide a progressive account, the description of PPP thus far has been simplified somewhat; many errors and biases occurring at the satellite and receiver have been omitted. Those particularly relevant to the work in this thesis are now discussed.

2.8.2.1 Multipath

Multipath is the term given to an error source that is caused by the signal from the GPS satellite taking one or more indirect routes to the antenna (Hofmann-Wellenhof et al., 2001). Signals that reflect in this way result in a range measurement that appears longer than it should. Mitigation strategies include site selection and use of high quality antennas.

Prior to PPP processing, GPS data can be pre-processed using a Linux command line software package known as Translation, Editing, and Quality Check (TEQC), which is used to quantify site specific issues such as multipath that may affect the quality of the end results. TEQC was developed by the University Navstar Consortium (UNAVCO) (Estey and Meertens, 1999) (`http://facility.unavco.org/software/teqc/teqc.html`) and is a widely used tool in the GPS research community (Afraimovich et al., 2003, Ogaja and Hedfors, 2007).

Amongst other things TEQC outputs the RMS values of the de-trended estimates of the P-code multipath on the two GPS carrier signals L1 and L2 (Estey and Meertens, 1999); these are referred to as MP1 and MP2. Figure 2.14 shows skyplots of the MP1 and MP2 values for each satellite track (top left and right) along with the azimuth and elevation spread of the satellites for the session (bottom left) and an azimuth and elevation spread of the MP1 values for each satellite track (bottom right). The plotting routines were created by Dr Norman Teferle at the Institute of Engineering Surveying and Space Geodesy (IESSG), University of Nottingham for his own research.

The multipath values can be used to either determine a station's suitability or identify specific sources of multipath error.

2.8.2.2 Absolute Antenna Phase Centre Corrections

The physical phase centres (one each for L1 and L2) of GPS receiver antennas are not measurable points for a user because they lie within the antenna housing. Instead they are determined by offsets from a measurable point on the antenna such as the Antenna Reference Point (ARP); these are referred to as Phase Centre Offsets (PCOs). Furthermore, the L1 and L2 electrical phase centres are actually theoretical points in

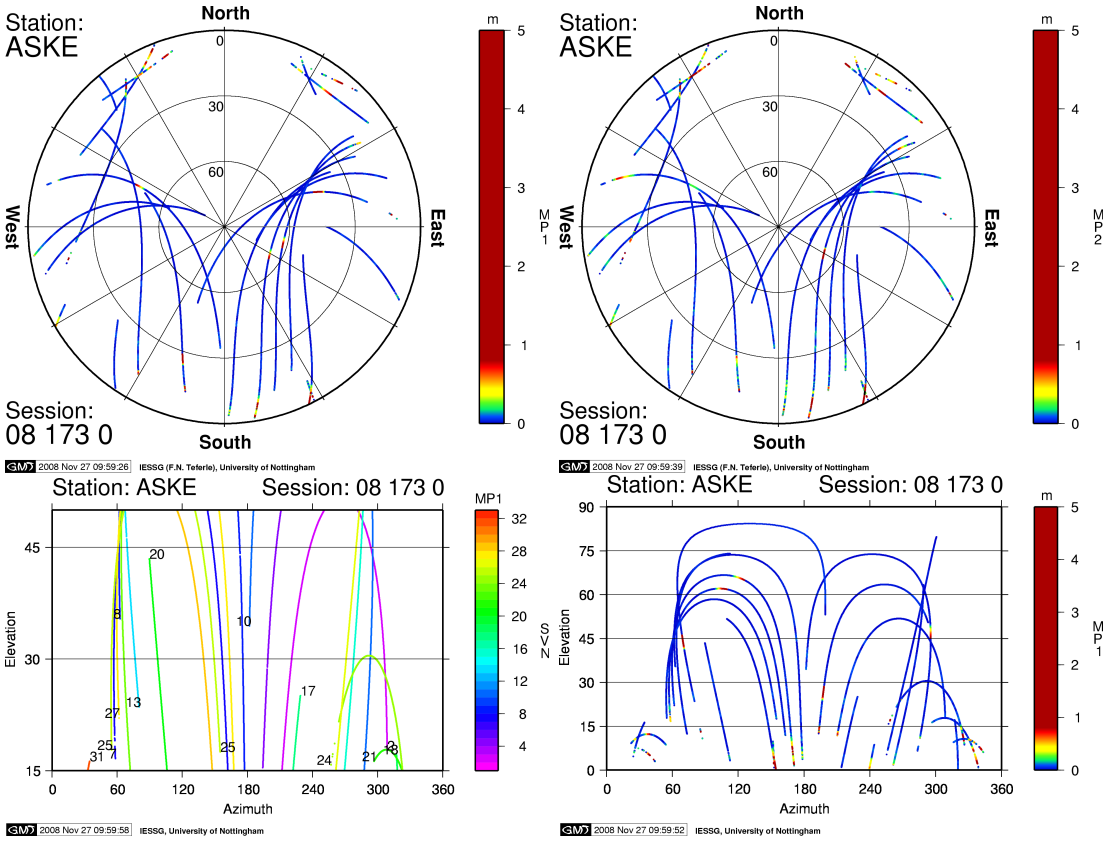

Figure 2.14: Examples of analysis of TEQC quality control output from a six hour session at Askerton Ordnance Survey Pillar (ASKE) on 21 June 2008. The two 'skyplots' (**top**) show the L1 (**left**) and L2 (**right**) P-code multipath values for individual satellites known as MP1 and MP2; the centre of these plots relate to the observers zenith. Multipath values ought to be low unless satellites are close to the horizon. The **bottom left** plot is a means of plotting the azimuth spread of satellite tracks and the **bottom right** plot is similar except MP1 values are used to colour code the tracks. These plots and others tend to be used to justify data rejection or to assess the suitability of a site.

space that vary with the elevation and azimuth of the satellite being tracked; these are referred to as Phase Centre Variations (PCVs), which in turn vary between antenna models. Strategies in the past to account for PCOs and PCVs in a given antenna involved calibration over a short baseline with a globally accepted reference antenna: the Allen Osborne Associates Dorne Margolin model T (AOAD/M_T). This process involved various assumptions and limitations which led to systematic errors in GPS results. For instance, the PCVs on the reference antenna were ignored (Schmid et al., 2005), not to mention the PCOs and PCVs on the satellite antennas.

Coinciding with the realisation of the International Terrestrial Reference Frame 2005 (ITRF2005) (`http://igscb.jpl.nasa.gov/network/refframe.html`), an ab-

solute antenna PCV and PCO strategy for both receivers and satellites has been adopted by the IGS (Schmid et al., 2007). As more and more antennas are absolutely calibrated, the IGS collates the offsets and variations and releases them periodically (`ftp://igscb.jpl.nasa.gov/pub/station/general`).

2.8.2.3 Ocean Tide Loading

Large open ocean water masses are redistributed around the globe because of the gravitational pull of mainly the Sun and the Moon; this has a deforming effect on the solid Earth surface known as Ocean Tide Loading (OTL). For a GPS station, this manifests mainly as cyclical vertical motion with some horizontal effect also over mainly diurnal and semi-diurnal periods. OTL varies spatially and temporally and can be described through the complex interaction of eleven tidal harmonics (Wilhelm et al., 1997). Site specific OTL coefficients computed using a range of models have been made available by Bos and Scherneck (2006).

2.8.2.4 Earth Body Tides

The solid Earth undergoes elastic deformation as it moves through the gravitational fields of the Moon and the Sun and these motions are known as Earth Body Tides (EBT) or solid Earth tides (Melchior, 1974). For geodesists, there are four tidal constituents of note; the diurnal and semi-diurnal effects of the Moon and the Sun. Rather than the complex interactions of harmonics that produce motion from OTL, EBT has a very much more direct and predictable effect on surface deformation and 98% of the effect can be adequately described using the dimensionless elasticity parameters known as the *Love* numbers and the *Shida* number. For further reading see Torge (2001) and Bomford (1980).

2.8.2.5 Tectonic Plate Motion

Tectonic plate motion has been an intense field or research for several decades and is a leading research topic for GPS scientists (`http://sideshow.jpl.nasa.gov/mbh/series.html`). As solutions from PPP processing are computed independently of a network, the Terrestrial Reference Frame (TRF) used to compute the positions of the

satellites is automatically implied in the station solutions. This is usually a global TRF, which unlike local TRFs such as the European TRF 1989 (ETRF89), is not fixed in time to a specific epoch. Plate tectonic motions will therefore be present in the solutions. As the motions are uniform on the time scale of millions of years for areas not close to plate boundaries, their removal is usually trivial (Lambeck and Canberra, 1989).

2.8.2.6 Tropospheric Delay

The troposphere is the region of the earth's atmosphere between the surface of the earth and an altitude of 17km. This region of the atmosphere causes delay in the propagation of GPS signals (and radio signals in general) typically between 2-3m (Kouba, 2009b). The troposphere is a non-dispersive medium so the delay experienced by both the L1 and L2 signals is the same. Also, the delay to pseudo-ranges is the same as that to carrier phase observations. The troposphere consists of a wet component and a hydrostatic component and the integrated total delay can be estimated using PPP techniques (Bevis et al., 1992). It can also be estimated from relative solutions, but often this causes a bias in the results, especially with smaller networks (<500km) (Gendt, 1998); this was an influencing factor in the choice of PPP for this work.

As mentioned, the integrated *total* tropospheric delay, which is the sum of the hydrostatic and wet delays, can be estimated from GPS data, but this is less useful than the wet delay alone, and usually the hydrostatic delay is subtracted. The hydrostatic delay is predictable as it is mainly a function of pressure and height, and it accounts for around 90% of the total delay. The wet delay is much harder to predict and is caused by the spatial variability of water vapour. The wet delay values have been shown to resemble real atmospheric water vapour estimates from water vapour radiometers (Bar-Sever et al., 1997), and consequently for some, it is not just another error term, it has useful real world and research applications (Bevis et al., 1994, Williams et al., 1998, Wadge et al., 2002, de Haan et al., 2006), including those detailed in this thesis. Figure 2.15 is an example of a near real-time Zenith Total Delay (ZTD) map of Japan (Iwabuchi et al., 2006) computed from a network of CGPS PPP solutions; this is used to estimate Integrated Water Vapour (IWV).

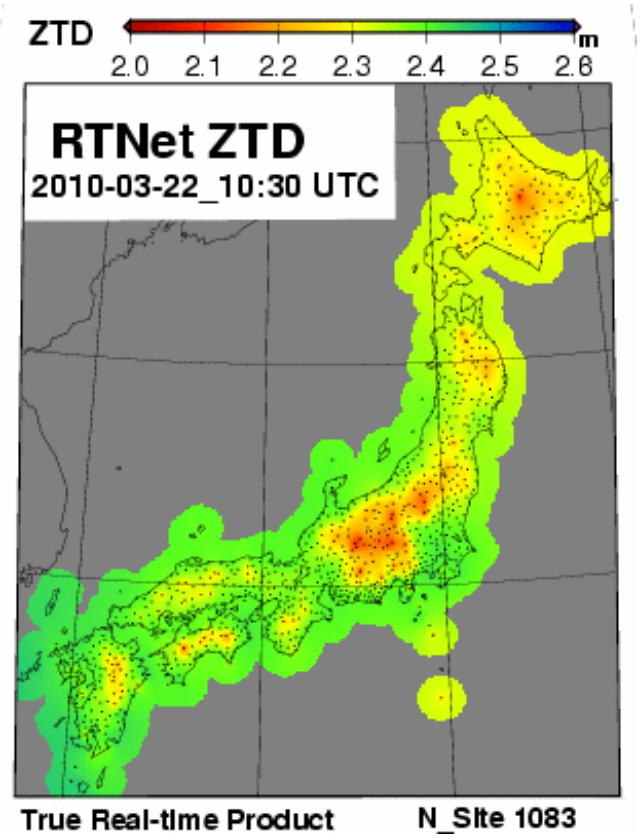

Figure 2.15: A ZTD map of Japan. CGPS stations stationed around Japan each compute their own ZTD values which are used to form a ZTD map of the area; this can be used in weather nowcasting © GEONET.

Because observations are not normally made in the zenith direction, the GPS tropospheric delay term is estimated from a cone of observations above the station antenna, the size of which is dependent on the elevation mask. These estimates are then mapped to zenith and a single weighted average estimate termed the ZTD is estimated (Bevis et al., 1994) from which the ZWD can be derived. To prevent solution instability in the SRIF, usually only one tropospheric delay value is estimated per epoch, either as a stochastic variable or as random parameters valid over short intervals spanning several epochs (Kouba, 2009b).

The hydrostatic component can be modelled in various ways, including as a single polytropic layer (Hopfield, 1970) or as a function of height and pressure (Saastamoinen, 1972). Pressure values are required for both of these, for instance the simplified Saastamoinen equation (Saastamoinen, 1972) is given by:

$$ZHD = P \cdot 0.00227 \cdot e^{(-0.000116 \cdot h)} \tag{2.33}$$

where ZHD is the Zenith Hydrostatic Delay, P is pressure in millibars and h is the station orthometric height in metres. If this pressure value is not available, then a default standard atmospheric pressure will be assumed of 1013.25mb. Kouba (2009a) suggests that the best solutions for ZHD are obtained using station pressure values which is why they were employed in this project.

Because the amount of troposphere encountered by a GPS signal is dependent on the elevation angle, it is also standard practice to employ a mapping function to account for this in PPP solutions. There are a large number of mapping functions and comprehensive reviews exists detailing their respective merits (Mendes and Langley, 1998, Witchayangkoon, 2000, Kouba, 2009b). Kouba (2009b) concludes that the current state-of-the-art Global Mapping Function (GMF) is the Vienna Mapping Function-1 (VMF1) (Boehm et al., 2006a), hence its choice for this project. VMF1 was computed from an archive of forty years of empirical data from the European Centre for Medium-Range Weather Forecasts (ECMWF) and provides global grids of 2.0° in latitude by 2.5° with a temporal resolution of six hours of hydrostatic and the wet mapping functions (`http://ggosatm.hg.tuwien.ac.at/DELAY/`).

2.9 Summary

Several subjects relevant to this thesis have been reviewed. Firstly, the basics of SAR and InSAR were discussed followed by an examination of the PSI technique. GPS and the more advanced PPP processing technique were then examined. These subjects now form the basis of the literature review in the next chapter.

Chapter 3

InSAR Integration Review

This chapter begins with a brief review of how InSAR has been integrated with other geodetic observations over the years. There then follows a review of the problems of atmospheric delay in InSAR and the use of GPS in meteorology. This sets the scene for a focussed review of the current state of the art in research concerning the integration of InSAR (including PSI) with GPS and other data sources. This includes the mitigation of atmospheric phase artefacts in InSAR and the use of corner reflectors. There then follows a section discussing the knowledge gaps in InSAR integration that motivated this research followed by a brief summary.

3.1 Introduction

The reasons for integrating InSAR with other geodetic or meteorological observations are wide and varied. In its infancy, modern InSAR was used for DEM creation, and survey observations provided a means of ground control to constrain errors in the process; examples of this are numerous (Small et al., 1996, Slob et al., 2000, Mallorqui et al., 2001, Crosetto, 2002). The ultimate InSAR integration for DEM construction is undoubtedly the Shuttle Radar Topography Mission (SRTM) which utilised GPS transects as the main method for verifying the geolocation accuracy of the data and employed corner reflectors as a means of ground truth.

Another reason for integration is to validate the InSAR process itself, to understand its sources of error and potentially improve it. Examples of this include corner

reflectors for radiometric calibration and validation studies with some higher order observations used as a truth measurement.

A third class of reasons for InSAR integration is employed by those who want to utilise the complimentary nature of InSAR with other techniques to improve their results. For instance, deformation studies may be improved with the addition of GPS or meteorological models.

The main focus of this literature review is the integration of InSAR (including PSI) and GPS with special attention paid to corner reflector experiments and atmospheric delay mitigation.

3.2 InSAR Integration Research

3.2.1 Atmospheric Delay Background

InSAR images tend to exhibit irregular artefacts which according to Zebker et al. (1997), Delacourt et al. (1998), Hanssen (1998) and Massonnet and Feigl (1998) are due to spatial and temporal atmospheric inhomogeneity across the SAR scene. In particular, Zebker et al. (1997) state that these artefacts result mainly from variations in atmospheric water vapour. Variations in pressure and temperature also contribute to the distortions, but these effects are much smaller in magnitude.

Early attempts to define and correct for atmospheric effects in radio signals from satellites determined relationships for the altitude dependence of pressure, humidity and temperature (Hopfield, 1970, Saastamoinen, 1972). These were good at estimating the more predictable *hydrostatic* delay which suited many applications as this represents around 90% of the total delay. The wet portion of the delay, however, is far less predictable. Hanssen and Feijt (1996) and Zebker et al. (1997) applied the problem of atmospheric error correction specifically to InSAR, suggesting modification of Saastamoinen's relationship using meteorological data. In the same paper, Zebker et al. (1997) also suggested stacking independent interferograms as a means of averaging out tropospheric errors.

The use of GPS in meteorology had been suggested as early as 1992 (Bevis et al.,

1992), and this was utilized by Delacourt et al. (1998) who proposed a model using GPS and Doppler Orbitography and Radiopositioning Integrated by Satellite (DORIS) measurements as a means of correcting InSAR atmospheric delay. Their results showed that tropospheric corrections reached two fringes for some interferograms, and that on average the accuracy of the interferograms was about plus or minus one fringe after the corrections were applied. This approach and Zebker's multiple interferogram approach condensed potential solutions to the issue in to two groups; calibration and stacking. Stacking is a simple averaging of interferograms and is not discussed further in the context of atmospheric delay. Interested readers should refer to Zebker et al. (1997), Williams et al. (1998), Sandwell and Price (1998) and Ferretti et al. (1999). Calibration, however, is one of the dominant arguments for InSAR integration and is discussed in detail below.

3.2.2 InSAR Atmospheric Calibration

A major focus for InSAR integration is that of atmospheric determination or mitigation. This is most often conducted as a strategy to attempt to remove all or some part of the atmospheric contribution in InSAR images, although it has also been suggested that such integrations may be useful as a tool for high resolution water vapour mapping (Hanssen et al., 1999).

Bock and Williams (1997) experimented with GPS zenith delay corrections in the densely distributed Southern California Integrated GPS Network (SCIGN) and reported through a cross validation analysis that in areas where the GPS network was sufficiently dense, more than 90% of the atmospheric delay in a SAR image could be corrected using Kriging interpolation. Success was roughly halved in regions where the GPS stations were less dense and it should be noted that this level of density and worse is more common outside of the SCIGN. Other validation experiments followed later, notably with Webley et al. (2002) and Janssen et al. (2004).

Williams et al. (1998) proposed using much sparser GPS zenith delay observations with a model based on variations in atmospheric water vapour developed by Treuhaft and Lanyi (1987). Williams et al. (1998) postulated that the variations approximate a power law dependence on frequency, characteristic of Kolmogorov

turbulence. They showed that sparsely distributed GPS data can be used to reduce the long wavelength effects in the more densely distributed InSAR data. Bonforte et al. (1999) calibrated interferograms using GPS zenith delay measurements and compared them to interferograms calibrated using ground meteorological data; the conclusion was that meteorological data, GPS data or both were all valid means for calibrating InSAR data. In Hanssen (2001), relative delays were compared between GPS observations and InSAR interferograms, although results suffered due to the fact that there was limited variation in the troposphere on the acquisition days. Hanssen (2001) concluded that using double differenced GPS data introduced error margins in the zenith delay estimates that exceeded the atmospheric delay variation. He then went on to say that GPS networks may rarely be optimally scaled for such purposes; they are very often too sparse, but also they may be too dense as the ZWD estimates are resolved from a wide 'cone' of data which results in an increased smoothing of the signal whenever GPS receivers are too close. Van der Hoeven et al. (2000) showed that under favourable atmospheric conditions, long-wavelength effects of InSAR delay could be reduced using a single GPS time series coupled with knowledge of wind speed and direction. As long as the wind conditions were similar for both passes, it was possible to correlate delay variation between the techniques. In a similar experiment, Onn and Zebker (2006) suggested using Taylor's frozen-flow hypothesis with GPS zenith delay observations from before and after an acquisition to infer a dense spatial network from one that is sparse. This led to a 31% reduction in RMS errors from simple time interpolation of GPS zenith delay estimates alone. Other significant contributions to GPS corrected InSAR include Li et al. (2004, 2005) and many other examples of InSAR correction using meteorological data exist, most notably Wadge et al. (2002), Foster et al. (2006) and Puysségur et al. (2007) although these efforts were often limited by the poor resolution of the models and data compared to the highly variable atmospheric refractive index (Onn and Zebker, 2006).

3.2.3 Corner Reflectors in InSAR

The use of corner reflectors in radar technologies has been an established means of calibration for a number of years. NASA's Apache Point Observatory Lunar Laser-

ranging Operation (APOLLO) missions (Murphy et al., 2007) in the 1960s and 70s placed man-made retro-reflectors on the moon in order to determine lunar distances. Discourse on radiometric calibration using corner reflectors and their optimisation for remote sensed SAR include Curlander and McDonough (1991), Ulander (1991), Groot and Otten (1994), Corona and Ferrara (1995), Sarabandi and Chiu (1995) and Jezek et al. (2003).

Directly integrating precisely surveyed artificial point targets with InSAR observations is less established; the potential for using them in precise change detection experiments became possible with the arrival of SAR platforms of sufficient resolution. As a footnote to a paper discussing speckle and noise in InSAR images, Prati et al. (1989) postulated a number of applications for which precisely located corner reflectors may be of use in SAR remote sensing. Three years later in March 1992, some of these hypotheses were tested using the newly launched ERS-1 satellite. Taking advantage of the three day repeat cycle during the satellite's initial phases, 19 corner reflectors were placed linearly along a 15km stretch of land to the west of Bonn in what later became commonly referred to as 'The Bonn experiment' (Monti Guarnieri et al., 1993). The work was an important proof of concept for ESA, and its success at measuring sub-centimetric motion in blindly adjusted corner reflectors heralded a new era in European remote sensing geodesy. An obvious follow-up challenge was to then observe real, verifiable ground motion using surveyed corner reflectors in known areas of instability (Coulson, 1993). Timmen et al. (1996) noted however, in a successful experiment to observe deformation using corner reflectors in a mining area in Germany, that artificial point targets were not immune to atmospheric error.

Gray and Farris-Manning (1993) used corner reflectors as part of their experiment to conduct repeat-pass interferometry using airborne radar. The corner reflector was moved between passes and they detected this movement to an accuracy of around 1mm. (Xia et al., 2002) discussed the potential for corner reflectors for improving coregistration in areas of low coherence. Reflectors were mounted on an unstable slope detecting motion of 1cm over four months.

Marinkovic et al. (2004) used corner reflectors and PSI to compare the quality of ERS-2 and ENVISAT phase observations with precise levelling observations. A double

differenced (in height and time) comparison between levelled heights and PS points mapped to metres in height, found InSAR phase measurements to have a precision of around 3.5-4mm. In a follow-up experiment, with the benefit of more observations and a better treatment of errors, Marinkovic et al. (2008) revised these estimates to sub 3mm stating that PSI has the potential to approach levelling precision in the right circumstances.

3.3 Research Motivations

Following on from the literature review presented above, gaps in the research are now identified.

3.3.1 Corner Reflectors for PSI

Whilst there is comprehensive literature on many areas relating the integration of InSAR and other techniques, there remain some areas which would benefit from a slightly different approach. Integration strategies are wide and varied in standard InSAR, but there is currently very little research which integrates PSI with other geodetic measurements and very few PSI corner reflector experiments. If the corner reflectors were in place long enough to become persistent scatterers in a stack large enough for a valid PSI analysis, many fresh opportunities arise:

- Utilising artificial 'test' PS points permits direct comparison with natural PS points. This could provide a better understanding of the physical nature of real PS points and why some are selected and others not.
- A comparison of the velocities from GPS and PSI at precisely the same point could enable a better quantification of error sources and their mitigation.
- PSI provides velocities of PS points relative to a reference point along the satellite line of sight. If the reference point were a corner reflector in place throughout the stack, with a time series of GPS data overlapping the PSI acquisitions, it would be possible to remove the reference point bias and derive

absolute velocities. This would lead to simpler, more direct comparisons with other observations.

One difficulty of corner reflector surveys, especially in urban situations, is finding enough secure sites where reflectors can be left in place. Unlike GPS, placing them on roofs etc is not usually an option as the surrounding clutter may preclude their visibility in the imagery. On the other hand, constantly deploying and then dismantling the reflector for each pass may compromise the accuracy of its position. There is currently no research involving 'episodic' corner reflector networks, which are able to precisely and repeatedly relocate into position, ideally into a pre-existing monument or structure. The project sponsor, BGS, have shown interest in the potential for making corner reflector surveys for PSI more routine straightforward and repeatable anywhere in the UK, as they have their own corner reflector network.

3.3.2 Atmospheric Phase Assumptions

PSI is regarded as a solution to the problem of atmospheric phase mitigation in InSAR by many, but the validity of the APS approach is questionable, especially in light of experiments such as the PSI Codes Cross-Comparison and Certification for Long-Term Differential Interferometry (PSIC4) (Racoules et al., 2006) which brought together the major PSI methods of the day to blindly compare results computed for a pre-selected test site. Part of the remit of PSIC4 was a comparison of the APSs which concluded that "In some cases there is practically no correlation between APS from different teams". The fact that the APS estimates between teams in PSIC4 varied so much, indicates that there is no single accepted method which is clearly favoured or superior which itself indicates that there is still work to be done in the field.

Many PSI techniques assume that a statistical model is sufficiently robust to remove the majority of atmospheric contribution. This may be true, but it may also be the case that phase contributions from deformation processes are partly consumed in this process. Atmospheric path delay is assumed to be low pass in the spatial domain, but uncorrelated temporally, whereas the non-linear deformation is assumed to be lowpass in both the spatial and temporal domains. It is straightforward to see how

these assumptions could be invalidated with either non-random atmospheric patterns or complex deformation behaviour such as fast non-linear deformations (Racoules et al., 2006). In such cases, it is hard to see how the situation could be resolved without resorting to augmentation data that may be used to weight or constrain observations.

An assumption of randomness over time (for sampling periods of thirty-five days or multiples thereof) is often made for atmospheric contributions (Ferretti et al., 2001, Mora et al., 2003), this enables them to be modelled as white noise. However, even large interferogram stacks of 100 images or more are unlikely to contain enough atmospheric phase to approximate normal distribution, because according to central limit theorem, the sample size is too small (Durrett, 1996). The main contribution to atmospheric inhomogeneity in interferograms is from spatial variations in water vapour content Zebker et al. (1997), Hanssen (1998), but water vapour is well understood to vary seasonally (Zawodny and Oltmans, 2001) and whether an interferogram stack is seasonally distributed well enough to attempt to account for this cannot necessarily be assumed.

3.3.3 GPS in PSI

Experiments that integrate GPS and InSAR or PSI often use double-difference carrier phase solutions (Stolk, 1997, Hanssen, 2001, Webley et al., 2002). This can be undesirable if attempting to characterise behaviour at a point as station errors will propagate through the network (Héroux and Kouba, 1995, King et al., 2002). Furthermore, GPS zenith delay parameters are relatively derived and the differencing process introduces noise into their solutions (Hanssen, 2001). When comparing GPS zenith delay with InSAR, further differencing is usually required (between master and slave dates), exacerbating the issue such that the resulting uncertainties in the ZWD values may be greater than the variations under examination (Hanssen, 2001). Also, GPS zenith delay estimated from relative solutions usually contains a bias in the results, especially for smaller networks (<500km) (Gendt, 1998). Network zenith delay solutions usually require at least one PPP zenith delay solution to calibrate the other stations (Kouba, 2009a) if the bias is to be accounted for.

3.3.4 PSI Validation

Whilst PSI shows great promise as a tool for creating deformation maps over wide areas, a number of questions remain about the accuracy and precision of PSI and consistency between rival PSI techniques. The PSIC4 project was designed as a validation exercise to assess these issues (Racoules et al., 2006). The project suffered a number of difficulties which included the non-linear nature of the motion at the test site and the fact that teams had no information as to the nature or location of potential deformation (participants argued that the blind nature of the experiment was in contrast to most scenarios involving PSI). The teams also had varying definitions of what constituted a PS point, which led to very different densities of PS points. These factors and more led to very different results from each of the teams.

PSI validation should also be seen in the light of the Terrafirma (Capes and Marsh, 2009) project. Terrafirma is a project funded through ESA which seeks to provide ground motion hazard information in Europe through a consortium of providers. This encompasses a Product Validation Workgroup (PVW) aimed at comparing PSI methods and results from different providers to determine their level of relative consistency and provide analysis of their deviation from comparable datasets; namely tachymetry and levelling. The validation exercise was divided in this way with hindsight of the comparison issues in PSIC4 (Racoules et al., 2006), and it was purposely designed to be less blind without compromising results. The experiment was declared a success (Crosetto et al., 2008) but did highlight certain areas: the quality of the ground truth data was not well defined; the deformation rates of the test sites were low (which can produce smooth and comparable statistics); and a requirement for further study was identified.

3.4 Summary of Limitations

Considering the review presented in the previous sections, a summary of the limitations can be outlined as follows:

- Research involving precisely repeatable episodic reflector sites is non-existent.

- Research involving long term reflector sites integrated with PSI studies is limited.
- Statistical assumptions involved when removing APS from PSI stacks requires validation.
- There is very little research integrating absolute GPS parameters with PSI.
- Whilst PSI is a useful tool for studying ground motion, further validation is required.

3.5 Summary

A review of the current state of the art research in InSAR integration has been presented and relevant areas that would benefit from further research have been highlighted. These involve integrating corner reflectors into PSI studies, questionable assumptions regarding atmospheric phase in PSI and ways in which GPS might be integrated with PSI. These issues were also set against the need for validation in PSI.

Chapter 4

The Nottinghamshire Site

This chapter discusses the choice of Nottingham as the chosen test area for this project. Following background information regarding the project's origins, details relevant to Nottingham's selection as a site for the project are discussed. This includes information regarding its geology and the availability of SAR and GPS data.

4.1 Introduction

Damage due to ground movement in the UK can be very significant. For example, it is estimated that such movements have cost the UK economy an estimated £3 billion over the last decade (NERC, 2010). The British Geological Survey (BGS) Urban Geoscience and Geohazards Programme is systematically assessing the extent of such hazards in the UK and has begun to monitor specific hazards on a regular basis with a view to monitoring them in the longer term. Part of this strategy is to contribute towards an ESA funded pan-European ground motion hazard information service based on PSI results; this is known as the Terrafirma project (Capes and Marsh, 2009).

Through geological research and evidence linked to the Terrafirma project, a short-list of potential sites for this work was created. Sites included Nottingham, Stoke on Trent, Bristol, London and Newcastle. Following further consultation with BGS, Nottingham City Council city development department and an extensive reconnaissance of the ground, Nottingham was chosen. The following sections provide the

specifics of the chosen site and the reasoning that influenced its choice.

4.2 Orientation

The Area of Interest (AOI) is centred on Nottingham in the UK, but encompasses a much wider area including much of the county of Nottinghamshire and including parts of Derbyshire, Leicestershire and Lincolnshire. Figure 4.1 shows the AOI with many minor roads and features omitted for ease of viewing. The boundaries of the AOI were chosen in order to incorporate areas of geological interest (discussed below) and as much urban conurbation as possible whilst not being too large for a PSI study.

4.3 Geography

The AOI consists of the major urban area of Nottingham and its suburbs. Outside of this are several satellite towns and villages, most notably Mansfield to the north and Newark to the northeast, and the city of Derby to the southwest. The area to the east of Nottingham is mainly sparsely populated agricultural land whilst the area to the west has many sizeable towns interconnected with major roads such as the north-south aligned M1 and the east-west aligned A52. Most of the area is mildly undulating, typically varying between 30 to 100m Above Mean Sea Level (AMSL). North of Nottingham and in the far west of the area, heights increase to a maximum of around 200m. The western edge of the AOI is marked by north-south ridgelines as the eastern edge of the Pennines is approached. The major water feature of the area is the River Trent and its floodplain and valley flowing from southwest to northeast. The floodplain is around 3km wide and the valley floor is relatively flat at 15-30m AMSL. Further east is the Vale of Belvoir, which is very flat marshland and agricultural fields.

4.4 Geological Setting

Nottingham lies on the boundary between the Palaeozoic rocks to the North and West, and Mesozoic and Cenozoic strata to the south and east (Bell et al., 2009).

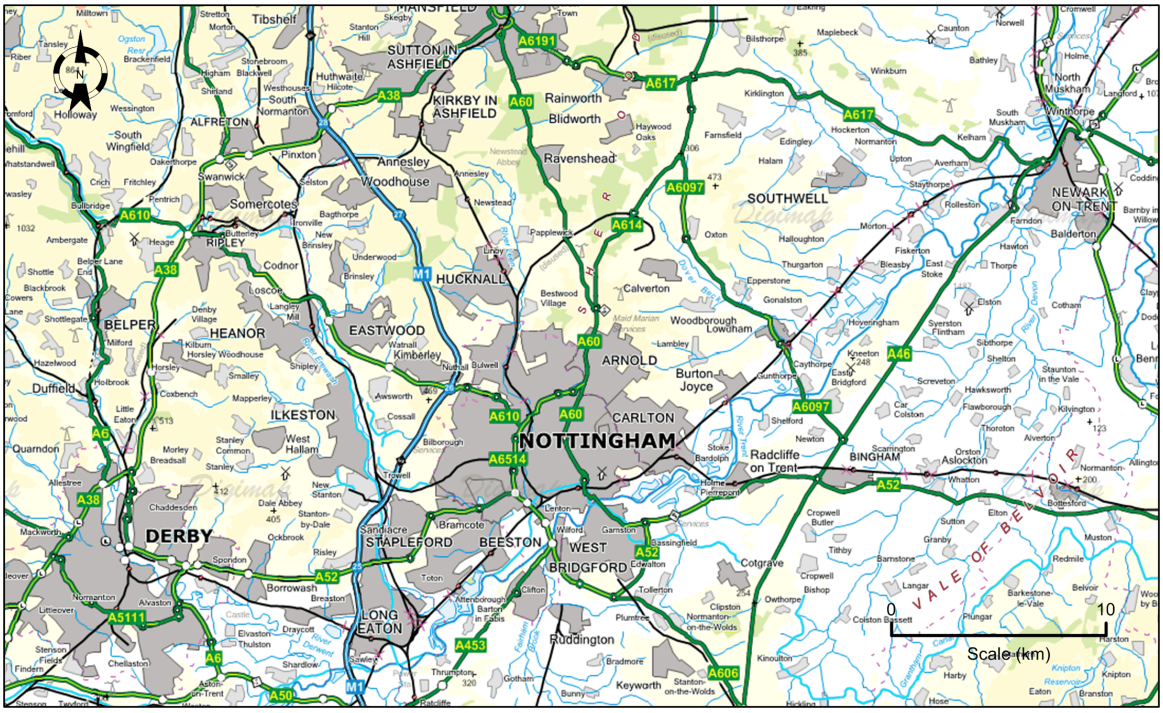

Figure 4.1: The Nottingham site AOI centred on Nottingham encompassing parts of Derbyshire, Leicestershire and Lincolnshire. Many features including smaller roads have been omitted for clarity. © Crown copyright/database right 2009, Ordnance Survey / EDINA.

Any area can be split into three geological tiers; bedrock, unconsolidated superficial or drift deposits and man-made or disturbed material at the surface.

The bedrock layer for the area consists of a wide variety of sedimentary rock types including sandstones, mudstones and coal (Charsley et al., 1990). The coal measures tend to thin towards the east where volcanic rocks become more common. Coal measures have been proved at depth over much of Nottingham and to the west of Nottingham. Many faults are apparent in the area, often running parallel along southeast-northwest lines.

The superficial layer consists of sand and gravels including alluvium mainly in the valleys and broad depressions south of the Trent.

The man-made and disturbed ground layer influence on the geology of the area has been substantial. Artificial deposits due to urban waste, construction and mineral extraction activities are widespread. In the past, the geological environment underpinned the economic development of the area through coal mining and many other extraction activities including gypsum extraction, brickmaking from clays and alluvial

sand and gravel extraction (Bell et al., 2009).

A number of environmental hazards have arisen from the exploitation of mineral deposits. These include changes in the groundwater levels, many abandoned mine shafts and a legacy of mining subsidence. Pre-industrial coal mining activities are a particular concern. Many shallow bell pits are thought to exist throughout the city and the surrounding areas (Charsley et al., 1990); the location and extent of most of these is unknown. The city itself is prone to the occasional collapse of artificial cavities in the sandstone and contaminated land left by industrial activities (Charsley et al., 1990, Bell et al., 2009). The area is also prone to infrequent landslides, rockfalls, swellshrink clay problems, flooding and minor earthquakes, which in the past have been attributed to coal mining (Bishop et al., 1993).

4.5 Potential Geohazards

Through consultation with BGS (Culshaw, 2006) and Nottingham City Council city development department (Thompson, 2007) and following examination of public sources (Charsley et al., 1990), the following points were considered worthy of note when considering potential areas of ground motion that may be visible in PSI studies.

4.5.1 Coal Mining

Coal was mined in the area for hundreds of years in the form of shallow 'bell pits', long-wall mining and opencast mining. The excavation and removal of material whether on the surface or sub-surface leaves voids or pits. Furthermore, opencast mines or quarries may have had material added as fill (see below). Many of these activities started before records began and shallow bell pit mining in particular has left a legacy of potential hazards as a lack of knowledge exists as to their location, extent and depth. Following legislation and formal recording in 1872, records still didn't show levels or provide any geological information. Subsidence is assumed to have ceased from all but the most recent workings, which were Gedling and Cotgrave; both of these closed in the early 1990s (Charsley et al., 1990). Subsidence due to coal extraction is a function (mainly) of the depth of the seam; the greater the depth, the wider the effects are

spread which results in less damage to the surface. Subsidence starts within hours of extraction and can last for more than 10 years (McLean and Gribble, 1985, Donnelly, 1999).

An indirect source of subsidence from underground mines is caused by water displacement. Mine voids can serve as low-pressure sinks inducing the displacement of groundwater resulting in dewatering of nearby geology which can have a destabilising effect (Cifelli and Rauch, 1986). In addition, there is evidence to suggest that when mines close and water pumps are shut down, the groundwater level rebounds which can cause ground motion (Dumpleton et al., 2001).

4.5.2 Boreholes

There are five public water supply boreholes that draw water from the Sherwood Sandstones; Basford, Bestwood, Lambley, Epperstone and Burton Joyce. Consultation with BGS (Culshaw, 2006) and established research (Kim and Choi, 2005) suggested that ground motion may be apparent close to these sites.

4.5.3 Caves

There are a huge amount of caves in Nottingham, especially in the city centre where there are over 200 in the square kilometre of the Lace Market alone (Charsley et al., 1990, Bell et al., 2009). The vast majority of these are sandstone and at varying levels of stability.

4.5.4 Alluvial Deposits

Urban loading on uncompressed alluvial sediments, such as those in the Trent Valley has been known to cause subsidence (Devleeschouwer et al., 2007). BGS have highlighted the Trent alluvial plain as a potential source of ground motion for this reason.

4.5.5 Made Ground

When fill is deposited onto an original ground surface, artificial landforms are created. If the fill is composed of low strength or highly compressible material or of organic

waste, compaction may occur; this process can take years (Charsley et al., 1990). There are many areas of made ground running through the city particularly along the south bank of the Trent.

4.6 Climate and Meteorology

The climate in Nottingham and the UK is classed as a mid-latitude oceanic climate (Peel et al., 2007) which involves a moderately varying temperature range and copious precipitation. The convergence boundary between tropical and polar air currents lies over the UK creating atmospheric turbulence at the micro, meso and synoptic scales that characterises the unsettled nature of UK weather. The main effects of this in the field of InSAR are high temporal decorrelation due to the abundance of vegetation and a strong potential for turbulent atmospheric conditions during acquisitions. This turbulence is directly related to high variability of spatial water vapour in the troposphere leading to non-homogeneous atmospheric phase in interferograms (Zebker et al., 1997, Delacourt et al., 1998, Hanssen, 1998, Massonnet and Feigl, 1998).

4.7 Logistics and Resources

It can not be overstated that from a logistics and resources point of view, the Nottingham site had major advantages over other choices. Field parties conducting observations at potential sites can deploy and return within a standard working day and consequently the project budget can be stretched much further than otherwise. The cost of operating at any of the alternative sites would certainly have precluded field observations during every available satellite pass and the quality of the resulting dataset would be far inferior to Nottingham's. Also located in Nottinghamshire is the main PhD sponsor, BGS, who have a fleet of vehicles ideally suited to field observations. Their offer of these for observations in the local area was another influencing factor.

4.8 Data Sources

This section provides details of the available data sources and datasets for Nottingham at the start of the project.

4.8.1 SAR Data

The requirement from the projects aims and objectives was for a project area with multiple potential reflector sites at which GPS data could be collected concurrently with SAR acquisitions suitable for InSAR. The SAR platforms at the time included ENVISAT, the Canadian RADARSAT-1 satellite and the Japanese Earth Resources Satellite (JERS). ERS was operational at the time but was in gyro-less mode and therefore unsuitable for standard interferometry.

4.8.2 Continuous GPS Stations

Two CGPS stations were operating within the Nottingham AOI during the planning stages; Nottingham (NOTT) operated by the Ordnance Survey (OS) and the IESSG station (IESG) at the University of Nottingham. NOTT was later shutdown on 15 August 2007 and replaced with Keyworth (KEYW) at a different site with an overlap of two months. A number of other CGPS stations operate outside of the AOI. Table 4.1 gives details of the stations and figure 4.2 shows their approximate locations with respect to the AOI.

Station Name (4 fig code)	Date from	Date to	Agency
Hoober (HOOB)	24 May 2004	Current	OS
IESSG (IESG)	27 April 1997	Current	IESSG
Keyworth (KEYW)	8 June 2007	Current	OS
Leek (LEEK)	24 May 2004	Current	OS
Lichfield (LICF)	24 May 2004	Current	OS
Lincoln (LINO)	24 May 2004	Current	OS
Nottingham (NOTT)	2 January 2000	15 August 2007	OS

Table 4.1: CGPS stations in and around the AOI.

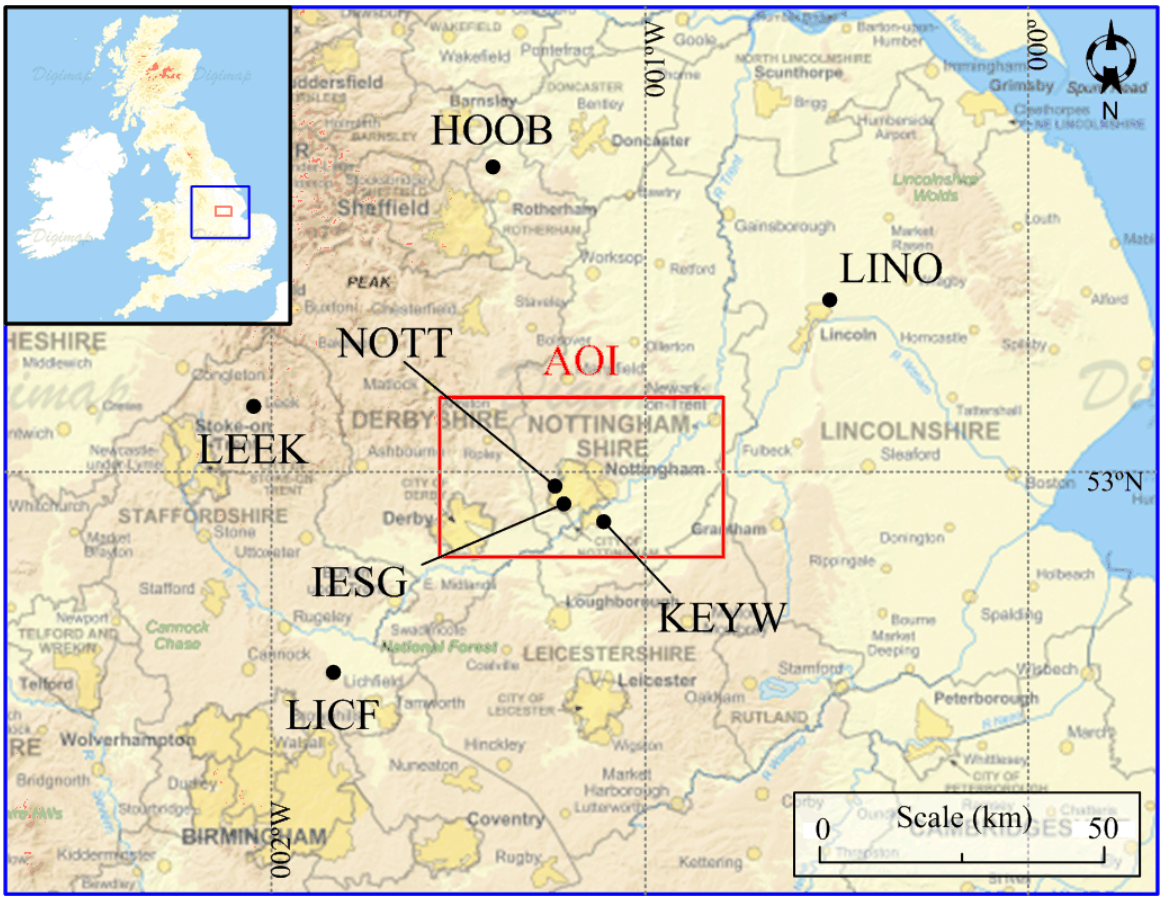

Figure 4.2: CGPS stations shown as black dots in and around the AOI shown with a red box. The top left of the image gives an indication as to where the AOI is in relation to the rest of the UK. © Crown copyright/database right 2009, Ordnance Survey / EDINA.

4.9 Summary

Information regarding Nottingham's suitability as a site that could fulfil the project's aims and objectives have been presented. Nottingham's geological setting and in particular its history of coal mining make it an ideal candidate for the study of ground motion and the integration of PSI with other techniques and datasets. The availability of GPS and SAR data, past and future, add to the case and its location make logistical costs more bearable than elsewhere.

Chapter 5

Data Acquisition

The previous chapter discussed how Nottingham was deemed the most suitable test area for the project. This chapter leads on from that describing specifically what field observations were required to fulfil the aims and objectives. The establishment of the corner reflector network is discussed at length along with the reasoning behind the design and implementation of the fieldwork. This includes a section testing the outcomes of various GPS data collection strategies. Finally, an analysis of the datasets post field observations is provided including a reflector visibility analysis.

5.1 Introduction

Before field observations could begin in earnest, a number of tasks were apparent:

- Establish a corner reflector array in the area of interest
- Arrange for the acquisition of suitable SAR data encompassing the network
- Design a field observation plan around this network

These are now discussed in turn.

5.2 The Nottinghamshire Corner Reflector Array (NCRA)

This section describes the concept, planning and establishment of the project reflector network (Leighton et al., 2007), hereafter referred to as the NCRA.

5.2.1 Size Constraints

Passive trihedral corner reflectors designed for SAR applications usually consist of three mutually perpendicular plates bolted or welded together and mounted on a stand. These reflectors vary in size, from around 80cm to 2.5m per side. The six trihedral reflectors used in this project were procured from Nigel Press Associates Ltd (NPA) and are pre-trimmed to save on weight and bulk so that they offer only the effective, hexagonal area when viewed along the axis of symmetry. The sides would measure 0.8m from apex to apex if the plates were triangular. They are made of light alloy and are fitted with a stand which can be used to adjust and fix the elevation. The NPA reflectors are small in comparison to reflectors for other projects, but their size meant they could fit inside the BGS field vehicles without being completely dismantled. This was desirable because of the episodic nature of some of the reflector locations (see §5.2.4), the preservation of orthogonality of the plates and the pre-set elevation angles. Discourse on the theory of corner reflector design for SAR is in Appendix A. The type of reflector used in the project can be seen in figure 5.1.

5.2.2 Site Selection Criteria

The rationale behind the selection of reflector sites is firstly set against the available resources. The sites had to be close enough to Nottingham city centre to be able to deploy and recover field teams in a single day; they also had to be accessible by two wheel drive vehicles and preferably secure enough to leave unattended. The more technical aspects of site requirements are outlined below.

Figure 5.1: Trihedral corner reflector used in the NCRA, supplied by NPA. The reflector has an adjustable elevation and has sides measuring 0.8m from apex to apex making them transportable by car.

5.2.2.1 Stability

Reflectors positioned at locations with zero deformation would inevitably make future comparisons and calibrations simpler. BGS (Culshaw, 2006) and publicly available sources (Charsley et al., 1990, Donnelly, 1999, Howard et al., 2010) were reviewed and sites were examined for potential stability issues. Obviously this provided no certainty that sites would indeed be stable, but meant that areas with a history of deformation and areas with higher probabilities of deformation could be avoided. These included areas with a mining history, areas on or near alluvial plains such as rivers, areas near water pumping stations and sites on recently made ground. Where possible, sites with existing foundations were favoured over sites that would require new monumentation which may have a settling period.

5.2.2.2 GPS Considerations

The main desirable criteria affecting site choice in terms of GPS are low multipath and minimal obstructions, such as open areas with a low horizon in all directions.

5.2.2.3 Site Clutter

To be unambiguously identifiable, corner reflectors should ideally be placed in areas with minimal background clutter, especially in the line of sight direction. The ground range pixel spacing of modern SAR platforms tends to be around 20m, therefore sites with a minimum clutter free radius of 50m were sought. As there were no previously acquired amplitude images available at the time, and as very few sites completely passed the 50m test, it was difficult to predict the backscattering properties of some sites and say whether a reflector would be visible or not. There was also a requirement to place at least one reflector on the University of Nottingham main campus for reasons that will become apparent below. This area has many large green spaces, but none on which a corner reflector would be tolerated: building roofs were the only choice here. In the end, a range of sites were chosen which varied from those in areas of probable low backscatter intensity, where they would almost certainly be seen, to others in more urban areas which were less certain.

5.2.3 NCRA Sites

The six chosen sites are summarised in table 5.1.

5.2.4 Reflector Modifications

Low cost, secure, permanent sites were in short supply and a means of repeatedly and precisely re-locating reflectors was sought. Three of the reflectors were modified to interface with standard OS triangulation pillars. OS pillars are part of the UK's historic geodetic monument network; they are usually constructed from concrete, 1.2m high and where possible attached to underlying bedrock or they have a substantial foundation. They have a brass 'spider' in the top with a large screw thread housing in

Station (4 fig code)	Latitude (N)	Longitude (W)	Remarks
Askerton Pillar (ASKE)	53°00'26".3821	000°48'23".3152	OS pillar
British Geological Survey (BGS1)	52°52'47".7904	001°04'49".2403	Bolted to a concrete plinth
Milford Pillar (MILF)	53°00'07".5675	001°29'07".3909	OS pillar
University 1 (UNI1)	52°56'28".84764	001°11'20".3472	Roof of the Coates building
University 2 (UNI2)	52°56'27".7419	001°11'16".8040	Roof of the L2 building
West Notts College Pillar (WNCO)	53°07'15".7116	001°11'38".8489	OS pillar

Table 5.1: NCRA Site Locations. Three locate precisely into existing OS triangulation pillars (ASKE, MILF and WNCO) and can therefore be sited temporarily as and when required (§5.2.4) whilst the other three are sited permanently (BGS1, UNI1 and UNI2).

the centre; this was originally designed to fix survey lights for night observations and provided an ideal opportunity to interface a reflector with any servicable OS pillar.

A hollow mount was designed to screw inside the light housing, inside which a modified reflector base with a locating spindle or a GPS antenna with a brass adaptor could be fitted. Figure 5.2 is a diagram of the modified reflector base and associated triangulation pillar mount. Figure 5.3 shows how a reflector or a GPS antenna interface with the pillar mount.

5.2.5 Alignment

Bhattacharyya and Sengupta (1991) state that as long as trihedral reflectors are nominally aligned in both elevation and azimuth, then the drop off in response is minimal for pointing errors of up to a few degrees. However, because of the relatively small reflector size (see §5.5.2), optimal alignment was sought in order to offer the optimum Radar Cross Section (RCS) to the radar line of sight. Good alignment also meant that a consistent backscatter signal in the radar intensity images would aid in NCRA reflector identification.

A diagram of a perfect corner reflector is shown in figure 5.4, where three mutually perpendicular lines can be defined; OA, OB and OC. These are given by the intersection of the three reflector planes, as the axes of a three-dimensional cartesian

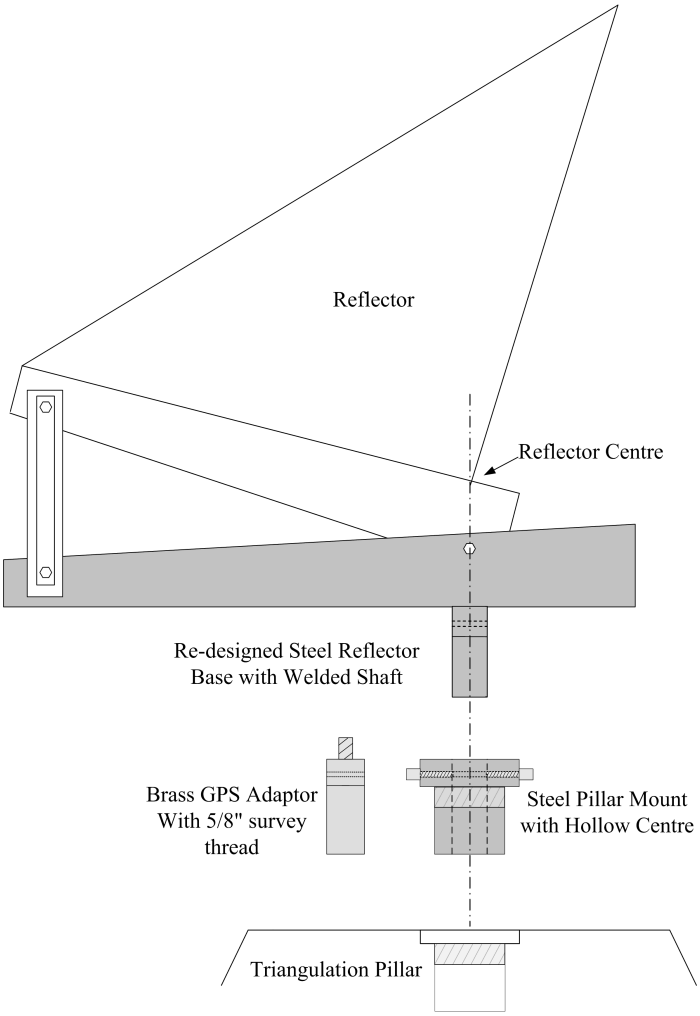

Figure 5.2: Reflector base modifications and OS pillar mount. The reflector base has been modified with a spindle that locates precisely into a mount. Alternatively, a brass insert can be placed in the mount onto which a GPS antenna can be fixed via a standard survey tribrach. The mount itself screws into any standard OS triangulation pillar.

coordinate system. The unit vector $\overrightarrow{OA}$ is defined as the vertical (z) axis, with coordinates $(0, 0, 1)$. The alignment vector $\overrightarrow{OD}$ is a unit vector given by

$$\frac{(1, 1, 1)}{\sqrt{3}} \tag{5.1}$$

and is equidistant from each axis, and should point directly at the satellite if optimal RCS is to be achieved. The angle between $\overrightarrow{OD}$ and $\overrightarrow{OA}$ is therefore given by

$$\theta = Cos^{-1}\frac{1}{\sqrt{3}} \tag{5.2}$$

Figure 5.3: The OS pillar mount. **(A)** An OS pillar with the thread exposed. **(B)** The mount fitting into an OS pillar. **(C)** A reflector with modified base in the mount. **(D)** A GPS antenna in the mount.

Thus, if the incidence angle of the satellite (with the surface normal) is α, the reflector must be tilted back by an amount of $\theta - \alpha$ to give the optimal RCS.

Subtracting the mid swath incidence angle from θ gives an angle of 31°. The NCRA reflector elevations were set (allowing for the local incidence angle) using an engineering grade clinometer. Once set they were fixed in place and checked periodically.

Horizontal alignment was computed by calculating the ellipsoidal azimuth (Vincenty, 1975) from the sensor's far to near range positions along a given range line. For descending passes, this is around 103° from true north at these latitudes. Using a Wild GAK1 Gyro theodolite attachment, suitable bearing pickets were identified at each site. These are points, which when lined up with aiming grooves cut into the base of the reflectors, ensure that horizontal reflector alignment can be repeatably

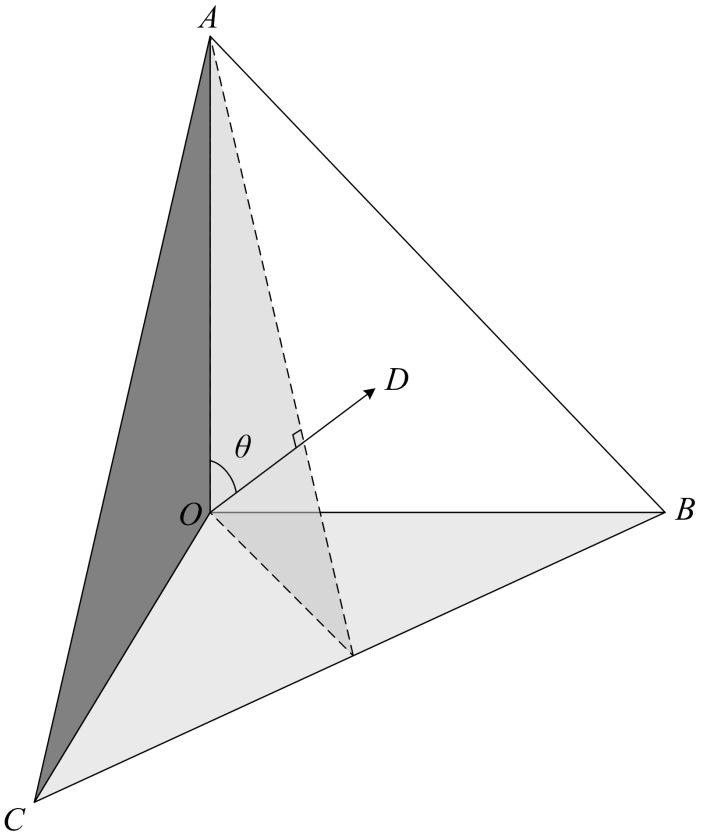

Figure 5.4: To maximise the reflector's RCS, $\overrightarrow{OD}$ should be aligned with the SAR look vector, which is defined by the local incidence angle θ. For ENVISAT, this means tilting the reflector back about 31°.

achieved to within half a degree, if care is taken. The bearing pickets usually took the form of a physical mark a few metres from the point and another on the horizon marked on a photograph. The GAK1 accuracy is around 30" of arc (Deumlich and Staiger, 2002) and therefore well within requirements.

5.2.6 Permanent Sites

At the reflector sites not involving OS pillars (BGS1, UNI1 and UNI2), the reflectors were permanently fixed to concrete structures and horizontal alignment was achieved using the Wild GAK1 Gyro theodolite. BGS1 had a 2m deep plinth of concrete sunk into a mound in the grounds of the BGS headquarters at Keyworth, Nottingham. UNI1 and UNI2 are on building roofs at University Park which is the main campus for the University of Nottingham.

5.3 SAR Data

Of the available platforms recording SAR data suitable for interferometry, ESA's ENVISAT platform was an obvious choice. Amongst others, ENVISAT carries the C-band Advanced SAR (ASAR) instrument; this can operate in several modes, the standard for interferometry being image mode which is a narrow swath configuration which defaults to VV polarisation. There was a reasonable back catalogue of ASAR data for Nottingham in this mode (fourteen images starting in November 2002). At the time the system was less than four years old and expected to continue past the end date of the project, acquiring SAR data suitable for interferometry. Hereafter, references to ENVISAT are taken to mean the ENVISAT ASAR instrument in image mode.

5.3.1 Cat-1 Project

A category-1 (Cat-1) project with ESA with Dr Andrew Sowter at the University of Nottingham as the principal investigator was established (Sowter and Leighton, 2006). Not only was this a means by which to order catalogued data, requests for future ENVISAT passes in the required mode could also be specified. Cat-1 projects are generally for academic, non-commercial use and as such are given lower priority status compared to paying commercial users. A certain amount of risk is therefore involved with Cat-1 status projects, in that spacecraft conflicts with commercial users are usually resolved in their favour. This was deemed an acceptable risk due to the following factors:

- At the time (October 2005), there existed a potential of forty acquisitions between then and the planned thesis submission date of 30 September 2009, which is a reasonable margin above the recommended thirty scenes (Ferretti et al., 2001) for a statistically valid PSI analysis.
- The recent image mode acquisition rate over Nottingham suggested that it was realistic to expect enough observations would be forthcoming.

- The cost of acquiring new ENVISAT scenes via a commercial arrangement though ESA or from a different SAR platform was prohibitive.

5.3.2 ENVISAT Pass Geometries

The AOI was overlapped by six different ENVISAT pass geometries. To prioritise these, the available archived data for each pass geometry was examined; despite the lack of reflectors in these scenes, they are useful for coherence analysis, training and acquiring preliminary PSI results. The best of these was track 366, which had fourteen archived scenes between 30 November 2002 to 19 November 2005 and within this, floating frame 2538 was chosen as Nottingham was roughly central within it. This is a descending orbit, passing over the AOI at around 10:30UTC every thirty-five days. Figures 5.5 shows the location of the entire frame and the selected subscene.

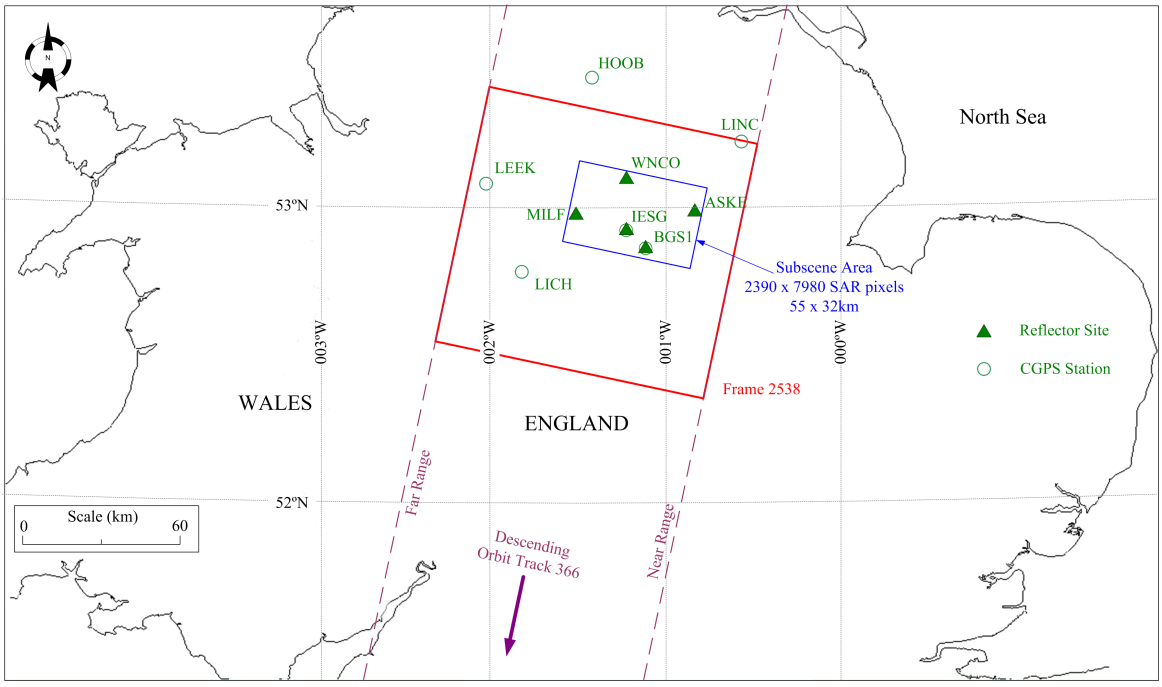

Figure 5.5: Central UK, the ASAR Frame and the AOI with selected sites. The red box shows the boundaries of floating frame 2538 in orbit track 366. The blue box shows the project AOI, with CGPS and reflector sites in green.

5.3.3 Selecting the AOI

The AOI was chosen to be large enough to incorporate the reflector sites, encompass the largest conurbations around Nottingham and encompass an area large enough for significant spatial atmospheric variability. Figure 5.6 is an enlarged version of figure 5.5. The resulting AOI is approximately 50km from near to far range and 33km in the azimuth direction. This equates to 2390 range and 1596 azimuth pixels when multilooked at a ratio of 1:5.

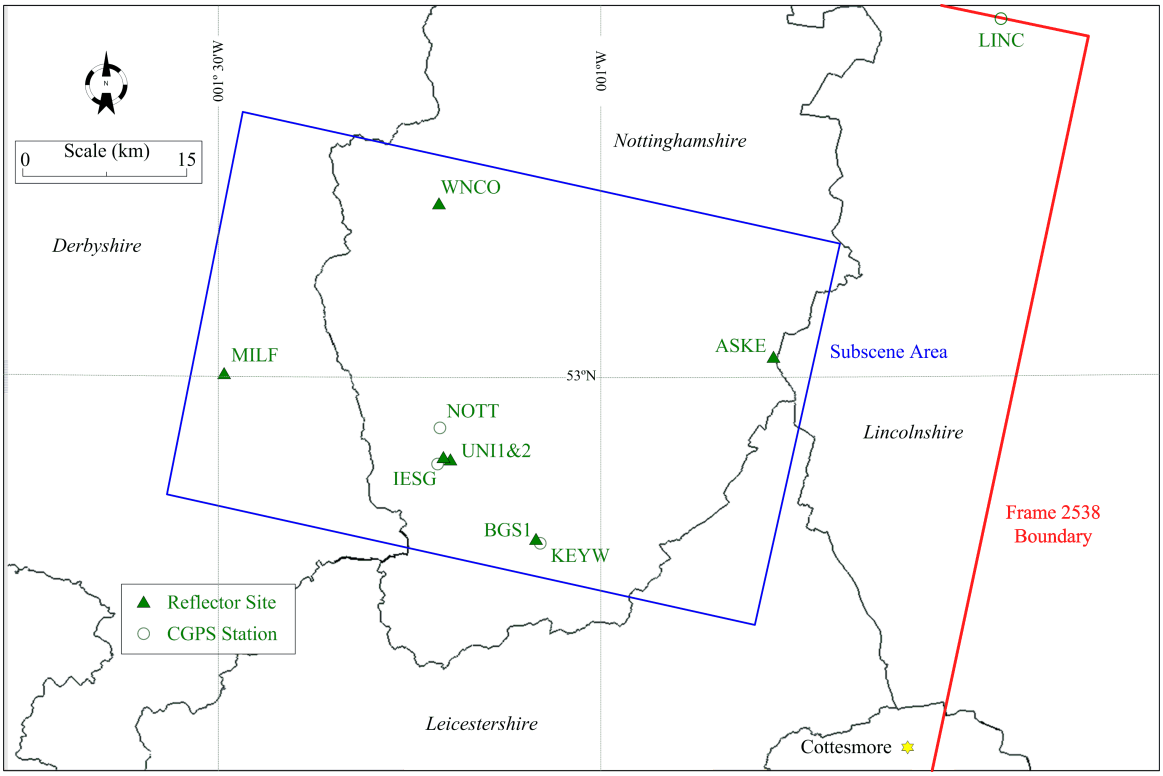

Figure 5.6: An enlarged map of figure 5.5.

5.4 Field Observation Planning

The design of the field observation campaign was mainly governed by the available resources. For any given acquisition day, two field teams of two people each were budgeted for and four dual frequency Leica SR530 geodetic GPS receivers were available. Three high quality Leica AT504 choke ring antennas were also used along with a standard Leica AT502 antenna.

Although it was not possible to conduct GPS observations at all six sites for every pass, a compromise was reached whereby the GPS receiver at BGS1 was left unmanned at their secure site, field team 1 remained static at ASKE during most passes and the second field team cycled between MILF and WNCO. The fourth GPS receiver was set up the day before the pass at either UNI1 or UNI2; because both of these reflectors were on roofs, the equipment was not set up during periods of high wind. This provided two sites with good GPS data continuity (ASKE and BGS1 - which also contained the least clutter around the reflectors) and another four with reasonable GPS time series. Whether GPS was observed or not, all six reflectors were put in place for each ENVISAT pass.

5.4.1 GPS Observation Planning

A number of decisions were required prior to observing GPS data, such as:

- Processing aims
- Session length
- Session timing

These are now discussed in turn.

5.4.2 Processing Aims

The required parameters from the GPS data were position and ZWD estimation. Whilst position is a fairly common requirement from GPS data, ZWD is not and processing choices are limited. Whether the the position is determined in a relative or non-relative sense is another fundamental choice. PPP (Zumberge et al., 1997a) offered some key advantages over relative positioning.

The parameters estimated at a ground station are not biased either by the propagation of network errors or by real motions at a base station; any unmodelled real motion in a network base station can be misinterpreted, either changing the error ellipse at the unknown station or worse, the motion may be attributed to the unknown station

(King et al., 2002). Also, because the differencing element is eliminated, the noise normally generated in this process is absent; this means any subsequent differencing necessary for comparison with InSAR data (such as between master and slave dates) ought to have a higher SNR than otherwise. Furthermore, ZWD estimates from relative processing techniques have been shown to contain biases not present in PPP results, especially with network baselines <500km (Gendt, 1998).

PPP provides direct access to a global TRF, this is because the reference frame of the results is implied by the satellite orbits rather than reference stations. When the results are required in a global TRF, this removes the need for transformation to a local frame which can introduce error.

Lastly, PPP approaches generally offer much greater control over processing than standard relative techniques, such as the incorporation of up-to-date modelling strategies. GPS Inferred Positioning System and Orbit Analysis Simulation Software II (GIPSY-OASIS II or GOA-II) V5.0 (Zumberge et al., 1997a, Webb and Zumberge, 1997, Lichten et al., 2005) was used, as this has been widely used in academic research (Larson et al., 1997, Xu et al., 2006, Brunt et al., 2010).

5.4.3 Session Length

Observation periods of twenty-four hours are common for PPP solutions because this is an obvious way to archive data from continuously operating stations. Also a twenty-four hour session encompasses cycles of diurnal length and below which allows for their mitigation or removal. Observing for 24 hour periods at the NCRA reflector sites was not usually possible as the sites were either not secure enough to leave the equipment in place or had to be loosely manned for health and safety reasons (such as UNI1 and UNI2 sited on roofs). The one exception was BGS1; this station was operated by staff at BGS and left running to observe for twenty-four hours or more. For the others, the decision to observe for a minimum of six hours was based on the fact that this was still a substantial amount of data for a static observation and it could be encompassed into a day's work from a logistical and cost point of view. Tests regarding how six hour data might impact position and ZWD values when compared to twenty-four hour data were undertaken and are discussed in the next section.

5.4.4 Session Timing

Because both GPS ZWD and position vary temporally, optimal data collection would involve GPS observations concurrent with the ENVISAT pass at around 10:30UTC every thirty-five days. However, the mount shown at figure 5.3 was designed to incorporate either the GPS antenna or the reflector, but not both, which precluded uninterrupted concurrent observations. This intentional design aspect was to avoid problems in either of the datasets; the GPS antenna altering the RCS of the reflector or the reflector creating multipath issues for the GPS antenna. This left three obvious choices:

a. Observe GPS before the pass: 04:30 to 10:30.

b. Observe GPS after the pass: 10:30 to 16:30.

c. Observe GPS either side of the pass: 07:30 to 10:25 and 10:40 to 13:45.

To evaluate these choices, tests were conducted using GPS data from six CGPS stations (HOOB, IESG, KEYW, LEEK, LINO and NOTT). Results from 24 hour sessions were compared against the three different six hour sessions mentioned above and a fourth running from 07:30 to 13:45 with no gap, to evaluate how a gap might affect results. Position values were estimated every 300 seconds from GOA-II kinematic processing and ZWD values were estimated every 300 seconds from GOA-II static processing (see §6.1 for GOA-II processing details). Note that because results were processed as kinematic solutions (to show position behaviour over a session) their accuracies are generally much lower that the static solutions computed later in this thesis (§6.4).

The ZWD values were also compared against Near RealTime (NRT) ZWD estimates processed by Dr Richard Bingley at the IESSG as part of the IESSG's contribution to the European National Meteorological Services Network (EUMETNET) GPS water vapour programme (de Haan et al., 2006); this data was only available sporadically from June 2008 onwards. The NRT ZWD estimates are produced using the previous hour's data only, as they are designed for inclusion into the constantly updated Met Office's numerical weather model. It is therefore not surprising that

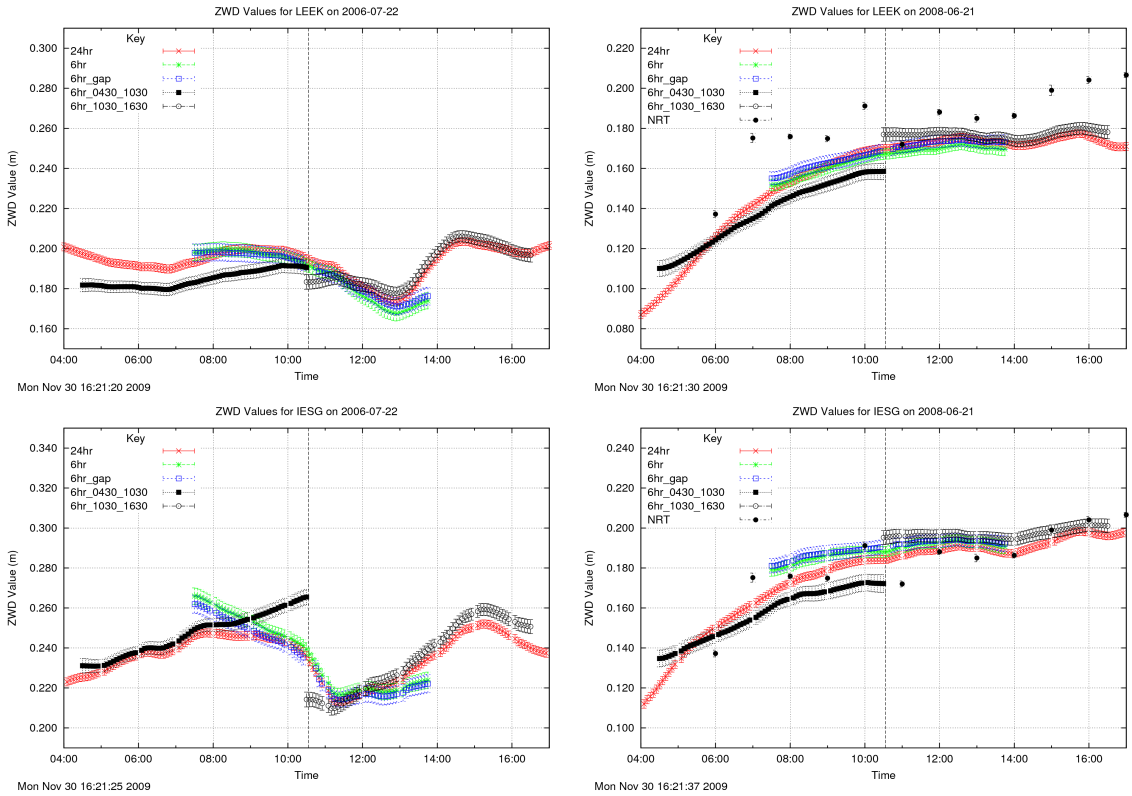

Figure 5.7: Examples of ZWD profiles for two stations on two different dates as shown in the titles. The plots compare GPS ZWD values estimated every five minutes processed using GOA-II from a twenty-four hour session (red), and four types of six hour sessions as shown. NRT ZWD are also shown in the **right** hand plots; these are only processed using the previous hours data for the Met Offices numerical weather model.

there is disagreement between the NRT estimates and the GOA-II estimates, and their inclusion was intended only as a gross error check. The GPS data was supplied by the British Isles continuous GNSS Facility (`www.bigf.ac.uk`) for thirty ENVISAT acquisition dates from 30 November 2002 onwards (where available).

Four example plots of the estimated ZWD values computed from all the various strategies and sessions for a given station on a given day are shown in figure 5.7. Figure 5.8 shows how the position estimates vary. For clarity, the position comparisons only show the 07:30 to 13:45 sessions, with (blue) and without (green) the gap against the 24 hour data (red). Separate sub plots are shown for the different position elements. The dashed line represents the ENVISAT acquisition time in both figures.

The selected ZWD processing examples in figure 5.7 show that whilst the six hour sessions behave unpredictably, the 07:30 to 13:45 sessions with and without the gap

are closer to the twenty-four hour session, especially at the acquisition time which is key here. This behaviour may be due to the modified Kalman filter used in GOA-II modelling the ZWD parameter as a random walk process (Kouba and Héroux, 2000).

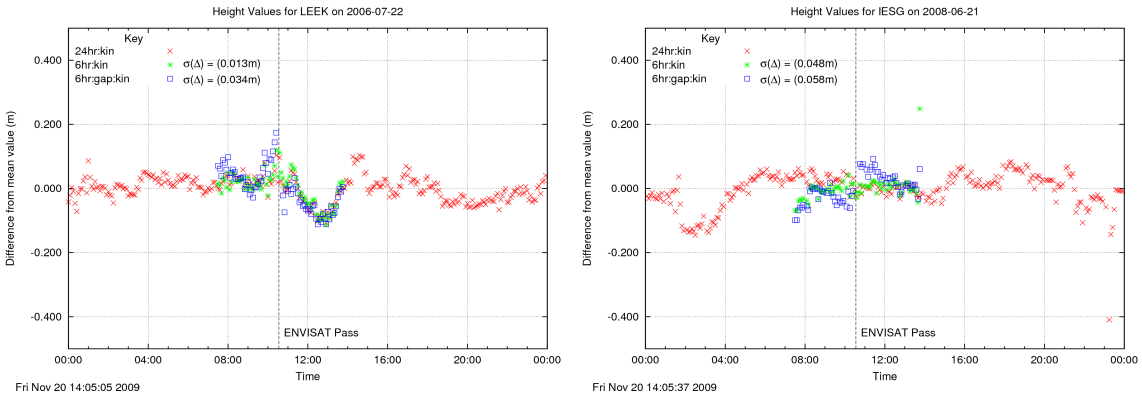

Figure 5.8: Examples of kinematic height profiles for the different processing strategies for two stations (LEEK and IESG). The six hour data sets with and without an enforced gap to simulate the ENVISAT pass are compared to twenty-four hours of data in red.

The position plots are more erratic when comparing the 24 and 6 hour sessions. In particular, the gap introduced into the six hour data can have pronounced effects. To evaluate this fully, a comparative quantitative analysis of all the ZWD and height estimates was conducted.

5.4.5 Session Test Analysis

Table 5.2 is a statistical analysis of all the ZWD and kinematic height profiles. The table contains the mean and standard deviation of differences in results for all available acquisition dates between a given six hour session and the twenty-four hour session for a given station at the time closest to the acquisition. For instance, the first column contains the statistics of the differences seen at HOOB at 10:30, between the 04:30 to 10:30 sessions and the twenty-four hour sessions. The number in brackets after the station name is the number of acquisition dates that had reliable twenty-four sessions from which to compute the means and standard deviations. The four rows per station relate to the following:

1. The mean of the differences in ZWD ($\bar{\Delta}Z$).

2. The standard deviation of the differences in the ZWD ($\sigma\Delta Z$).

3. The mean of the differences in height ($\bar{\Delta}H$).

4. The standard deviation of the differences in height ($\sigma\Delta H$).

Discussing the session columns in turn, the sessions computed before the acquisition (04:30 to 10:30) show $\bar{\Delta}Z$ values of ∼2mm and $\sigma\Delta Z$ values at around 4-6mm with one at 20mm (IESG). The $\bar{\Delta}H$ values are about 17-20mm with one of 85mm (HOOB) and $\sigma\Delta H$ values from 6-14cm with one of 34cm (HOOB). The same figures for the centred session with no gap are the best of the four sessions; $\bar{\Delta}Z < 1$mm, $\sigma\Delta Z$ ∼3-5mm, $\bar{\Delta}H$ scattered between 6mm and 9cm and $\sigma\Delta H$ ∼3-8cm except for HOOB at 40cm. The introduction of the 20 minute gap halfway through the data brings about a general increase in values; $\bar{\Delta}Z$ ∼1-3mm, $\sigma\Delta Z$ 5-10mm with one at 20mm (HOOB), $\bar{\Delta}H$ ∼2-10cm and $\sigma\Delta H$ ∼10-16cm with one at 49cm (HOOB). Figures for data after the acquisition (10:30 to 16:30) are similar in some cases, but in others worse. The increase in noise in solutions for HOOB was later shown to be linked to sporadic changes in data slip activity (§6.1.2) the source of which is unknown.

Considering the test analysis, the choices for session timing were between observing before the acquisition or centred around the acquisition and as differences between the two were not significant, the latter, logistically simpler option was chosen.

5.5 The NCRA Dataset

This next section discusses the GPS and SAR data acquired during the project. Table 5.3 summarises the acquisition dates along the top row and summarises the activity at each site.

5.5.1 Dataset Analysis

Overall, the field campaign was a success, albeit with some important caveats. Several factors had an impact on the amount of ENVISAT scenes acquired:

Station	04:30-10:30	07:30-13:30	07:30-13:30 +gap	10:30-16:30
HOOB[27] $\bar{\Delta}Z$	0.0018	0.0009	0.0022	-0.0057
HOOB $\sigma\Delta Z$	0.0068	0.0051	0.0095	0.0285
HOOB $\bar{\Delta}H$	-0.0856	-0.0997	0.0109	-0.0503
HOOB $\sigma\Delta H$	0.3418	0.3936	0.4875	0.2707
IESG[34] $\bar{\Delta}Z$	-0.0021	0.0006	-0.0033	-0.0005
IESG $\sigma\Delta Z$	0.0204	0.0030	0.0196	0.0078
IESG $\bar{\Delta}H$	0.0176	-0.0005	-0.0186	0.0141
IESG $\sigma\Delta H$	0.0811	-0.0361	0.0778	0.0750
KEYW[9] $\bar{\Delta}Z$	-0.0015	0.0002	-0.0020	-0.0037
KEYW $\sigma\Delta Z$	0.0041	0.0032	0.0059	0.0059
KEYW $\bar{\Delta}H$	-0.0187	-0.0095	0.0228	0.0226
KEYW $\sigma\Delta H$	0.0474	0.0317	0.1033	0.1072
LEEK[26] $\bar{\Delta}Z$	-0.0008	-0.0009	-0.0006	0.0005
LEEK $\sigma\Delta Z$	0.0045	0.0041	0.0048	0.0063
LEEK $\bar{\Delta}H$	-0.0048	0.0060	-0.0449	-0.0422
LEEK $\sigma\Delta H$	0.0770	0.0260	0.1380	0.1116
LINO[27] $\bar{\Delta}Z$	-0.0011	0.0006	-0.0010	-0.0005
LINO $\sigma\Delta Z$	0.0058	0.0044	0.0050	0.0058
LINO $\bar{\Delta}H$	-0.0197	-0.0069	0.0006	0.0105
LINO $\sigma\Delta H$	0.0603	0.0250	0.1061	0.0608
NOTT[23] $\bar{\Delta}Z$	-0.0020	-0.0009	-0.0014	-0.0001
NOTT $\sigma\Delta Z$	0.0060	0.0028	-0.0060	0.0062
NOTT $\bar{\Delta}H$	0.0174	0.0391	-0.0746	-0.0267
NOTT $\sigma\Delta H$	0.1498	-0.0787	0.1624	0.0487

Table 5.2: GPS profile analysis. Means of differences and standard deviations of differences (for ZWD values and height) between the six hour sessions in each column and the relevant twenty-four hour session are shown; differences and means are computed using the GPS values closest to the acquisition time (around 10:33UTC). All available ENVISAT acquisition dates are used and the number in square brackets after station names indicates how many days were available at that station. All figures shown are in metres.

- Requesting future acquisitions from ESA is not possible without an accepted Cat-1 proposal. This was submitted in November 2005 but was not accepted until February 2006.
- Spacecraft conflicts from March 2006 to February 2009 were much higher than expected; only twenty-two requests from a potential thirty-two were successful.
- New ENVISAT orbit parameters introduced after the February 2009 acquisition made the SAR data unsuitable for standard interferometry (ESA, 2010).

Station	20060304	20060408	20060513	20060617	20060722	20060826	20060930	20061104	20061209	20070113	20070217	20070324	20070428	20070602	20070707	20070811	20070915	20071020	20071124	20071229	20080202	20080308	20080412	20080517	20080621	20080726	20080830	20081004	20081108	20081213	20090117	20090221
ASKE	!	!	b	b	b	b	b	b	b	b	b	!	b	!	b	b	!	!	b	!	b	b	!	!	b	!	o	b	b	b	o	b
BGS1	!	!	-	b	b	r	r	b	b	b	b	!	b	!	b	b	!	!	r	!	b	b	!	!	b	!	r	r	b	b	b	b
MILF	!	!	b	b	b	b	r	b	r	r	r	!	r	!	r	r	!	!	r	!	b	o	!	!	b	!	o	r	b	o	r	b
UNI1	!	!	r	r	r	r	b	r	b	r	b	!	r	!	r	b	!	!	b	!	r	b	!	!	r	!	r	r	r	r	r	r
UNI2	!	!	-	-	-	-	-	r	b	r	b	!	r	!	r	b	!	!	b	!	b	r	!	!	b	!	r	r	r	r	r	r
WNCO	!	!	r	r	r	r	b	r	r	b	r	!	b	!	r	r	!	!	r	!	r	b	!	!	o	!	o	b	r	b	r	o

Table 5.3: Reflector sites and ASAR acquisition dates. Key: '-' reflector not yet established, '!' spacecraft conflict, 'b' both GPS and reflector observations, 'r' reflector observations only, 'o' no observations.

These three factors meant that from a total of forty potential acquisitions, only twenty-two were acquired. The implications of this are discussed below in §5.7.

It is worth noting here that the design of the pillar mount (§5.2.4) proved to be very successful. For each occupation, the height of the reflector above the pillar was measured and found to vary less than 1mm for any of the sites. Furthermore, the GPS antenna heights were measured four times for each of the acquisition days at the non-permanent sites (at the beginning, at the end and either side of the ENVISAT pass), remembering of course that the GPS antenna had to be removed prior to the ENVISAT pass and then re-established afterwards. Special procedures were put in place whereby the GPS tribrach would only require very minimal adjustment, and this resulted in better antenna height precision than at the permanent reflector sites requiring a tripod for the GPS antenna.

5.5.2 Site Visibility

Because of the logistical reasons mentioned, the passive trihedral reflectors chosen for the experiment were smaller than any used with published ENVISAT research before and are comparable to the smallest reflectors used in any openly published SAR corner reflector research. With an RCS of 135.8m^2, it was apparent at the start of the project that it might be some time before enough acquisitions were available to unambiguously say whether the reflectors were definitely visible. During the site selection process it was clear that ASKE and BGS1 both have minimal clutter within a 50m radius. MILF has similar characteristics, except for ground sloping away steeply towards the look direction which had the potential to give foreshortening issues. WNCO has between 25 and 50m with very little clutter, after which there are several large potential scatterers. UNI1 and UNI2 are both in the University campus science park on building roofs. These reflectors both posed serious challenges as the possibility of them being dominant was limited. Furthermore, shortly after the siting of UNI1, several air conditioning units were installed next to it which exacerbated matters and after siting UNI2, building work commenced on the construction of a new office block within 30m of the reflector. This does not obstruct the line of sight but complicates the identification of the reflector in the intensity image.

To compute the location of the reflectors in the intensity images, the GPS results of the reflector positions were transformed to RDC using the polynomial determined when resampling the SRTM DEM to RDC during PSI processing (§6.2.2.4). Using table 5.3, six averages (one per site) of the intensity images were created; these were optimised by site as certain reflectors only appear in certain images. The thirteen acquisitions that took place prior to any reflector deployment were also averaged and a reflector visibility analysis was undertaken using the before and after averaged intensities.

As corner reflectors in SAR images produce a Sine Cardinal (SinC) signal pattern, this is the most appropriate interpolator to analyse the target responses (Jerri, 1977). 16 x 16 pixel grids of the sites cropped from the intensity images, with the estimated reflector position in the centre, were SinC interpolated by a factor of 8 by means of a

zero-padded inverse Fourier transform as shown in figure 5.9.

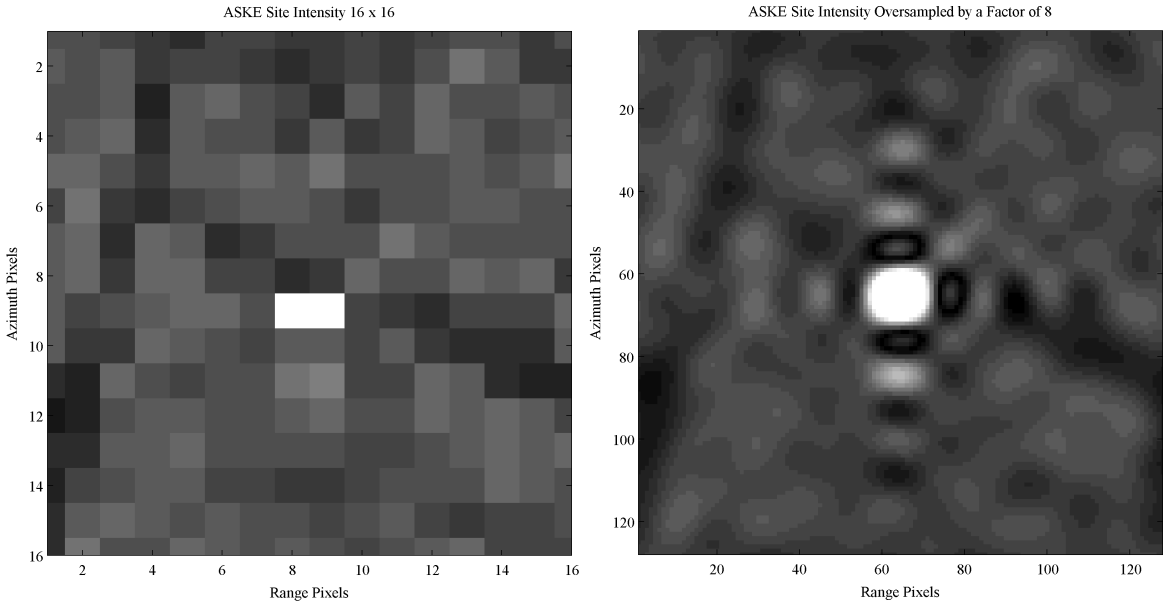

Figure 5.9: SinC interpolation of corner reflector sites. A 16 x 16 pixel area centred on ASKE (**left**) is SinC interpolated by a factor of 8 by means of a zero-padded inverse Fourier transform (**right**).

The different sites were analysed using this method alongside the 'dark', pre-reflector intensity. Figure 5.10 shows the various sites with their before and after intensities along with 3D plots of the SinC function responses.

Stations ASKE and BGS1 both have strong SinC related responses along with unambiguous before and after averaged intensity images. MILF and WNCO are less certain, but do show amplitude spikes at the correct locations that did not exist before although the SinC responses from both of these reflectors are cluttered. UNI1 and 2 also show higher than before intensity values at the correct locations, but in both cases, this may be due to nearby changes to the area mentioned above. Furthermore, their SinC responses are both extremely noisy and therefore visibility of these two sites is uncertain.

5.6 Existing PSI Results and Levelling

A separate, commercial PSI result was commissioned by BGS using 117 scenes of ERS data, all of which dates before the ENVISAT data (1993-1999). Because of

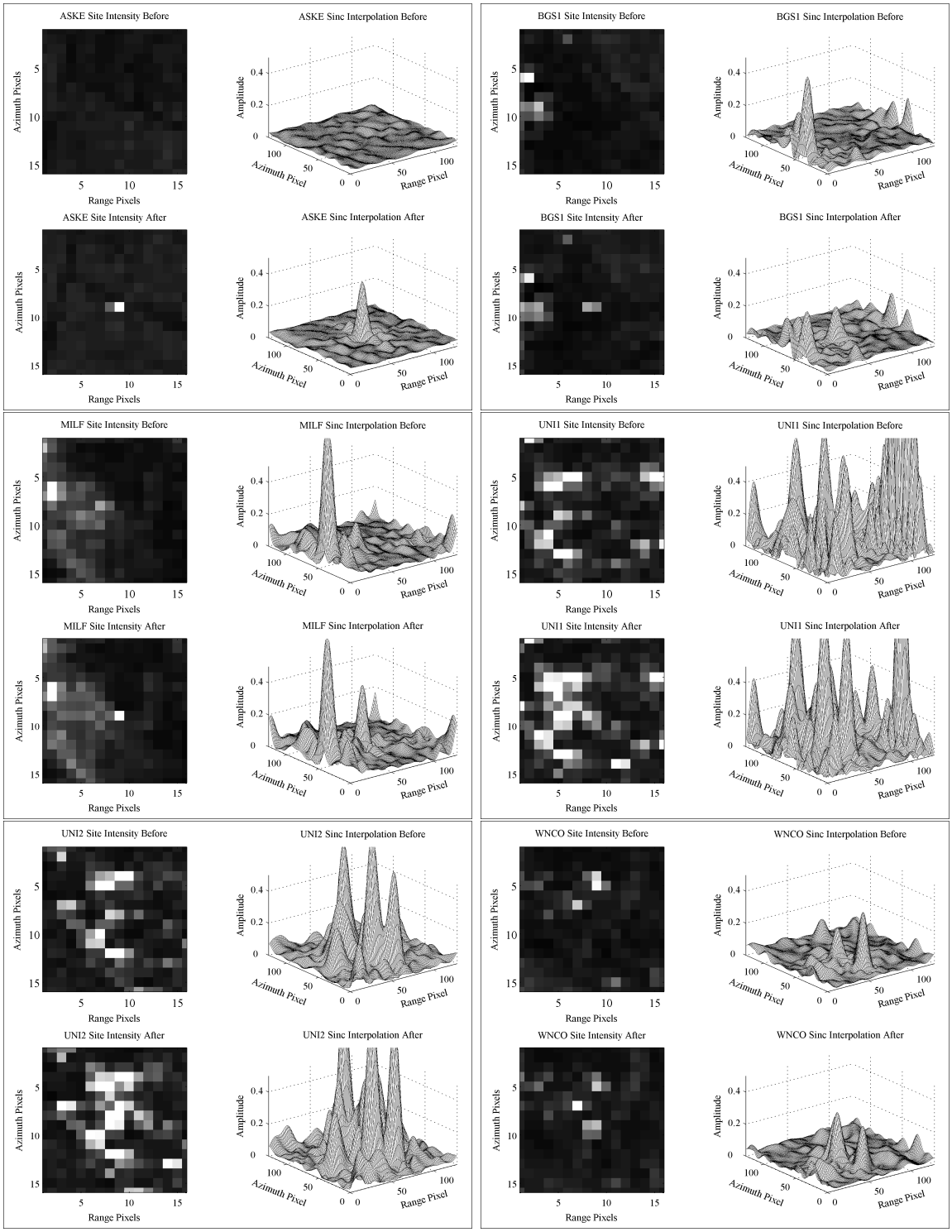

Figure 5.10: Before and after 16 x 16 averaged amplitudes are shown for each reflector site. The corresponding SinC interpolations are plotted alongside in three dimensions. Some sites clearly show responses that are related to the reflector whilst others are more ambiguous.

its commercial sensitivity, the results cannot be shown here or discussed at length. However, through private communication with BGS, specific areas of Hucknall were highlighted as area of potential motion. Because of this, it was decided to undertake a one year precise levelling campaign between August 2007 and August 2008. The aim was to determine the relative motion between a point outside of the deforming area and a point in the centre of the deforming area. This can then be used as a comparison against the PSI results generated in this project.

5.7 Implications of the Reduced Dataset

Only twenty-two scenes were acquired with the reflectors present, this is normally seen as an insufficient quantity of images with which to conduct a robust PSI analysis (Ferretti et al., 2001, Mora et al., 2003). The archived ENVISAT data together with the twenty-two scenes collected during the field campaign comprises a total of thirty-six scenes.

In order to ascertain the consequences of a reduced stack using the IPTA method, two test PSI analyses were conducted; one using the twenty-two scene stack (stack A) and the other the thirty-six scene stack (stack B). As expected, the reflectors in stack A show as persistent scatterers (candidate and confirmed) whilst in stack B they do not. However, many aspects of the results for stack A caused concern; the deformation rate uncertainties were much higher and in some cases PSI points for the different stacks show phase histories in opposite directions. Because of these and other factors, it was decided to abandon the idea of a PSI stack containing only images with reflectors present, and instead incorporate the fourteen archived scenes.

Using the augmented thirty-six scene stack, opportunities for novel research still existed which satisfy the aims and objectives. These are now stated as follows:

- Compute absolute ZWD values for all available GPS stations inside and surrounding the NCRA using PPP techniques.
- Examine the correlation between ZWD values and APSs.

- Interpolate ZWD screens of the AOI for ENVISAT acquisition dates and map values to the radar line of sight.
- Use ZWD screens to augment a PSI analysis.
- Conduct comparisons between PSI results with and without ZWD screens and also against GPS and levelling data.

5.8 Summary

The NCRA was successfully established, consisting of both episodic and permanent corner reflectors sites. A Cat-1 proposal was submitted and accepted around which an observation programme was devised based on a robust analysis of test data. Observations were conducted at the reflector sites from May 2006 to February 2009. Through analysis of before and after SinC responses of the reflector sites, the submetre reflectors used in the NCRA are unambiguously visible in ENVISAT ASAR data in areas of sufficiently low backscatter intensity. Despite lost acquisitions due to spacecraft conflicts or other reasons, a strategy involving novel integration of GPS and InSAR was devised which fulfils the project's aims and objectives.

Chapter 6

Methodology and Results

This chapter presents the processing methodologies used to process the GPS and SAR datasets. The results of both are then presented, drawing attention to their respective quality. As well as their internal consistency, the datasets are also compared to other sources or information wherever possible. The methodology and results of the precise levelling campaign are also presented. Finally, the PSI and GPS datasets are compared with each other which naturally leads into the next chapter.

6.1 GPS Data Processing

6.1.1 Overview

As discussed in chapter 5, GPS data was collected at reflector sites episodically by field teams and obtained from CGPS stations within or close to the AOI (supplied by the The British Isles continuous GNSS Facility (BIGF): `www.bigf.ac.uk`). Unless otherwise stated, GPS position estimates were resolved using an undifferenced PPP approach whereby receiver parameters, such as the receiver clock, are solved or mitigated through modelling rather than being differenced away. Precise orbit and clock products computed from a globally distributed network are used to assist in this process. PPP processing was conducted using GOA-II which is a Linux suite of command line programs written by JPL. Interested readers are referred to Zumberge et al. (1997a), Webb and Zumberge (1997), Gregorius (1996) and Lichten et al. (2005).

As well as PPP processing, pre and post processing checks were used to monitor the integrity of the data and of the results. The various stages of the GPS processing strategy are now reviewed in detail.

6.1.2 Pre-Processing Checks

It was noted repeatedly that the PPP process is very sensitive to noisy data. Therefore, prior to PPP analysis, a thorough set of pre-processing checks were conducted on all GPS data. TEQC (see §2.8.2.1) was used to conduct this (Estey and Meertens, 1999) which is widely used in the GPS community, including the IGS who conduct daily quality control checks using TEQC on all their stations (`http://igscb.jpl.nasa.gov/network/list.html`). Pre-processing involved the following steps:

- Convert all data to the Receiver Independent Exchange (RINEX) format
- Check header information and correct where necessary
- Crop files to within the acquisition calendar day
- Reject files with less than 80% of the expected observations
- Analyse P-code multipath RMS values
- Assess data for cycle slips

Figures 6.1 and 6.2 show two sub-plots per station for NCRA GPS stations and CGPS stations respectively. Each data point represents a GPS session that coincides with an ENVISAT pass over the AOI. The bottom plots show three sets of superimposed data; red and blue circles are the RMS values of the de-trended estimates of the P-code multipath on the two GPS carrier signals L1 and L2 respectively (MP1 and MP2), the green circles represent the amount of data slips per 1000 observations (approximately four hours of data). Data slips here are defined as either a slip in the ionospheric delay observable or a slip on both MP1 and MP2 occurring during the same epoch (Estey and Meertens, 1999). The top plots show the ratio of the amount of collected data over the amount of expected data expressed as a percentage. The

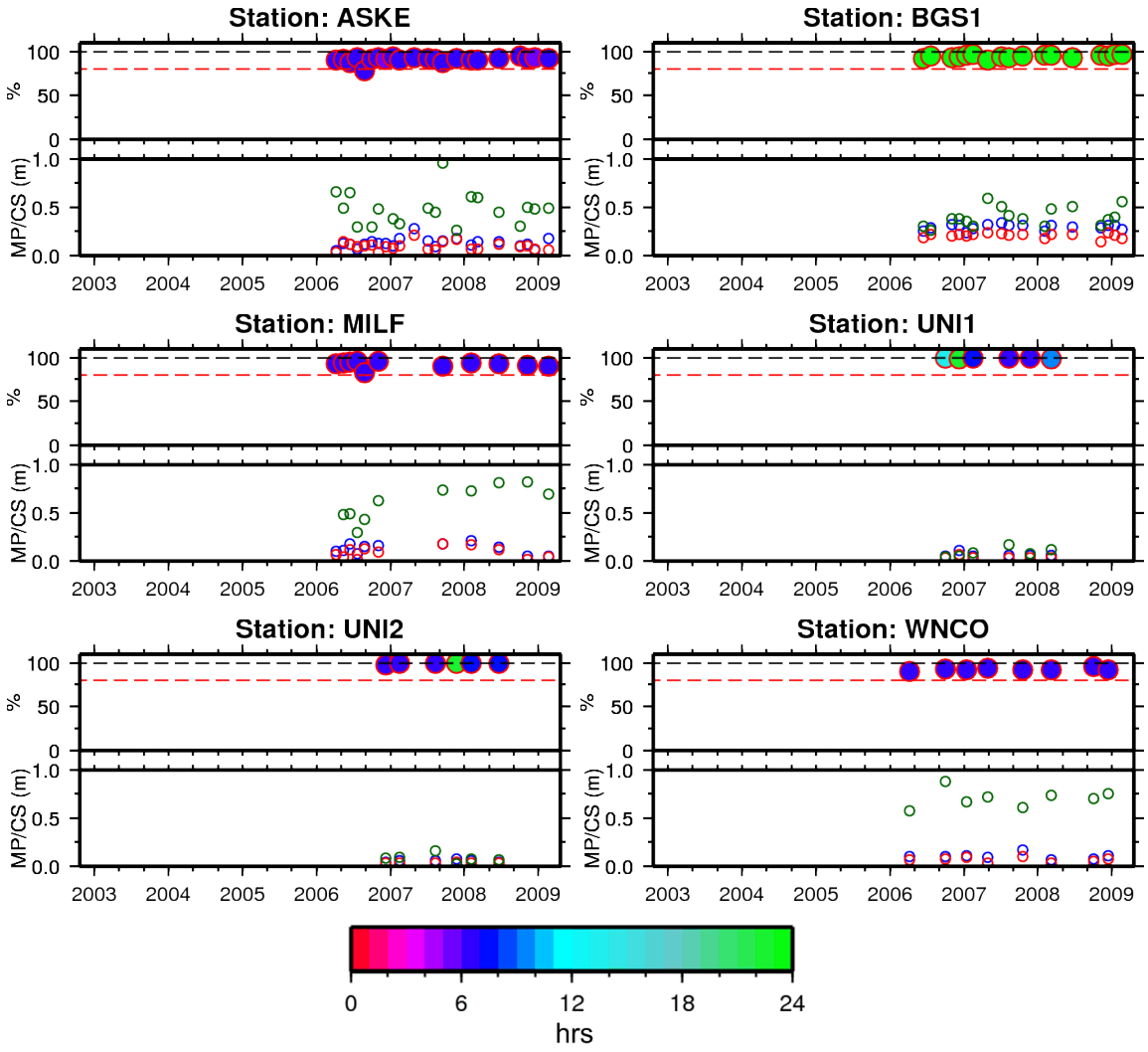

Figure 6.1: GPS Pre-processing checks for NCRA Stations. Each data point represents an ENVISAT acquisition day. In the bottom plots for each station, red and blue circles are the RMS values of the L1 and L2 multipath estimates. Green circles represent data slips/1000 observations. The top plots show the ratio collected over expected data expressed as a percentage. The red hashed line is the 80% cut-off below which sessions were rejected; circle fill relates to session length as indicated by the scale bar at the bottom of the figure.

red hashed line is the 80% cut-off below which sessions were omitted from further processing. The colour of the circles in the top plots represents the session length, as per the scale bars at the bottom of each figure.

The most important information is the multipath estimates and the percentages. As shown, CGPS stations NOTT and LICF had several days worth of data rejected. NOTT shows above average noise in its continuous daily time series (§6.10) when compared to other UK OS sites, which may go some way to explaining why the

station was abandoned in 2007 and replaced with KEYW.

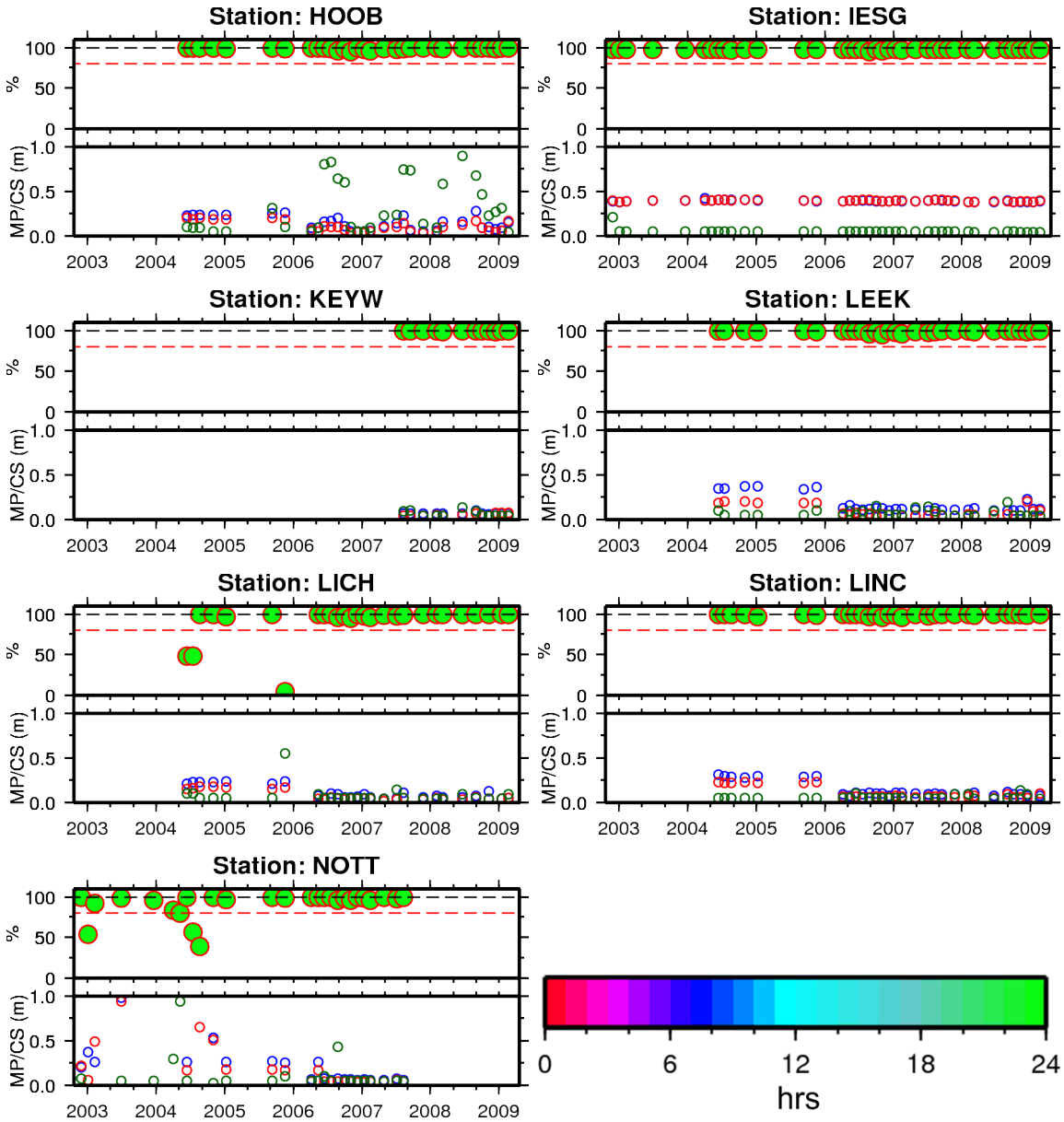

Figure 6.2: GPS Pre-processing checks for CGPS Stations. Each data point represents an ENVISAT acquisition day. In the bottom plots for each station, red and blue circles are the RMS values of the L1 and L2 multipath estimates. Green circles represent data slips/1000 observations. The top plots show the ratio collected over expected data expressed as a percentage. The red hashed line is the 80% cut-off below which sessions were rejected; circle fill relates to session length as indicated by the scale bar at the bottom right of the figure.

IESG has slightly elevated MP2 values, which whilst odd, was not considered a major concern. In general, changes in station behaviour are regarded as more of an issue than the values themselves (Teferle, 2003). A sudden jump in multipath or

observation ratio might indicate new sources of noise warranting site investigation.

Apart from rejecting sessions with less than 80% of their expected data, no other action was taken at this stage. As is usually the case with GPS time series, these results were used to investigate issues further along the processing chain.

6.1.3 A Priori Position Estimates

A priori station positions are required to seed PPP processing. Although station estimates are present in the session headers, these tend to be navigation quality only for unknown stations such as those in the NCRA. Here, double difference carrier phase solutions were estimated using Leica Geo Office; the five nearest CGPS stations were used as control. IGS final product precise orbits were used and the maximum baseline was ∼76km. Accumulated position estimates for each station with respect to ETRS89 were averaged. For the CGPS stations, the published geodetic quality coordinates (`http://www.ordnancesurvey.co.uk/oswebsite/gps/`) were used as the a priori position estimates. Any difference between ETRS89 and ITRF05 for these purposes was considered insignificant.

6.1.4 PPP Processing

The PPP approach (Zumberge et al., 1997a) is a means of deriving high accuracy positioning based on the data from a single receiver. As opposed to relative positioning, which eliminates parameters such as the receiver clock through differencing, PPP treats these as unknowns and they are estimated using a statistical model. The model used in GOA-II utilises the SRIF (Blewitt, 1993), which is a modified Kalman filter.

Solutions are computed in three main steps:

- Fit the satellite positions from the precise orbits files to the orbit model using the associated Earth Rotation Parameters (ERPs).
- Pre-process the clocks and RINEX observations to detect and eliminate clock jumps and cycle slips.

- Reduce data with iterative post-fit cleaning to examine carrier phase and code data for outliers.

Various models are incorporated into this process. The sections below describe the models and augmentation data chosen for this processing strategy. Particular attention is paid to details which set this strategy aside from the standard PPP processing methodology. See §2.8 for a wider discussion of PPP theory.

6.1.4.1 Orbits and Clocks

Orbit and clock products provided by JPL are derived from a globally distributed network of GNSS stations known as the FLINN network (NASA, 1991), which is a subset of the IGS network. Unlike other IGS stations, FLINN stations are often equipped with a hydrogen maser clock or a good quality rubidium or caesium clock; this provides a very stable time reference which is useful when estimating satellite clock corrections (Capra and Dietrich, 2008).

Standard fiducial orbits that are used to constrain terrestrial observations automatically imply the TRF of the orbit onto the station solutions. However, as well as these standard products, JPL also offer non-fiducial (or fiducial free) orbits (Heflin et al., 1992) which were used for PPP processing for this work (final products in all cases). When producing non-fiducial orbits, the FLINN network is largely unconstrained; this means that the relative geometry of the orbits is determined by the GPS data alone and the orbits are therefore not perturbed by any imperfect knowledge of the ground stations (Panafidina and Malkin, 2001). Once solutions are obtained, a daily transformation file (X-file), also produced by JPL, is used to remove the uncertainty in the solutions and express them in ITRF05.

In December 2009, JPL retrospectively reprocessed FLINN fiducial and non-fiducial orbits and clocks from 1996 to 2009; this was part of a wider strategy to incorporate the latest models and product formats into historic JPL products (Desai, 2009). Daily median orbit accuracies improved from 5.4 to 3.2cm and the average variance reduction was 65% (ibid).

6.1.4.2 Absolute Antenna Phase Centre Corrections

On 5 November 2006 (GPS week 1400), the IGS 2005 (IGS05) TRF was introduced (`http://igscb.jpl.nasa.gov/network/refframe.html`), realised from a subset of 132 high quality IGS stations. IGS05 stations adopted various strict conventions including a consistent strategy for PCOs and PCVs for receiver and satellite antennas (Schmid et al., 2007). IGS05 is the basis for the realisation of the ITRF05 and therefore for consistency, IGS05 antenna PCOs and PCVs were adopted for all stations and satellites used in this study (Kouba, 2009a).

Consistency is also maintained for data collected prior to 5 November 2006 as JPL reprocessed orbit and clock products from 1996 to 2009 using the IGS05 absolute phase centre strategy (Desai, 2009).

6.1.4.3 Solid Earth Tides

Vertical and horizontal displacements of the solid Earth due to gravitational attractions from celestial bodies is accounted for using the Wahr model (Wahr, 1981) which was incorporated into the PPP processing strategy. This is a description of how the tidal coefficients known as the Love numbers and the Shida number vary with latitude and tidal frequency. Interested readers should refer to Bomford (1980) and McCarthy and Petit (2003).

6.1.4.4 Polar Tides

In order to maintain consistency with the way in which the orbit and clock products are computed, changes in the Earth's spin axis are accounted for using polar tide corrections; that is, these corrections must be subtracted from the position solutions in order to be consistent with ITRF (McCarthy and Petit, 2003).

6.1.4.5 Ocean Tides

OTL coefficients were explicitly computed for all sites in the network using the Finite Element Solution 1999 (FES99) model. This is based on the resolution of the tidal barotropic equations on a global finite element grid which has been improved with

the assimilation of 700 tide gauges and 687 TOPEX/Poseidon altimeter measurements (Lefevre et al., 2002). This data was provided pre-formatted via M.S. Bos' and H.G. Scherneck's OTL provider website (`www.oso.chalmers.se/~loading`). The choice of model was influenced by Penna et al. (2005), which described inconsistencies in later models when changes in processing strategy occurred in August 2007. FES99 was not corrected for the centre of mass motion of the Earth due to ocean tides for consistency, as FLINN orbits are not computed in this way either.

6.1.4.6 Hydrostatic Troposphere Mapping

VMF1 was used to map the hydrostatic estimates of the troposphere to zenith. VMF1 utilises forty years of empirical data from the ECMWF and, unlike its predecessors, it is date and latitude dependent. Implementation of VMF1 at Very Long Baseline Interferometry (VLBI) stations has been shown to yield improvements in baseline repeatabilities (Boehm et al., 2006b).

6.1.5 Post-Processing Checks

The Automatic Precise Positioning Service (APPS) is a means of obtaining a PPP result through an internet interface; this is operated and maintained by JPL (`apps.gdgps.net`) and was formerly known as Auto-GIPSY. This service was used periodically to assess the validity of GOA-II results during the learning and testing stages.

6.1.6 Tropospheric Zenith Delay Estimates

A main requirement of the PPP results was the estimation of ZWD values. ZWD estimates can be derived from GOA-II processing which usually uses an assumed atmospheric model to remove the ZHD. In this case however, hourly mean sea level pressure data from the UK's Met Office were used to compute the station ZHD estimates making the resulting ZWD estimates more realistic (Kouba, 2009a).

ZHD values for the time of the ENVISAT pass were computed using hourly pressure values from the UK Met Office (when available) for a number of met stations in the area; as the ENVISAT pass occurred around 10:30 UTC, the 10:00 and 11:00

estimates were averaged. An examination of the pressure values from different met stations revealed how little pressure varied over the AOI (between 0.1 and 0.6mb over a distance of ∼28km between Watnall and Cranwell met stations on any particular day). ZHD at a GPS station was therefore computed by identifying the nearest met station and scaling the pressure by the height difference between the GPS and the met stations through application of the relationship identified by Saastamoinen (1972) which assumes smoothly decreasing pressure with height:

$$ZHD = P \cdot 0.00227 \cdot e^{(-0.000116 \cdot h)} \tag{6.1}$$

where P is the pressure of the met station at mean sea level, and h is orthometric height of the GPS station. Geoid separation values were accounted for as Met Office pressure values are referenced to mean sea level whereas GPS heights are referenced to the Geodetic Reference System 1980 (GRS80) ellipsoid.

The ZWD estimates are determined as a parameter in the SRIF. ZWD values were estimated every 300 seconds with the final FLINN non-fiducial products held fixed. After one full estimation of station coordinates, ZWDs and station biases, the process is iterated using the output from the previous run. Convergence occurs after two to three iterations.

6.2 SAR Data Processing

As discussed in previous chapters, a suitable site was identified to satisfy the aims and objectives laid out in §1.6. Twenty-two ENVISAT ASAR scenes were acquired for this site over a period of three years (13 May 2006 to 21 February 2009), see table 5.3. Along with an archived dataset of fourteen scenes, the entire Nottingham stack therefore consists of thirty-six scenes running from 30 November 2002 to 21 February 2009. This next section describes the processing chain involved to obtain the fully formed PSI results from the SLC data (ESA data designation: ASA_IMS_1P).

6.2.1 Overview

The processing strategy firstly involved choosing a master scene for coregistration purposes, cropping it to the AOI and resampling a DEM covering this area into SAR geometry. Slave images were then coregistered and cropped to the same area. Multi-reference interferograms were then created and stacked. The stacking result was used to yield early indications of likely areas of motion in the AOI and to aid in precise baseline estimation as discussed in §6.2.2.6.

Candidate PS points were then selected in the coregistered SLC images and interferograms were formed between a chosen interferometry master scene and the slave scenes. Using the SRTM DEM, differential interferograms were created followed by a quality control check of the candidate PS points. A reference PS point was then selected followed by an iterative process to estimate optimal height corrections, deformation estimates, baseline parameters, and residual phases from the differential interferograms. PSI processing was conducted using modules of the Gamma software (Werner et al., 2003) which is a suite of command line programs designed to run on a Linux platform.

6.2.2 PSI Preparation

PSI preparation is defined here as steps required prior to PS candidate point selection. The raw ASAR data was pre-processed into SLC format by the Italian Processing and Archiving Facility (IPAF) at Matera and supplied by ESA through Cat-1 proposal 3518 (Sowter and Leighton, 2006).

6.2.2.1 Calibration

ESA ASAR external calibration files (ASA_XCA files: `http://envisat.esa.int/services/auxiliary_data/asar/`) were used to determine the platform parameters and to assist with radiometric calibration (Levrini and Zink, 2002). The main calibration steps were:

- Range spreading loss correction.

- Antenna gain correction.
- Normalization reference area correction.
- Absolute calibration using the calibration constant.

6.2.2.2 Orbits

ESA final delivery orbits based on SLR and DORIS observations were obtained and used throughout the processing stages (`ftp://diss-nas-fp.eo.esa.int/vor` through a pre-arranged account). The absolute accuracy of these products is thought to be around 10cm with a radial orbit error of 3cm (Otten and Boomkamp, 2004). The option of using Delft processed EIGEN-CG03C orbits was considered, but these were not available for the whole period.

6.2.2.3 Baselines

A perpendicular baselines chart computed with respect to the reference date of 17 Jun 2006 is shown in figure 6.3.

6.2.2.4 DEM Preparation

The 90m SRTM DEM (Jordan et al., 1996) was used to create the topographic phase. The 1 degree x 1 degree tiles that covered the AOI were mosaicked, re-projected to Universal Transverse Mercator (UTM) and oversampled to a pixel spacing of 10m; this is so the pixel sizes of the respective geometries are roughly the same which reduces gaps when interpolating. The transformation to UTM is useful later as it provides a means of presenting results in a meaningful reference frame. The 10m UTM DEM was then geocoded into RDC using the method stated in Wegmüller (1999), the resampling method used was nearest neighbour.

Initially, the DEM was first transformed to RDC using the orbits. Then a lookup table was iteratively refined between a pre-cropped SLC coregistration master and the DEM using cross-correlation and the estimation of a third order transformation polynomial; to aid coregistration a version of the DEM was created as though observed from SAR look geometry (ibid). Following this the DEM data was resampled to the

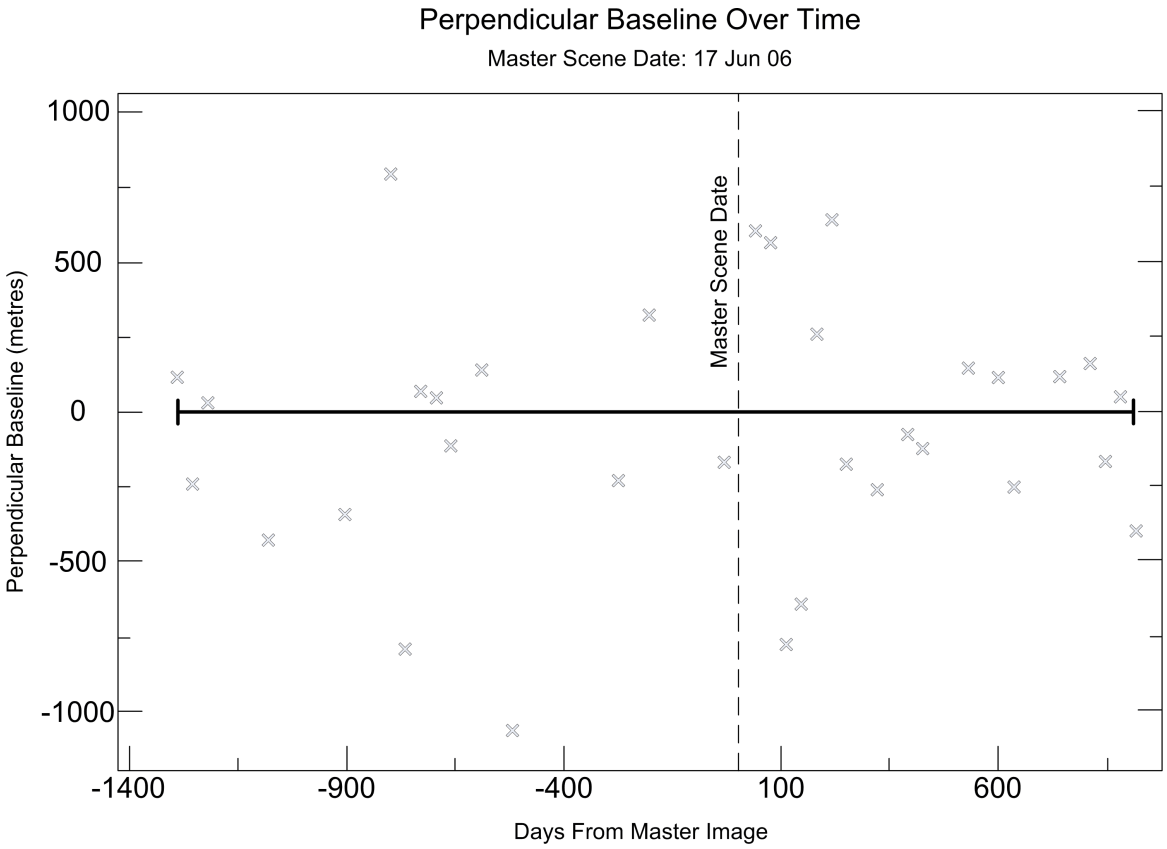

Figure 6.3: Perpendicular baseline chart. Crosses mark each ENVISAT acquisition in time and in terms of its perpendicular baseline with respect to the reference date of 17 Jun 2006.

geometry of the master. The end product is a DEM in RDC (RDC DEM) with a pixel spacing equivalent to that of the coregistration master. The reported cross-correlation offsets between the RDC DEM and the master at the end of the process were <0.01 pixels.

6.2.2.5 Slave Scene Coregistration

The slave scenes were coregistered using the lookup table process described above, except that the RDC DEM itself was used to correct for terrain effects. This was first conducted at 1:5 multilooked resolution followed by a refinement involving full resolution; SinC interpolation is used as the interpolation algorithm. The averaged multi-looked intensity image from all thirty-six scenes was created for displaying results; this can be seen alongside the master multi-looked intensity image in figure 6.4.

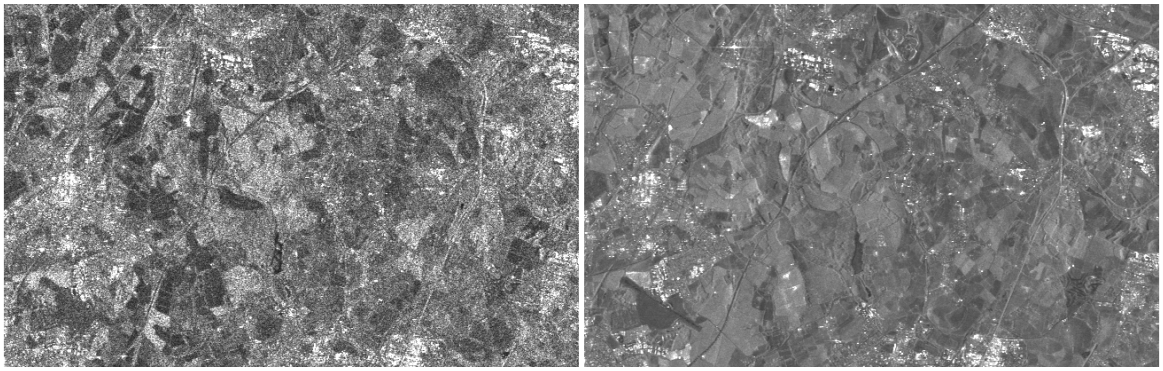

Figure 6.4: A section of the master multi-looked intensity image **(left)** and the averaged multi-looked intensity image from thirty-six coregistered scenes **right**.

6.2.2.6 Stacking

Stacking is a means of averaging multiple interferograms of the same areas to estimate linear displacement rates; the averaging improves the ratio between the differential phase and the atmospheric error, assuming that the atmospheric statistics are stationary from one observation to the next (Wegmüller et al., 2000). The stacking result prior to PSI processing was useful for the following reasons:

- Adjusting the AOI. Prior knowledge of linear deformation rates across a wide area means that the PSI process can operate in a more focused manner.
- As an a priori deformation rate for the PSI process.
- Reference point selection. Selecting a PSI reference point in an area with no deformation motion or at least estimated deformation makes relative deformation estimates more meaningful.
- Baseline modelling. Linear trends in the atmospheric phases or deformation signals can be absorbed by poorly modeled baselines. The stacking result is used here to omit unstable points from the Ground Control Point (GCP) selection process (see below) in the baseline refinement

To create the stacking result, differential interferograms were created by subtracting the topographic phase scaled by the baselines from each of the sixty-four multi-reference SLC pairs with $B_\perp$ values less than 200m and B_T values less than 500 days;

baselines were estimated from precise orbits. The differential interferograms were then adaptively filtered based on their individual power spectra using the algorithm developed by Goldstein and Werner (1998), this vastly reduced the number of phase residues and consequently subsequent phase unwrapping was far more successful with this step.

Phase unwrapping of the filtered differential interferograms was conducted using the Minimum Cost Flow approach (MCF) (Costantini, 1998) tied to a Delaunay triangulation network (Bern and Eppstein, 1992); the integration of these two strategies was achieved by Werner et al. (2002). The MCF process seeks to minimize the total cost of phase discontinuities. The process was weighted using coherence values which dictate where discontinuities ought to and ought not to occur.

Using the unwrapped phase, improved baselines were then estimated using Ground Control Points (GCPs). The GCP list of 2304 points were compiled from a mixture of the GPS stations, known survey marks (both transformed to RDC using the lookup table mentioned in §6.2.2.4) and automatically selected GCPs from the RDC DEM. Corresponding unwrapped interferometric phase values were then extracted for the GCP locations, permitting estimates of baseline parameters using a non-linear Single Value Decomposition (SVD) method (Wegmüller and Werner, 1997). Analysis of the resulting quality parameters showed that the technique was poor at estimating short baselines due to their low fringe rate; only pairs with $B_{\perp}$ >30m were therefore used.

The improved baselines were then used to recreate the differential interferograms, adaptively filter them and unwrap them. The unwrapped differential interferograms were then stacked using the method stated in Strozzi et al. (2000) and line of sight deformation rates in millimetres per year were estimated. The deformation rates estimated from stacking along side an image of the standard deviation of the deformation rates with respect to a reference pixel can be seen in figure 6.5. The reference pixel was chosen because it was phase stable and because it was very close to the IESG CGPS station which has an eleven year time series describing no significant vertical motion (§6.4.1).

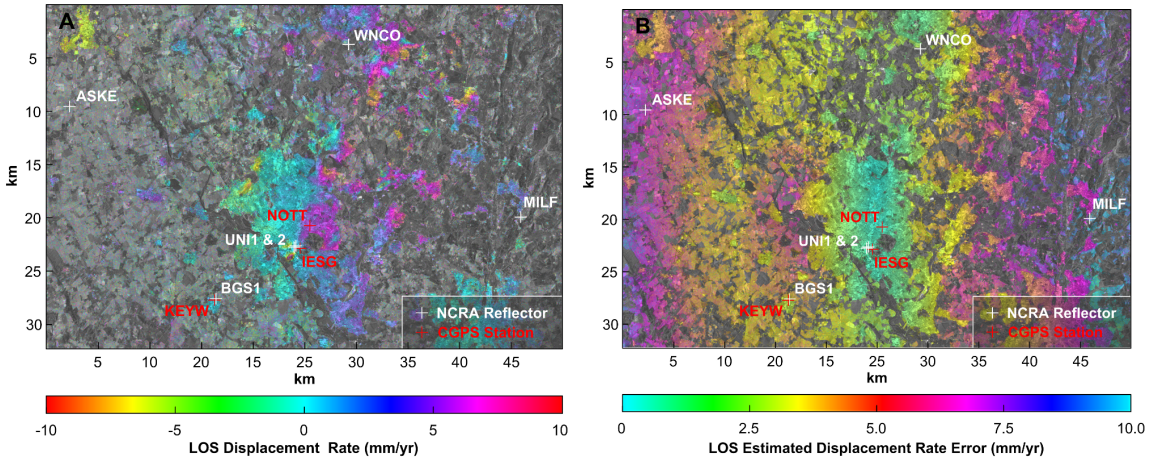

Figure 6.5: **(A)**The deformation rate map from the stacking result and **(B)** the deformation rate standard deviation with respect to a reference pixel near the IESG CGPS station. In the image on the left, the brightness of the pixel values are scaled by the product of the amplitudes which gives an idea of areas of phase stability. Images are shown in RDC geometry.

6.2.3 PSI Processing

The adopted PSI processing strategy is now detailed. Despite the fact that there are techniques that can approximate higher order deformation, the PSI processing adopted here is based on a linear model. This strategy was adopted because the emphasis of the work concerns integration with GPS as opposed to providing discourse on the merits of advanced PSI processing techniques. Furthermore, the other datasets involved in this work are only sampled at rates suitable for linear regression and therefore a linear PSI strategy is a more meaningful choice.

It should be noted however, that whilst the deformation rates are modelled linearly, the APSs are filtered for non-linear deformation and this is added to the linear deformation estimates at the end of the processing. The end result is deformation histories that are very well approximated by a linear fit, but also have small interpretable non-linear components. Figure 6.6 is an overview of the adopted PSI processing chain.

Readers should also note that unlike most PSI softwares, the IPTA method (Werner et al., 2003) used here, does not use every pixel of the entire image for PSI processing once candidate points have been chosen. Instead, all PSI operations are conducted on only the points themselves.

The methodology may give the impression that the PSI processing stages were fully

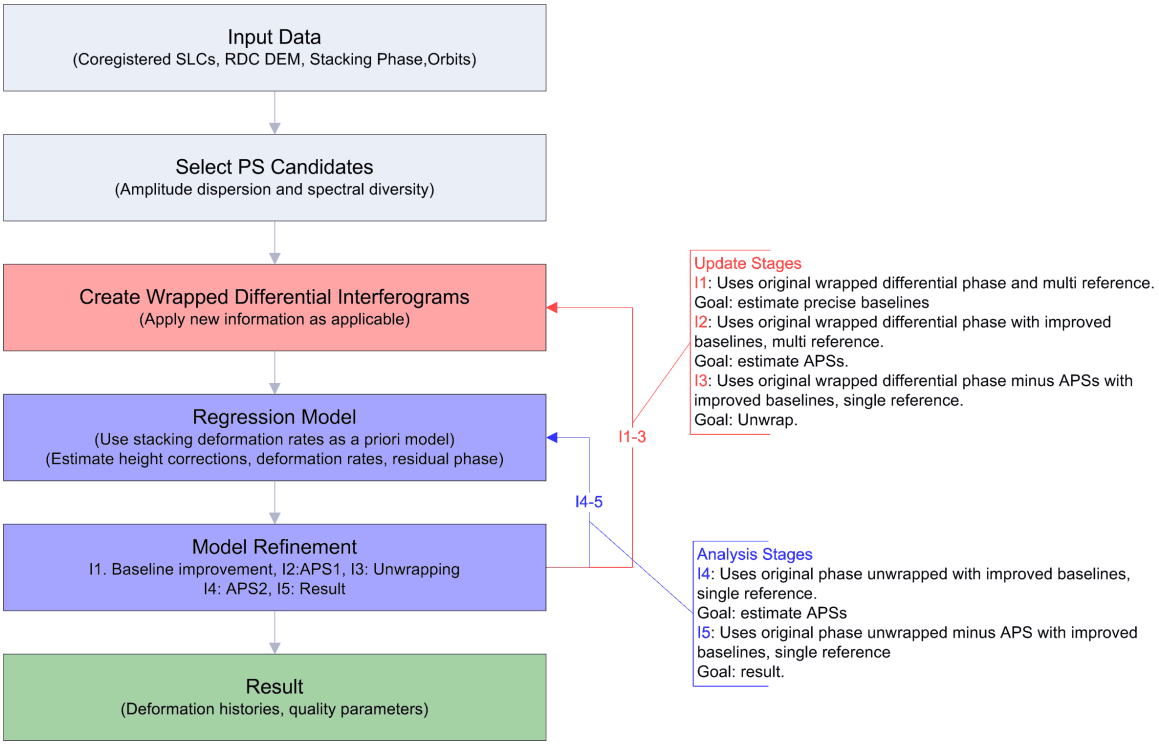

Figure 6.6: The PSI processing flow. Five iterations through a regression model are involved, each time making improvements to knowledge about the differential phase.

automated. This was by no means the case and many manual interactions are required throughout the process such as the reference point selection process and visual checks after stages such as phase unwrapping.

The next sections describe a process involving five iterations of a regression model which seeks to gradually increase knowledge of the differential phase components, eventually resulting in optimised linear deformation estimates.

6.2.3.1 Candidate PS Selection

The PS point selection strategy involves initially selecting a large number of candidate points by setting selection criteria with moderate thresholds. This means many points are rejected during the course of the processing (there are six PS quality checks during the course of the PSI processing) using more realistic phase standard deviation thresholds. This strategy is adopted because there is no stage involving a fresh search for new PS points, but old rejected points can be re-examined and re-introduced. Gross error checks were also employed whereby the scene was examined for PS points

where none could exist, such as in a body of water.

Candidate PS points were selected on two separate criteria, following which, the lists were merged. Firstly, pixels were selected based on amplitude dispersion. Taking each pixel in turn, the ratio of the (temporal) mean over the standard deviation of a pixels amplitude was examined (Ferretti et al., 2001). Pixels dominated by a point scatterer should show less random speckle behaviour over time and they ought to show similar intensity when viewed from different angles. Points with an intensity below 0.5 (relative to the spatial average) were ignored and a minimum threshold of 1.4 was used for the ratio.

The second criteria used for selection was based on the spectral diversity of the amplitude (Werner et al., 2003). This is based on the theory that dominating point targets in a resolution cell have a spectral diversity different to that of distributed targets, even when viewed from different directions. Rabus et al. (2004) found that combining the backscatter and spectral diversity methods seemed to produce more robust results for stacks with less than 40 scenes than Ferretti's original method.

From the two combined lists, a total of 343,989 PS points were selected as candidates which is around 9% of the total pixels in the AOI and just over 208 PS/km^2.

6.2.3.2 Quality Control

Following selection of the reference scene (17 June 2006; the scene closest to the centre of the stack with optimal baselines), differential interferograms were created with the current knowledge available; baselines computed from orbits and the simulated topographic phases from the RDC DEM.

A quality control of PS candidates was then conducted. Here, the phase standard deviation between pairs of neighbouring PS points was used as the quality estimator. This stage is equivalent to a phase regression analysis of a delaunay triangulated network except the only objectives are to determine phase standard deviation for reference point selection and reject PS points with a phase standard deviation above 0.7 rad. Unwrapping was then undertaken to determine the phase standard deviations per PS point.

6.2.3.3 Regression Analyses

As discussed, an iterative cycle of five regression analyses (see §2.6 for an explanation of the purpose of the regression) was undertaken to determine height corrections and linear deformation rates; phase that fitted neither of these models was assumed to contain non-linear deformation, atmospheric phase, phase due to baseline error and noise. Temporal unwrapping was then used to reveal the height corrections and deformation rates per point. After every regression, new differential interferograms were created whereby the updated topographic phases were subtracted from the original interferograms. Each regression run also created new PS phase standard deviations and a threshold of 1.2 rad (unless otherwise stated) was used to reject PS points. The whole process is now described in more detail.

6.2.3.4 First Regression

The phase stability of a chosen global reference point is fundamental to the quality of the PSI result because the resulting PS deformation rates are determined with respect to this point. The selection of a reference point with negligible motion through the stack also ensures that these relative velocities are closer to their absolute values.

With these points in mind, a low phase standard deviation (0.34 rad) reference point was chosen as close to the IESG CGPS station as possible (701m). The assumption is made that the absolute reference point velocity is similar to that of IESG, this assumption is reinforced by the available geological sources (Charsley et al., 1990, Donnelly, 1999, EDINA, 2009, Howard et al., 2010). IESG has a long, high quality GPS time series spanning over eleven years with a very low estimated velocity rate of 0.2 ± 0.3mm/yr. This time series was processed using Bernese GPS software (Dach et al., 2007), see §6.4 for more details.

Following reference point selection, the deformation phases, height corrections and residual phases were estimated in the first regression. At this early stage, all phase contributions were present in the differential phases and the baselines had not yet been optimised; the differential phase therefore contains variations that may hinder unwrapping. To that end, a patch-wise method was used for this regression. Here,

the stack is spatially divided into patches, each of which has its own local reference point. The regression is conducted between these reference points and the PS point neighbours in each patch, following which interferograms are unwrapped as a whole. The deformation rates from the stacking result were used to constrain the regression (Werner et al., 2003). Following this, the initial candidate point list was re-examined using the 1.2 rad threshold; points above the threshold were rejected and good points that had been previously falsely rejected were re-introduced.

6.2.3.5 Baseline Improvement

A re-examination of the baselines was then made using the same method stated in §6.2.2.6, smoothing the differential interferograms prior to unwrapping. Points with a deformation rate (from the stacking result) of larger than ±0.5mm/yr were ignored for GCP selection. Differential interferograms were then re-estimated using the improved baselines (which are used in all subsequent stages). Note that the smoothed interferograms mentioned here were only used for the baseline improvement step.

6.2.3.6 Second Regression

The second regression also used the patch-wise method on wrapped differential interferograms (created above). The residual phase was then spatially filtered using a radius of 1km to estimate the APSs. The filtering fits weighted least squares planes through areas of points defined by a given radius. The weighting is based on the distance to the pixels from the centre. Note that APS layers were created *per SLC* rather than *per layer*. This is possible because the two dimensional regression plane does not go through zero rad for zero time and zero baseline, but the plane has an offset which is directly related to the atmosphere and phase noise of the corresponding point of the reference SLC (Wegmüller et al., 2003). New differential interferograms were then created which have the the atmospheric phase estimates subtracted.

6.2.3.7 Third Regression

The third regression was conducted using a single global reference point (see §6.2.3.4); the single reference point method is used from this point forward. Following this, the topographic phases are updated with the new height corrections. The differential interferograms were then created using the original interferograms; this means that the residual phases are (intentionally) re-introduced here. The differential interferograms are then unwrapped spatially.

6.2.3.8 Fourth Regression

For the fourth regression, unwrapped differential interferograms were used to estimate the model parameters. Because the residual phases were present in the standard deviation threshold was increased to 2 rad. Spatial filtering was then used to estimate the APSs from the residual phases using the same method given in §6.2.3.6. Differential interferograms (minus the APSs) were then created for the last time using the best height and deformation rate estimates.

6.2.3.9 Fifth Regression

The final regression was undertaken creating final updates for the height and deformation estimates. The APSs were then temporally filtered for non-linear deformation estimates as before (§6.2.3.6), which were removed and added to the linear deformation estimates. The PS point quantity at the end of the regression was 174,487, a reduction of nearly 50% from the original candidate list. The PS point results are analysed in §6.5.

6.3 Precise Levelling

As proposed in §5.6, a precise levelling was conducted in the area of Hucknall, this area is highlighted as A2 in §6.5.1.

6.3.1 Levelling Methodology

The design of the campaign involved three levelling loops arranged in a line between an area thought not to have any active motion and another showing uplift in the BGS PSI result (§5.6). Twenty-five staff position were permanently marked with maximum distance of 60m between any two staff points. The instrument positions were also measured and marked in order to ensure backsights and foresights were kept equal. The area is very flat and therefore refraction error was negligible. The staff positions and the area in question is shown in figure 6.7.

Figure 6.7: The Hucknall precise levelling campaign. White diamonds show the permanently marked staff positions.

A Wild NA2000 digital level capable of measuring to a precision of ±0.4mm/km was used in conjunction with a barcode levelling staff.

6.3.2 Levelling Results

Levelling precision is measured as a function of the distance where the maximum permissible error (E) is expressed as a coefficient of the adopted precision level (C)

multiplied by the square root of the distance in kilometres (K)

$$E = C\sqrt{K}$$

The maximum loop misclosure was 2.2mm, with a mean of 0.9mm. The levelling loops were 1.10km, 0.82km and 1.04km. In first order levelling, $C = 4$ (Chandra, 2007) which translates to maximum permissible misclosures of 4.2mm, 3.6mm and 4.1mm over the distances involved. The levelling campaign is therefore well within first order levelling criteria. The levelling results are analysed against PSI results in the next chapter (§7.2.2).

6.4 GPS Results and Analysis

The CGPS stations discussed in §4.8.2 and the NCRA GPS stations discussed in §5.2.3 were processed with GOA-II using the rationale addressed in §5.4.1, with the resulting dataset discussed in §5.5. This next section focusses on the quality of the GPS results.

6.4.1 GPS Time series

Figure 6.8 shows the NCRA GPS station time series sampled at the ENVISAT acquisition dates and figure 6.9 shows the CGPS station time series. The green (accepted) and red (outlier) points correspond to coordinates at the acquisition dates and the blue trendlines are linear regression fits. The software used to generate the time series is Create and Analyse Time Series (CATS) (Williams, 2008) which is based on a Maximum Likelihood Estimator (MLE) that allows the computation of a linear trend, periodic signals, coordinate offset magnitudes and stochastic noise amplitudes, assuming both white an coloured noise. Periodic signals were not estimated for the acquisition date only GPS time series as they were considered too sparse.

Any individual solution with an RMS value greater than three times the time series RMS was flagged as an outlier and not used for computing the rate and trendline. Outlier rejection is iterative and occurs until no further outliers are found. All stations

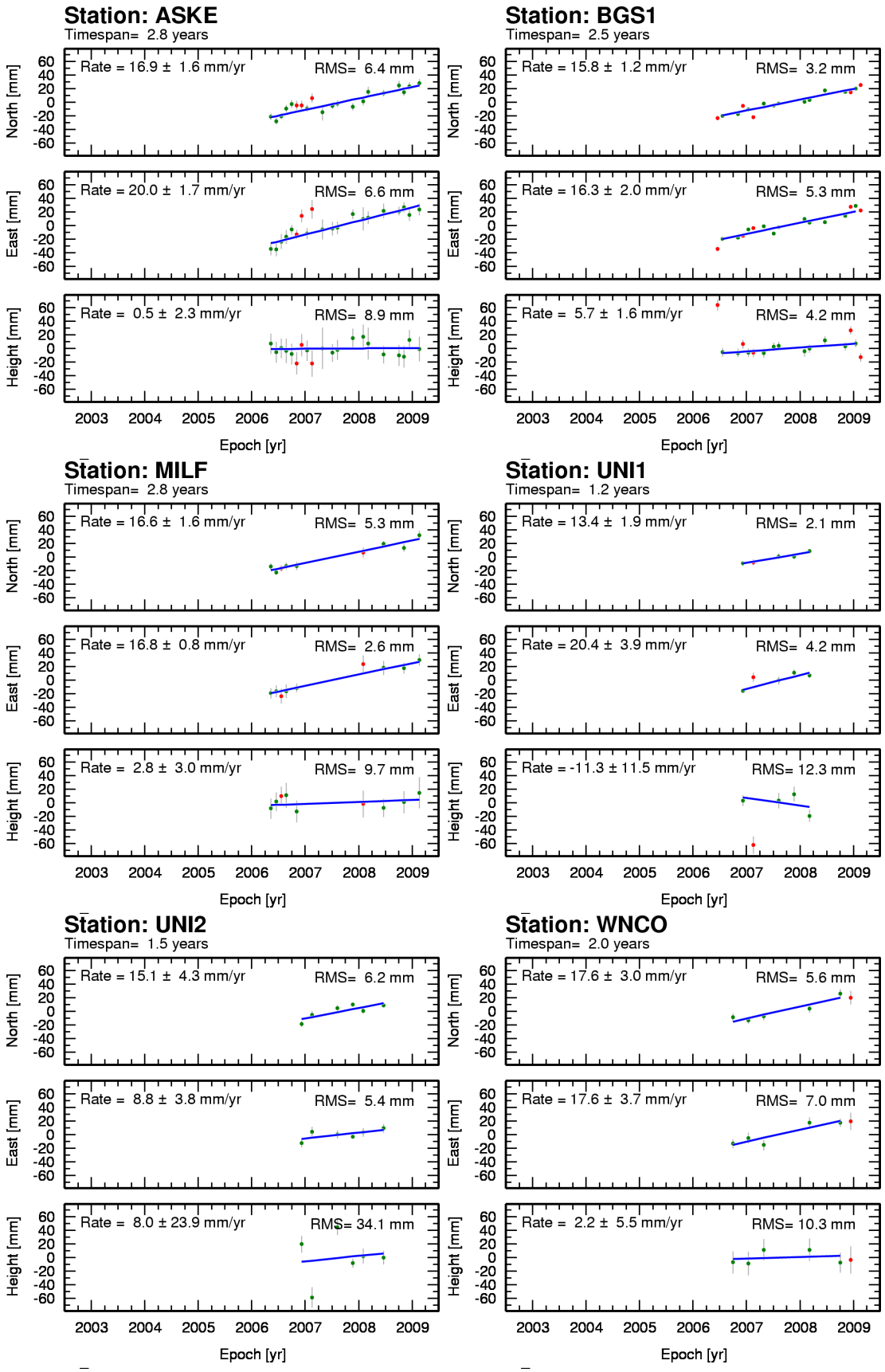

Figure 6.8: GPS position time series for NCRA stations transformed into a north, east and height reference frame. Green and red (outliers) dots represent GPS data collected on ENVISAT acquisition days. Blue lines represent the linear trends of the green dots.

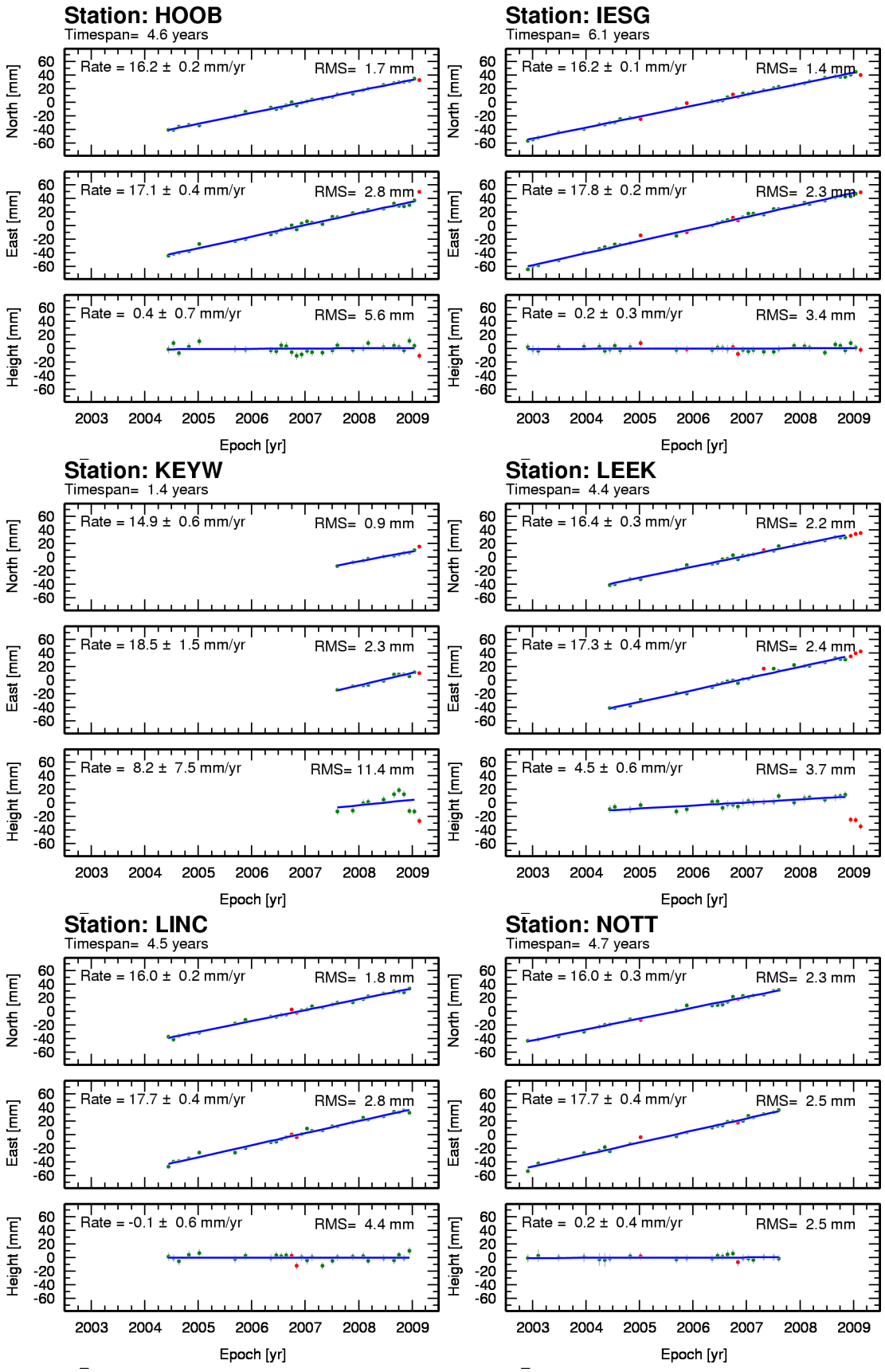

Figure 6.9: The GPS position time series for CGPS stations transformed into a north, east and height reference frame. Green and red (outliers) dots represent GPS data collected on ENVISAT acquisition days. Blue lines represent the linear trends of the green dots.

show a uniform northeasterly velocity over time. This is the expected motion of stations on this part of the Eurasian tectonic plate with respect to ITRF2005 (`http://sideshow.jpl.nasa.gov/mbh/all/table2.txt`).

RMS values are noticeably smaller for the CGPS time series, which is mainly attributable to the fact the CGPS solutions were usually computed from twenty-four hours of data. NOTT has an above average amount of noise in its dataset (§6.1.2 and figure 6.10), but following the rejection of three days of data, the acquisition date time series is comparable to the other CGPS stations. Most solutions have outliers and for the NCRA stations, it is assumed that these are mainly due the session length. Also, because of the episodic nature of the NCRA station observations (especially for the tripod stations:UNI1, UNI2 and BGS), there are bound to be small setup errors and whilst potential blunders are guarded against with procedure, their presence is possible.

UNI1 and 2, which are both permanently fixed reflector sites at the University of Nottingham main campus, have larger RMS values than the temporary triangulation pillar sites despite the fact that these two stations were often left running for much longer than the required six hours. An explanation for this may be due to the fact that UNI1 and 2 are both on roofs, with more potential for multipath and signal degradation; although the station pre-processing checks (§6.1.2) do not show this. It is also possible that building expansion may be affecting these points which has been known to affect stations in these situations (Çelebi et al., 1998). Also, UNI1 and 2 both require a tripod setup, which will undoubtedly be less stable than the pillar sites. BGS1 also requires a tripod, but this was left in place for the majority of the campaign and is in a more stable location. Whilst there are still outliers for BGS1, RMS values are comparable or better than the other NCRA stations, despite the fact that only a standard surveying antenna was available for this station.

There is a lack of data apparent in some of the time series, particularly for UNI1 and UNI2. Reasons for this are given in §5.4 and 5.5. As the precision of the time series for both of these stations is relatively poor, their usefulness from the perspective of the aims and objectives is limited in any case.

Table 6.1 summarises the results by showing the north, east and height RMS values

Station	North [mm]	East [mm]	Height [mm]	North [mm/yr]	East [mm/yr]	Height [mm/yr]
ASKE	6.4	6.6	8.9	16.9 ± 0.6	20.0 ± 0.9	0.5 ± 0.8
BGS1	3.2	5.3	4.2	15.8 ± 0.8	16.3 ± 0.3	5.7 ± 1.0
HOOB	1.7	2.8	5.6	16.2 ± 0.0	17.1 ± 0.1	0.4 ± 0.1
IESG	1.4	2.3	3.4	16.2 ± 0.1	17.8 ± 0.1	0.2 ± 0.0
IESG(B)	1.5	1.2	4.4	16.2 ± 0.1	17.8 ± 0.2	0.2 ± 0.3
KEYW	0.9	2.3	11.4	14.9 ± 0.3	18.5 ± 0.3	8.2 ± 3.8
LEEK	2.2	2.4	3.7	16.4 ± 0.0	17.3 ± 0.2	4.5 ± 0.3
LICF	1.8	2.8	4.4	16.0 ± 0.0	17.7 ± 0.1	-0.1 ± 0.2
MILF	5.3	2.6	9.7	16.6 ± 0.0	16.8 ± 0.0	2.8 ± 0.0
NOTT	2.3	2.5	2.5	16.0 ± 0.2	17.7 ± 0.1	0.2 ± 0.2
NOTT(B)	1.4	1.2	4.3	16.0 ± 0.3	17.7 ± 0.4	0.2 ± 0.4
UNI1	2.1	4.2	12.3	13.4 ± 0.6	20.4 ± 1.0	-11.3 ± 2.7
UNI2	6.2	5.4	34.1	15.1 ± 1.1	8.8 ± 1.1	8.0 ± 4.2
WNCO	5.6	7.0	10.3	17.6 ± 0.9	17.6 ± 0.6	2.2 ± 0.7

Table 6.1: The RMS statistics and station velocity estimates for north, east and height components. The (B) after IESG and NOTT denote the Bernese processed, daily time series, processed by staff at the IESSG.

along with the component velocities for each station. With the exception of UNI1 and 2, the results are reasonably consistent. Ignoring UNI1 and 2, the north and east velocities for the other ten stations have uncertainties of up to 0.9mm/yr; the assumption being that the north and east velocity rates ought to be similar for all stations in the network due to the overriding dominant plate motion affecting them all similarly.

In addition to the internal consistency checks above, comparing the acquisition date processed time series with the full daily time series for CGPS stations IESG and NOTT computed by independent means gives another perspective on the validity of the dataset. The results for the IESG and NOTT daily time series are included in table 6.1 and the time series are shown in figure 6.10. The time series were computed from double differenced coordinate solutions using 120 stations from the BIGF network and approximately 50 IGS stations. This was conducted using an in-house modified version of Bernese version 5.0 (Dach et al., 2007) by Dr Norman Teferle at the IESSG,

University of Nottingham for his own research. Re-processed satellite orbits and Earth orientation parameters were used (Steigenberger et al., 2006) absolute satellite and receiver antenna phase centres (Cardellach et al., 2007, Schmid et al., 2007) were modelled. The tropospheric delays were based on standard pressure and the GMF model (Boehm et al., 2006a). The time series was processed using Create and Analyse Time Series (CATS) software (Williams, 2008).

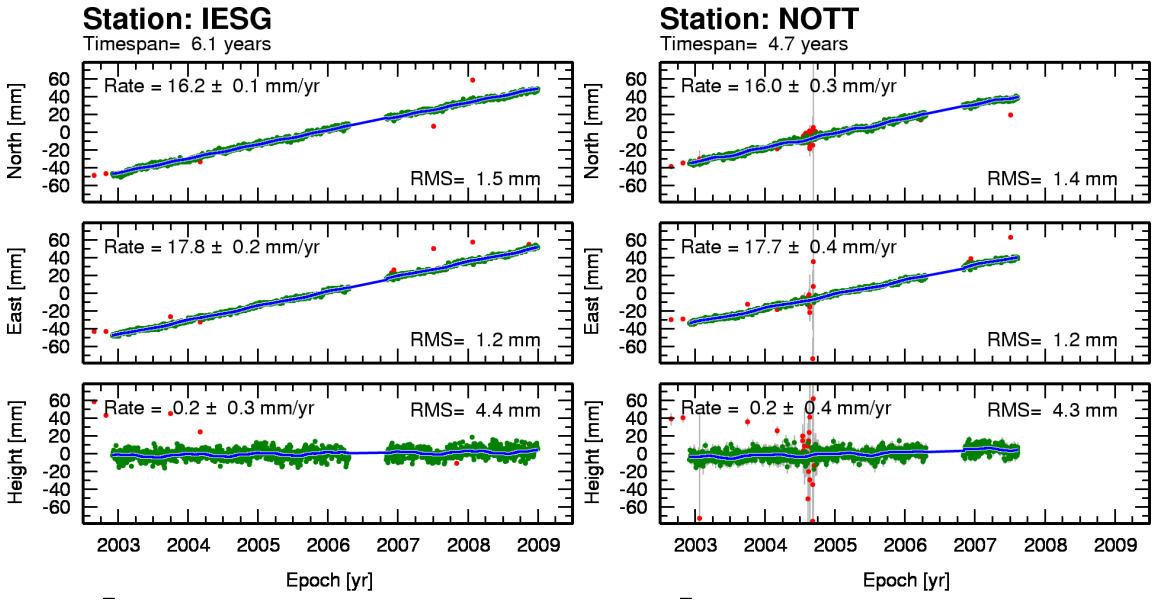

Figure 6.10: The GPS position time series for CGPS stations transformed into a north, east and height reference frame. Green and red (outliers) dots represent GPS data collected on ENVISAT acquisition days. Blue lines represent the non-linear trendlines of the green dots.

Both the daily time series were cropped to within the ENVISAT dataset period to provide a more consistent comparison. The rates for the daily time series and acquisition date time series for both IESG and NOTT compare at the sub 0.1mm/year level; this is a strong indication that results from GOA-II PPP processing strategy compare well with previously validated results processed from entirely different methods. When the entire (uncropped) daily time series for IESG (28 April 1997 to current) and NOTT (2 January 2000 to 13 August 2007) are compared to the ENVISAT date only time series, sub mm/yr differences in the rates are apparent. This further indicates that the shorter, ENVISAT date only time series, compares well with significantly longer time series.

6.5 PSI Results and Analysis

Figure 6.11 shows the PSI result for the whole subscene projected to UTM with reflectors, CGPS stations and the PSI reference point marked. The 174,487 remaining PS points at the end of the process are scattered over 1650km^2 which equates to 109 per km^2. Evidently, these are not evenly spread, as the urban conurbations in the AOI are clumpy and mainly exist on the western side. Mostly, the point velocity rates are fairly flat, as would be reasonably expected in Nottingham, with some interesting exceptions. Not considered for this study is the area of apparently high motion in the northwest of the AOI. It could not be satisfactorily established whether this is a real signal or the result of unwrapping issues.

A more in-depth discussion of the PSI result now follows, focussing on deformation signals in the city centre.

6.5.1 Nottingham City Centre

There are four areas of motion of particular interest close to the city centre. Figure 6.12 shows an area cropped from figure 6.11 which is centred around Nottingham city. Firstly, there appears to be a large area of uplift to the West (A1) and North (A2) of the centre, these are the Wollaton and Hucknall areas respectively. Also, there are areas of subsidence in the West (A3), around Dunkirk, and in the East (A4), in the Gedling area. These are now discussed along with comment on the possible causes of the deformation signals.

6.5.1.1 Uplift in the Wollaton Area (A1)

An extensive amount of uplift can be seen in this area mainly encompassing typical suburban residential houses and Wollaton Park. The total area of uplift is large at around 12km^2 with average rates of around 2 to 3mm/yr. Figure 6.14 shows the phase history of four persistent scatterers, two of which (P3 and P4) lie in the Wollaton area. Online geological mapping (EDINA, 2009) indicates that this area lies within the Pennine middle coal measures but provides no data on mining activity that can be directly correlated with the deformation zone. However, another publicly available

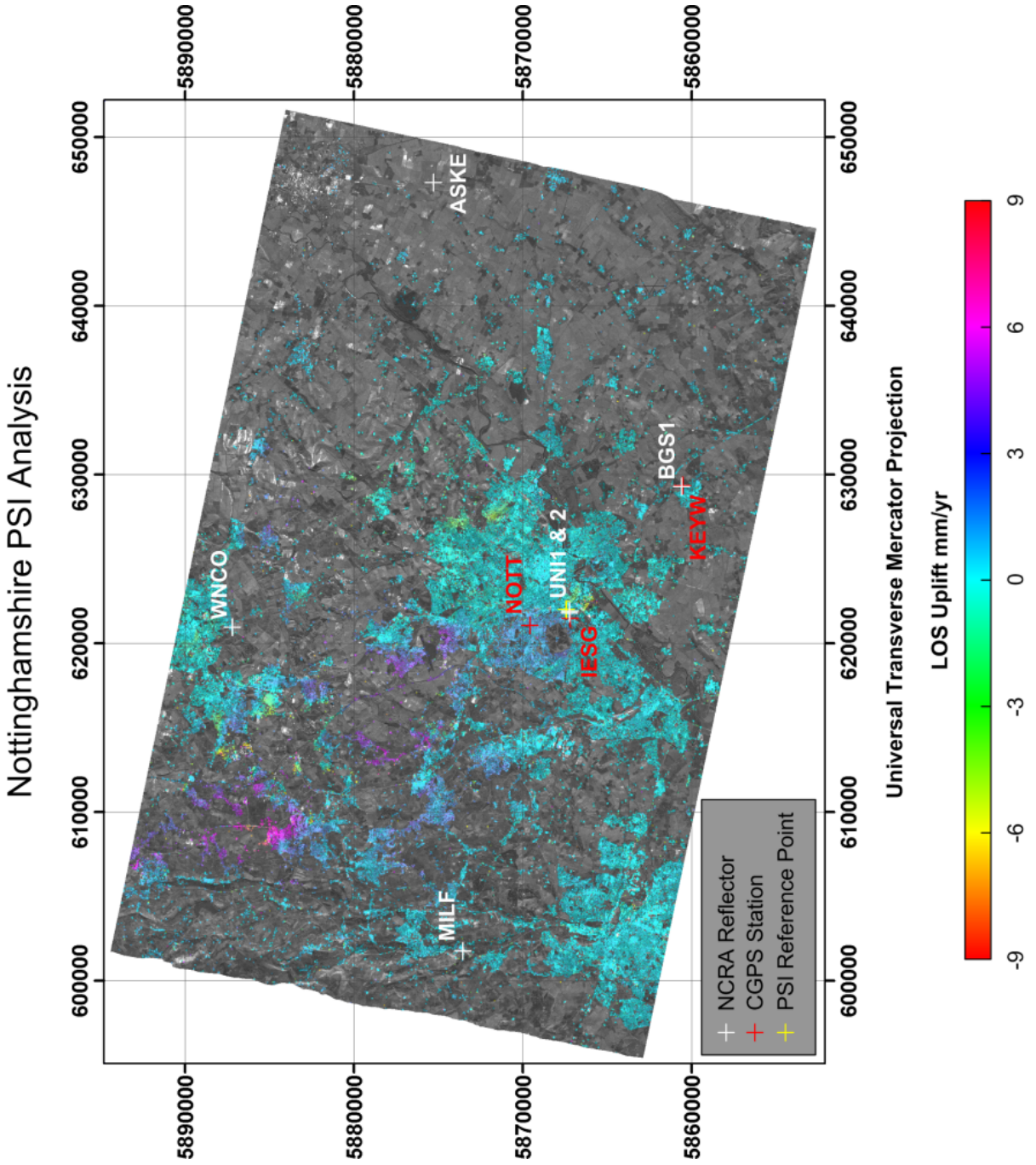

Figure 6.11: Nottinghamshire PSI result in the UTM projection. The PSI reference point in yellow lies very close to IESG and UNI1 and UNI2.

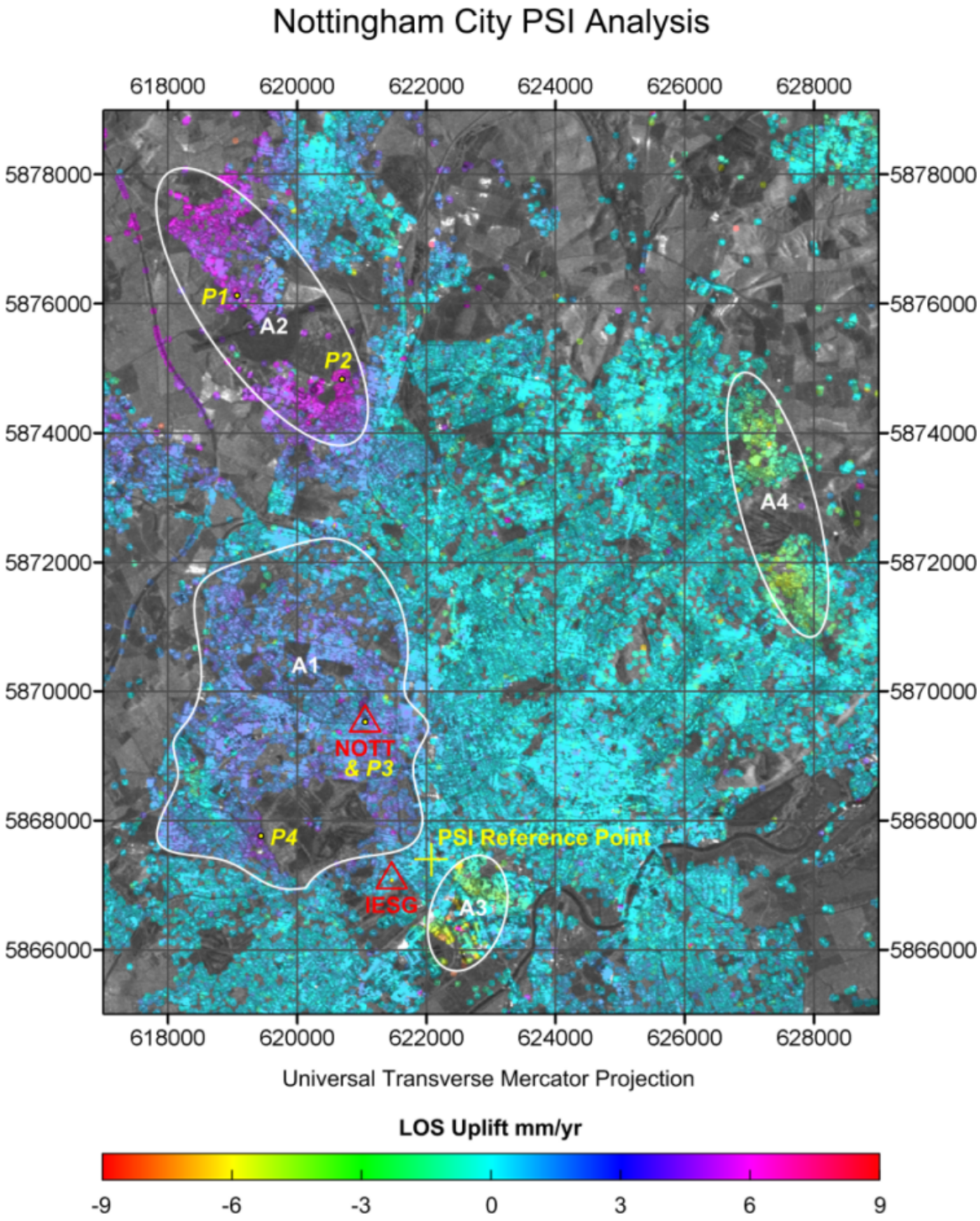

Figure 6.12: Nottingham city PSI result in the UTM projection. Four areas of note, A1 to A4, have been highlighted for further comment. Points P1 to P4 are scatterers selected within A1 and A2; their phase histories are shown in figure 6.14

source (Charsley et al., 1990) gives a more detailed description of coal mining activity. Indeed, a comparison with maps of the extent of the mineworks, in figure 6.13, shows that the boundary of the mined areas (highlighted in both images) and the boundary of the uplift region, particularly to the West of the city, are in remarkably close agreement.

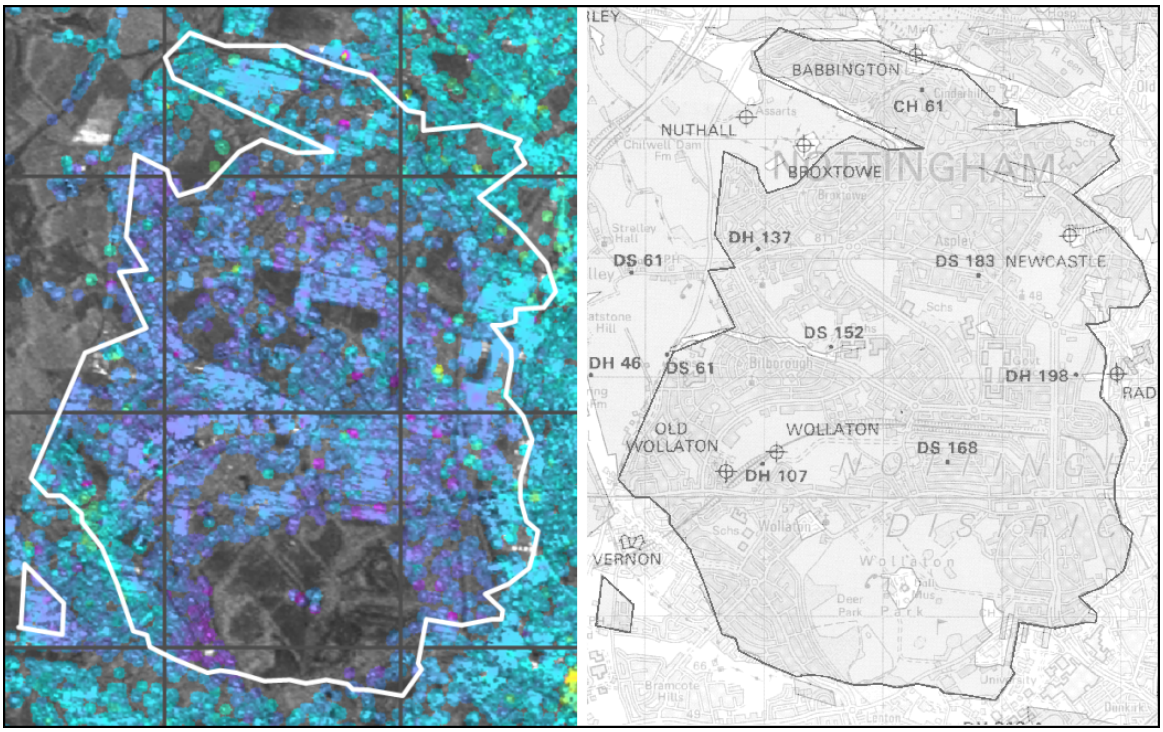

Figure 6.13: The Nottingham city PSI result in the West of Nottingham **(left)** compared to a mining and geology map (Charsley et al., 1990) **right**. The mining boundary, which is part of the geology map, has been overlaid onto the PSI result.

6.5.1.2 Uplift in the Hucknall Area (A2)

Area A2 lies to the North of A1 around Hucknall and also indicates an area of uplift. The two areas may or may not be independent, with A2 showing rates typically around 4 to 5mm/yr (see P1 and P2 in figure 6.14) clustered around Hucknall Airfield. There is a geological fault line running North-South at the Eastern end of the subsiding area, but these are not uncommon around the AOI and on the whole, do not generally correlate with other areas of motion. No coal mining data or superficial deposits of any kind are marked in EDINA (2009). However, it is understood that Hucknall was a colliery town from 1861 to 1986 with extensive mineworks which are mentioned in

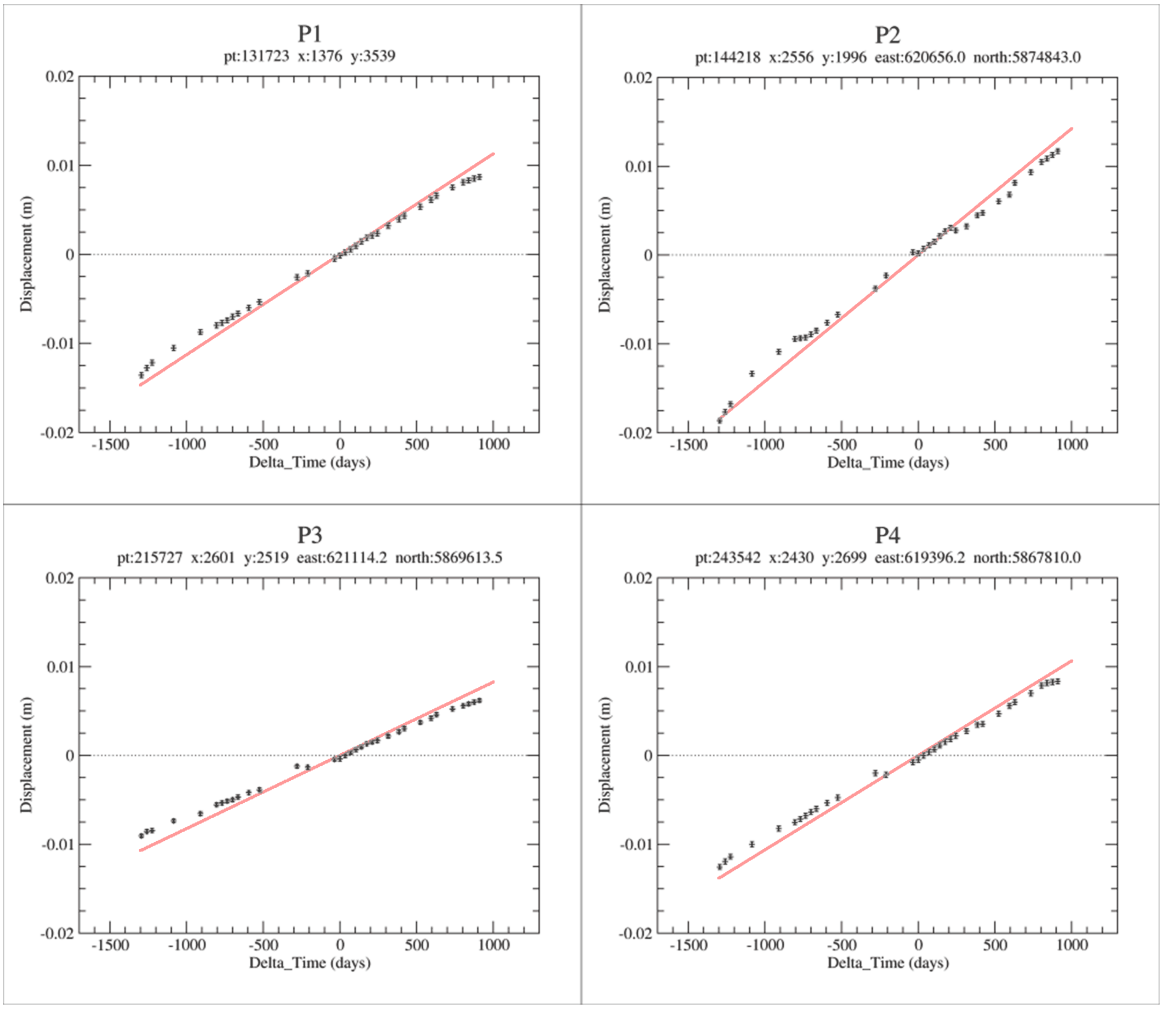

Figure 6.14: Phase histories of PS points P1 to P4 marked in figure 6.12. Uplift is shown in each phase history and the fact that PS points do not lie directly on the regression line is a consequence of filtering the atmospheric phase screens for non-linear deformation and adding these estimates to the linear deformation at the end of the PSI process.

a number of tertiary sources (Wikipedia, 2009, AddItNow, 2005), not to mention a bronze statue of a coal miner in the town centre! Although nothing can be found on public record detailing the locations of shafts, the colliery building itself was within the area of motion and coal extraction seems to be the most likely explanation for the observed ground motion.

An alternative explanation is tied to the airfield at the centre of the deformation signal. RAF Hucknall, as it used to be known, dates back to the early twentieth century making it one of the oldest airfields in the UK. It has a bunker network which is now used by Rolls Royce as part of their engine testing facility; this includes a fire

tunnel (International, 1962). The exact location of the bunker network could not be established. A third explanation could be that the motion is due to a combination of both the mining activities and airfield bunker system, as they are probably close together.

The fact that A1 and A2 are (perhaps counter intuitively) uplifting rather than subsiding is not necessarily a reason to cast doubt on the results. Water ingress can lead to mine works causing rebound after pumping ceases (Dumpleton et al., 2001, Cuenca and Hanssen, 2008) and the void left by a mine can refill and empty with the water table which may occur seasonally or because of more complex cycles or events, such as underground collapse (Bekendam and Pottgens, 1995, Mouélic et al., 2002).

6.5.1.3 Subsidence in the Lenton Industrial Area (A3)

Area A3 is a region of subsidence in a small but well-defined zone to the West of the city. It is an area of industrial units and, more recently, hypermarkets, bowling facilities, restaurants and a multi-screen cinema. Members of Nottingham city council were able to verbally corroborate that the area is known as being an area of landfill from the 1950s, variously overfilled at times with the current units sitting on rafts above the substrate dating back to the 1970s and early 1980s. The cinema area is particularly notorious for being over landfill as the methane generated has to be pumped out throughout the year, the pumps being noticeable features above-ground.

6.5.1.4 Subsidence in the Gedling Area (A4)

Area A4 extends approximately in a North-South direction for 4km through a suburban residential area. It follows a shallow ridge of topography at low level in the South to a relatively high altitude in the North. In the centre of the subsidence zone is a golf course to the west and a landscaped area to the east that was used for colliery waste in the past (Charsley et al., 1990); although this area has no PS points, it is reasonable to assume that the signal to the north and south are connected here.

The subsidence area was definitely mined for coal (Charsley et al., 1990), but this can be said of most of north Nottingham. There is nothing on public record to indicate the most recent mining activity in terms of depth and extent. There is however a

history of subsidence in the region including damage to the nearby Mapperley railway tunnel in 1926 (Anderson, 1973) and ongoing subsidence on a playing field within A4 (KKP, 2003). The site of Gedling Colliery is less than a kilometre east of the centre of the subsidence signal. Gedling colliery closed in 1991 and was the last mine to close in Nottingham; this is fourteen years from the temporal average of the stack, which is a reasonable period for subsidence due to coal mining to still continue to occur (McLean and Gribble, 1985, Donnelly, 1999).

6.5.2 PSI Statistics

The following sections provide a statistical evaluation of the PSI results.

6.5.2.1 Geocoding Accuracy

To assess the accuracy of the geocoding, sub pixel RDC coordinates of the reflectors taken from the SinC responses computed in §5.5.2 were transformed to the World Geodetic System 1984 (WGS84) in UTM and compared to the averages of the GPS processed results for the reflectors. Differences between ITRF2005 and WGS84 were assumed to be negligible for these purposes. The average error vector was 8.4m, which is better than the quoted horizontal accuracy of the SRTM 90m DEM (Farr et al., 2007) on which the geocoding accuracy mainly depends.

6.5.2.2 PSI Consistency

Three histograms are shown in figure 6.15 that provide a summary of statistics computed from the PS points. The mean of the residual phase standard deviations is just over 1 rad. A significant part of the residual phase may be due to remaining atmospheric contributions that did not fit the applied model.

The deformation rates are, as might be expected, mostly very low. The histogram is slightly offset from zero with a mean of 0.62mm/yr and a standard deviation of 1.48mm/yr. The bottom left plot shows the difference between the RDC DEM (resampled from the SRTM 90m DEM) and the final PSI height estimates; note that these are with respect to the reference point height correction which is unknown,

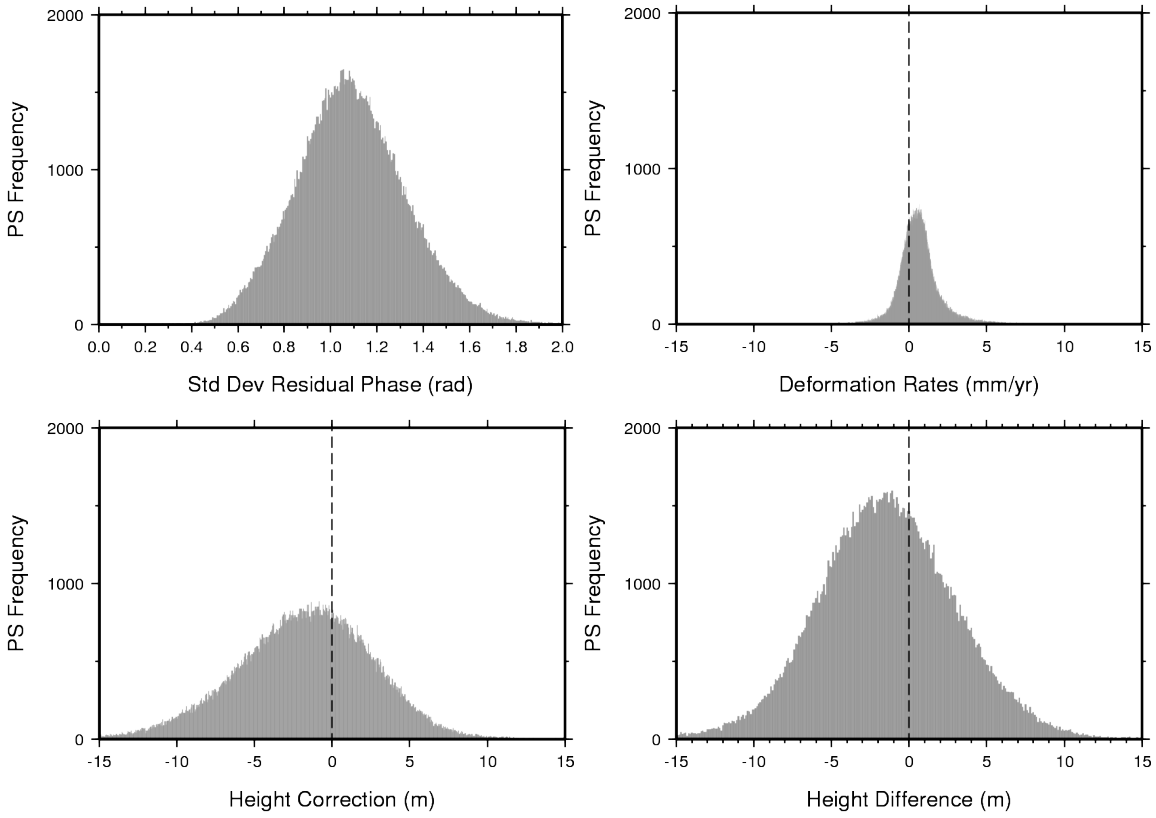

Figure 6.15: Histograms of the 174,487 PS points that remained at the end of the PS processing. Shown are the standard deviations of the residual phases **(top left)**, the deformation rates **(top right)**, the height corrections **(bottom left)** and the comparison with the NEXTMap 5m DSM **(bottom right)**.

but the discussion here concerns variations in the height corrections and therefore absolute values are irrelevant. With urban PSI studies, marked variations in the height corrections locally are often correlated with how many tall buildings exist in the area. Nottingham being a fairly average UK city typically has many buildings ranging from 5 to 20m or more and most of the large height corrections are clustered nearer the centre. Also, the building sizes in plan compared to the SAR pixel spacing of 20m in ground range will often mean misrepresented heights in urban areas. A higher resolution DEM in this case is not directly useful as it would still require undersampling to the SAR pixel size, during which detail will be lost.

The bottom right plot shows the difference in height between the RDC DEM and the NEXTMap 5m Digital Surface Model (DSM) (Intermap Technologies, 2008). The DSM is an airborne InSAR product with vertical accuracy of 1m RMSE. Because of its resolution, building heights are modelled much better than in the SRTM DEM.

The comparison between the RDC DEM and the DSM was not straightforward as the PS points must be transformed to the WGS84 datum using the SRTM DEM which relies on the Earth Gravitational Model 1996 (EGM96), whereas the DSM was in a local datum with heights derived from the Ordnance Survey National Geoid Model (OSGM91). The difference between the geoid models was not accounted for, although Bingley et al. (2002) suggests the difference is at the sub metre level. The plot suggests that height differences in order of a few metres are common. The mean is -1.521m with a standard deviation is 4.713m. The comparison mainly relies on the horizontal accuracies of the geocoding (§6.5.2.1) and the accuracy of the DSM which are 8m and 1m respectively; therefore many points, especially near or on tall buildings, may still be incorrectly represented here.

6.6 PSI and GPS Comparison

Comparing the GPS data with the PSI result can be done in a number of ways. If the surveyed reflector sites are also PS points, then the most logical comparison would be a direct one, as long as the reflector PS point was typical for that area. However, for the reasons discussed in §5.5.1 and 6.2.3, fourteen scenes had to be incorporated into the ENVISAT stack which occured prior to the establishment of the NCRA which precluded the chance that the reflectors would become stable PS points.

Instead, a slight variation of the method used by Bingley et al. (2007) was adopted. Here, the authors considered that PS points within 300m of a GPS station could be assumed to be on the same geological setting and the PS point velocities fitting this criteria were averaged. The deformation rate standard deviations were examined and statistical outliers were removed. In this study, the overall rate is achieved by averaging PS points epoch by epoch, again rejecting statistical outliers iteratively. In all cases, the 300m assumption is made and this is consistent with available geological data (Charsley et al., 1990, Donnelly, 1999, EDINA, 2009, Howard et al., 2010). Also, prior to the establishment of the NCRA, advice was sought from subject matter experts at BGS (Culshaw, 2006) who stated that “there is no reason to suspect that the geological setting around the chosen reflector sites is not stable”.

The comparison of PSI and GPS results was undertaken for all GPS stations within the AOI apart from ASKE and MILF, which had no PS points within 300m, and UNI1 and 2 for the reasons mentioned in §6.4. Figure 6.16 is a series of plots showing the correlation between GPS and PS time series. GPS data is depicted by green dots with associated error bars in grey and associated trendlines in blue. The PSI data is shown using red dots, black error bars and orange trendlines which represent the velocity of the slope of the derived deformation.

It is worth remembering that all the PS point velocities are relative to the reference point. The chosen reference point was the closest point to IESG that had a phase standard deviation below 0.4 rad. The PSI and GPS rates both suggest that IESG itself is not moving up or down appreciably and it is assumed this is also the case for the reference point which is 701m away. It follows then that if the deformation phases have been accurately modelled, then the other PSI velocities will be close to their absolute values with the understanding that this becomes less valid with increasing distance from the reference point due to atmospheric phase errors.

The rates for both PSI and GPS are positive in all cases. For IESG and NOTT, the two trends are comparable with differences in the GPS and PSI rates of 0.6 and 1.6mm/yr respectively. For BGS1, KEYW and WNCO the rates do not compare as well, and most of the GPS points are flagged as outliers from the perspective of the PSI time series. As it has been established that the GPS velocities are close to their true values, then the issue can be assumed to be due to the PSI result. These stations are significantly further from the reference point than IESG or NOTT and therefore there is less chance that atmospheric phase contributions are being accurately modelled. As discussed in §3.3, constraining the PSI process satisfactorily so that the various constituents of the phase are correctly attributed, especially over the distances involved here, is difficult without resorting to augmentation data. This is addressed in the next chapter.

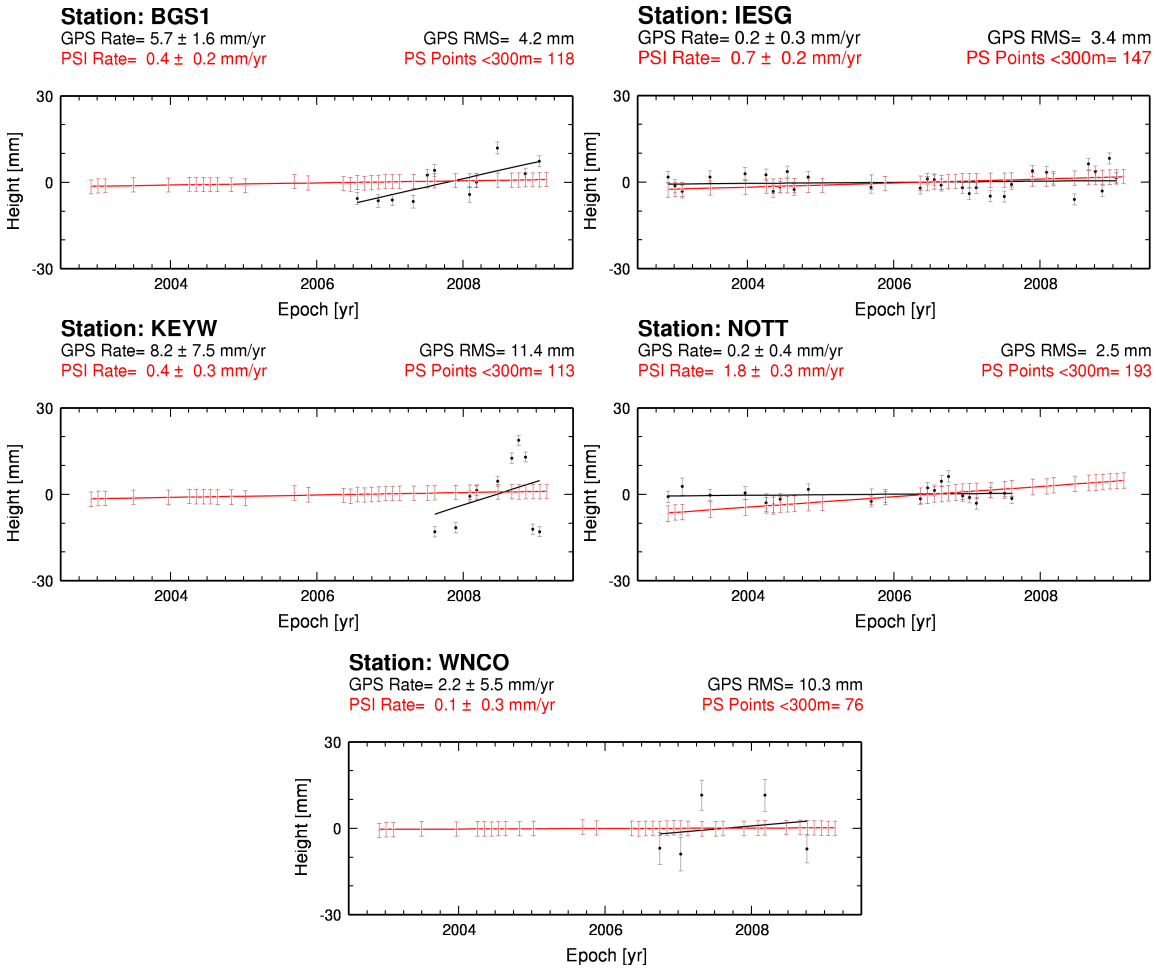

Figure 6.16: GPS and PSI velocity estimates comparisons; black represents GPS and red represents PSI. PSI velocities are estimated by averaging velocities epoch by epoch for all the PS points within 300m of a given GPS station.

6.7 Summary

The processing strategies for the GPS and SAR datasets have been presented. The GPS results are consistent with other more established processing methods. This indicates that the adopted field observation model and processing strategy are both valid means for satisfying the aims and objectives. The PSI result indicates some areas of motion in the city centre, some of which show good correlation with existing sources of information. The GPS and PSI velocities agree within 2mm for stations close to the reference point but stations further away are less correlated with the PSI result with differences of 6 to 8mm; this may be due to atmospheric phase errors which tend to be proportional to the distance to the reference point. The next chapter addresses

the issue of augmentation data for PSI studies by using ZWD values to correct the APSs.

Chapter 7

ZWD Correction for PSI

This chapter uses the GPS results processed in chapter 6 to compute ZWD estimates for the ENVISAT acquisition times at stations inside and outside the AOI. ZWD values for every pixel in the AOI are then interpolated and the estimates are integrated into a PSI analysis. The results from this are then analysed against the existing PSI analysis, the precise levelling data and the height components of the GPS station velocities.

7.1 APS Correction using ZWD

A discussion of the assumptions usually made when determining APSs was given in §3.3.2. These assumptions are tested here to improve PSI results through the integration of ZWD screens into the process. As the spatial resolution of the GPS stations will not be sufficient to estimate small scale atmospheric variabilities, the aim here is to mitigate the long wavelength variations that are not estimated from standard spatial sampling techniques which assume white noise behaviour.

It should also be noted here that the statistical tests (Pearson's correlation and the t-test) used in this chapter concerning the APSs, assume random behaviour. For the reasons stated in §3.3.2, it may be that the atmospheric phase contains non-random elements within it. This non-random aspect is assumed to be at a low enough level such that Pearson's correlation and the t-test are still valid estimators.

7.1.1 ZWD Estimates

ZWD estimates were determined in the PPP process as discussed in §6.1.6 and the quality of the GPS results from which they are derived is discussed in §6.4. Where available, real pressure data measurements from the UK Met Office were used to subtract the hydrostatic delay from the total delay in order to realistically determine the wet delay. Table 7.1 lists all the SLC dates used on the stack, their respective $B_\perp$ and B_T values and whether pressure data was available. For dates with no pressure data, a standard atmospheric pressure of 1013.25mb was used.

No.	Date	$B_\perp$ (m)	B_T (days)	P	No.	Date	$B_\perp$ (m)	B_T (days)	P
01	20040612	69.581	-735	N	16	20070217	-176.777	245	Y
02	20040717	35.712	-700	N	17	20070428	-259.903	315	Y
03	20040821	-112.568	-665	N	18	20070707	-69.603	385	Y
04	20041030	136.618	-595	N	19	20070811	-119.849	420	Y
05	20050108	-1056.685	-525	N	20	20071124	137.813	525	Y
06	20050910	-226.642	-280	N	21	20080202	109.682	595	Y
07	20051119	320.339	-210	N	22	20080308	-248.414	630	Y
08	20060513	-168.411	-35	Y	23	20080621	117.443	735	Y
09	20060617	0.000	0	Y	24	20080830	158.678	805	Y
10	20060722	604.639	35	Y	25	20081004	-164.770	840	Y
11	20060826	559.634	70	Y	26	20081108	51.498	875	Y
12	20060930	-779.055	105	Y	27	20081213	-394.466	910	Y
13	20061104	-643.095	140	Y	28	20090117	212.694	945	Y
14	20061209	254.233	175	Y	29	20090221	-92.881	980	Y
15	20070113	640.179	210	Y					

Table 7.1: The ZWD corrected PSI interferogram stack. The reference SLC date is 20060617. The 'P' column shows whether pressure data was available on that date.

7.1.2 Observation Geometry

The respective geometry of the GPS and SAR data sources are quite different. The ZWD for a given station and epoch is computed from the zenith-mapped weighted average from a cone of GPS observations described by the station elevation mask. Naturally, the choice of elevation mask affects not only the location and quantity

of the incoming observations used in the average, but also the diameter of the cone described at a given height. The elevation mask angle therefore influences how the ZWD can be reasonably compared with SAR data. Figure 7.1 is a diagram of the overlapping GPS and SAR geometries.

7.1.2.1 Elevation Mask

An elevation mask is usually employed as a means of reducing station multipath effects and recommendations for setting the mask usually range from anywhere between 7° to 20°. Also, a major part of the tropospheric error results from low elevation satellites which necessarily must transmit through a thicker layer of troposphere. This suggests a high elevation mask would both reduce these effects and narrow the GPS cone. As figure 7.1 suggests, a narrower cone also implies that the computed ZWD value is comparable to a smaller area of the SAR image. This is potentially desirable if there are many stations close together as it can result in higher resolution ZWD screens. However, this must be balanced against the loss of observations implied by a high elevation mask and the decrease in the GPS Geometrical Dilution of Precision (GDOP), that lower elevation satellites offer. To resolve this, GPS data for IESG was processed using 10°, 15° and 20° elevation masks. The reduction of low elevation observations led to an excessive increase in noise in the height elements and 15° elevation masks were used to estimate the ZWD values.

7.1.2.2 ZWD and APS Comparison Model

Before ZWD values are integrated into a PSI analysis, it is prudent to analyse the level of correlation between ZWD values and PSI estimated APSs. For a valid comparison between a ZWD value computed from a cone of GPS observations and an APS computed from SAR data, some averaging of APS values around a station must occur, and this must somehow be representative of the GPS geometry. Averaging around a point for a given radius describes a SAR tube of observations that must overlap with the GPS cone at a pre-determined height. It has been shown from radiosonde data that over half the wet delay estimate results from the lower portion of the troposphere at heights below 1.4km (Hanssen, 2001). This estimate was made with respect to a

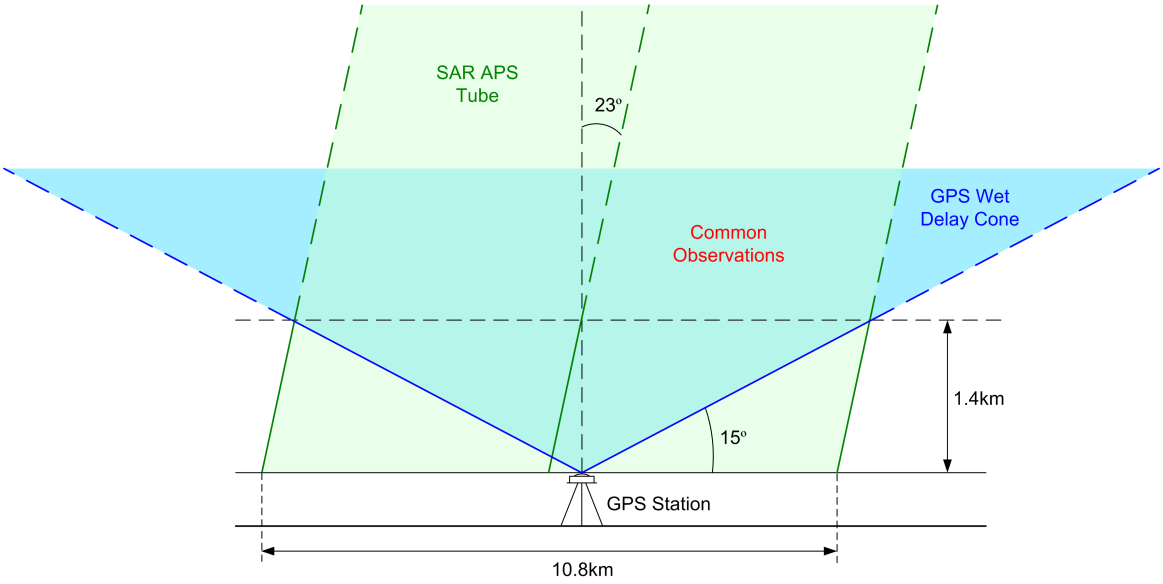

Figure 7.1: GPS wet delay and APS geometry. The GPS 'cone' of observations that contribute towards the ZWD and a SAR 'tube' of PS points can be overlapped at 1.4km height which is where over half the wet delay results from (Hanssen, 2001). Not to scale.

test area in the northern Netherlands and it is assumed to also be valid for Nottingham as it has a similar altitude, climate and latitude. Therefore a SAR tube around the GPS station that has a diameter equivalent to the cone at a height of 1.4km offers the best overlap in the respective geometries. Because of the SAR incidence angle, the GPS station lies slightly offset from the centre of the tube (0.6km at mid-swath), and with a 15° elevation mask, the tube has a diameter of 10.8km at mid-swath.

It is worth noting at this stage that most PSI methods estimate the APS values at each PS point and then interpolate for every pixel in the image (Ferretti et al., 2001). For the PSI method adopted here (Werner et al., 2003), the APSs are not interpolated and hence APS values only exist at the PS point locations. As the width of the SAR tubes exceeds 10km, this is not an issue as this will encompass many hundreds of PS points and the average value should therefore be representative of the area.

7.1.3 ZWD and APS Correlation

Using the common geometry model shown in figure 7.1, the correlation between the ZWD observations and the APS estimates was examined. PS point atmospheric phase estimates computed in §6.2.3.8, were converted to metres and mapped to zenith using

the inverse of the cosine of the incidence angle. These were then averaged around the GPS stations as described in §7.1.2.2 above, making allowances for the varying incidence angle and the concentric nature of the SAR tube.

7.1.3.1 Undifferenced Comparison

Because neither the ZWD or the APS observations are (effectively) differenced (see sections 6.1.4 and 6.2.3.8 for respective explanations why), a direct comparison between the two is possible once values have been zero meaned. This undifferenced comparison should result in a reduction in noise which is characteristic of differencing. Figure 7.2 shows the correlation between the ZWD and APS estimates at a given GPS station over time. Figure 7.3 is a scatter plot of all 191 common ZWD and APS values. KEYW was not included in the comparison as it is very close to BGS1; it is however included in the ZWD correction process as the difference in the GPS solutions between BGS1 and KEYW is relevant to the analysis. UNI1 and UNI2 have been omitted from all further processing because of the reasons mentioned in §6.4 and because they are close enough to other higher quality GPS stations to be able to positively influence the end outcome.

7.1.3.2 Results

Typically, the plots vary between ±10mm and the magnitude variations between the datasets is very similar. Correlation in the results is measured using Pearson's formula (Dalgaard, 2008) which is confidence tested at the 95% level using the t-test; this passes in all cases. The correlations themselves range from between 0.56 to 0.82, which is within expectations. Assuming that the APSs account for atmospheric phase to some degree, and also assuming that ZWD is representative of atmospheric water vapour and that this is the largest source of atmospheric phase variation, then the expectation is that the two datasets should be correlated to a certain extent, but variations will also be evident. This can be seen in figure 7.2 where certain epochs such as 2006.5 appears to have a pronounced bias at all stations; this is in fact due to the atmospheric conditions not being represented well by the PSI atmospheric model. Because the model used to estimate the APSs assumes the atmospheric term

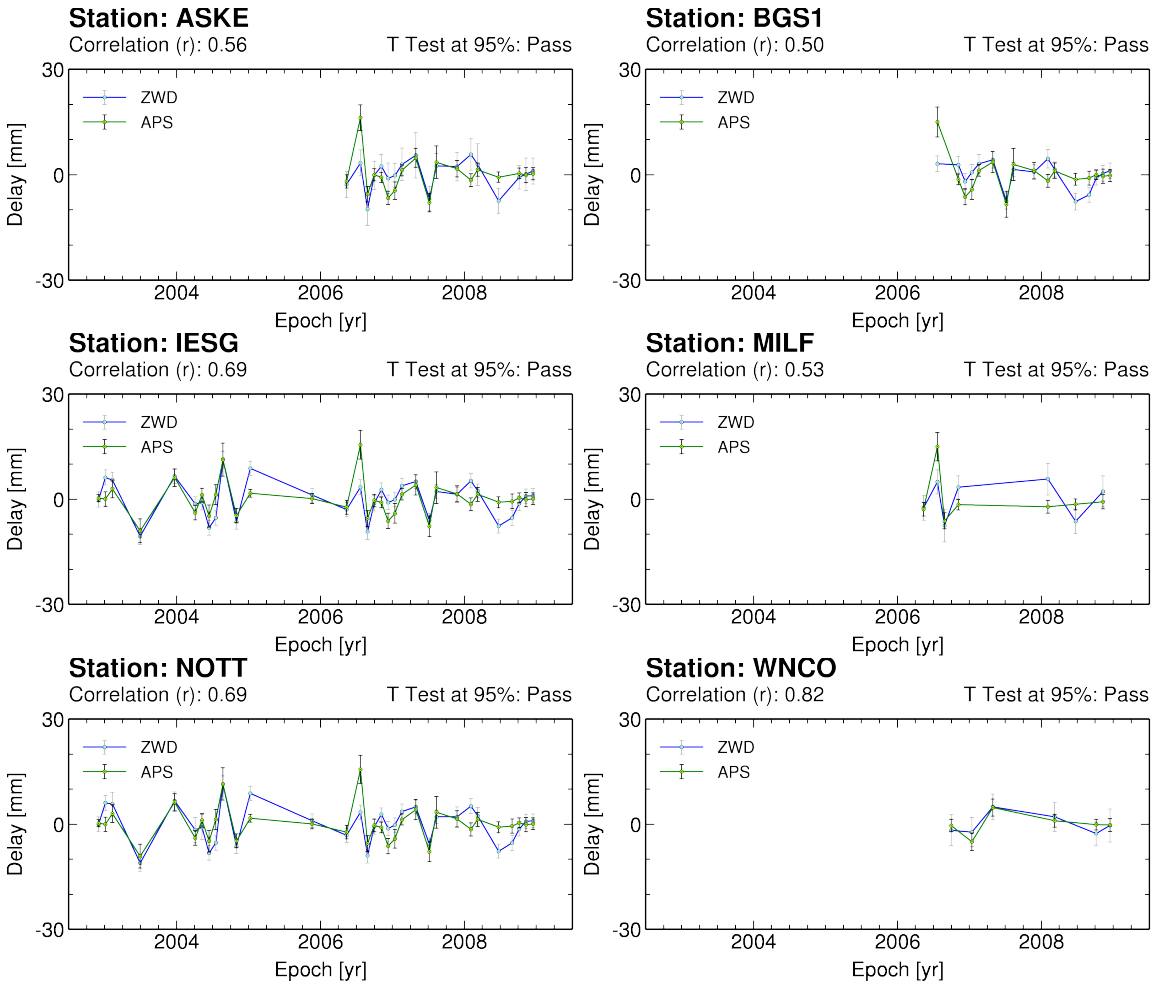

Figure 7.2: ZWD and APS correlation for GPS stations within the AOI. Correlation is T tested at the 95% level.

to be random over time (Ferretti et al., 2001, Mora et al., 2003), the amount that the ZWD and the APS vary, will to some degree depend on how non-random the real atmosphere was over the sampled dates involved. In a normal PSI processing scenario, this means that any non-random (temporal) variability that is also spatially correlated at small scales could either remain as residual phase or might be misinterpreted as non-linear deformation. The reverse of this is also true; non-linear deformation exhibiting random behaviour may be consumed into the APSs. Although non-linear deformation is not considered for this work, the adaptation of this method for non-linear studies is not precluded.

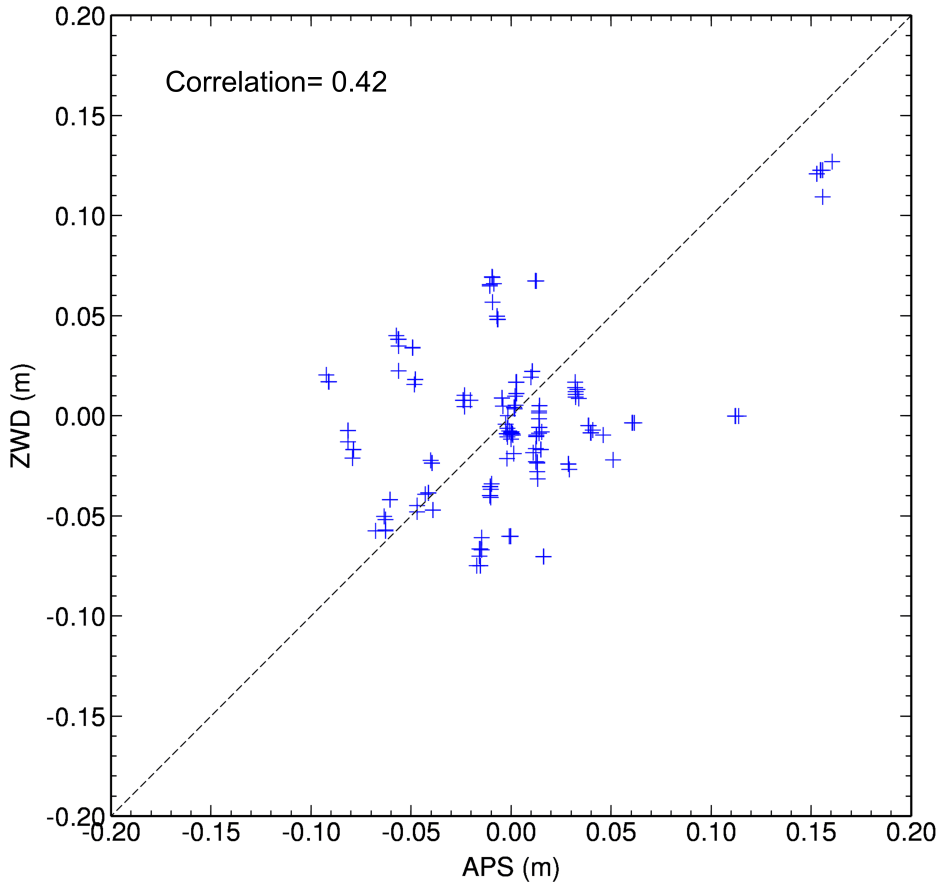

Figure 7.3: ZWD and APS scatterplot for all data points for ever date for which an APS value and a ZWD value can be determined. Whilst correlation is moderate at 0.42, this is not unexpected as variations will exist if the APS do not correctly model real atmospheric phase.

7.1.4 ZWD Screens

Eleven GPS stations from both inside and outside the AOI were used to create the ZWD screens. These stations comprised of the seven CGPS sites discussed in §4.8.2 and four of the six NCRA stations discussed in §5.5. ZWD values were collated from the GPS stations that were active on any given ENVISAT acquisition date. ZWD screens were then created for the entire interpolation area which is shown along with the GPS stations in figure 7.4. Green circles are scaled representations of the GPS cone areas used to compute the ZWD values.

To create the screens, a least squares method of biharmonic spline interpolation was used based on a linear combination of Green functions (Sandwell, 1987) centred at each point. This method has been used successfully to interpolate smooth surfaces

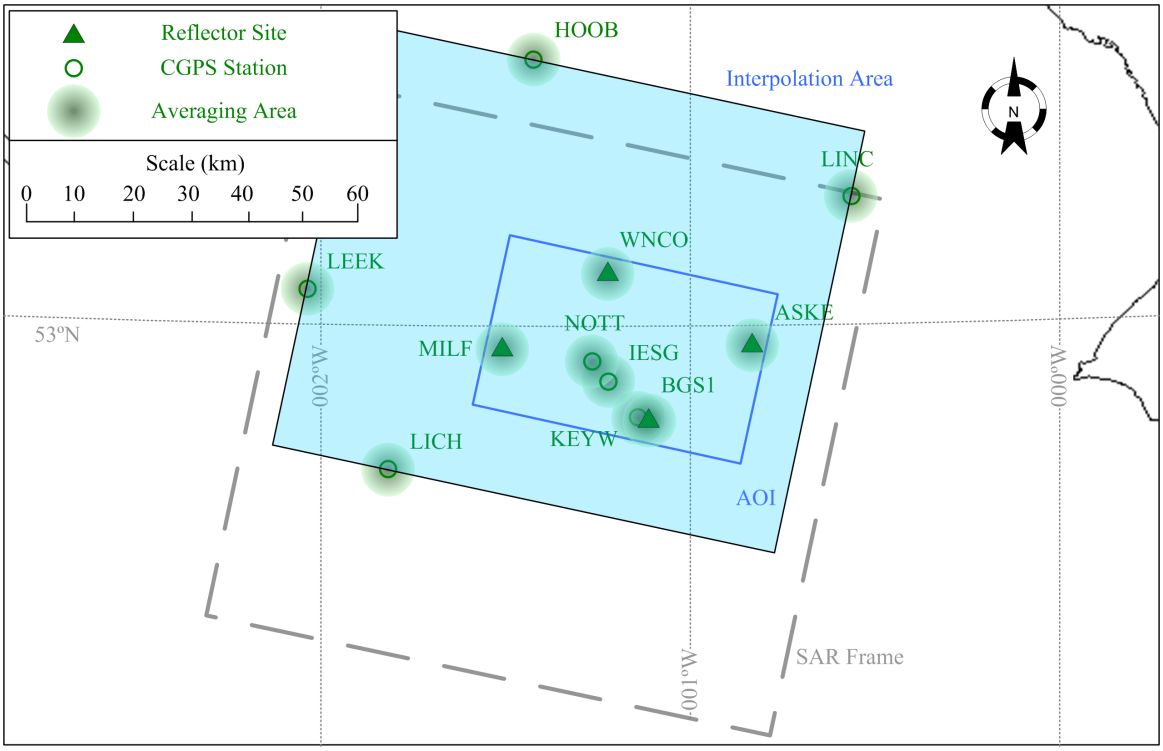

Figure 7.4: GPS stations used to interpolate the ZWD screens. The green circles are scaled representations of the GPS cones at 1.4km height used to compute the ZWD screens.

from sparse and irregularly spaced data such as altimeter data (Sandwell, 1987, Brooks et al., 1999).

7.1.4.1 Interpolation Testing

A test was conducted whereby each station's ZWD value for each date was estimated using the interpolator; these were then compared to the real ZWD values and standard deviations of the differences for each station were computed. As might be expected, the interpolator performed better for stations close to the centre of the AOI and for stations close to other stations. IESG is both close to the centre and close to another station and the standard deviation of the differences for IESG over all the dates was 4.2mm. ASKE however is on the eastern edge of the AOI with no stations within 24km, and not being bounded by other stations. The standard deviation of the differences here was 54mm. To put this in context, the spatial ZWD variation for this dataset on any one day varies between 14mm and 85mm. Therefore the standard deviations at the edges of the interpolation might exceed the variation across the scene

and hence the method is less valid here. Having said that, the main focus is on the stations closer to Nottingham, which all show standard deviations between 4.2 and 6.3mm which are well within the variations seen on any given day.

7.1.4.2 AOI ZWD Values

A three dimensional example of a ZWD screen for 11 August 2007 is shown in figure 7.5. The area represented here covers all the GPS stations and is therefore much larger than the AOI. The surface is interpolated from the eight ZWD values available on the date; the ZWD values have been demeaned and the geometry and pixel spacing for the plot is RDC multilooked by a ratio of 1:5. The plot shows how the (interpolated) ZWD values vary over an area of just over 8400km^2.

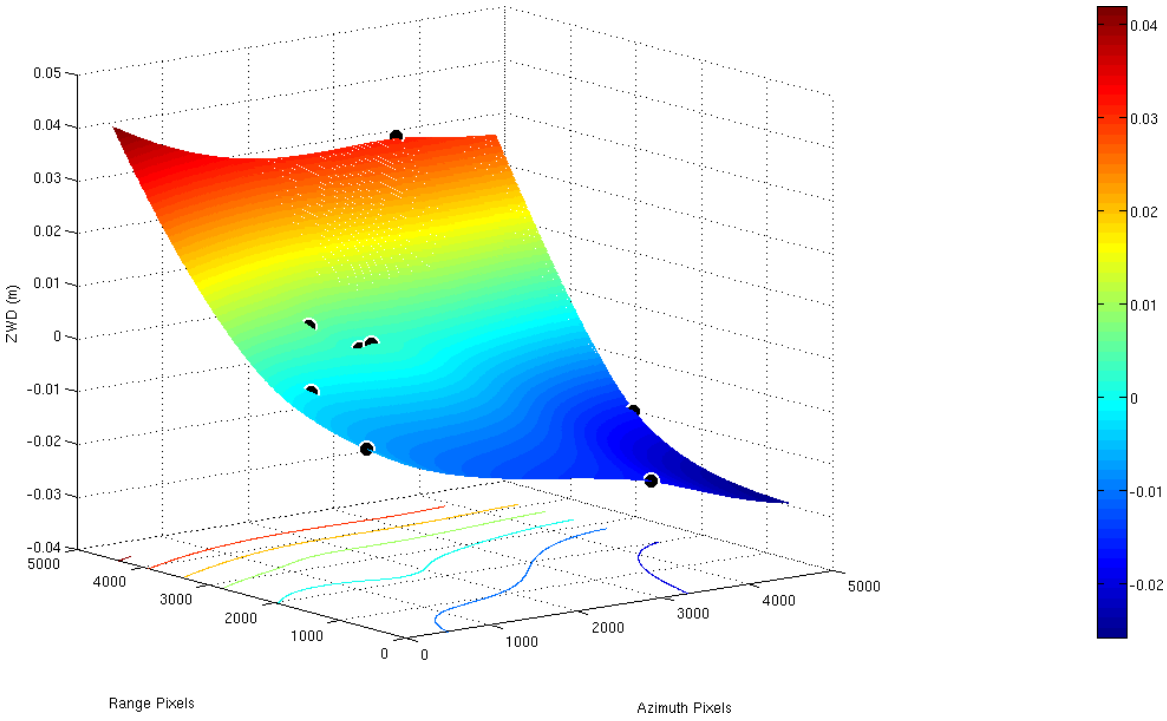

Figure 7.5: A 3D representation of the ZWD screen computed for the ENVISAT pass on 11 August 2007. Eight ZWD observations from GPS stations (marked with black circles) both inside and outside the AOI were used interpolating the surface using the biharmonic spline method which seeks to estimate the smoothest surface from a sparse set of data (Sandwell, 1987).

From these wider area ZWD screens, ZWD values covering the AOI were cropped, converted to phase measurements and mapped to the radar line of sight using the inverse of the cosine of the radar incidence angle.

Unfortunately the dataset does not permit ZWD screen estimation on every date in the stack. Seven of the dates have only two GPS stations (NOTT and IESG) operating on any one day and these are within a few kilometres of each other. Figure 7.6 shows twenty-eight of the twenty-nine ZWD screens created for the stack, the last being omitted purely for reasons of space. Below each figure is the acquisition date followed by the number of GPS stations used to create it in brackets.

7.1.5 ZWD Integration

Using the the differential interferograms already created, a new PSI analysis was initiated using only the twenty-nine layers (see table 7.1) for which ZWD screens could be created. Using all the scenes, some with ZWD correction and some without, would have biased the results in unpredictable ways and it was decided to process the stack without them. The SLC stack used comprised of the scenes shown in figure 6.3 minus the first seven dates.

The processing method used was identical to that described in §6.2.3 except that the ZWD values were extracted for each PS point location from the ZWD screens. These were then are subtracted from the differential interferograms. This was done after the candidate PS points had been selected; therefore the quantity and locations of the PS (at this stage) were identical to the uncorrected PSI analysis conducted in chapter 6.

This method was chosen in preference to subtracting the ZWD screens at the very start of the PSI process for practical considerations. Introducing them at the start of the PSI process makes very little difference to the overall outcome, but does change the choice and indexing of the points, which means that comparison between the results is less straightforward.

Following the subtraction of the ZWD screens, the process continues as before.

7.2 Results and Analysis

The results of the ZWD corrected PSI stack are now analysed. As well as a general comment on the quality of the results, several comparisons with other data can be

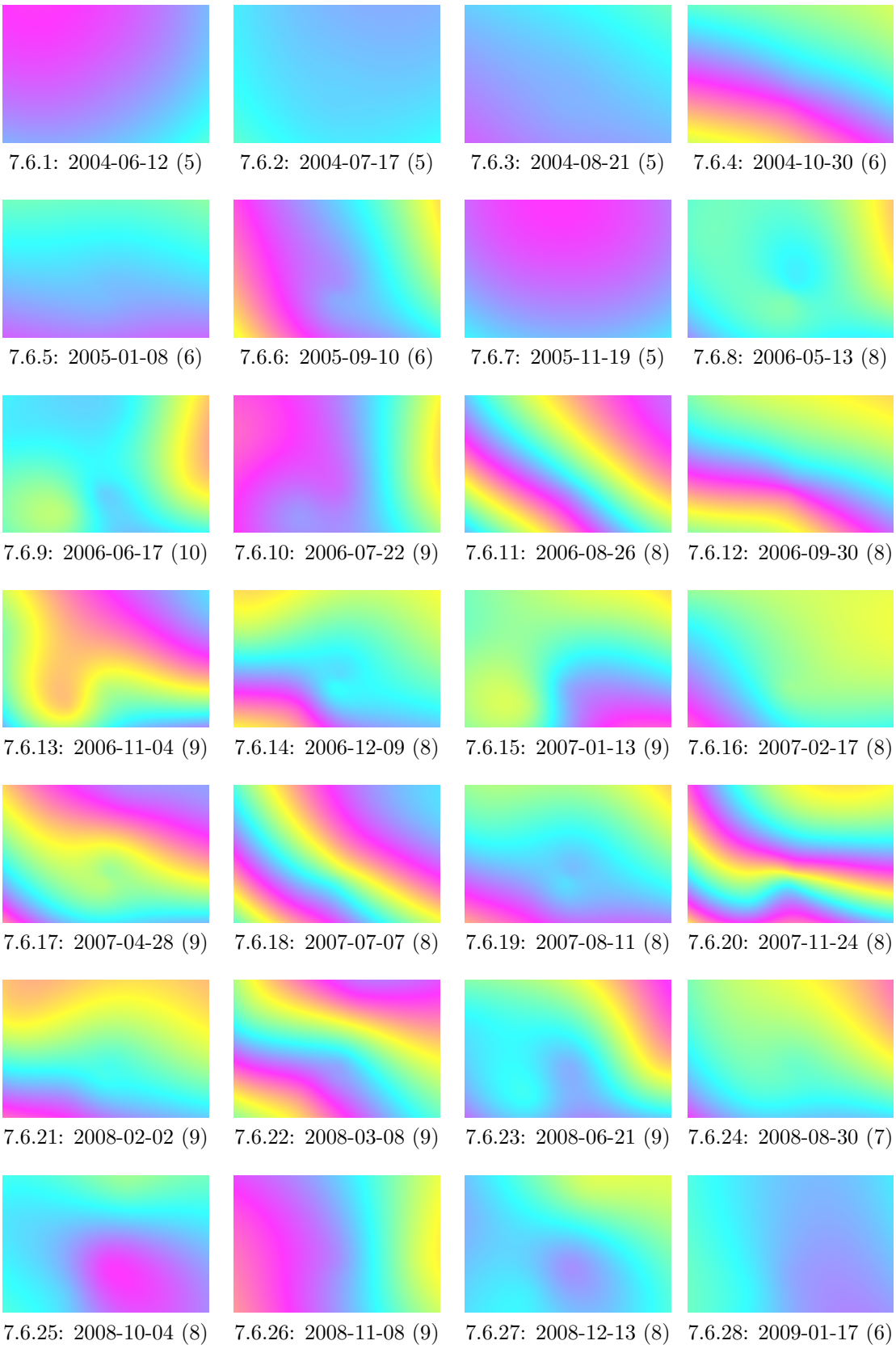

Figure 7.6: The ENVISAT acquisition date ZWD screens interpolated from GPS stations inside and outside the AOI. One colour cycle represents 8cm of ZWD. The number in brackets for each sub-caption indicates the amount of GPS stations available to create the screen.

made:

- Comparison with the ZWD uncorrected PSI result
- Comparison between the precise levelling results and either PSI result
- Comparison with the GPS velocities

7.2.1 PSI Result Comparison

The ZWD PSI result is shown in figure 7.7 in RDC geometry. From a purely qualitative standpoint, the result looks similar to the ZWD uncorrected result, with the same areas of motion and a similar spread of PS points. Just over 4000 more PS points were rejected in the regression stages of the corrected result. This is a reduction of about 3%, but the rejected points do not occur in any particular area, they are scattered throughout the image.

7.2.1.1 PSI Rejection

Rejection criteria is based upon phase standard deviation. During the estimation of height corrections and deformation phase, the phase differences between neighbouring scatterers are analysed as to how they vary over time. High standard deviations for these differences reveal noisy PS points which are then rejected if they exceed a threshold. The reasons for the increase in phase standard deviation may be due to the seven rejected scenes. Because the rejected points are scattered over the whole image, it is unlikely that they are being rejected because of the ZWD screens, as this would be more likely to show PS being rejected towards the edges, especially in the eastern part of the image where GPS stations are most scarce. This is where errors in the ZWD screens are at their highest and therefore the increased variations between neighbouring points should give rise to higher standard deviations.

7.2.1.2 Deformation Rates

The deformation rates in both results are similar when taken as a whole. Taking into account the common PS points only, the mean, minimum, maximum, standard

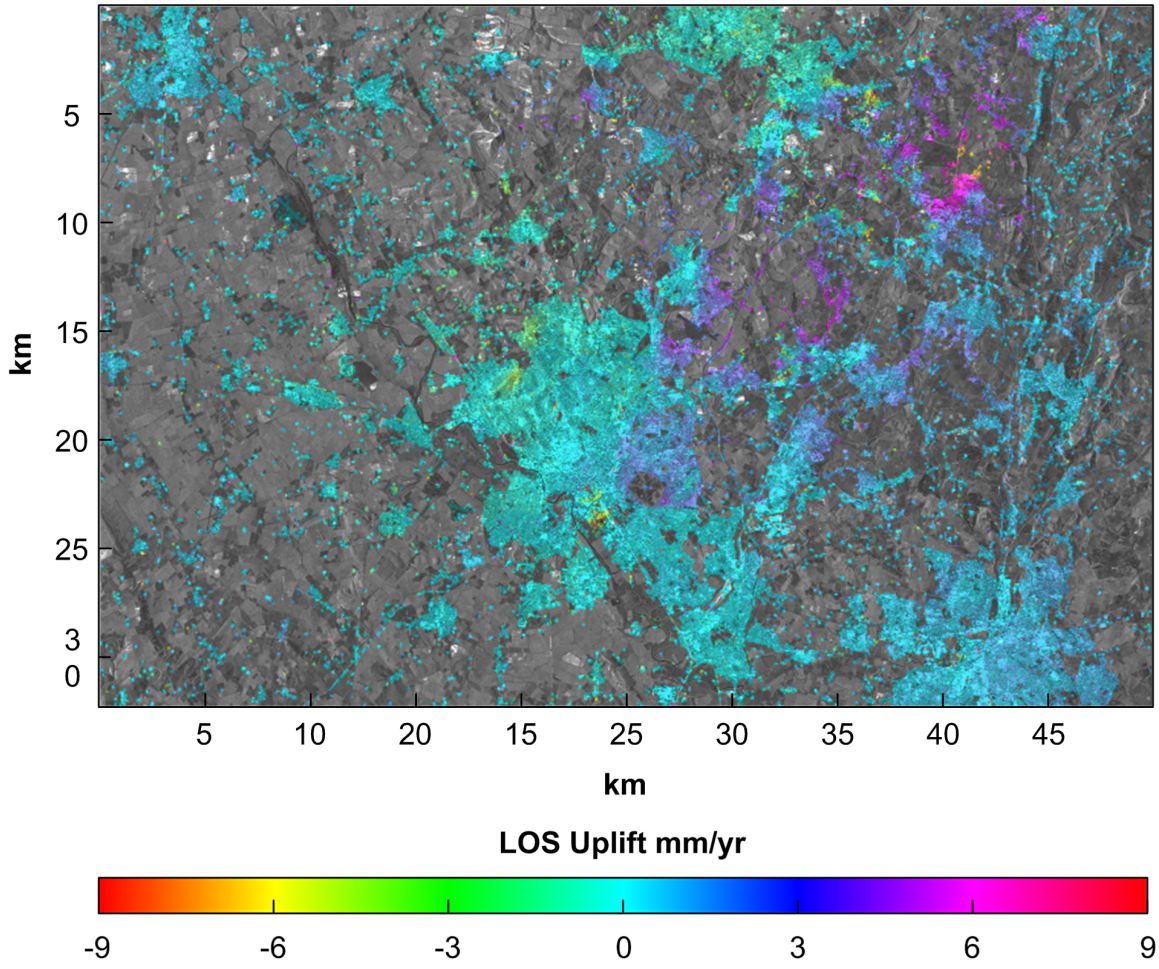

Figure 7.7: The ZWD corrected PSI result. ZWD screens were subtracted from the initial differential interferograms once the candidate points had been selected.

deviation and median values are all within 1.5mm/yr of each other. This is perhaps not surprising with PS point quantities of over 170,000. When the differences in deformation rates are viewed spatially however, a different picture emerges. Figure 7.8 is a map of the differences in deformation rates (corrected result minus uncorrected result) shown in RDC geometry. Both results use the same reference point and both reference point velocities are almost identical (a difference of 0.032mm/yr; the fact that the reference point has a velocity at all is an artefact of the IPTA method (Werner et al., 2003)). This is useful because it facilitates a direct comparison between the results. The image shows a surprising amount of variation across the scene, albeit at mainly low magnitudes, with PS points of similar magnitudes clustered in groups.

The deformation rates are initially estimated through an analysis of how phase

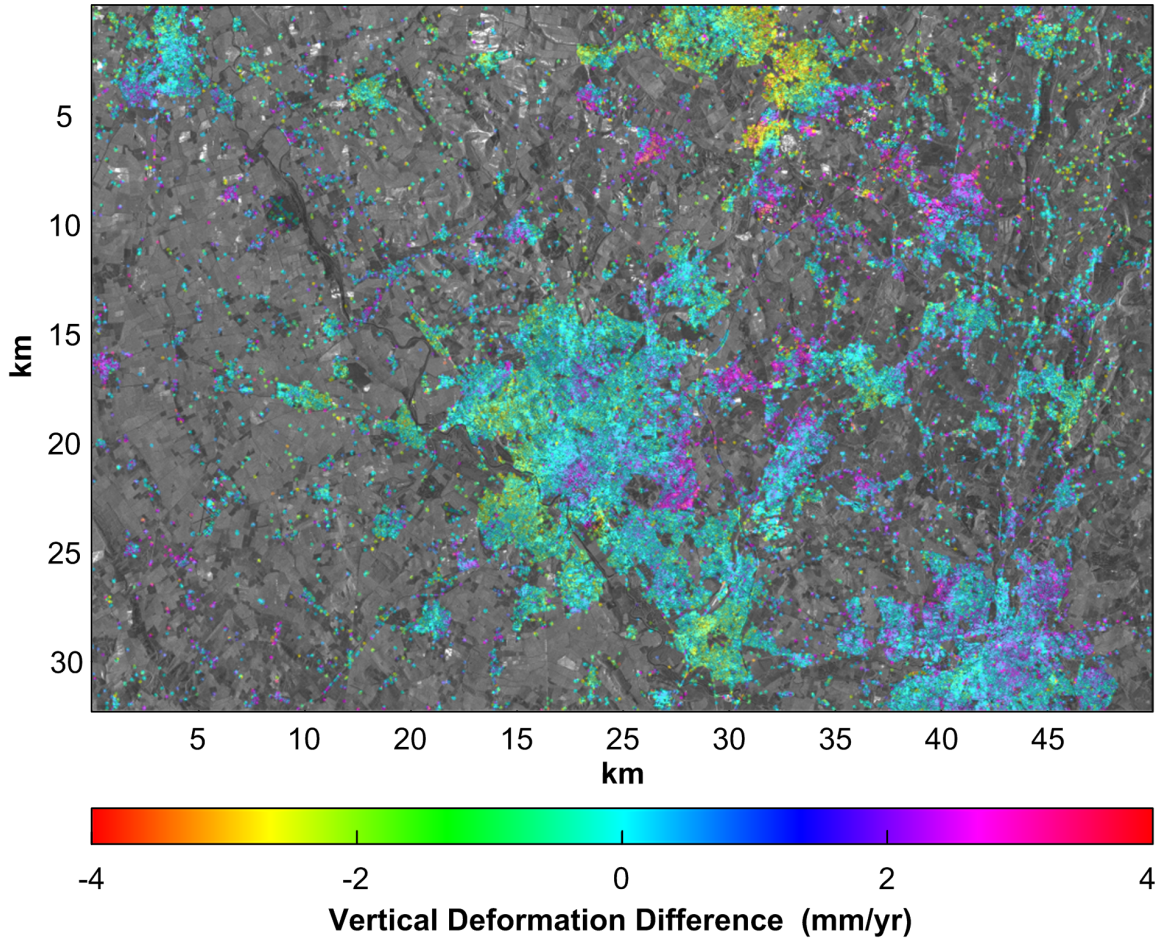

Figure 7.8: Differences in deformation rates between the two PSI analyses; the ZWD corrected minus the uncorrected PSI analyses. A clustering effect is evident across the scene. Checks reveal that these differences are not directly related to the seven extra APS screens present in the ZWD uncorrected PSI result.

differences between neighbouring points vary over time. These differences are later unwrapped to reveal the deformation rates at each point (with respect to a reference point). As the ZWD screens are smoothly varying surfaces, it is unlikely that their subtraction from the differential phase would directly introduce errors into the deformation rate estimation process in the clustered manner shown in figure 7.8. One explanation may be that the ZWD screens introduce systematic differences to the PSI process, which affects how phase is unwrapped and whether this is representative or not, this manifests itself (partly) as clustered differences in the deformation rates.

If the removal of the ZWD screens do result in less long-wavelength atmospheric phase in the differential interferograms, then this ought to mean that there is less residual phase that is spatially correlated, but temporally uncorrelated. However, as

discussed in §3.3, the assumption that the atmospheric phase behaves in a temporally random manner is not necessarily statistically valid for the sample sizes typically involved in PSI. If then, the subtraction of the ZWD screens also removes non-random looking atmospheric contributions which might otherwise be interpreted as deformation, then this should lead to an improvement in the deformation rates.

One other explanation is that the velocity differences relate to the extra seven APSs present in the ZWD uncorrected result. Comparing the differences with the mean of the seven APSs does not bear this out however.

7.2.1.3 Residual Phase

An examination of the residual phase standard deviations for the two PSI results in figure 7.9 show some interesting differences. The values for the ZWD corrected PSI result are spread over a wider range with a standard deviation (of the standard deviations) of 0.31 rad as opposed to 0.24 rad for the ZWD uncorrected PSI result. However, the corrected result has a lower mean value of 0.92 rad compared to 1.07 rad for the uncorrected result.

The wider spread of values suggests that in some areas the residual phase is noisier than before. This may be because the ZWD screens are introducing spurious phase values in areas where they are not representative. The lower mean however, indicates that on average, there is less noise in the PS phase regressions.

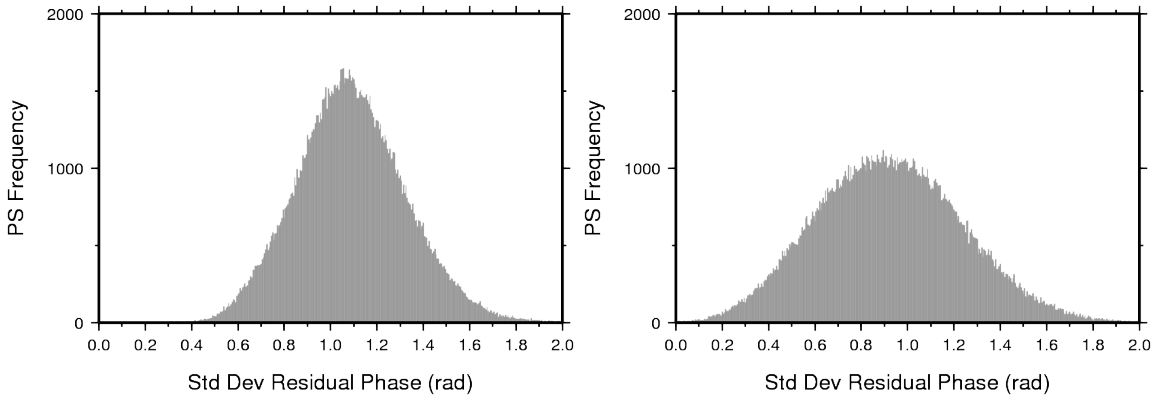

Figure 7.9: Residual phase standard deviations for the ZWD uncorrected PSI result **(left)** and the corrected result **(right)**. The corrected result has a wider spread but a higher mean, this may be indicative of ZWD screens that are representative in the central AOI but less so towards the edges.

If the ZWD screens are (on average) representative of atmospheric phase, then it is logical to assume that a reduction in the average residual phase would follow. Furthermore, the standard PSI model assumes atmospheric phase to be temporally uncorrelated (Ferretti et al., 2001, Mora et al., 2003), yet statistically it is difficult to see how this would be so with such a small sample (see §3.3 for a discussion on this). Therefore, any spatially correlated but (apparently) non-temporally random phase in a normal PSI study might manifest either as non-linear deformation or unquantified noise left over at the end on the process in the residual phase.

7.2.1.4 Deformation Uncertainties

Figure 7.10 shows histograms of the deformation uncertainties for the ZWD uncorrected (left) and the ZWD corrected PSI results. The term 'uncertainty' used here refers to a statistic which is output by the regression covariance matrix which is related to the standard deviation of the deformation phase. It is a measure of the statistical quality of the goodness of fit in the regression slopes. Whilst it can be under or over-optimistic to varying degrees, the difference between the noise in the phase measurement and the deformation rate uncertainty is a linear scale factor (Werner et al., 2003) and therefore it is a useful parameter for a comparison such as this.

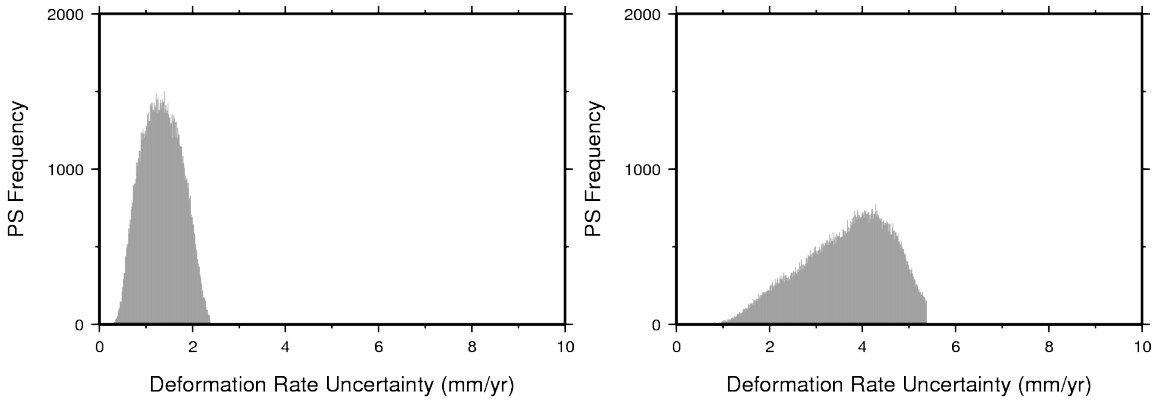

Figure 7.10: Deformation uncertainties for the ZWD uncorrected PSI result **(left)** and the corrected result **(right)**. The uncertainties are a measure of the statistical quality of the goodness of fit in the regression slopes. The corrected result is not symmetrical as would be expected, this may be due to the ZWD screens being unrepresentative towards the edges of the AOI introducing systematic bias in the uncertainties.

The maximum values are more than double that of the uncorrected result and the

spread is also larger. An inspection of the spatial distribution of the deformation uncertainties reveals that these higher values are not clustered in any way and therefore it is likely that the increase in values has arisen from the reduced number of images in the corrected result. Figure 7.11 shows the spatial distribution of deformation uncertainties across the AOI for the ZWD corrected study.

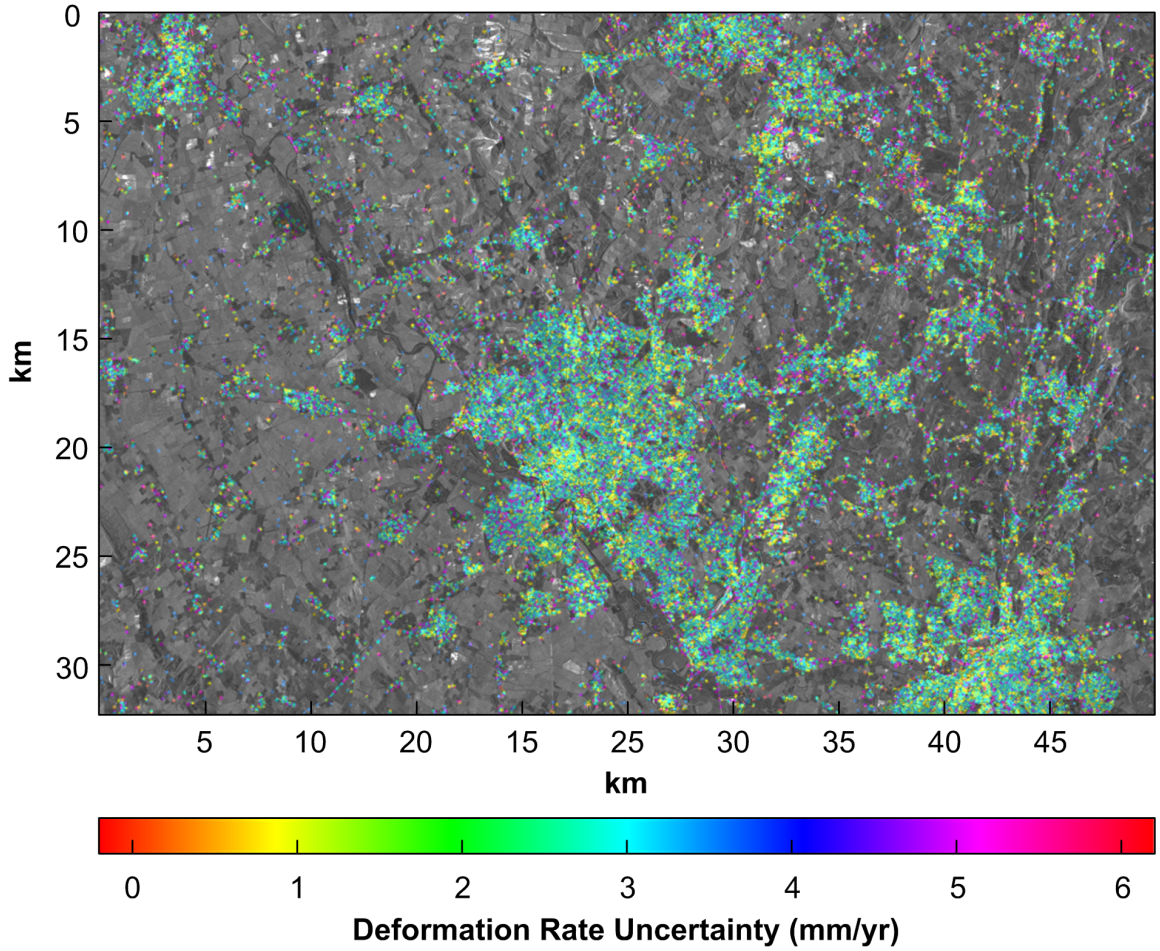

Figure 7.11: The spatial distribution of the increased deformation uncertainties in the ZWD corrected PSI result. The random spread indicates that the increase is probably not due to the introduction of the ZWD screens.

The deformation rate uncertainties for the corrected result are skewed in a non-symmetrical manner. This means that the goodness of fit in the estimations of the regression slopes is no longer evenly distributed about a mean. There is no obvious reason why this would be so; a skewed distribution however is unlikely to be due to a decrease in the number of images in the corrected result. This could be seen as evidence that the ZWD screens have introduced a systematic bias into the corrected

result, albeit, a reasonably small one.

7.2.1.5 Height Corrections

An examination of the respective height corrections in figure 7.12 shows almost no difference between the results. An examination of the perpendicular baselines in each study also shows almost no difference; it is therefore reasonable to expect little variation in the height corrections. This is because the PSI method first analyses pairs of points in the temporal domain to examine how phase differences may be correlated with the perpendicular baselines (the slope of regression for each PS point indicating the required height correction). This shows that the baseline improvement process detailed in §6.2.3.5 has not been biased through the introduction of the ZWD screens. A comparison with the NEXTMap 5m DEM mentioned in §6.5.2.2 unsurprisingly also provides very similar results between the two PSI studies.

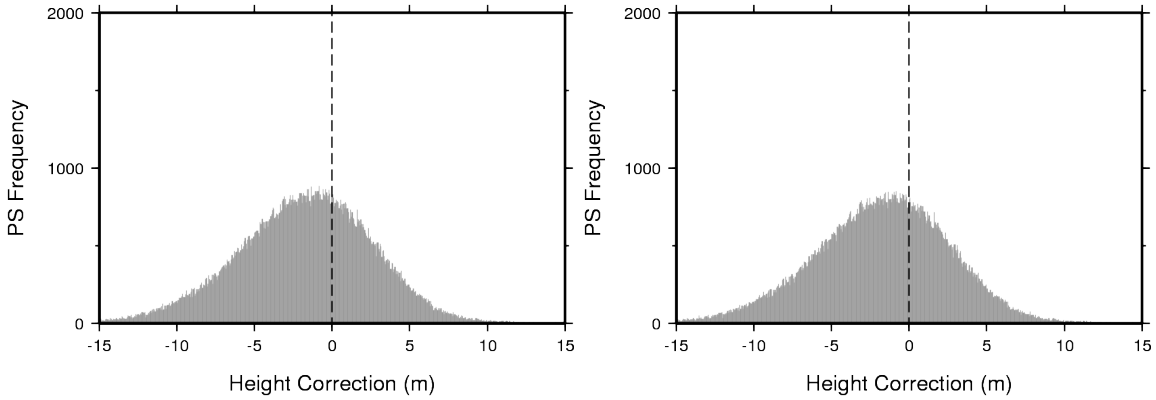

Figure 7.12: Height corrections between the SRTM 90m DEM and the resulting PSI heights between the ZWD uncorrected result **(left)** and the corrected result **(right)**. The height correction histograms are almost identical.

7.2.2 Levelling Comparison

As discussed in §6.3, a precise levelling campaign was undertaken following advice from members of BGS that the area was prone to ground motion; this arose mainly from a commercially sensitive PSI study using ERS data between 1993 and 1999. Comparing levelling and PSI is not a straightforward process. Levelling is a spatial difference between two directly measurable points, whilst PSI is a temporally based

difference between two SLC dates, Marinkovic et al. (2008) sums up the issues well. A comparison is possible through a double difference in time and space. An overview of the area with the levelling staff positions and the PS points is shown in figure 7.13; PS points shown here are taken from the corrected result. The distance between the start point in the northeast of the image and staff point 24 is 1km.

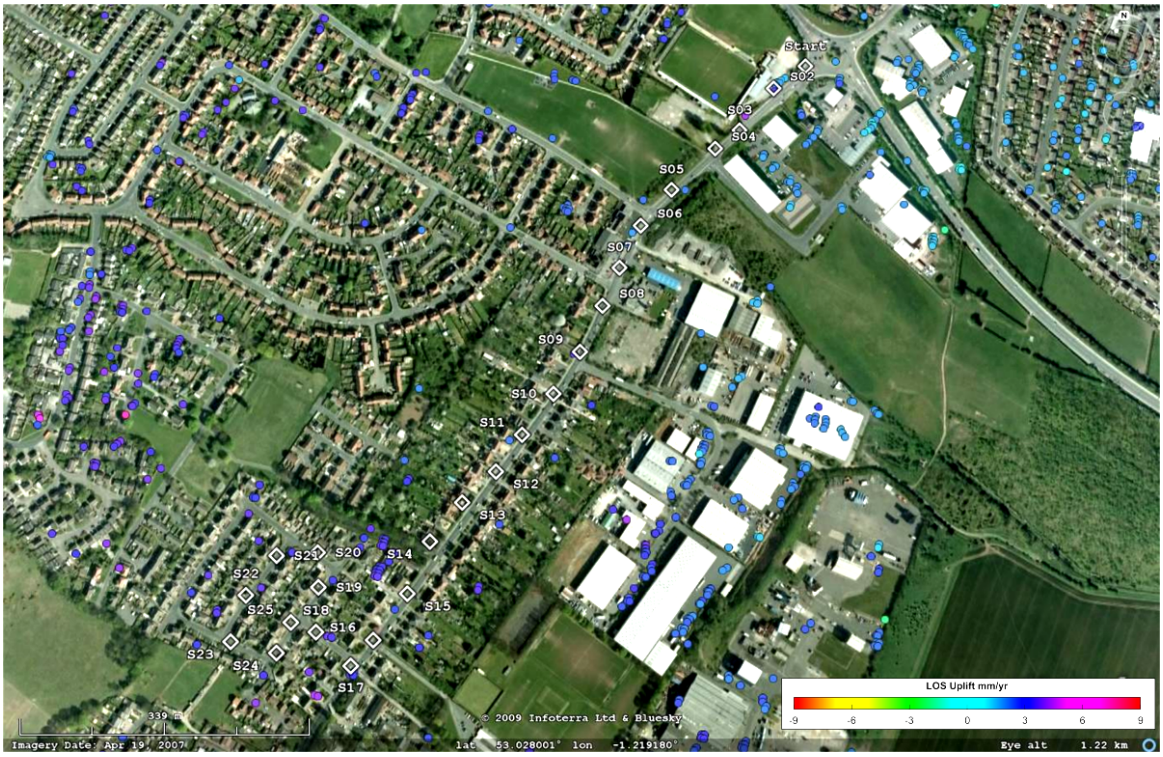

Figure 7.13: The Hucknall precise levelling campaign. White diamonds show the staff positions observed four times of the twelve month period from August 2007 to August 2008, coloured dots represent the PS points.

The start point was given an arbitrary height and all other points were levelled with respect to this four times over the course of a year. The levelling spatial difference was computed between the point labelled 'Start' and an average of the heights observed for the eight staff points labelled S17 to S25. The PSI spatial difference was taken from an average of the points within a 100m radius of the start and from those within a 100m radius of S25.

The temporal difference for both datasets is taken between 21 August 2007 (the date of the first levelling observations) and each one of the three successive levelling dates. Because these dates are not coincident with ENVISAT passes (but they are within ten days) the displacements for the PS points were linearly interpolated.

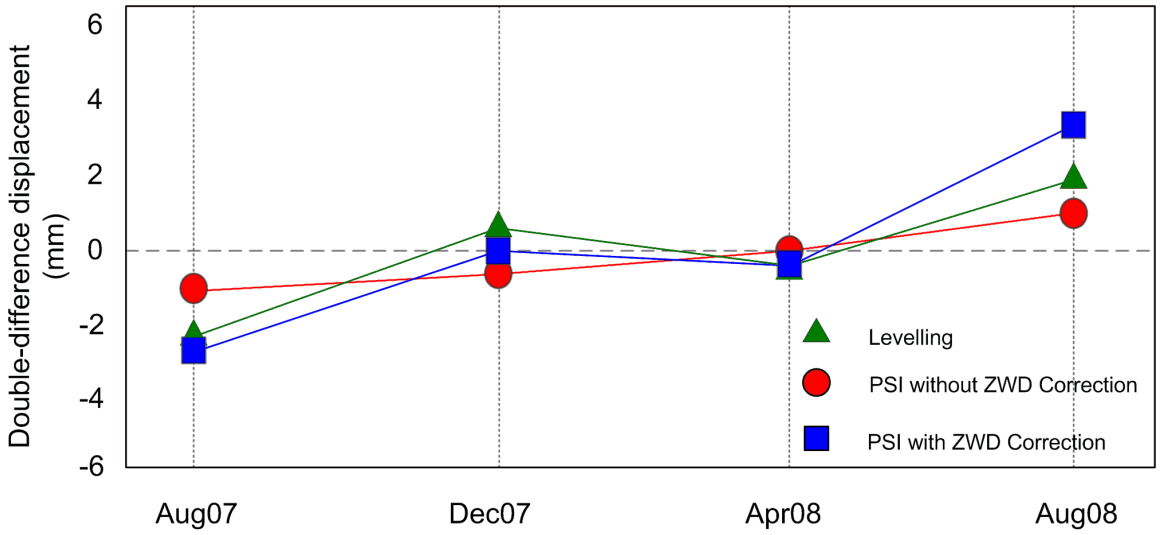

Figure 7.14: The Hucknall precise levelling results showed against the two PSI studies. Observations have been double-differenced (in space and time) to provide a meaningful comparison. The correlation between the levelling and the ZWD uncorrected PSI result is 0.67 and 0.81 between the levelling and the ZWD corrected PSI result.

Figure 7.14 is a plot of the double differences. The correlation between the levelling and the ZWD uncorrected PSI result is 0.67 and 0.81 between the levelling and the ZWD corrected PSI result. The t-test was used to test the significance of the correlations at the 95% level with both correlations passing the test. Although the corrected result shows improvement, the dataset is small, as are the variations. Error bars were not plotted for ease of viewing, but the mean PS point deformation uncertainties for the corrected result were slightly higher at 1.7mm compared to 1.2mm for the uncorrected result.

7.2.3 GPS Comparison

A comparison of the GPS and two PSI results is shown in figure 7.15. GPS errorbars have been omitted for clarity; the quality of the GPS results is addressed in §6.4. The ZWD uncorrected and corrected PSI results are shown in red and blue respectively. The error bars for the PSI result relate to the deformation uncertainties discussed in §7.2.1.4 and outliers in all datasets have been removed during their respective processing. Correlation coefficients (r_c for the corrected result and r_u for the uncorrected result) were computed between the PSI results and the corresponding GPS

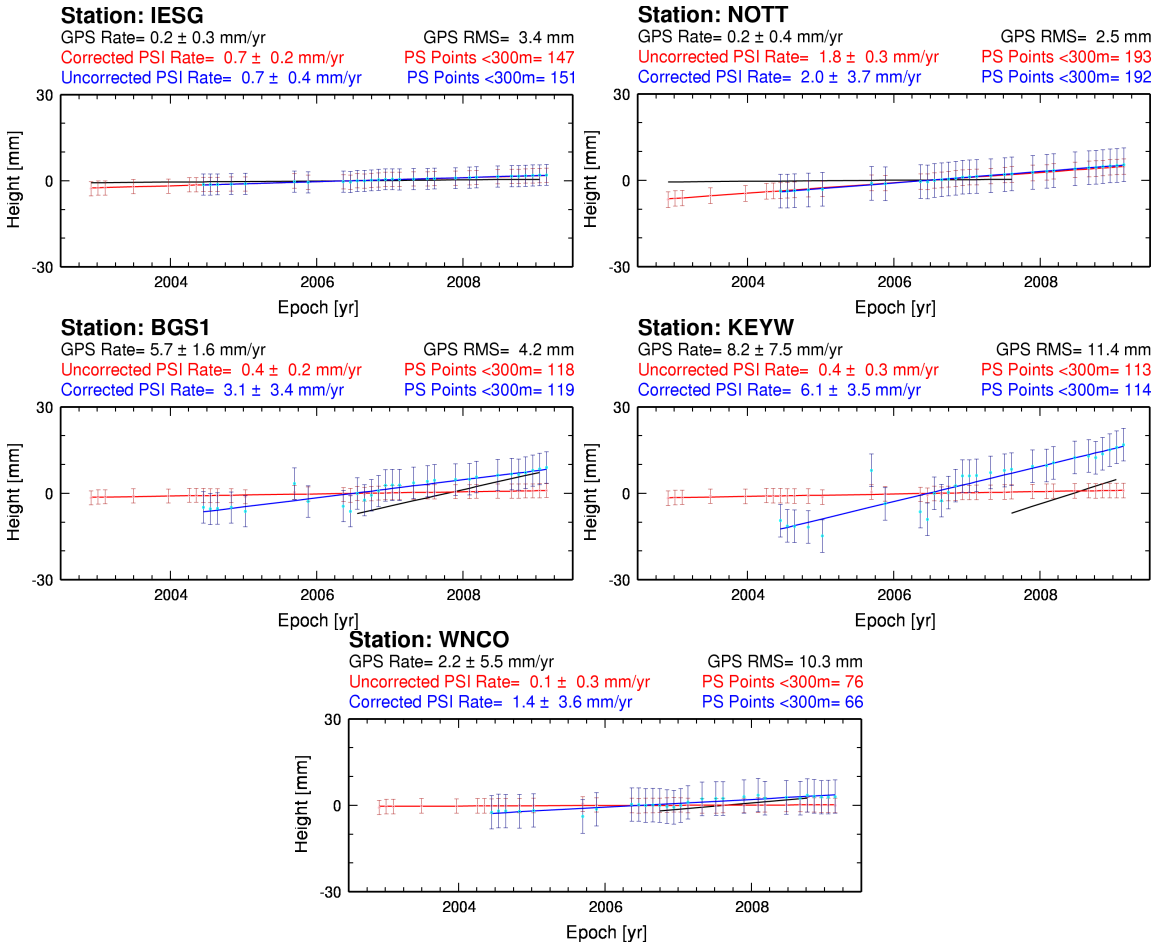

Figure 7.15: GPS and the two PSI result's velocity estimates. Black represents GPS while red and blue represent the ZWD uncorrected and corrected PSI results as indicated above each plot.

result. Significance was determined using the t-test at the 95% confidence level, all correlations pass the test unless otherwise stated.

7.2.3.1 NOTT and IESG

The CGPS stations IESG and NOTT offer the longest and highest quality GPS time series for stations within the AOI. Both PSI results are in very good agreement with the GPS result for IESG with no appreciable difference in rates; correlation coefficients are close to 1 for both PSI results. Because errors in the atmospheric term are spatially correlated, it is not surprising that results at IESG agree so well. Agreement at (effectively) the reference point suggests that there are no evident systematic biases in the results of the different datasets.

At NOTT, again the PSI results are very similar but deviate from the GPS rate by just over 1.5mm/yr; r_c=0.77 and r_u=0.73. There is also a marked difference between the uncertainties of the two PSI results. This maybe due to the smaller time series used for the corrected result. NOTT is approximately 3km from the reference point, and so it is possible that some minor spatially correlated errors have influenced the rates. It is also possible that non-linear deformation in the residual phases has caused the disparity.

7.2.3.2 BGS1 and KEYW

At BGS1, the GPS rate is a much more marked 5.7mm/yr. The small increase in the RMS and uncertainties compared to IESG or NOTT are minor. The PSI rates also show a marked difference, the uncorrected rate is almost flat, whereas the corrected rate is 3.1mm/yr; r_c=0.65 whereas r_u=0.45. The corrected rate again is slightly noisier than the uncorrected with an increase in the deformation uncertainly of 3mm/yr. This uncertainty means the the corrected rate at BGS1 could be as low as the uncorrected rate.

A similar result occurs at KEYW which is only a few hundred metres from BGS1. Here, the corrected PSI result is again much closer to the GPS result, but according to the t-test, the correlation coefficient is not significant for the degrees of freedom available at the 95% level; significance occurs at the 77% level. This is probably due the low sample size and high noise in the GPS timeseries (§6.4.1).

7.2.3.3 WNCO

Again, the GPS time series at WNCO shows moderate uplift and the corrected PSI rate shows better agreement with this than the uncorrected. The differences however are minimal (r_c=0.77 and r_u=0.73) and the uncertainty in both the GPS results and the corrected PSI results are greater than the estimated quantities.

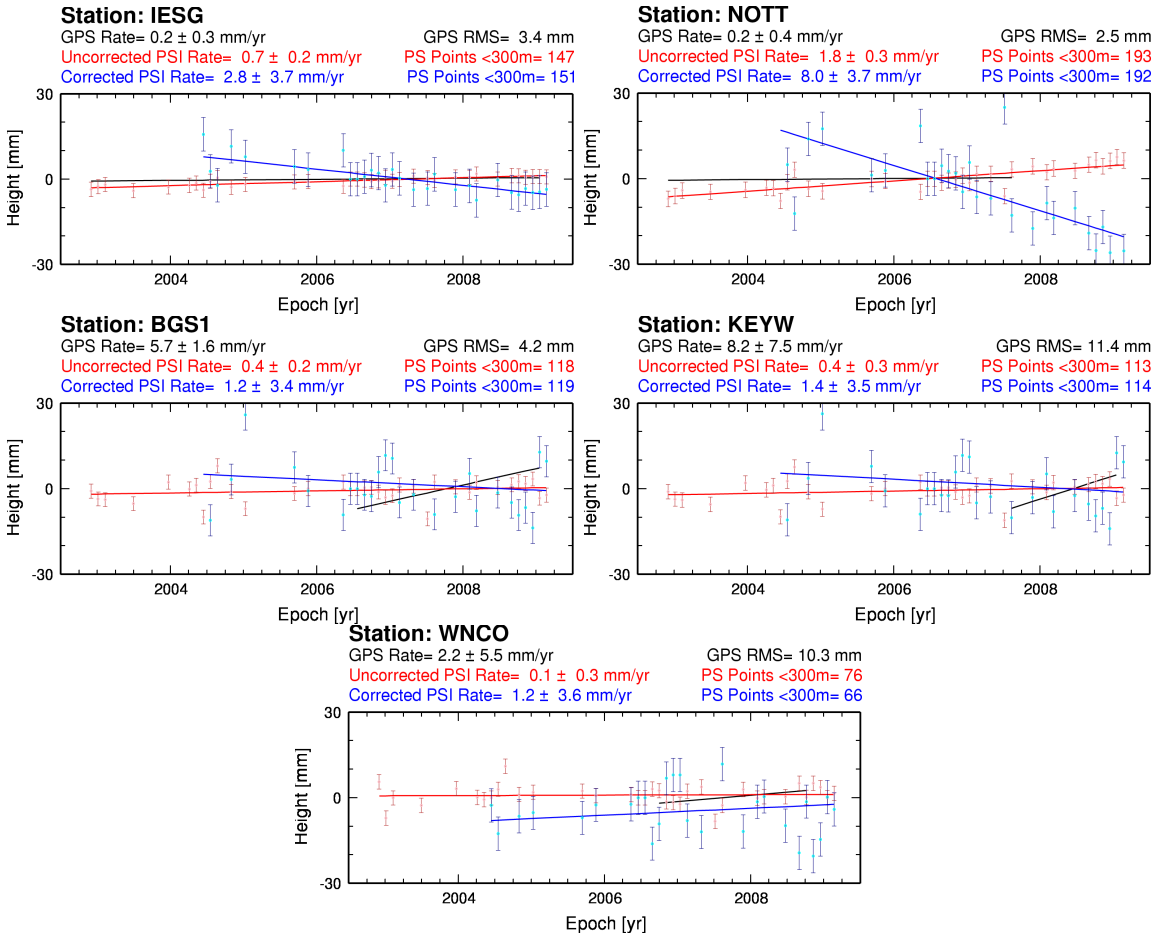

Figure 7.16: GPS and the two PSI result's velocity estimates computed with the atmospheric phase screens added to the PSI time series at the end of processing. Black represents GPS while red and blue represent the ZWD uncorrected and corrected PSI results as indicated above each plot.

7.2.4 Atmospheric Effects on PSI Time Series

A further comparison of the GPS and two PSI results is shown in figure 7.16, this time with the atmospheric phase screens added back to the PSI result at the end of processing.

The figure shown is in stark contrast to figure 7.15. Clearly both time series exhibit a good deal more noise as would be expected, but the rates for the uncorrected time series are virtually unchanged whilst the rates for the corrected time series are very different. An explanation for this may stem from the fact that the APSs in the ZWD uncorrected result are all attributable to random (over time) noise, which has little or no overall effect on the PSI rates. In contrast to this, the ZWD corrected results

have random and non-random atmospheric effects removed; the overall effect of this when added back to the result at the end of the processing is pronounced biases in the time series.

7.3 Discussion

Comparisons between two PSI results show that the ZWD corrected result has a broader range of residual phase standard deviations, although the mean is lower. It is difficult to say whether the broader range is due to the reduced stack or whether the ZWD screens have have influenced the process negatively. Evidence for the former stems from the fact that the extra rejected PS candidates in the ZWD corrected result are scattered throughout the image rather than being clustered in areas where the ZWD screen is not representative. The lower mean residual phase standard deviation indicates a reduction (on average) in the noise, although this is not apparent at the PS points close to GPS stations. This reduction may have resulted from a general decrease in atmospheric phase due to the subtraction of the ZWD screens; it is also possible that the ZWD screens better represent any non-temporally random atmospheric artefacts, which might otherwise be classified as residual phase (or non-linear deformation). As discussed in §7.2.1.2, a reduction in mean residual phase might be indicative of an improvement in deformation rates, which to some degree, is evident in the levelling and GPS comparisons discussed in sections 7.2.2 and 7.2.3 respectively.

The fit of the ZWD screens varies from good to bad over the AOI; in the principally important area of Nottingham city, the measured fit (see §7.1.4.1) is good. As expected, it is particularly poor where the GPS network is sparse or does not completely encompass the AOI such as in the southeast. The systematic errors this introduces into the PSI process may explain the skew introduced into the deformation uncertainty histogram in §7.2.1.4. Also apparent is a more general increase in the deformation uncertainties for the ZWD corrected result; these increases occur in no particular area and are therefore probably attributable to the reduction in the stack.

Overall, the results have shown that the introduction of ZWD screens can have a positive influence on PSI studies. Comparison with levelling and GPS results show

improvement when compared to results without ZWD screens, although the datasets involved are sparse and the statistical significance is at times limited.

When the ZWD corrected and uncorrected PSI time series have the atmospheric estimates added back to the deformations phase and shown against the GPS time series (figure 7.16, stark differences are noted. The ZWD uncorrected rates are virtually unaffected whereas the ZWD corrected results display pronounced biases introduced by the corrected APSs. It is therefore reasonable to presume that ZWD corrected APSs are indeed not random over time which creates unpredictable linear regressions in the deformation rates when re-introduced. It should be noted that the level and unpredictability of the noise shown maybe an indicator of the multi-stage iterative processing methodology. These signals may otherwise have been interpreted as non-linear deformation or residual phase. This further strengthens the case that PSI analyses can be improved using ZWD correction because (apparently) non-random atmospheric artefacts are removed and not misinterpreted.

7.4 Summary

An experiment to integrate PSI and GPS has been undertaken which fulfils the aims and objectives originally stated in §1.6. ZWD screens were interpolated from discrete points and these were subtracted from differential interferograms used in a PSI study. Comparisons were then made between the ZWD corrected PSI result and a previously determined ZWD uncorrected PSI result, a precise levelling campaign and GPS station heights. A critical analysis was made of the two PSI results together, analysing differences between them and suggesting reasons for them. The ZWD screens improved the correlation between the PSI results and the levelling by 0.14. Comparison with the GPS results showed improvements typically of the order of 1.5-6mm/yr, although the uncertainties in both the GPS and the PSI study mean that statistical significance is at times limited. When PSI time series are viewed with the APSs added back at the end of the processing runs, the ZWD corrected time series exhibits strong non-random signals which would otherwise be interpreted as either non-linear deformation or residual phase.

Chapter 8

Conclusions and Recommendations

This chapter reviews the main elements of the thesis. The aims and objectives are restated after which each aim is visited in turn, summarising how it was achieved, to what level of success and what could be done in future to improve results. This leads to a list of recommendations for future work.

8.1 Review of Aims and Objectives

Chapter 1 included a set of aims and objective for the project. The aims were stated as follows:

- Study background areas and conduct a literature search concerning GPS and PSI integration.
- Analyse what value corner reflectors might bring to PSI.
- Consider how GPS might be integrated with PSI.

The objectives were:

- Identify gaps in GPS and PSI integration research.
- Investigate the potential for long-term corner reflectors and their use as artificial PS points.
- Investigate the potential for reference point bias removal using corner reflectors.

- Consider how GPS might be used to improve PSI atmospheric phase screens.
- Determine how GPS might be used to validate PSI studies.

These are now discussed in the context of what was achieved and what could be improved upon. Following this, recommendations for further work are made.

8.2 Integration Research

Major topics relevant to the project were explained in chapter 2 which also referenced definitive sources for further information. State of the art research concerning atmospheric delay, calibration for SAR interferograms, corner reflectors in InSAR were then discussed in chapter 3. This led naturally on to the research motivations including how corner reflectors might be used in PSI studies, assumptions about atmospheric phase, the use of GPS in PSI studies and the validation of PSI. The chapter concluded with a summary of the current gaps in research concerning these subjects.

8.3 Corner Reflectors in PSI

Nottingham was chosen as the test site for the project as it had clear advantages over other alternatives. Firstly, it is a geologically interesting area, as was shown in §4.5 and indicated in §6.5. It is also well served by geological literature (Charsley et al., 1990, Donnelly, 1999, EDINA, 2009, Howard et al., 2010), being home to the headquarters of BGS. A major advantage was the proximity of the reflector network to the University, the consequences of this being a larger dataset as more funds were available for observation campaigns. The existing GPS and SAR data archives (§4.8) were comparable or better than other potential site choices.

The NCRA consists of six corner reflector sites: three permanent reflectors and three non-permanent (§5.2). The three non-permanent reflectors use an innovative pillar mount which interfaces between the pillar and a modified reflector or a GPS antenna (§5.2.4); the achievable positional precision of these sites is very close to that of a permanent site (§5.5.1). Also, the modification of the reflectors and the design

of the pillar mount make possible the potential for many other sites in the UK from the 6000+ existing triangulation pillars. This of course could be extended to other countries such as Ireland that also use the OS pillar design.

8.3.1 Observation Model

The design of the observation model was an exercise in achieving the optimal outcome with the time and resources available (§5.4); in this respect, the adopted strategy fulfilled the requirements. Tests showed that PPP processed six hour GPS sessions, even with a fifteen minute gap in the middle, can still provide results comparable with standard daily solutions (§5.4.5). The increase in uncertainty is apparent, but not to the extent that the observations become unusable.

8.3.2 ENVISAT Data

The existing ENVISAT dataset prior to the start of the project consisted of fourteen archived scenes of the area (§4.8.1), which was comparable or better than the other potential project sites. It was initially envisioned that these scenes would be used for checking coherence and other lower priority tasks. Following the above average ENVISAT instrument conflicts that occurred over Nottingham between 2006 and 2009 (§5.5.1), the archived scenes became crucial to satisfying the project aims and objectives. The reduction in data was exacerbated when ESA redesigned the orbit cycle making acquisitions after February 2009 unsuitable for SAR interferometry.

It was not possible therefore to build an ENVISAT catalogue of sufficient size (with the time available) to properly integrate the reflector network into the PSI analysis (§5.7). Thus an alternative focus for the project was sought which utilised the data available and fulfilled the project aims and objectives.

8.3.3 Reflector Visibility

The reflectors used in this project, when placed in areas with medium to low clutter, were unambiguously visible in the SAR data (§5.5.2) and appear as candidate and confirmed PS points using the PS selection method chosen for this project (§6.2.3.1).

At the outset of the project, no published research could be found involving corner reflectors this small with ENVISAT SAR data; therefore there was no evidence that they would be visible or qualify as PS points. Furthermore, at the time the sites were being selected, the Cat-1 proposal had not yet been agreed by ESA and therefore no existing dataset was available for checking site amplitude variation. These risks were balanced against the available research involving both small corner reflectors and similar SAR instruments.

8.3.4 Field Observations

Over 800 hours of GPS data was collected by field teams for the six NCRA reflector sites. Many more hours were added to this from the CGPS stations in and around Nottingham. This data coincided with the twenty-two successful ENVISAT acquisitions. This is a valuable field observation archive that may be useful to future projects.

In light of evidence that arose in April 2007, a precise levelling campaign was devised (§6.3) to assess an area of potential ground motion. The levelling campaign lasted for a year and the precision of the results was better than the allowable precision for first order levelling.

8.3.5 Discussion

Given a longer lead-in time, a more thorough search for secure sites could be made as UNI1 and UNI2 both proved to be inadequate; the reflectors were not visible in the SAR imagery (§5.5.2), they were too close together to be useful for the ZWD correction and the GPS time series were poor (§6.4).

The pillar mount was designed to accommodate either a reflector or a GPS antenna but not both. This is because it was assumed that each of the instruments might have a negative impact on the other's results. The author knows of no tests that have established this as fact and it may be worth further investigation (perhaps utilising an anechoic chamber) to experiment with different configurations of GPS antenna and reflector mount. A successful outcome would make possible truly concurrent GPS

and SAR observations and also eliminate any gaps in the GPS data, which can have unpredictable consequences (§5.4.4) when processing data using PPP methods that use a Kalman filter. The same objective could be achieved using a tripod set over the corner reflector, but this would probably not be as stable as a modified reflector with an antenna attachment. Furthermore, a tripod setup would rely on varying antenna heights measured with a tape in the field rather than a fixed offset that can be measured precisely under laboratory conditions and checked periodically.

The existing GPS dataset for the Nottingham area was reasonable although it was unfortunate that the two stations with the longest GPS time series (IESG and NOTT: §6.4.1) were so close together and the other CGPS stations in the area were too far away to include within a reasonably sized PSI processing area. Further problems ensued when NOTT was abandoned by the OS in 2007 and KEYW was established in its place, very close to BGS1. In general, CGPS networks have been densifying over the last ten years as location based services such as Virtual Reference Station (VRS) becomes more and more popular (`http://www.ordnancesurvey.co.uk/oswebsite/gps/commercialservices/`). This obviously would make the PSI ZWD correction method more viable, although there are also upper limits to the usefulness of spatially dense GPS networks (discussed below in §8.5).

Suggesting an idealised corner reflector network is not straightforward as it depends on the objectives. An ideal corner reflector for this project would be one secure enough to leave unattended, with fixed continuously operating GPS equipment (see above), with low backscatter but close to urban areas, close to areas of ground motion but stable themselves and present in as large an archive of SAR images as possible. For tropospheric delay experiments, the spatial density of the reflector network would be based on the measurable spatial variation in the troposphere; no less than 10.8km if this is conducted using GPS ZWD. A balanced geometry is also a desirable characteristic for a reflector network as results from tasks such as interpolation are less likely to contain areas which are not representative of the values being interpolated.

One of the key points in PSI analyses is that all PS motions are relative to the motion of the reference point. If therefore, the reference point is a precisely known

point with a precisely known positional time series, then it would be possible to derive the absolute motions of all the PS points. This could be made possible through the integration of one or more precisely surveyed corner reflectors, although this was not possible in this study for the reasons already stated.

The importance of the availability of an existing SAR archive during the planning stages of projects such as this cannot be overstated. Firstly it means a short list of reflector sites can be established prior to a field reconnaissance. If there are sufficient scenes for a PSI analysis, then reflectors can be optimally sited close to the areas which indicate motion suitable for further investigation.

It is difficult to see how the spacecraft conflict issue can be easily resolved. Cat-1 projects are necessarily low priority for ESA as there is no financial benefit to them and ordering data at commercial prices is beyond the reach of most research projects. The only solution is to plan as much redundancy into the project as possible and be flexible with the objectives.

The levelling campaign introduced midway into the project was a useful addition. In retrospect, a more extensive levelling campaign would have been invaluable such as a two or three year campaign with observations temporally close to every successful ENVISAT pass.

The results of the levelling undertaken here had to be double-differenced to be comparable with the PSI data (§7.2.2). This may be avoidable with a well chosen PSI reference point. If the reference point were a corner reflector with a stable GPS time series indicating no motion, and if this reference point were within reasonable levelling distance from an area of PSI indicated ground motion then a more rigorous validation experiment could be devised. Failing this, it would also be possible to level from the reference point to an artificially moveable point. Assuming zero motion at the reference point and assuming concurrent levelling observations and ENVISAT passes, the PSI and levelling results would be directly comparable. An experiment of a similar nature to this has been conducted (Marinkovic et al., 2008), but double differencing was necessary as the reference point strategy mentioned above was not part of the work.

8.4 GPS and PSI Integration

A novel means of integration between GPS and PSI was found in which absolutely derived ZWD data was used to remove part of the atmospheric component in the differential interferograms used in a PSI analysis (§7.1.5).

8.4.1 Data Quality

Prior to the integration stage, the quality of the GPS data was determined prior to PPP processing and some data had to be rejected (§6.1.2). Following PPP processing, results were compared to established GPS time series (§6.4), independently processed using entirely different algorithms. The quality of the PSI results was also examined whereby deformation signals in Nottingham City were linked to sources of information that might explain them (§6.5).

8.4.2 PPP Processing Model

It was argued that a PPP method for computing GPS parameters was the best means of providing realistic ZWD values (§5.4.2). The adopted PPP processing model was optimised for ZWD estimation (§6.1.4). When available, real pressure data was used to compute the ZHD estimates (§6.1.6, 7.1.1). Also, the best available tropospheric delay mapping function (Kouba, 2009b) was used for mapping delays to zenith (§6.1.4.6).

8.4.3 PSI Processing Model

An optimised method for PSI processing was sought (§6.2.3). Although the method used here is lengthy and complex compared to many other PSI strategies, there is very little compromise in the method: precise baselines were used initially which were later improved using GCPs, a stacking step was used to improve several initial PSI stages, the reference point was carefully selected following a quality check on the PS points, there was very little filtering, full resolution interferograms were used throughout and the final regression was computed using the original untouched differential interferograms.

8.4.4 Geometry and Interpolation

Correlation between GPS ZWD and PSI was then thoroughly investigated (§7.1.3). Whilst the degree of correlation was not high (0.42 overall), it was argued that this was in line with expectations. The ZWD values were then interpolated across the AOI in to ZWD screens. The interpolation method was tested and shown to produce good results in areas close to GPS stations and in areas bound by other GPS stations (§7.1.4.1).

8.4.5 ZWD Correction

Results between a ZWD uncorrected PSI analysis and a corrected PSI analysis were compared. Here the statistics indicated that whilst improvements were evident in the ZWD corrected PSI result, such as a lower mean residual phase standard deviation, there was also a slight increase in deformation rate uncertainties. The ZWD corrected PSI results were also compared to levelling and GPS results which both indicated improvements in the PSI deformation rate estimation (§7.2), although statistically some of these results were not conclusive.

When atmospheric phase screens for both the ZWD corrected and uncorrected PSI studies were added back to the deformation phase, the respective effects on the results were marked. The uncorrected deformation rate regression lines were unaffected whereas the corrected results showed unpredictable behaviour with linear deformation rates that were clearly not in agreement with GPS rates. It was assumed that these differences were due to the fact that only temporally random atmospheric phase is removed in the uncorrected PSI study, whereas the ZWD corrected result also has non-temporally random atmospheric phase removed; these signals may have otherwise been interpreted as non-linear deformation or residual phase.

8.4.6 Discussion

As stated by Hanssen (2001), there is an upper limit to densification at which more GPS stations are not useful. With a GPS elevation mask of 15° and considering overlapping GPS and SAR geometries at 1.4km above the ground (§7.1.2), this is

10.8km, because this is the area over which the GPS tropospheric delay estimates are sampled and averaged in order to estimate the ZWD value. This also means that using this technique, it is not possible to account for atmospheric variations below this spacial limit and therefore the technique is restricted to the longer wavelength effects of tropospheric delay. With the prospect of multi-GNSS receivers which are sure to become available once projects such as ESA's Galileo project (`http://www.esa.int/esana/galileo.html`) become operational, slant wet delay correction may become a viable option for which the geometric restrictions placed on ZWD estimation will not apply.

8.5 Recommendations for Further Work

The following items are drawn from the discussion points which indicate that further research may be useful and perhaps lead to significant results:

- Investigate a configuration whereby a GPS antenna mount and a corner reflector could be incorporated in such a way the the presence of one instrument does not inhibit the other.
- Conduct PSI analyses whereby the position and motion of the chosen reference point is precisely known through the integration of a precisely surveyed corner reflector. This could then lead on to important validation work whereby real ground motion could be directly compared to PSI results without the requirement for differencing.
- With a suitable constellation of GNSS satellites, investigate the potential for GNSS Slant Wet Delay correction of PSI results.

8.6 Summary

A review of the work conducted for this thesis has been presented. The aims and objectives were restated and discourse on how these were achieved was provided, discussing each objective in turn. A critical analysis was also made suggesting areas

for improvement and areas for new research. These new research areas were then listed as recommendations for future work.

References

Adam, N., Kampes, B. M., Eineder, M., Worawattanamateekul, J., Kircher, M., 2003. The development of a scientific permanent scatterer system. In: ISPRS Workshop High Resolution Mapping from Space, Hannover, Germany, 2003. p. 6 pp.

AddItNow, 2005. Mine exploration, photographs and mining history for mine explorers, industrial archaeologists, researchers and historians. Online, accessed 17 Jan 2010.

Afraimovich, E., Demyanov, V., Kondakova, T., 2003. Degradation of GPS performance in geomagnetically disturbed conditions. GPS Solutions 7 (2), 109–119.

Amos, J., 2007. London's small but relentless dip. Online, BBC News.
URL `http://news.bbc.co.uk/1/low/sci/tech/6231334.stm`

Anderson, H. P., 1973. Forgotten railways: the East Midlands. Vol. 2. David & Charles.

Bamler, R., 1992. A comparison of range-Doppler and wave-number domain SAR focusing algorithms. IEEE Transactions on Geoscience and Remote Sensing 30 (4), 706–713.

Bamler, R., Hartl, P., 1998. Synthetic aperture radar interferometry. Inverse Problems 14, R1–R54.
URL `http://enterprise.lr.tudelft.nl/doris/Literature/bamler98.pdf`

Bar-Sever, Y., Kroger, P., Borjesson, J., 1997. Estimating horizontal gradients of tropospheric path delay with a single GPS receiver. Journal of Geophysical Research-Solid Earth 103, 5019–5035.

Bekendam, R., Pottgens, J., 1995. Ground movements over the coal mines of southern Limburg, The Netherlands, and their relation to rising mine waters. IAHS Publications-Series of Proceedings and Reports-Intern Assoc Hydrological Sciences 234, 3–12.

Bell, F., Culshaw, M., Forster, A., Nathanail, C., 2009. The engineering geology of the Nottingham area, UK. Engineering Geology Special Publications 22 (1), 1.

Berardino, P., Fornaro, G., Lanari, R., Sansosti, E., 2002. A new algorithm for surface deformation monitoring based on small baseline differential SAR interferograms. IEEE Transactions on Geoscience and Remote Sensing 40 (11), 2375–2383.

Bern, M., Eppstein, D., 1992. Mesh generation and optimal triangulation. Computing in Euclidean geometry 1, 23–90.

Bevis, M., Businger, S., Herring, T. A., Anthes, R. A., Rocken, C., Ware, R. H., 1994. GPS meteorology: mapping Zenith Wet Delays onto precipitable water. Journal of Applied Meteorology 33 (3).

Bevis, M., Businger, S., Herring, T. A., Rocken, C., Anthes, R. A., Ware, R. H., 1992. GPS meteorology: remote sensing of atmospheric water vapor using the Global Positioning System. Journal of Geophysical Research 97, 15,787–15,801.

BGS, 2002. Earthwise issue 18, geology and planning. Tech. Rep. 18, BGS.

Bhattacharyya, A., Sengupta, D., 1991. Radar Cross Section analysis and control. Artech House on Demand.

Bierman, G., 1977. Factorization methods for discrete sequential estimation. Academic Pr.

Bingley, R., Ashkenazi, V., Penna, N., 1999. Monitoring changes in regional ground level, using high precision GPS. Tech. rep., Environment Agency, Bristol (United Kingdom).

Bingley, R., Penna, A., Baker, T., 2002. Using a GPS/MSL geoid to test geoid models in the UK. In: Vertical reference systems: IAG symposium, Cartagena, Colombia, February 20-23, 2001. Springer Verlag, p. 197.

Bingley, R. M., 2005. GNSS Principles and Observables: part 2. Institute of Engineering Surveying and Space Geodesy.

Bingley, R. M., Teferle, F. N., Orliac, E. J., Dodson, A. H., Williams, S. D. P., Blackman, D. L., Baker, T. F., Riedmann, M., Haynes, M., Aldiss, D. T., Burke, H. C., Chacksfield, B. C., Tragheim, D. G., 2007. Absolute fixing of tide gauge benchmarks and land levels: measuring changes in land and sea levels around the coast of Great Britain and along the Thames estuary and River Thames using GPS, absolute gravimetry, Persistent Scatterer Interferometry and tide gauges. Tech. rep., Department for Environment, Food and Rural Affairs, FD2319/TR.

Bishop, I., Styles, P., Allen, M., 1993. Mining-induced seismicity in the Nottinghamshire coalfield. Quarterly Journal of Engineering Geology & Hydrogeology 26 (4), 253.

Blewitt, G., 1993. Advances in Global Positioning System technology for geodynamics investigations: 1978-1992. Contributions of Space Geodesy to Geodynamics: Technology 25, 195–213.

Blewitt, G., 2008. Fixed point theorems of GPS carrier phase ambiguity resolution and their application to massive network processing: Ambizap. J. geophys. Res 113.

Bock, Y., Williams, S., 1997. Integrated satellite interferometry in Southern California. EOS 78 (29), 293–300.

Boehm, J., Niell, A., Tregoning, P., Schuh, H., 2006a. Global Mapping Function (GMF): a new empirical mapping function based on numerical weather model data. Geophysical Research Letters 33, L07304.

Boehm, J., Werl, B., Schuh, H., 2006b. Troposphere mapping functions for GPS and Very Long Baseline Interferometry from European centre for medium-range

weather forecasts operational analysis data. Journal of Geophysical Research-Solid Earth 111 (B2), B02406.

Bomford, G., 1980. Geodesy, Clarendon Press. Oxford, UK.

Bonforte, A., Ferretti, A., Prati, C., Puglisi, G., Rocca, F., 1999. Calibration of atmospheric effects on SAR interferograms by GPS and local atmosphere models: first results. Journal of Atmospheric and Terrestrial Physics .

Born, M., Wolf, E., Bhatia, A. B., 1959. Principle of optics; electromagnetic theory of propagation, interference and diffraction of light. Pergamon Press, New York.

Bos, M., Scherneck, H., 2006. Onsala space observatory. Online, chalmers University of Technology.
URL http://www.oso.chalmers.se/~loading/index.html

Brooks, I., Goroch, A., Rogers, D., 1999. Observations of strong surface radar ducts over the Persian Gulf. Journal of Applied Meteorology 38 (9), 1293–1310.

Brunt, K., King, M., Fricker, H., Macayeal, D., 2010. Flow of the Ross Ice Shelf, Antarctica, is modulated by the ocean tide. Journal of Glaciology 56 (195), 157.

Capes, R., Marsh, S., 2009. The Terrafirma atlas: terrain-motion across Europe. Tech. rep., European Space Agency, last accessed 15 Feb 2010.
URL http://www.terrafirma.eu.com/index.htm

Capra, A., Dietrich, R., 2008. Geodetic and geophysical observations in Antarctica: an overview in the IPY perspective. Springer-Verlag.

Cardellach, E., Elósegui, P., Davis, J., 2007. Global distortion of GPS networks associated with satellite antenna model errors. Journal of Geophysical Research-Solid Earth 112 (B7), B07405.

Castel, F., 2000. Curtain falls on European satellite success story. online, accessed 2 January 2009.
URL http://www.space.com/scienceastronomy/planetearth/ERS_fails_000321.html

Çelebi, M., Prescott, W., Stein, R., Hudnut, K., Behr, J., Wilson, S., 1998. GPS monitoring of structures: recent advances. NIST SPECIAL PUBLICATION SP , 515–528.

Chandra, A., 2007. Plane Surveying. New Age International.

Charsley, T., Rathbone, P., Lowe, D., 1990. Nottingham: a geological background for planning and development. Technical report WA/90/1, British Geological Survey, Keyworth.

Childe, V., 1950. The urban revolution. The Town Planning Review , 3–17.

Cifelli, R., Rauch, H., 1986. Dewatering effects from selected underground coal mines in north-central West Virginia. In: Proceedings of the Second Workshop on Surface Subsidence Due to Underground Mining, COMER, West Virginia University, Morgantown, West Virginia. pp. 249–263.

Colesanti, C., Ferretti, A., Locatelli, R., Savio, G., 2003a. Multi-platform permanent scatterers analysis: first results. In: Second GRSS/ISPRS Joint Workshop on "Data Fusion and Remote Sensing over Urban Areas", Berlin, Germany, 22–23 May, 2003. pp. 52–56.

Colesanti, C., Ferretti, A., Novali, F., Prati, C., Rocca, F., 2003b. SAR monitoring of progressive and seasonal ground deformation using the permanent scatterers technique. IEEE Transactions on Geoscience and Remote Sensing 41 (7), 1685–1701.

Corona, P., Ferrara, G., 1995. Phase mathematical modelling for corner reflectors in remote sensing synthetic aperture radar applications. In: International Geoscience and Remote Sensing Symposium, Florence, Italy, 10–14 July 1995. pp. 763–766.

Costantini, M., 1998. A novel phase unwrapping method based on network programming. IEEE Transactions on geoscience and remote sensing 36 (3), 813–821.

Coulson, S. N., 1993. SAR interferometry with ERS-1. Earth Observation Quarterly 40.

Crosetto, M., 2002. Calibration and validation of SAR interferometry for DEM generation. ISPRS Journal of Photogrammetry and Remote Sensing 57 (3), 213–227.

Crosetto, M., Monserrat, O., Adam, N., Parizzi, A., Bremmer, C., Dortland, S., Hanssen, R., van Leijen, F., 2008. Validation of existing processing chains in Terrafirma stage 2. Tech. rep., European Space Agency.

Cuenca, M. C., Hanssen, R. F., 2008. Subsidence and uplift at Wassenberg, Germany due to coal mining using Persistent Scatterer Interferometry. In: 13^{th} FIG International Symposium on Deformation Measurements and Analysis, Lisbon, Portugal, 12–15 May, 2008. Lisbon, Portugal, pp. 1–9.

Culshaw, M., 2006. Personal communication 8 Feb 2006. Geologist.

Curlander, J. C., McDonough, R. N., 1991. Synthetic Aperture Radar: systems and signal processing. John Wiley & Sons, Inc, New York.

Dach, R., Hugentobler, U., Fridez, P., Meindl, M., 2007. Bernese GPS software version 5.0. Astronomical Institute, University of Bern .

Dalgaard, P., 2008. Introductory statistics with R. Springer Verlag.

de Haan, S., Jones, J., Vedel, H., 2006. The EUMETNET GPS water vapour (EGVAP) 2006. Tech. rep., The Network of European Meteorological Services.

Delacourt, C., Briole, P., Achache, J., 1998. Tropospheric corrections of SAR interferograms with strong topography. Application to Etna. Geophysical Research Letters 25 (15), 2849–2852.

Delaunay, B., 1934. Sur la sphere vide. Izv. Akad. Nauk SSSR, Otdelenie Matematicheskii i Estestvennyka Nauk 7, 793–800.

Desai, S., 2009. Gipsy user group meeting 2009 Fall AGU. Presentation.

Deumlich, F., Staiger, R., 2002. Instrumentenkunde der vermessungstechnik. Herbert Wichmann Verlag.

Devleeschouwer, X., Declercq, P., Petitclerc, E., 2007. Ground subsidence related to soft and recent alluvial sediments (Brussels, Belgium). In: Abstract book of the Geohazards 2007 Workshop. ESRIN-ESA, pp. 1661–1669, frascati, Italy.

Donnelly, L., 1999. Fault reactivation induced by mining in the East Midlands. Mercian Geologist 15 (1).

Dumpleton, S., Robins, N., Walker, J., Merrin, P., 2001. Mine water rebound in South Nottinghamshire: risk evaluation using 3-D visualization and predictive modelling. Quarterly Journal of Engineering Geology & Hydrogeology 34 (3), 307.

Duro, J., Inglada, J., Closa, J., Adam, N., Arnaud, A., 2004. High resolution differential interferometry using time series of ERS and ENVISAT SAR data. In: ENVISAT Symposium, Salzburg. p. 72.

Durrett, R., 1996. Probability: theory and examples. Duxbury Press Belmont, CA.

EDINA, 2009. BGS 1:50,000 Nottingham geology. Online, http://edina.ac.uk/projects/sharegeo/.

ESA, 2010. Envisat mission extension beyond 2010. Online.
URL `http://earth.esa.int/object/index.cfm?fobjectid=6293`

Estey, L., Meertens, C., 1999. TEQC: the multi-purpose toolkit for GPS/GLONASS data. GPS Solutions 3 (1), 42–49.

Eyers, R. D., Mills, J. P., 2002. Subsidence detection using integrated multi-temporal airborne imagery. The International Archives of the Photogrammetry, Remote Sensing and Spatial Information Sciences 34.

Faig, W., 1984. Subsidence monitoring in mountainous terrain - an example of four dimensional photogrammetry. In: ISPRS 1984 : proceedings of the XVth Workshop, Rio de Janeiro, Brazil, 1984. pp. 276–285.

Farr, T. G., Rosen, P. A., Caro, E., Crippen, R., Duren, R., Hensley, S., Kobrick, M., Paller, M., Rodriguez, E., Roth, L., Seal, D., Shaffer, S., Shimada, J., Umland,

J., Werner, M., Oskin, M., Burbank, D., Alsdorf, D., 2007. The Shuttle Radar Topography Mission. Rev. Geophys. 45, 33.

Feltens, J., Schaer, S., 1998. IGS Products for the Ionosphere. In: Proceedings of the IGS Analysis Center Workshop, ESA/ESOC Darmstadt, Germany. pp. 225–232.

Ferretti, A., Prati, C., Rocca, F., 1999. Permanent scatterers in SAR interferometry. In: International Geoscience and Remote Sensing Symposium, Hamburg, Germany, 28 June–2 July 1999. pp. 1–3.

Ferretti, A., Prati, C., Rocca, F., 2000a. Measuring subsidence with SAR interferometry: applications of the permanent scatterers technique. In: Carbognin, L., Gambolati, G., Johnson, A. I. (Eds.), Land subsidence; Proceedings of the Sixth International Symposium on Land Subsidence. Vol. 2. CNR, pp. 67–79.

Ferretti, A., Prati, C., Rocca, F., 2000b. Nonlinear subsidence rate estimation using Permanent Scatterers in differential SAR interferometry. IEEE Transactions on Geoscience and Remote Sensing 38 (5), 2202–2212.

Ferretti, A., Prati, C., Rocca, F., 2001. Permanent scatterers in SAR interferometry. IEEE Transactions on Geoscience and Remote Sensing 39 (1), 8–20.

Foster, J., Brooks, B., Cherubini, T., Shacat, C., Businger, S., Werner, C. L., 2006. Mitigating atmospheric noise for InSAR using a high resolution weather model. Geophysical Research Letters 33 (L16304), doi:10.1029/2006GL026781.

Fruneau, B., Achache, J., Delacourt, C., 1996. Observation and modelling of the Saint-Etienne-de-Tine landslide using SAR interferometry. Tectonophysics 265, 181–190.

Gabriel, A. K., Goldstein, R. M., Zebker, H. A., 1989. Mapping small elevation changes over large areas: differential radar interferometry. Journal of Geophysical Research 94 (B7), 9183–9191.

Galloway, D., Ingebritsen, S., Riley, F., Ikehara, M., Carpenter, M., 1999. The role of science in land subsidence in the United States. Tech. Rep. 1182, USGS.

Gendt, G., 1998. IGS combination of tropospheric estimates–experience from pilot experiment. In: Proceedings of 1998 IGS Analysis Center Workshop, JM Dow, J. Kouba and T. Springer, Eds. IGS Central Bureau, Jet Propulsion Laboratory, Pasadena, CA. pp. 205–216.

Ghiglia, D. C., Pritt, M. D., 1998. Two-dimensional phase unwrapping: theory, algorithms, and software. John Wiley & Sons, Inc, New York.

Gold, R., Dixon, R., 1998. Method and apparatus for despreading spread spectrum signals. US Patent 5,761,239.

Goldstein, R. M., Engelhardt, H., Kamp, B., Frolich, R. M., 1993. Satellite radar interferometry for monitoring ice sheet motion: application to an Antarctic ice stream. Science 262, 1525–1530.

Goldstein, R. M., Werner, C. L., 1998. Radar interferogram filtering for geophysical applications. Geophysical Research Letters 25 (21), 4035–4038.

Goldstein, R. M., Zebker, H. A., Werner, C. L., 1988. Satellite radar interferometry: two-dimensional phase unwrapping. Radio Science 23 (4), 713–720.

Gray, A. L., Farris-Manning, P. J., 1993. Repeat-pass interferometry with Airborne Synthetic Aperture Radar. IEEE Transactions on Geoscience and Remote Sensing 31 (1), 180–191.

Gregorius, T., 1996. GIPSY-OASIS II: how it works... Department of Geomatics, University of Newcastle upon Tyne.

Groot, J., Otten, M., 1994. SAR imaging of corner reflectors larger than the spatial resolution. IEEE Transactions on Geoscience and Remote Sensing 32 (3), 721–724.

Hanssen, R., 1998. Atmospheric heterogeneities in ERS tandem SAR interferometry. Delft University Press, Delft, the Netherlands.
URL `http://enterprise.lr.tudelft.nl/doris/Literature/hanssen98i.html`

Hanssen, R., Bamler, R., 1999. Evaluation of interpolation kernels for SAR interferometry. IEEE Transactions on Geoscience and Remote Sensing 37 (1), 318–321. URL http://enterprise.lr.tudelft.nl/doris/Literature/hanssen99b.html

Hanssen, R., Feijt, A., 1996. A first quantitative evaluation of atmospheric effects on SAR interferometry. In: 'FRINGE 96' workshop on ERS SAR Interferometry, Zürich, Switzerland, 30 Sep–2 October 1996. ESA SP-406, pp. 277–282. URL http://enterprise.lr.tudelft.nl/doris/Literature/hanssen96a.pdf

Hanssen, R., Weckwerth, T., Zebker, H., Klees, R., 1999. High-resolution water vapor mapping from interferometric radar measurements. Science 283 (5406), 1297.

Hanssen, R. F., 2001. Radar interferometry: data interpretation and error analysis. Kluwer Academic Publishers, Dordrecht.

Heflin, M., Bertiger, W., Blewitt, G., Freedman, A., Hurst, K., Lichten, S., Lindqwister, U., Vigue, Y., Webb, F., Yunck, T., et al., 1992. Global geodesy using GPS without fiducial sites. Geophysical Research Letters 19 (2).

Henriksen, J., Lachapelle, G., Racquet, J., Stephen, J., 1996. Analysis of stand-alone GPS positioning using post-mission information. In: Proceedings of ION GPS. Vol. 9. Institute of Navigation, pp. 251–259.

Héroux, P., Kouba, J., 1995. GPS Precise Point Positioning with a difference. Geomatics 95, 13–15.

Hofmann-Wellenhof, B., Lichtenegger, H., Collins, J., 2001. Global Positioning System, theory and practice. Springer-Verlag, Wien.

Holzner, J., Eineder, M., Schattler, B., 2002. First analysis of ENVISAT/ASAR image mode products for interferometry. In: Proceedings of Envisat Calibration Review. ESTEC, Nordwijk, The Netherlands, pp. 1116–1121.

Hooper, A., 2006. Persistent scatterer radar interferometry for crustal deformation studies and modeling of volcanic deformation. Ph.D. thesis, Stanford University.

Hooper, A., Pedersen, R., 2008. Deformation at Katla, Eyjafjallajökull and Upptyppingar, Iceland, from multi-temporal InSAR: a combined persistent scatterer and small baseline method. IAVCEI 2008 General Assembly, Reykjavik .
URL http://www.iavcei2008.hi.is

Hooper, A., Zebker, H., Segall, P., Kampes, B., 2004. A new method for measuring deformation on volcanoes and other non-urban areas using InSAR persistent scatterers. Geophysical Research Letters 31, L23611, doi:10.1029/2004GL021737.

Hopfield, H., 1970. Tropospheric effect on electromagnetically measured range: prediction from surface weather data. Radio Science 6, 357.

Howard, A., Warrington, G., Carney, J., Ambrose, K., Young, S., Pharaoh, T., Cheney, C., 2010. 2010 Geology of the Nottingham district : memoir for 1:50,000 geological sheet 126 (England and Wales). British Geological Survey.

Intermap Technologies, 2008. NEXTMap 5m Digital Surface Model.
URL http://www.intermap.com/index.php

International, F., 1962. Hucknall: Rolls-Royce installation and flight development establishment. Flight International Magazine , 195–199.
URL http://www.flightglobal.com/pdfarchive/view/1962/1962%%20-%201385.html

Iwabuchi, T., Rocken, C., Lukes, Z., Mervart, L., Johnson, J., Kanzaki, M., 2006. PPP and network true real-time 30 sec estimation of ZTD in dense and giant regional GPS network and the application of ZTD for nowcasting of heavy rainfall. In: Proceedings of the 19th International Technical Meeting of the Satellite Division of the Institution of Navigation, ION GNSS 2006. pp. 56–62.

Janssen, V., Ge, L., Rizos, C., 2004. Tropospheric corrections to SAR interferometry from GPS observations. GPS Solutions 8 (3), 140–151.

Jerri, A., 1977. The Shannon sampling theorem - its various extensions and applications: a tutorial review. proc. IEEE 65 (11), 1565–1596.

Jezek, K., Farness, K., Carande, R., Wu, X., Labelle-Hamer, N., 2003. RADARSAT 1 Synthetic Aperture Radar observations of Antarctica: modified Antarctic mapping mission, 2000. Radio Science 38 (4), 8067.

Jordan, R. L., Caro, E. R., Kim, Y., Kobrick, M., Shen, Y., Stuhr, F. V., Werner, M. U., 1996. Shuttle Radar Topography Mapper (SRTM). In: Proceedings of SPIE Vol. 2958, microwave sensing and Synthetic Aperture Radar. Bellingham, Wash. : SPIE–the International Society for Optical Engineering, c1996., pp. 412–422.

Just, D., Bamler, R., 1994. Phase statistics of interferograms with applications to Synthetic Aperture Radar. Applied Optics 33 (20), 4361–4368.

Kampes, B., 2006. Radar interferometry: persistent scatterer technique. Springer.

Kemeling, I., van Leijen, F., Petley, D. N., Allison, R. J., Long, A. J., 2004. Monitoring mining subsidence in rural areas with a temperate climate using radar interferometry. In: ENVISAT & ERS Symposium, Salzburg, Austria, 6–10 September, 2004. p. 7.

Ketelaar, V., 2009. Satellite radar interferometry: subsidence monitoring techniques. Springer Verlag.

Kim, H., Lee, B., 2007. Optimal design of retroreflection corner-cube sheets by geometric optics analysis. Journal of Optical Engineering 45.

Kim, K., Choi, J., 2005. Estimation of ground subsidence near an abandoned underground coal mine using GIS and neural network. In: 2005 IEEE International Geoscience and Remote Sensing Symposium, 2005. Vol. 7. pp. 234–240.

King, M., Edwards, S., Clarke, P., 2002. Precise Point Positioning: breaking the monopoly of relative GPS processing. Engineering Surveying Showcase , 33–34.

KKP, 2003. Gedling Borough Council playing pitch assessment. Tech. rep., Gedling Borough Council, accessed online 01 Mar 2010.
URL `http://www.gedling.gov.uk/2._playing_pitch_assessment_-_2003.pdf`

Knott, E., 2006. Radar Cross Section measurements. SciTech.

Kouba, J., 2009a. A guide to using International GNSS Service (IGS) products. Online, accessed: 28 January 2010.

Kouba, J., 2009b. Testing of global pressure/temperature (GPT) model and global mapping function (GMF) in GPS analyses. Journal of Geodesy 83 (3), 199–208.

Kouba, J., Héroux, P., 2000. GPS Precise Point Positioning using IGS orbit products. GPS solutions 5 (2), 12–28.

Lachapelle, G., Cannon, M., Qiu, W., Varner, C., 1996. Precise aircraft single-point positioning using GPS post-mission orbits and satellite clock corrections. Journal of Geodesy 70 (9), 562–571.

Lambeck, K., Canberra, A., 1989. The Fourth Dimension in Geodesy Observing the Deformation of the Earth. Lecture Notes in Earth Science (29): Developments in Four-Dimensional Geodesy, FK Brunner and C. Rizos (Eds.), Spring-Verlag , 1–14.

Larson, K., Freymueller, J., Philipsen, S., 1997. Global plate velocities from the Global Positioning System. Journal of Geophysical Research 102, 9961–9981.

Lasswell, S., 2002. History of SAR at Lockheed Martin (previously Goodyear Aerospace). In: Proceedings of SPIE. Vol. 5788 of Society of Photo-Optical Instrumentation Engineers (SPIE) Conference Series. SPIE, pp. 1–12.

Lee, J. S., Hoppel, K. W., Mango, S. A., Miller, A. R., 1994. Intensity and phase statistics of multilook polarimetric and interferometric SAR imagery. IEEE Transactions on Geoscience and Remote Sensing 30, 1017.

Lefevre, F., Lyard, F., Le Provost, C., Schrama, E., 2002. FES99: a global tide Finite Element Solution assimilating tide gauge and altimetric information. Journal of Atmospheric and Oceanic Technology 19 (9), 1345–1356.

Leick, A., 1994. GPS Satellite Surveying. John Wiley and Sons, New York.

Leick, A., 2004. GPS satellite surveying. Wiley.

Leighton, J. M., Sowter, A., Tragheim, D., Teferle, F. N., Bingley, R. M., 2007. Episodic geodetic reflector networks for Persistent Scatterer Interferometry (PSI) analyses. In: Proceedings of the 2007 Annual Conference of the Remote Sensing and Photogrammetry Society (RSPSoc2007), Newcastle upon Tyne, 11 - 14 September 2007. pp. 79–86.

Levrini, G., Zink, M., 2002. The ASAR User Guide. ESA, 8-10 rue Mario Nikis, 75738 Paris, France.
URL `http://envisat.esa.int/handbooks/asar/CNTR1.htm`

Li, Z., Bethel, J., 2008. Image coregistration in SAR interferometry. In: ISPRS08. p. B1: 433 ff.

Li, Z., Muller, J.-P., Cross, P., Fielding, E. J., 2005. Interferometric Synthetic Aperture Radar (InSAR) atmospheric correction: GPS, Moderate Resolution Imaging Spectroradiometer (MODIS), and InSAR integration. Journal of Geophysical Research 110 (B03410), doi:10.1029/2004JB003446.

Li, Z. W., Ding, X. L., Liu, G., 2004. Modeling atmospheric effects on InSAR with meteorological and continuous GPS observations: algorithms and some test results. Journal of Atmospheric and Solar-Terrestrial Physics 66 (doi:10.1016/j.jastp.2004.02.006), 907–917.

Lichten, S., Bar-Sever, Y., Bertiger, W., Heflin, M., Hurst, K., Muellerschoen, R., Wu, S., Yunck, T., Zumberge, J., 2005. GIPSY-OASIS II: a high precision GPS data processing system and general satellite orbit analysis tool. Technology , 24–26.

Lillesand, T., Kiefer, R., Chipman, J., 2004. Remote sensing and image interpretation. John Wiley & Sons Ltd Chichester, UK.

Lyons, S., Sandwell, D., 2003. Fault creep along the southern San Andreas from interferometric Synthetic Aperture Radar, permanent scatterers, and stacking. J. Geophys. Res 108, 2047.

Madisetti, V., Williams, D., 1998. The Digital Signal Processing Handbook. CRC Press.

Mallorqui, J. J., Rosado, I., Bara, M., 2001. Interferometric calibration for DEM enhancing and system characterization in single pass SAR interferometry. In: International Geoscience and Remote Sensing Symposium, Sydney, Australia, 9–13 July 2001. pp. cdrom, 3 pages.

Marinkovic, P., Ketelaar, G., Hanssen, R., 2004. A controled Envisat/ERS permanent scatterer experiment, implications of corner reflector monitoring. In: CEOS SAR Workshop, Ulm Germany, 27–28 May 2004. p. submitted.
URL http://enterprise.lr.tudelft.nl/doris/Literature/marinkovic04.pdf

Marinkovic, P., Ketelaar, G., van Leijen, F., Hanssen, R., 2008. InSAR quality control: analysis of five years of corner reflector time series. In: Fifth International Workshop on ERS/Envisat SAR Interferometry, 'FRINGE07', Frascati, Italy, 26 Nov-30 Nov 2007. p. 8 pp.
URL http://enterprise.lr.tudelft.nl/doris/Literature/marinkovic08.pdf

Massonnet, D., Briole, P., Arnaud, A., 1995. Deflation of Mount Etna monitored by spaceborne radar interferometry. Nature 375, 567–570.

Massonnet, D., Feigl, K. L., 1998. Radar interferometry and its application to changes in the earth's surface. Reviews of Geophysics 36 (4), 441–500.
URL http://enterprise.lr.tudelft.nl/doris/Literature/massonnet98.pdf

Massonnet, D., Rossi, M., Carmona, C., Adagna, F., Peltzer, G., Feigl, K., Rabaute, T., 1993. The displacement field of the Landers earthquake mapped by radar interferometry. Nature 364 (8), 138–142.

Matheron, G., 1963. Principles of geostatistics. Economic geology 58 (8), 1246.

McCarthy, D. D., Petit, G., 2003. IERS conventions: chapter 7 displacement of reference points. Tech. rep., International Earth Rotation and Reference System Service, Frankfurt.

McLean, A., Gribble, C., 1985. Geology for civil engineers. Taylor & Francis.

Melchior, P., 1974. Earth tides. Surveys in Geophysics 1 (3), 275–303.

Mendes, V., Langley, R., 1998. Optimization of tropospheric delay mapping function performance for high-precision geodetic applications. Proc. DORIS Days , 27–29.

Messina, P., 1996. Radar mapping techniques and applications. online, accessed 31 December 2008.
URL http://www.geo.hunter.cuny.edu/terrain/radarii.html

MIT, 1952. MIT Radiation Laboratory Series 1947-1952. McGraw-Hill Book Company, New York.

Monti Guarnieri, A., Parizzi, F., Prati, C., Rocca, F., 1993. SAR interferometry experiments with ERS-1. In: International Geoscience and Remote Sensing Symposium, Tokyo, Japan, 18–21 August 1993. pp. 991–993.

Mora, O., Mallorqui, J., Broquetas, A., 2003. Linear and nonlinear terrain deformation maps from a reduced set of interferometric SAR images. IEEE Transactions on Geoscience and Remote Sensing 41 (10), 2243–2253.

Mouélic, S. L., Raucoules, D., Carnec, C., King, C., Adragna, F., 2002. A ground uplift in the city of Paris (France) revealed by satellite radar interferometry. Geophysical Research Letters 29, 1853.

Murphy, T. W., Adelberger, E. G., Battat, J. B. R., Carey, L. N., Hoyle, C. D., Leblanc, P., Michelsen, E. L., Nordtvedt, K., Orin, A. E., Strasburg, J. D., Stubbs, C. W., Swanson, H. E., Williams, E., 2007. APOLLO: the Apache Point Observatory Lunar Laser-ranging Operation: instrument description and first detections. Publications of the Astronomical Society of the Pacific 120, 20–37.
URL http://www.citebase.org/abstract?id=oai:arXiv.org:0710.0890

NASA, 1991. Major emphasis areas for solid earth science in the 1990s: report of the NASA coolfont workshop. Tech. Rep. 4256, National Aeronautics and Space Administration, NASA Technical Memorandum.

NERC, 2010. Ground shrinkage and subsidence. Online, accessed 10 March 2010.
URL http://www.bgs.ac.uk/science/landUseAndDevelopment/shallow_geohazards/shrinking_and_swelling_clays.html

O'Brien, D. C., Faulkner, G. E., Edwards, D. J., 1999. Optical properties of a retroreflecting sheet. Appl Opt 38 (19), 4137–4144.

Ogaja, C., Hedfors, J., 2007. TEQC multipath metrics in MATLAB. GPS Solutions 11 (3), 215–222.

Onn, F., Zebker, H. A., 2006. Correction for Interferometric Synthetic Aperture Radar atmospheric phase artifacts using time series of Zenith Wet Delay observations from a GPS network. Journal of Geophysical Research 111 (B09102), doi:10.1029/2005JB004012.

Otten, M., Boomkamp, H., 2004. Estimation of the absolute orbit accuracy of ENVISAT. Tech. rep., European Space Operations Centre, Robert-Bosch Strasse 5, D-64283 Darmstadt.

Paganelli, F., Hooper, A., 2008. Deformation at Fogo volcano, Cape Verde, detected by persistent scatterer InSAR. EGU General Assembly 2008, Vienna 10, EGU2008–A–07819.
URL http://meetings.copernicus.org/egu2008

Panafidina, N., Malkin, Z., 2001. On computation of a homogeneous coordinate time series for the EPN network. Proceedings 'Vistas for Geodesy in the New Millennium', IAG , 2–7.

Parkinson, B. W., Spilker, J. J., 1996. Global Positioning System: theory and application. Vol. 2. American Institute of Aeronautics and Astronautics.

Peel, M., Finlayson, B., McMahon, T., 2007. Updated world map of the Köppen-Geiger climate classification. Hydrology and Earth System Sciences Discussions 4 (2), 439–473.

Penna, N., Clarke, P., Edwards, S., 2005. An assessment of Ocean Tide Loading models for precise GPS positioning in Great Britain. RICS Research .

Perski, Z., Hanssen, R., Marinkovic, P., 2008. Deformation of the margin of Sudety mountains (Southern Poland), studied by persistent scatterers interferometry. In: Fifth International Workshop on ERS/Envisat SAR Interferometry, 'FRINGE07', Frascati, Italy, 26 Nov-30 Nov 2007. p. 4 pp.
URL http://enterprise.lr.tudelft.nl/doris/Literature/perski08.pdf

Prati, C., Rocca, F., Monti Guarnieri, A., 1989. Effects of speckle and additive noise on the altimetric resolution of Interferometric SAR (ISAR) surveys. In: Proc. IGARSS'89, Vancouver. pp. 2469–2472.

Puysségur, B., Michel, R., Avouac, J. P., 2007. Tropospheric phase delay in InSAR estimated from meteorological model and multispectral imagery. Journal of Geophysical Research in press.

Rabus, B., Werner, C., Wegmüller, U., McCardle, A., 2004. Interferometric Point Target Analysis of RADARSAT-1 data for deformation monitoring at the Belridge/Lost Hills oil fields. In: 2004 IEEE International Geoscience and Remote Sensing Symposium, 2004. IGARSS'04. Proceedings. Vol. 4. pp. 2611– 2613.

Racoules, D., Bourgine, B., de Michele, M., Cozannet, G. L., Luc, C., Bremmer, C., Veldkamp, H., Tragheim, D., Bateson, L., Crosetto, M., Agudo, M., Engdahl, M., 2006. PSIC4: Persistent Scatterer Interferometry: independent validation and intercomparison of results. Tech. rep., BRGM, BRGM/RP-55640-FR.

Saastamoinen, J., 1972. Atmospheric correction for the troposphere and stratosphere in radio ranging of satellites. In: First International Symposium the use of artificial satellites for geodesy and geodynamics. Vol. 15. American Geophysical Union, pp. 247–251.

Sandwell, D., 1987. Biharmonic spline interpolation of GEOS-3 and SEASAT altimeter data. Geophysical Research Letters 14 (2), 139–142.

Sandwell, D. T., Price, E. J., 1998. Phase gradient approach to stacking interferograms. Journal of Geophysical Research 103 (B12), 30183–30204.

Sandwell, D. T., Sichoix, L., 2000. Topographic phase recovery from stacked ERS interferometry and a low resolution digital elevation model. Journal of Geophysical Research 105 (B12), 28211–28222.

Sarabandi, K., Chiu, T., 1995. Optimum corner reflectors for calibration of imaging radars. In: International Geoscience and Remote Sensing Symposium, Florence, Italy, 10–14 July 1995. pp. 2241–2243.

Schaeffer, J. F., Tuley, M. T., Knott, E., 1985. Radar Cross Section. Artech House, New Jersey.

Schmid, R., Mader, G., Herring, T., 2005. From relative to absolute antenna phase center corrections. In: Celebrating a Decade of the International GPS Service, Workshop and Symposium 2004. pp. 209–221.

Schmid, R., Steigenberger, P., Gendt, G., Ge, M., Rothacher, M., 2007. Generation of a consistent absolute phase-center correction model for GPS receiver and satellite antennas. Journal of Geodesy 81 (12), 781–798.

Seeber, G., 2003. Satellite geodesy. Walter De Gruyter Inc.

Skolnik, M., 1990. Radar handbook. McGraw-Hill Professional.

Slob, S., Kervyn, F., Lavreau, J., Odida, J., Kyagulanyi, D., 2000. InSAR DEM Calibration for topographic mapping in eastern Uganda. International Archives of Photogrammetry and Remote Sensing 33, 1011–1018.

Small, D., Pasquali, P., Fuglistaler, S., 1996. A comparison of phase to height conversion methods for SAR Interferometry. In: Geoscience and Remote Sensing Symposium, 1996. IGARSS'96.'Remote Sensing for a Sustainable Future.', International. Vol. 1. pp. 342 – 344.

Smith, G., 2002. London, the sinking city. Newspaper Article, The London Evening Standard.

Sowter, A., Leighton, J., 2006. Establishing geodetic control in the monitoring of urban subsidence using InSAR - a case study over Nottingham. Online, ESA CAT-1 Proposal:3518.
URL http://eopi.esa.int/esa/esa

Spilker Jr, J., 1978. GPS signal structure and performance characteristics. Navigation 25, 121–146.

Spreckels, V., 1999. Monitoring of hard coal mining subsidence by airborne high resolution stereo scanner data. In: ISPRS Joint Workshop on Sensors and Mapping from Space, Hannover. pp. 695–704.

Steigenberger, P., Rothacher, M., Dietrich, R., Fritsche, M., Rülke, A., Vey, S., 2006. Reprocessing of a global GPS network. Journal of Geophysical Research 111, B05402.

Stolk, R. M., Oct. 1997. GPS and SAR interferometry, a comparative analysis of estimating tropospheric propagation delays: The GISARE GPS experiment. Master's thesis, Delft University of Technology, Delft.

Strozzi, T., Wegmuller, U., Werner, C., Wiesmann, A., 2000. Measurement of slow uniform surface displacement with mm/year accuracy. In: IEEE 2000 International Geoscience and Remote Sensing Symposium, 2000. Proceedings. IGARSS 2000. Vol. 5. pp. 2239 – 2241.

Teferle, F., 2003. Strategies for long term monitoring of tide gauges using GPS. Ph.D. thesis, Institute of Engineering Surveying and Space Geodesy.

Thompson, S., 2007. Personal communications 25 july 2007. Nottingham City Council City Development Department.

Thumm, M., 2007. Historical german contributions to physics and applications of electromagnetic oscillations and waves. Universität Karlsruhe, Institut für Höchstfrequenztechnik und Elektronik, Kaiserstraße 12, D-76128 Karlsruhe, Germany.

Timmen, L., YE, X., Reigber, C., Hartmann, R., Fiksel, T., Winzer, W., Knoch-Weber, J., 1996. Monitoring of small motions in mining areas by SAR interferometry. ESA SP(Print) .

Torge, W., 2001. Geodesy. Walter de Gruyter.

Towne, D., 1988. Wave phenomena. Dover Publications.

Treuhaft, R. N., Lanyi, G. E., 1987. The effect of the dynamic wet troposphere on radio interferometric measurements. Radio Science 22 (2), 251–265.

Ulaby, F. T., Moore, R. K., Fung, A. K., 1982. Microwave remote sensing: active and passive. Vol. 1. Microwave Remote Sensing Fundamentals and Radiometry. Addison-Wesley, Reading.

Ulander, L. M., 1991. Accuracy of using point targets for SAR calibration. IEEE Transactions on Aerospace and Electronic Systems 27 (1), 139–148.

Van der Hoeven, A., Hanssen, R., Ambrosius, B., 2000. Cross-validation of tropospheric delay variability observed by GPS and SAR interferometry. GPS Nieuwsbrief 15 (2), 2–7.
URL `http://enterprise.lr.tudelft.nl/doris/Literature/hoeven00.pdf`

Vincenty, T., 1975. Direct and inverse solutions of geodesics on the ellipsoid with application of nested equations. Survey Review 22 (176), 88–93.

Wadge, G., Webley, P. W., James, I. N., Bingley, R., Dodson, A., Waugh, S., Veneboer, T., Puglisi, G., Mattia, M., Baker, D., Edwards, S. C., Edwards, S. J., Clarke, P. J., 2002. Atmospheric models, gps and insar measurements of the tropospheric water vapour field over mount etna. Geophysical Research Letters 29 (19), 11/1–4.

Wahr, J., 1981. Body tides on an elliptical, rotating, elastic and oceanless Earth. Geophys. JR Astr. Soc 64, 677–703.

Waltham, A. C., 1989. Ground Subsidence. Blackie.

Warren, M., 2007. The development of a 3-pass persistent scatterer algorithm using the integer ambiguity search method. Ph.D. thesis, Institute of Engineering Surveying and Space Geodesy.

Webb, F. H., Zumberge, J. F., 1997. An Introduction to GIPSY-OASIS II. Jet Propulsion Laboratory, Pasadena, CA.

Webley, P. W., Bingley, R. M., Dodson, A. H., Wadge, G., Waugh, S. J., James, I. N., 2002. Atmospheric water vapour correction to InSAR surface motion measurements on mountains: results from a dense GPS network on Mount Etna. Physics and Chemistry of the Earth, Parts A/B/C 29 (4-5), 363–370.

Wegmüller, U., 1999. Automated terrain corrected SAR geocoding. In: IEEE 1999 International Geoscience and Remote Sensing Symposium, 1999. IGARSS'99 Proceedings. Vol. 3. pp. 1712–1714.

Wegmüller, U., Strozzi, T., Tosi, L., 2000. ERS and ENVISAT differential SAR interferometry for subsidence monitoring. In: ERS - ENVISAT Symposium. pp. 685–692.

Wegmüller, U., Werner, C., 1997. Gamma SAR processor and interferometry software. In: T.-D. Guyenne & D. Danesy (Ed.), Third ERS Symposium on Space at the service of our Environment. Vol. 414 of ESA Special Publication. pp. 1687–+.

Wegmüller, U., Werner, C. L., Strozzi, T., 2003. GAMMA Interferometric Point Target Analysis Software (IPTA): Reference Manual.

Werner, C., Wegmüller, U., Strozzi, T., Wiesmann, A., 2003. Interferometric Point Target Analysis for deformation mapping. In: International Geoscience and Remote Sensing Symposium, Toulouse, France, 21–25 July 2003. pp. 3 pages, cdrom.

Werner, C. L., Wegmüller, U., Strozzi, T., 2002. Processing strategies for phase unwrapping for InSAR applications. In: Proceedings of the European Conference on Synthetic Aperture Radar EUSAR. pp. 4–6.

Wikipedia, 2009. Hucknall — Wikipedia: the free encyclopedia. [Online; accessed 17-January-2010].
URL http://en.wikipedia.org/w/index.php?title=Hucknall&oldid=334191866

Wilhelm, H., Zürn, W., Wenzel, H., 1997. Tidal phenomena lecture notes in earth sciences. Springer.

Williams, S., 2008. CATS: GPS coordinate time series analysis software. GPS Solutions 12 (2), 147–153.

Williams, S., Bock, Y., Fang, P., 1998. Integrated satellite interferometry: tropospheric noise, GPS estimates and implications for Interferometric Synthetic Aperture Radar products. Journal of Geophysical Research 103 (B11), 27,051–27,067.

Witchayangkoon, B., 2000. Elements of GPS precise point positioning. Ph.D. thesis, University of New Brunswick.

Woodhouse, I. H., 2006. Introduction to Microwave Remote Sensing. Taylor & Francis, Boca Raton, FL.

Worawattanamateekul, J., Adam, N., Hoffmann, J., Kampes, B. M., 2003. Urban deformation monitoring in Bangkok metropolitan (Thailand) using differential interferometry and the permanent scatterer technique. In: Third International Workshop on ERS SAR Interferometry, 'FRINGE03', Frascati, Italy, 1-5 Dec 2003. p. 22.

Xia, Y., Kaufmann, H., Guo, X., 2002. Differential SAR interferometry using corner reflectors. In: International Geoscience and Remote Sensing Symposium, Toronto, Canada, 24–28 June 2002. pp. 1243 – 1246.

Xu, C., Wang, H., Ge, L., Yonezawa, C., Cheng, P., 2006. InSAR tropospheric delay mitigation by GPS observations: a case study in Tokyo area. Journal of Atmospheric and Solar-Terrestrial Physics 68 (6), 629–638.

Zawodny, J., Oltmans, S., 2001. Seasonal variation of water vapor in the lower stratosphere observed in Halogen Occultation Experiment data. Journal of Geophysical Research 106 (D13), 14–313.

Zebker, H., Lu, Y., 1998. Phase unwrapping algorithms for radar interferometry: residue-cut, least-squares, and synthesis algorithms. Journal of the Optical Society of America A 15 (3), 586–598.

Zebker, H., Rosen, P., Earth, J., 1997. Atmospheric artifacts in Interferometric SAR surface deformation and topographic maps. J. Geophys. Res. Solid Earth 102, 7547–7563.

Zebker, H. A., Goldstein, R. M., 1986. Topographic mapping from interferometric Synthetic Aperture Radar observations. Journal of Geophysical Research 91 (B5), 4993–4999.

Zebker, H. A., Rosen, P. A., Goldstein, R. M., Gabriel, A., Werner, C. L., 1994. On the derivation of coseismic displacement fields using differential radar interferometry: the Landers earthquake. Journal of Geophysical Research 99, 19617–19634.

Zumberge, J., Heflin, M., Jefferson, D., Watkins, M., Webb, F., 1997a. Precise Point Positioning for the efficient and robust analysis of GPS data from large networks. Journal of Geophysical Research-Solid Earth 102, 5005–5017.

Zumberge, J., Watkins, M., Webb, F., 1997b. Characteristics and applications of precise GPS clock solutions every 30 seconds. Navigation(Washington, DC) 44, 449–456.

Appendices

Appendix A

Corner Reflector Theory

A.1 Man-made Passive Corner Reflectors

An object exposed to an electro-magnetic wave *scatters* incident energy in all directions and the object itself is referred to as a *scatterer*. SAR imaging works because some of the signal emitted is scattered back (called *backscattering*) to the source of the wave (Skolnik, 1990). This received energy is either reflected back directly (complex-conjugate reflection) or *retro-reflected*. Retro-reflection is a well understood phenomenon in the field of optics whereby the electromagnetic wave front is reflected back along a vector that is parallel to but opposite in direction from the wave's source (O'Brien et al., 1999). This is a natural phenomenon which occurs because some surfaces modify reciprocally the paths of the incoming and outgoing waves. This effect can be greatly enhanced through optimally designed reflectors which return a signal of much greater amplitude than might be expected from the physical size of the reflector; this effect is maintained over a wide set of incidence angles, especially for trihedral reflectors.

In measurable terms, the effect of using three plane surfaces in a trihedral arrangement is an increase in its RCS when compared to any other arrangement of the same three surfaces. RCS (assuming uniform radiation in all directions) is defined as the projected area of a metal sphere which if substituted for the scatterer would scatter the same power back to the radar. Any such hypothetical sphere would expand and contract significantly with the orientation of a scatterer with respect to the energy

source (Bhattacharyya and Sengupta, 1991)

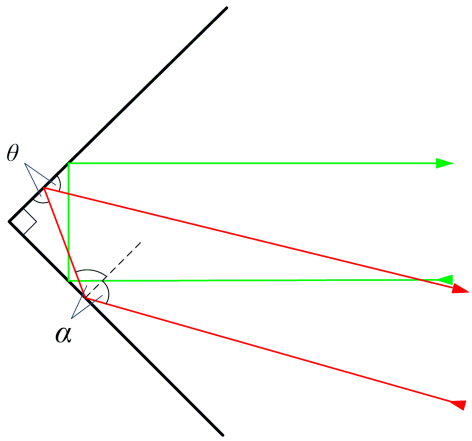

Figure A.1: Retro-reflectance in two dimensions. Outgoing electro-magnetic waves are returned along a path parallel to, but opposite in direction to incoming waves due to a pair of specular reflections.

Figure A.1 is an example of dihedral retro-reflection. The perpendicularity of the faces ensures that if a wave enters the aperture of the reflector, a pair of specular reflections occurs for which the angle of incidence equals the angle of reflection, as can be seen in figure A.1. This effect returns the wave in the direction it came. The radar cross section for a dihedral reflector (σ) is (Schaeffer et al., 1985):

$$\sigma = \frac{8\pi a^2 b^2}{\lambda^2} \tag{A.1}$$

where a and b are the dimensions of the sides and λ is the signal wavelength. However, because some signals reflected by one face will not be intercepted by the opposite face, a more general expression is:

$$\sigma \approx \frac{4\pi A_{eff}^2}{\lambda^2} \tag{A.2}$$

where A_{eff} is the *effective* projected area along the axis of symmetry. Dihedral reflectors provide a large RCS only in the plane perpendicular to the reflector. The addition of a third plate to form a trihedral reflector provides a large RCS in the other two planes also (Bhattacharyya and Sengupta, 1991) and echoes are received from single, double and triple bounce interactions with the triple bounce being dominant. Computation of the RCS for a trihedral reflector, as with a dihedral reflector, usually only involves the effective area; this only includes portions of the surfaces which

participate in the triple bounce which, when viewed perpendicular to the trihedral aperture, is the hexagonal area shown in figure A.2.

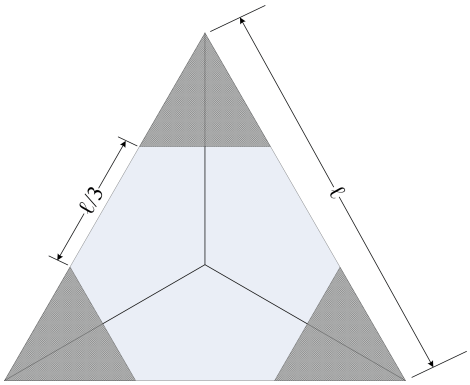

Figure A.2: When optimally aligned, the effective area of a trihedral reflector is only that which participates in the triple bounce mechanism and is hexagonal with sides of $\frac{\ell}{3}$.

The RCS for a trihedral reflector along the axis of symmetry using only the effective area is arrived at by inserting the area for a hexagon into equation A.2 (Knott, 2006):

$$\sigma \approx \frac{\pi \ell^4}{3\lambda^2} \tag{A.3}$$

which for reflectors with sides of 0.8m such as the ones used in this project is 135.8m^2. For a full mathematical description of retro-reflection and corner reflector design, see Bhattacharyya and Sengupta (1991) and Kim and Lee (2007).